

Numerical modelling and InSAR monitoring of settlement in Champlain clays

by

Amirhossein Shafaei Shahboulaghi

THESIS PRESENTED TO ÉCOLE DE TECHNOLOGIE SUPÉRIEURE
IN PARTIAL FULFILLMENT FOR THE DEGREE OF
DOCTOR OF PHILOSOPHY
Ph.D.

MONTREAL, OCTOBER 02, 2022

ÉCOLE DE TECHNOLOGIE SUPÉRIEURE
UNIVERSITÉ DU QUÉBEC



Amirhossein Shafaei Shahboulaghi, 2022



This Creative Commons licence allows readers to download this work and share it with others as long as the author is credited. The content of this work can't be modified in any way or used commercially.

BOARD OF EXAMINERS (THESIS PH.D.)

THIS THESIS HAS BEEN EVALUATED
BY THE FOLLOWING BOARD OF EXAMINERS

Mr. François Duhaime, Thesis Supervisor
Department of Construction Engineering, École de technologie supérieure

Mr. Louis Lamarche, President of the Board of Examiners
Department of Mechanical Engineering, École de technologie supérieure

Mr. Yannic A. Ethier, Member of the jury
Department of Construction Engineering, École de technologie supérieure

Mr. Saeid Homayouni, External Evaluator
National Scientific Research Institute (INRS)

THIS THESIS WAS PRESENTED AND DEFENDED
IN THE PRESENCE OF A BOARD OF EXAMINERS AND PUBLIC

ON MONDAY, AUGUST 30, 2022

AT ÉCOLE DE TECHNOLOGIE SUPÉRIEURE

FOREWORD

This thesis was written as a requirement for the Ph.D. in applied engineering, at École de technologie supérieure (ÉTS). The author worked on the subject between May 2017 and August 2022. The content is the original work of its author Amirhossein Shafaei Shahboulaghi.

ACKNOWLEDGMENT

First and foremost, I would like to thank my professor, Francois Duhaime, for undertaking the supervision of this study. Without his efforts, this dissertation would not have been possible. I really appreciate the fact that he thought me how to stay always determined, patient, detail-oriented, eager to learn and open to criticism throughout my PhD studies.

My thanks to the members of Ph.D. committee, Professors Saeid Homayouni, Yannic A. Ethier, and Louis Lamarche for reviewing this thesis and providing their valuable comments and suggestions, which indeed improved the content of this dissertation.

I also thank my friends and colleagues at LG2 group for all their support and friendships.

I also thank the city of Saint-Marthe for providing the access of their test site, NSERC for funding the project, and Professor Daniele Perissin and the SARPROZ team for providing the SARPROZ license.

My special thanks to my wife, Shirin, for her patience, understanding and wonderful kindness during my doctoral work. I have saved the last words of these acknowledgements for my family for their unconditional love and support. My beloved mother that supported me with her endless love from miles away. My dear brother, Pezhman, who has always been supportive and encouraging to me. My lovely sister, Parizad, a symbol of devotion and kindness in the family, for her endless supports since the early phases of my education.

MODÉLISATION NUMÉRIQUE ET SUIVI INSAR DU TASSEMENT DANS LES ARGILES CHAMPLAIN

Amirhossein Shafaei Shahboulaghi

RESUMÉ

La présence de dépôts d'argile de Champlain dans de vastes régions de l'est du Canada entraîne une probabilité plus élevée d'aléas géotechniques dans cette région. Le tassement des sols fait partie des aléas géotechniques fortement corrélés à la présence des argiles de Champlain. Une compressibilité élevée et des changements importants d'humidité du sol sont deux éléments clés impliqués dans le tassement des argiles de Champlain. L'affaissement du sol dans un sol à grain fin est souvent causé par une baisse excessive de la pression interstitielle. La modélisation numérique de la pression interstitielle au sein des aquitards argileux peut ainsi fournir des informations précieuses sur les causes et l'évolution du tassement.

Les fluctuations de pression interstitielle mesurées dans les aquitards profonds sont également corrélées à la charge d'humidité au-dessus. L'analyse des séries temporelles de la pression interstitielle corrigée pour les effets barométriques et les marées terrestres permet de quantifier cette corrélation. Cette relation est plus complexe dans les aquitards peu profonds en raison de leurs interactions plus fortes avec le milieu environnant. Les fluctuations saisonnières de la nappe phréatique sont un exemple de ces interactions. Ces fluctuations induisent des changements de pression interstitielle par écoulement transitoire. Dans la première partie de cette thèse, un modèle par éléments finis (MEF) a été développé avec COMSOL Multiphysics. Le modèle simule les changements de pression interstitielle dans un aquitard d'argile de Champlain à l'aide d'un modèle couplé écoulement-déformation. Un script MATLAB a également été préparé pour l'interface MATLAB LiveLink dans COMSOL sur la base d'une série d'équations hydrologiques. Le script MATLAB effectue une itération étape par étape sur des conditions aux limites de contrainte totale pour reproduire les données historiques de pression interstitielle obtenues sur le terrain. Ces données historiques ont été obtenues du site d'essai de Sainte-Marthe près de Montréal, Canada.

La deuxième partie de cette thèse est consacrée au suivi par interférométrie radar (InSAR) et à la modélisation numérique du tassement. Les mouvements verticaux du sol pour la période de mai 2017 à décembre 2019 ont été étudiés pour le site d'essai de Sainte-Marthe à l'aide de la modélisation numérique et de la technique InSAR à diffuseurs permanents (PSI). Un modèle numérique basé sur la méthode des éléments finis (FEM) et la théorie de la poroélasticité de Biot a été développé. Le modèle estime le tassement et l'expansion du sol à l'aide de mesures de la pression interstitielle dans le substratum rocheux et la couche d'argile fracturée, et de la température obtenue à partir d'un site d'étude à Sainte-Marthe, au Québec. Le modèle est capable de traiter la déformation séparément dans une couche superficielle qui est hydrauliquement plus active et une couche d'argile intacte qui est moins perméable et plus molle. Pour suivre le tassement au site d'étude, les déplacements verticaux ont été calculés à

plus grande échelle dans la région de Vaudreuil-Soulanges avec la technique PSI en utilisant SARPROZ avec des approches linéaires et non linéaires.

La dernière partie de cette thèse porte sur le suivi du tassement sur l'île de Montréal d'avril 2016 à février 2022. La vitesse de déplacement a été suivie à l'aide de la méthode PSI et d'une technique linéaire sur l'ensemble de l'île de Montréal. Le but de ce suivi était de détecter les principales zones de tassement important sur l'île de Montréal.

Le résultat de cette thèse peut être classé en trois sections. Les résultats de la première partie de cette thèse ont porté sur la modélisation numérique des changements de pression interstitielle. Ces résultats ont montré que le modèle peut reproduire raisonnablement bien la série temporelle historique de pression interstitielle. La mise en œuvre du script MATLAB pourrait améliorer considérablement les résultats d'optimisation. Concernant la modélisation numérique du tassement dans la deuxième partie de la thèse, les résultats montrent un accord raisonnable entre les simulations MEF et les estimations PSI. Une tendance saisonnière de déplacement avec une portée maximale de 15 mm a été estimée. Un affaissement aussi important que 55 mm a été estimé par le modèle MEF et l'approche PSI non linéaire sur une période de 30 mois. Le PSI non linéaire pourrait détecter plus efficacement le déplacement non linéaire du sol. La vitesse de déplacement était de -9 mm/an pour la méthode non linéaire contre -8 mm/an pour l'estimation MEF. Le suivi à long terme du tassement sur l'île de Montréal a révélé que des tassements importants jusqu'à -10 mm/an sont en cours dans certains secteurs de l'île de Montréal. Cette progression continue du tassement dans cette région pourrait être induite par la diminution de l'humidité de l'eau des sols associée aux effets du changement climatique.

Mots clés : argile Champlain, pression interstitielle du sol, tassement du sol, InSAR, PSI, méthode des éléments finis

NUMERICAL MODELLING AND INSAR MONITORING OF SETTLEMENT IN CHAMPLAIN CLAYS

Amirhossein Shafaei Shahboulaghi

ABSTRACT

The presence of Champlain clay deposits in vast areas of eastern Canada brings a higher probability of geotechnical hazards in this region. Soil settlement is one of the geotechnical hazards that is believed to be strongly correlated to the presence of Champlain clays. High compressibility and significant soil moisture changes are two key elements involved in settlement of Champlain clays. Land subsidence in fine-grained soil is often caused by an excessive pore pressure decline. Numerical modelling of the pore pressure within clay aquitards can thus provide valuable information on the causes and progress of settlement.

The pore pressure fluctuations measured in deep aquitards are also correlated to moisture loading above it. Analyzing the pore pressure record corrected for barometric and Earth tide effects allows this correlation to be quantified. This relationship is more complex in shallow aquitards due to their stronger interactions with the surrounding environment. Seasonal fluctuations of the water table are an example of these interactions. These fluctuations induce pore pressure changes through transient flow. In the first part of this thesis, a finite-element model (FEM) was developed with COMSOL Multiphysics. The model simulates the pore pressure changes within a saturated Champlain clay aquitard using a coupled flow-deformation model. A MATLAB script was also prepared for the MATLAB LiveLink interface in COMSOL based on a series of hydrological equations. The MATLAB script iterates step-by-step on a total stress boundary conditions to replicate the pore pressure time series obtained in the field. These data were obtained from the Sainte-Marthe test site near Montreal, Canada.

The second part of this thesis is dedicated to InSAR monitoring and numerical modelling of settlement. It investigates the vertical ground movements between May 2017 and December 2019 on the test site using numerical modelling and the Persistent Scatterer InSAR (PSI) technique. In this regard, a model based on the finite element method (FEM) and Biot's poroelasticity theory was developed. The model estimates soil settlement and expansion using pore pressure measurements in the bedrock and fractured clay layer, and temperature obtained from a study site in Sainte-Marthe, Quebec. The model is capable of addressing the deformation separately in a hydraulically more active superficial top layer and deeper intact clay layer. To monitor the settlement at the study site, vertical displacements were calculated at a larger scale in the Vaudreuil-Soulanges region with the PSI technique using SARPROZ with linear and non-linear approaches.

The last part of this thesis deals with the monitoring of settlement on Montreal Island between April 2016 and April 2022. The displacement velocity was monitored using the PSI method and a linear technique all over the Montreal Island. The aim of this monitoring was to detect the main areas with large settlements on Montreal Island.

The results in this thesis can be grouped in three parts. The results for the first part of this thesis dealt with numerical modelling of the pore pressure changes. These results showed that the model can reproduce the historical pore pressure time series reasonably well. Implementation of the MATLAB script could significantly improve the optimization results. Concerning the numerical modelling of settlement in the second part of the thesis, the results show a reasonable agreement between the FEM simulations and PSI estimates. A seasonal trend of displacement with a maximum range of 15 mm was estimated. Subsidence as large as 55 mm was estimated by the FEM model and non-linear PSI approach over a period of 30 months. Non-linear PSI could detect the non-linear displacement of the soil more effectively. The displacement velocity was -9 mm/year for the non-linear method compared to -8 mm/year for the FEM estimation. The long-term monitoring of the settlement on Montreal Island revealed that serious settlements up to -10 mm/year are in progress in certain areas of the Montreal Island. The continuous progress of settlement in this region might be induced by a decrease in the soil water moisture associated with the effect of climate change.

Keywords: Champlain clay, soil pore pressure, soil settlement, InSAR, PSI, finite element method

TABLE OF CONTENTS

	Page
INTRODUCTION	1
CHAPTER 1 HYDROLOGY AND GEOTECHNICAL PROPERTIES OF CHAMPLAIN CLAYS.....	11
1.1 Champlain clays formation	11
1.2 Stratigraphy of Champlain clays deposits	12
1.3 Particle size, mineralogy and distribution of Champlain clays	13
1.4 Hydraulic conductivity of Champlain clays	14
1.5 Mechanical properties of Champlain clays	16
1.5.1 Undrained Shear strength.....	17
1.5.2 Sensitivity	18
1.5.3 Preconsolidation pressure	19
1.5.4 Compressibility	20
1.5.5 Thermal properties.....	23
1.6 Sainte-Marthe Study site	26
CHAPTER 2 WATER BALANCE AND PORE PRESSURE CHANGES IN CHAMPLAIN CLAYS.....	31
2.1 Background Theory.....	32
2.1.1 Stress-deformation relationship of soil	32
2.1.2 Van der Kamp & Gale (1983) theory	34
2.1.3 Groundwater hydraulic equation (transient flow).....	35
2.1.3.1 Pore pressure response to loading stress.....	36
2.1.3.2 Pore pressure changes due to atmospheric pressure variation...	36
2.1.3.3 Pore pressure changes due to Earth tides.....	37
2.1.3.4 Vertical flow due to stress changes (Earth tides & barometric loading).....	37
2.1.3.5 Total pressure response to earth tides and barometric loadings and vertical flow (resulted from stress changes).....	38
2.2 Conceptual model.....	38
2.3 Data collection.....	41
2.3.1 Meteorological data	41
2.3.2 Pore pressure time series.....	42
2.4 Numerical approach	47
2.4.1 Boundary and initial conditions:	49
2.4.2 Material properties	50
2.4.3 MATLAB script.....	54
2.4.3.1 Perfect Stress Method (PSt).....	55
2.4.3.2 Net Water Balance Method (NWB).....	56

CHAPTER 3	NUMERICAL MODELLING OF SOIL DEFORMATION IN CHAMPLAIN CLAYS.....	61
3.1	Settlement definition	61
3.1.1	Soil settlement in cohesive clays	64
3.2	Linear poroelasticity.....	67
3.2.1	One dimensional deformation in porous media induced by thermal and mechanical loads.....	69
3.2.1.1	Frost deformations	71
3.3	Methodology	72
3.3.1	Numerical modelling of deformations of Sainte-Marthe study site.....	72
3.3.1.1	Conceptual Model.....	73
3.3.1.2	Partial differential equation (PDE) in COMSOL.....	74
3.3.1.3	Domain A.....	75
3.3.1.4	Domain B.....	75
3.3.1.5	Boundary conditions and initial values.....	76
CHAPTER 4	INSAR MONITORING OF THE DEFORMATION.....	78
4.1	InSAR Basics	79
4.1.1	Electromagnetic Radiation.....	80
4.1.2	Synthetic Aperture Radar (SAR).....	83
4.1.3	Sentinel-1	86
4.2	InSAR in geotechnical engineering.....	91
4.3	DInSAR.....	94
4.4	PSI-DInSAR analysis	97
4.4.1	SARPROZ.....	98
4.5	InSAR monitoring the deformation in the Sainte-Marthe area	100
4.5.1	InSAR Data (SAR Images, Saint Marthe area)	100
4.5.2	PSI-DInSAR-Pre-processing	101
4.5.2.1	Preparing the stack of interferograms	101
4.5.2.2	PSI-DInSAR-PS selection	102
4.5.3	Validation of the PS-InSAR results	103
4.6	InSAR monitoring the deformation in the Montreal area	105
4.6.1	InSAR data (SAR images, Montreal area).....	106
4.6.2	PSI-DInSAR-Pre-Processing	106
4.6.2.1	Preparing the stack of interferograms	107
4.6.2.2	PSI-DInSAR-PS selection	107
CHAPTER 5	RESULTS AND DISCUSSION.....	110
5.1	Water balance and pore pressure simulation.....	110
5.2	Numerical modelling of settlements in Sainte-Marthe.....	117
5.3	Comparison of deformation in Sainte-Marthe based on InSAR and FEM	122
5.4	InSAR monitoring of deformation in the Montreal area.....	126
5.4.1	InSAR deformation results for Saint-Jacques Escarpment (target area 1).....	127

5.4.2	InSAR deformation results for Parc d'entreprise pointe Sainte-Charles (target area 2)	129
5.4.3	InSAR deformation results on Roy Street (target area 3)	131
5.4.4	Other monitored large settlements	134
5.4.4.1	InSAR deformations on Boulevard de l'Île-des- Soeurs between Elgar and François Streets	134
5.4.4.2	InSAR deformations near the Evolo high rise building in l'Île-des-Soeurs	135
5.4.4.3	InSAR deformations in Pointe-Saint-Charles	137
5.4.4.4	InSAR deformations in the Village- Sainte Marie-Hochelaga-De Lorimier- Le Plateau Mont Royal-Angus.....	139
5.4.4.5	InSAR deformations in Villeray	142
5.4.4.6	InSAR deformations on Boulevard de la Verendrye (Angrignon Park)	144
5.4.4.7	InSAR deformations in Côte Saint Luc-Lachine	146
5.4.4.8	InSAR deformations on Notre Dame Island.....	148
5.4.4.9	InSAR deformations in Westmount- Côte des Neiges	149
5.4.4.10	InSAR deformations in Montreal East.....	151
5.4.4.11	InSAR deformations in Dorval- Pointe-Claire	153
5.4.4.12	InSAR deformations in Dollard des Ormeaux.....	155
5.4.4.13	InSAR deformations in Pierrefonds-Kirkland-Beaconsfield...	157
5.4.5	Summary of InSAR monitoring of displacements in Montreal Island	159
CONCLUSION AND RECOMMENDATIONS		164
6.1	Conclusion.....	164
6.2	Recommendations	167
APPENDIX I BIOT 1940 THEORY		171
APPENDIX II VAN DER KAMP AND GALE (1983) THEORY		174
APPENDIX III MATLAB CODE OF PORE PRESSURE TIME SERIES SIMULATION.....		176
BIBLIOGRAPHY.....		200

LIST OF TABLES

	Page
Table 1.1 Mineralogy of Champlain clays	14
Table 1.2 Reported Young's modulus of Champlain clays	23
Table 2.1 Poisson's ratios in sensitive clays.....	50
Table 2.2 The sensitivity of the strain and displacement to Poisson's ratio.....	51
Table 2.3 Geotechnical properties for the Sainte-Marthe study site	54
Table 3.1 Hydraulic, thermal, and displacement boundary conditions in the model	77
Table 4.1 Specifications of analyzed datasets with SARPRROZ.....	101
Table 4.2 GNSS stations locations and validation of PS-InSAR estimations (linear)	104
Table 4.3 Specifications of analyzed datasets with SARPRROZ (Montreal)	107
Table 5.1 Statistical comparison of the FEM and PSI displacement time series	125
Table 5.2 Number and percentage of the large settlements for each soil type	161
Table 5.3 Average displacement of PS pixels with velocity more than -7 mm/year.....	163

LIST OF FIGURES

	Page
Figure 1.1 The location of the Champlain Sea.....	12
Figure 1.2 Stratigraphy of Champlain clays deposits	13
Figure 1.3 Hydrological properties of Champlain clays	16
Figure 1.4 Typical stress-strain curve for a Champlain clay	21
Figure 1.5 Normalised stiffness degradation curve and the three strain levels.....	22
Figure 1.6 Thermal conductivity of a Champlain clay sample	24
Figure 1.7 Schematic of freezing in soils.....	26
Figure 1.8 Location of the Sainte-Marthe study site.....	27
Figure 1.9 Cross-sectional profile of the study site	28
Figure 1.10 Profile and geotechnical properties of the Sainte-Marthe study site	29
Figure 2.1 A giant sinkhole in Iran due to water depletion.....	32
Figure 2.2 Conceptual model	40
Figure 2.3 ETO calculator software	42
Figure 2.4 The Kansas Geological Survey Barometric Response software.....	44
Figure 2.5 Raw and Corrected hydraulic heads for barometric effects	45
Figure 2.6 An example of the filtered and non-filtered hydraulic head time series	46
Figure 2.7 A picture of developed mesh	48
Figure 2.8 Hydraulic and mechanical boundary conditions in the model.....	49
Figure 2.9 Simulated hydraulic head time series for different Poisson's ratio	51
Figure 2.10 Simulation steps in pore pressure correction	55
Figure 2.11 Components of the water balance equation	56
Figure 2.12 Schematic representation of the time-stepping scheme for the day i	59

Figure 3.1	Primary and secondary consolidation settlement	63
Figure 3.2	Porosity distribution of Champlain clay specimens under different stress levels	65
Figure 3.3	Scheme of ΔV_f function	72
Figure 3.4	Conceptual model	73
Figure 3.5	Mesh and geometry of the model in COMSOL	76
Figure 4.1	Electromagnetic wave.....	80
Figure 4.2	Electromagnetic spectrum	81
Figure 4.3	Coherent and non-coherent radar processing	82
Figure 4.4	Synthetic Aperture Radar	83
Figure 4.5	Acquisition geometry of synthetic aperture radar	84
Figure 4.6	A SAR image of an airport with clearly speckle effects	86
Figure 4.7	Sentinel-1 A satellite before launch.....	87
Figure 4.8	Sentinel- 1 satellites coverage	88
Figure 4.9	Sentinel-1 acquisition modes.....	89
Figure 4.10	A Sentinel-1 SLC product in IW mode	90
Figure 4.11	Scheme of deformation monitoring using DInSAR	96
Figure 4.12	Example of SARPROZ interface.....	99
Figure 4.13	Dataset and area of interest.....	101
Figure 4.14	Star graph showing temporal and perpendicular baselines of the analysed dataset by SARPROZ	102
Figure 4.15	PS distributions (a) and, connection network (b) of the PS pixels in SARPROZ	103
Figure 4.16	Locations of GNSS stations and study site.....	104
Figure 4.17	Validation of the PS-InSAR estimations (non-linear).....	105
Figure 4.18	Dataset and area of the interest for Montreal Island in central zone	106

Figure 4.19	Star graph of the SAR interferograms in InSAR processing of the Montreal.....	107
Figure 4.20	PS distributions (a) and, connection network (b) of the PS pixels in SARPROZ	108
Figure 5.1	Water level changes for BS, BWL, GWL, and OB time series.....	111
Figure 5.2	Simulated and observed hydraulic head time series for a depth of 12.2 m	112
Figure 5.3	Daily precipitation, evapotranspiration, mean temperatures and simulated and observed hydraulic head in Sainte-Marthe study site	113
Figure 5.4	Comparison of hydraulic head values for a constant stress.....	114
Figure 5.5	Estimated net moisture balances in BS, NWB and PS optimization.....	115
Figure 5.6	Total estimated and observed monthly runoff along with stress time series based on PS, NWB, and BS scenarios.....	117
Figure 5.7	Impact of M modulus on the simulated settlement time series along with the hydraulic head time series	119
Figure 5.8	Settlement times series (FEM) for four scenarios along with the monthly precipitation and thermal boundary conditions	120
Figure 5.9	The impact of the T_{frozen} on the simulated settlement time series.....	121
Figure 5.10	Vertical velocities of all processed PS pixels (mm/year) in time series analysis at Sainte-Marthe.....	123
Figure 5.11	Displacement time series of FEM (Scenario 2-no frost heave), FEM (Scenario 2 with frost heave) and SARPROZ (PS1, PS2)	124
Figure 5.12	Mean velocity map for the Montreal Island	127
Figure 5.13	Mean velocity map for the Saint-Jacques Escarpment.....	128
Figure 5.14	Settlement time series for PS pixel T1-3 in Saint-Jacques Escarpment	129
Figure 5.15	Mean velocity map of PESPC in Montreal	130
Figure 5.16	Settlement time series for PS pixel T2-1 in PESPC	130
Figure 5.17	Cracks in the parking area of the PESPC	131
Figure 5.18	Mean velocity map for the Roy Street area, Montreal.....	132

Figure 5.19	Settlement time series of PS pixel T3-1 in the Roy Street area.....	133
Figure 5.20	Settlement time series of PS pixel T3-2 in the Roy Street area.....	133
Figure 5.21	Mean velocity map for Boulevard de l'Île-des-Soeurs in Montreal.....	134
Figure 5.22	Settlement time series for PS pixel Z1	135
Figure 5.23	Mean velocity map of Evolo building in l'Île-des-Soeurs	136
Figure 5.24	Settlement time series for PS pixel Z2	136
Figure 5.25	Mean velocity map for the Pointe-Saint-Charles area.....	137
Figure 5.26	Settlement time series for PS pixel Z4	138
Figure 5.27	Settlement time series for PS pixel Z6	138
Figure 5.28	Settlement time series for PS pixel Z7	139
Figure 5.29	Mean velocity map of Gay village, Sainte Marie, Hochelaga, De Lorimier, Le Plateau Mont Royal, and Angus areas of Montreal.....	140
Figure 5.30	Settlement time series for PS pixel Z11	141
Figure 5.31	Settlement time series for PS pixel Z14	141
Figure 5.32	Settlement time series for PS pixel Z15	142
Figure 5.33	Mean velocity map for the Villeray area in Montreal	143
Figure 5.34	Settlement time series for PS pixel Z18	143
Figure 5.35	Settlement time series for PS pixel Z19	144
Figure 5.36	Mean velocity map of Boulevard de la Vérendrye next to the entry of the Angrignon Park.....	145
Figure 5.37	Settlement time series for PS pixel Z20	145
Figure 5.38	Asphalt cracks in Boulevard de la Verendrye	146
Figure 5.39	Mean velocity map for the Côte Saint-Luc and Lachine areas of Montreal.....	147
Figure 5.40	Settlement time series for PS pixel Z22	147
Figure 5.41	Mean velocity map for Notre Dame Island in Montreal.....	148

Figure 5.42	Settlement time series for PS pixel Z24 o	149
Figure 5.43	Mean velocity map for Westmount and Côte-des-Neiges.....	150
Figure 5.44	Settlement time series for PS pixel Z25	150
Figure 5.45	Settlement time series for PS pixel Z28	151
Figure 5.46	Mean velocity map for the eastern part of Montreal Island	152
Figure 5.47	Settlement time series for PS pixel Z29	152
Figure 5.48	Settlement time series for PS pixel Z31	153
Figure 5.49	Mean velocity map for Lachine, Dorval and Pointe-Claire.....	154
Figure 5.50	Settlement time series for PS pixel Z33	154
Figure 5.51	Settlement time series for PS pixel Z34	155
Figure 5.52	Mean velocity map of Dollard des Ormeaux.....	156
Figure 5.53	Settlement time series of PS pixel Z40.....	156
Figure 5.54	Settlement time series of PS pixel Z42.....	157
Figure 5.55	Mean velocity map of Pierrefonds, Kirkland and Beaconsfield areas of Montreal.....	158
Figure 5.56	Settlement time series of PS pixel Z46 in Pierrefonds area of Montreal.....	158
Figure 5.57	Large settlements on Montreal Island geolocated on the surficial geology map	159
Figure 5.58	Average cumulative displacement of PS pixels with settlement velocity larger than -7 mm/year with respect to average monthly atmospheric temperatural, rainfall deficit, and average monthly precipitation.....	162

LIST OF ABBREVIATIONS

APS	Atmospheric phase screen
ASC	Ascending
BE	Unit response function
BRF	Barometric response function
BS	Base Scenario
BWL	Bedrock water level
CPT	Cone penetration test
DEM	Digital elevation models
DInSAR	Differential interferometric synthetic aperture radar
ESD	Enhanced Spectral Diversity
ÉTS	École de technologie supérieure
EW	Extra-wide swath
FAO	Food and Agriculture Organization
FEM	Finite elements method
GWL	Groundwater level
GIS	Ground information system
GNSS	Global navigation satellite system
GPS	Ground Positioning system
GRD	Ground range detected
InSAR	Interferometric SAR
IW	Interferometric wide swath
LIDAR	Light detection and ranging

MRM	Multiple regression method
MT-InSAR	Multi-temporal InSAR
MW	Monitoring wells
NWB	Net water balance method
OB	Observed
OCR	Overconsolidation ratio
PDE	Partial differential equation
PSI	Persistent scatterer DInSAR
PSt	Perfect stress method
RTK	Real-time kinematic
SAR	Synthetic aperture radar
SARPROZ	SAR PROcessor by periZ
SBAS	Small baseline subset
SFCC	Soil freezing characteristic curve
SLC	Single look complex
SLC	Single look complex
SM	Strip map
SNR	Signal to noise ratio
VNIR	Visible/near InfraRed
VWP	Vibrating Wire Piezometer

LIST OF SYMBOLS

A	A constant that depends on properties of the fluid and the tortuosity of the pore network
A_{wet}	The water available for evapotranspiration
A_{wr}	Water available for runoff
B	Physical constant
B_d	The width of the loaded area
BE	Unit response function
Br	Barometric pressure
Br_{avg}	Average barometric pressure
B_s	Bandwidth of the retransmitted pulse
C_s	The shape and rigidity factor
C_{sp}	Specific surface
cu	Undrained shear strength
cu_r	Remoulded undrained shear strength
d_{los}	Displacement in line of sight
d_r	The distance between the target point and the sensor in the range direction
e	Void ratio
e_0	Initial void ratio
E	Young's modulus
E_{max}	Maximum Young's modulus
ET	Evapotranspiration rate

XXVIII

$ET(i)$	The total evapotranspiration for the day i
ET_r	The evapotranspiration of liquid water (from rain source)
ET_s	The evapotranspiration of snow (from snow source)
f_r	Frequency
G	Shear modulus
g	Gravitational acceleration
G_{max}	Maximum shear modulus
g_{sp}	Specific gravity of the solid phase
H	Hydraulic head
H_{br}	Hydraulic head in the bedrock
H_{wl}	Hydraulic head associated with groundwater level
h_{frost}	Frost heave
H_{intp}	The initial hydraulic head is calculated using linear interpolation with respect to the initial hydraulic of the top and bottom boundaries
K'	Confined modulus of elasticity
K_b	Bulk modulus
k_{eff}	Effective thermal conductivity
K_f	Bulk elasticity modulus of water
K_h	Hydraulic conductivity
k_p	Intrinsic permeability
l	length of physical SAR antenna
L_0	The initial thickness of the soil layer

L_A	The length of the synthetic aperture in the azimuth direction
L_e	Loading efficiency
M	Constrained modulus
m_a	The average of the amplitude
M_b	Biot modulus
MP_1	The distance between satellite in position M and target point of P1
MP_2	The distance between satellite in position M and target point of P2
MP_2	The distance between satellite in position M and target point of P2
m_v	Soil compressibility
n	Porosity of the material
OCR	Overconsolidation ratio
P_d	Amplitude dispersion index
PI	Plasticity index
P_R	Precipitation rate
P_r	Sum of precipitation as rain
P_{rc}	The rain which is stored as near-surface groundwater
P_{sc}	The Snow which is stored as snow cover (equivalent water height)
q'	The magnitude of the uniformly distributed load
R	Runoff rate
$r(i)$	Regression coefficient
R_{max}	Maximum runoff rate
R_r	The amount of rain leaving the system as runoff

XXX

R_s	The amount of snow leaving the system as runoff
s'	3D storage coefficient
SD_ϕ	Temporal standard deviation of the phase
SP_1	The distance between satellite in position S and target point of P1
SP_2	The distance between satellite in position S and target point of P2
S_s	Specific storage coefficient
S	Storage coefficient
SP	Segregation potential
S_t	Sensitivity of the soil
ST_i	The immediate settlement
ST_c	The total consolidation settlement
s_w	Wind speed at 2 m height
S_c	Constrained specific storage
t_{FR}	Freezing duration time
T	Temperature
T_{2m}	Mean daily air temperature at 2 m height
T_{frozen}	Freezing temperature
T_{init}	The depth-dependent initial conditions for temperature
T_{initp}	The initial temperature head is calculated using linear interpolation with respect to the initial temperatures of the top and bottom boundaries
T_{seg}	Segregation freezing temperature
u	Pore pressure

$u^* (i)$	Measured pore pressure on day i
$u'_j(i)$	FEM pore pressure on day i for iteration j of the Newton-Raphson method
u_{water}	Pore water pressure at the ice lens
u_{ice}	Pore water pressure at frozen fringe
u_{init}	depth-dependent initial conditions for pore pressure
$U_{w'}$	Corrected pore pressure
U_w	Uncorrected pore pressure
u_x	Displacement component in x direction
V_p	Wave propagation speed in a vacuum environment
vp_a	Actual vapour pressure
vp_s	Saturation vapour pressure
V_s	Shear wave velocity
V_s^*	Normalized shear wave velocity
v_y	Displacement component in y direction
WL	Liquid limit
Wn	Natural water content
w_z	Displacement component in z direction
α	Biot-Willis coefficient
α_T	Thermal expansion coefficient
β	A physical constant ranging from 0 to 1
γ^p	Psychrometric constant
γ_w	Specific weight of the water

Δ'	Slope of the vapour pressure curve
Δe_p	Void ratio reductions in the primary compression
Δe_s	Void ratio reductions in the secondary compression
$\Delta\phi_{int}$	Interferometric phase
ϵ	Volumetric strain
ϵ_T	Vertical strain due to earth tide
ϵ_{xx}	Normal strain in x direction
ϵ_{yy}	Normal strain in y direction
ϵ_{zz}	Normal strain in z direction
λ_l	Wavelength
μ	Dynamic viscosity of water
$(\rho c_p)_{eff}$	Effective volumetric heat capacity at constant pressure
N_{ra}	Net radiation at the crop surface
ρ_d	Dry density
ρ_{tot}	Bulk density
ρ_r	Resolution of the SAR image in range direction
ρ'_r	Resolution of the SAR image in azimuth direction
ρ_i	Density of ice
ρ_w	Density of water
σ	Total stress
σ'	Effective stress
σ_B	Atmospheric pressure

σ'_{ins}	In situ effective stress
$\sigma_j(i)$	Total stress on day i for iteration j of the Newton-Raphson method
σ'_p	Preconsolidation pressure
σ_t	Octahedral normal stress
σ'_v	Vertical effective stress
σ_{xx}	Normal total stress in x direction
σ_{yy}	Normal total stress in y direction
σ_{zz}	Normal total stress in z direction
τ_p	Pulse duration
ν	Poisson's ratio
$\varphi.DP$	The displacement phase in line of sight
$\varphi.re(atm)$	Residual atmospheric phase
$\varphi.re(noise)$	residual noises
$\varphi.re(orb)$	Residual orbital error
$\varphi.re(tp)$	Residual topographic phase
$\varphi.sct-M$	Shifted phases of the target pixel in satellite positions M
$\varphi.sct-S$	Shifted phases of the target pixel in satellite positions S
$\varphi.TP$	Topographic phase
φ_M	The measured phases for the target pixel from the satellite's positions of M
φ_S	The measured phases for the target pixel from the satellite's positions of S
Γ_h	Soil heat flux density

INTRODUCTION

Land settlement is a crucial issue in geotechnical engineering. For some structures, even a very small settlement might result in failure of the foundation and catastrophic consequences. For example, the Surfside condominium collapse that occurred in 2021 in Florida was later linked with the subsidence of the foundations in the 90s (1993-1999, Fiaschi, & Wdowinski, 2020). These settlements were monitored after the failure by observing the historical satellite images.

The frequency of settlement in a region is strongly associated with the presence of soils that are prone to deformation. In general, there are specific mechanical properties that make a soil more vulnerable to natural settlement or settlement due to an applied load. These properties include high compressibility for soft clays and materials with a high porosity such as peat and loose sand. Unstable materials such as acidic peat and organic soils can also be associated with settlements. Unstable particle size distributions can also lead to internal erosion and settlement.

A large extent of eastern Canada and the lowlands of the St. Lawrence River valley are covered with Champlain clays. These fine-grained soils are very prone to deformation. They have a high compressibility and they rapidly lose their shear strength when loaded. The existence of Champlain clays in these regions brings a higher probability of geotechnical hazards. Other than settlements and cracks in building foundations (e.g., Morin & Gervais, 1987; Silvestri et al., 1990), a large number of landslides have also occurred in Champlain clays (e.g., Hugenholtz & Lacelle, 2004; Tavenas et al., 1971).

In general, settlement studies involve three main tasks:

- Determining the soil mechanical behaviour;
- Finding a numerical approach that can accurately model soil settlement;
- Obtaining accurate settlement measurements.

Several studies have been conducted on the mechanical properties of Champlain clays (e.g., Leroueil et al., 1983b, Lafleur et al., 1982). The most important parameters controlling the

mechanical behaviour of Champlain clays are their high compressibility, high sensitivity, and high water content. Among these, the water content plays a crucial role in settlements. The mechanical behaviour of Champlain clays can be significantly affected by changes in the degree of saturation (Delage & Lefebvre, 1984), for instance in the oxidized crust near the ground surface. By definition, consolidation of saturated clays is always associated with a decrease in the water content. As a result, studying the hydrological characteristics of Champlain clays is a crucial step in investigation of their behaviour for all types of deformation, including settlement.

Subsurface pore pressures time series can provide valuable information on the hydrological state of shallow aquitards of Champlain clays. Moreover, pore pressure monitoring can be used to analyze the soil behaviour during geological and geomorphological phenomena such as earthquakes, landslide and land subsidence (Chen et al., 2015; Ishihara et al., 1981; Mavko & Harp, 1984). Tracking the pore pressure fluctuations before and during a slope failure is an example of these analyses (Harp et al., 1990). Other than deformation and stability analysis, hydraulic and geotechnical properties of the formation, can also be calculated by analyzing the pore pressure records (e.g., Hendry et al., 2017; Marefat et al., 2015; Smith et al., 2013; van der Kamp, 2001).

The relationship between pore pressure and soil deformation is closely linked with the concept of effective stress. The total stress in a soil is borne by both the pore pressure and the soil skeleton. The later is referred to as the effective stress. Interactions between solid deformation and fluid flow are complex and interlinked with other factors such as hydraulic and elastic properties of the formation or the total acting stress. These interactions balance the internal forces within porous media (Shafaei et al., 2019). Volume change and excess pore pressure induced by mechanical loading are examples of these internal interactions.

These complex interactions have been investigated so far through coupled and uncoupled approaches. The coupled approach is based on the Biot (1941) theory which itself was derived from the Terzaghi (1925) consolidation theory. The uncoupled approach is based on Theis

(1935) and mainly used for groundwater hydrology (Gambolati et al., 2000). The focus of the uncoupled approach is fluid dynamic while the coupled approach concerns both fluid flow and solid deformation.

Based on the Biot (1941) theory, a one-dimensional (1D) numerical approach was developed by van der Kamp & Gale (1983) to describe the relation between the pore pressure and a vertical mechanical loading on a saturated homogenous isotropic medium. Their main assumptions were that the mechanical loading acted on a large area and that the lateral deformations induced by pore pressure changes were negligible. In deep confined aquifers where the effects of transient flow due to seasonal fluctuation of groundwater level are minimum, the pore pressure changes mainly reflect the moisture loading above the aquifer (van der Kamp & Schmidt, 2017). Confined aquifers thus can be used as low-cost geological weighing lysimeters (van der Kamp & Maathuis, 1991). Several studies have demonstrated the usefulness of the geological weighing lysimeters in confined aquifers (e.g., Marin et al., 2010; Sophocleous et al., 2006; Toll & Rasmussen, 2007; van der Kamp & Schmidt, 2017).

Thick clay aquitards are also promising candidates to implement the van der Kamp & Gale (1983) approach. Their low permeability reduces the impact of transient flow and isolates their deeper parts from these effects. It is also easier in clay-rich aquitards to subtract the barometric and tidal effects from the hydraulic head fluctuations. This comes from their high compressibility that results in a loading efficiency close to one (Barr et al., 2000). Loading efficiency is the ratio of hydraulic head response in a porous medium to the change in barometric pressure. The implementation of piezometric weighing lysimeters in thick aquitards has been investigated in a number of studies (e.g., Anochikwa et al., 2012; Barr et al., 2000; van der Kamp & Schmidt, 1997). These studies showed a strong correlation between the moisture loading above the aquitard and pore pressure fluctuation after removal of barometric pressure and tidal effects. The van der Kamp & Gale (1983) approach has also been used for purposes other than soil moisture monitoring. Study of solute transport in saturated porous medias (Chang & Yeh, 2016), analysis of the responses of confined aquifers to river stage variation (Pacheco & Fallico, 2015), and investigation of the relation between displacements

and the mechanical loading acting over the vast area of soil (Murdoch et al., 2015) are examples of other applications of this approach.

For shallow aquitards, piezometer readings can be influenced by transient flow. As a result, pore pressure analyses are more complicated for shallow aquitards than for thick aquitards. To have a more realistic simulation, a coupled approach with accurate dynamic boundary conditions is necessary. The boundary conditions should reflect, to the extent possible, the pore pressure and the stress changes pertaining to the seasonal fluctuations of the water table.

The replication of pore pressure time series within a shallow aquitard can bring a better understanding of the mechanical interactions occurring within the soil. However, numerical approaches such as the one presented by van der Kamp & Gale (1983) are not enough to simulate the settlement of the shallow aquitard. There are factors other than pore pressure changes that deal with the deformation within the soil. Even without any applied load, other elements still exist such as temperature gradients effects or soil moisture changes that can induce the settlement.

Settlements related to climate in sensitive clays have several causes and their modelling is generally complex. The deformation mainly occurs at the top of the clayey layer and is closely related to changes in soil water storage (Silvestri, 2000). Increasing and reducing the soil moisture can result in swelling and shrinking of the soil, respectively. Volume changes in the shallow parts of the clay layer can also be due to freeze-thaw cycles and other temperature effects (Yu et al., 2020a; Yu et al., 2020b; Konrad et al., 1995). Part of these deformations is seasonal and induced by annual variability of temperature or water balance (Baracos & Bozozuk, 1957). Non-seasonal deformations are linked to multi-year dry and wet periods. Deeper settlements can be associated with long-term pore pressure and temperature changes and the influence of trees (Bozozuk & Burn, 1960; Hammer & Thompson, 1966). Pore pressure changes can be complex, especially in urban areas (Silvestri et al., 1990). Even if the phenomena governing settlements in changing climate are complex, there is still an opportunity to use simple numerical modelling for parametric studies.

In order to have a validation set as a base of comparison for verifying the numerical modelling of settlement, we need a robust and accurate method to measure the settlement. The settlement measurements available in the literature for the sensitive clays of Eastern Canada have been obtained through the installation of reference pins on structures, extensometers or displacement gauges in the soil (e.g., Eden, 1997; Konrad et al., 1995; Silvestri, 2000). Baracos & Bozozuk (1957) used multi-rod and telescoping concentric gauges for monitoring the seasonal vertical movements of a Champlain clay deposit in the Ottawa area. Settlements of up to 38 mm were recorded over a few years. Silvestri (2000) monitored vertical movements at the clay surface and for buildings between 1990 and 1992 with reference pins and settlement plates on five buildings in Montreal. Settlements of up to 80 and 50 mm were measured for surface and building respectively. Settlements around a specific building or for different buildings in the same neighbourhood were usually quite variable. Information on settlements can also be inferred from changes in water content. Silvestri et al. (1994) presented water content profiles for different time of the year and at different distances from trees in a park in Montreal.

Most of the settlement values available in the literature are point measurements and instruments are usually not monitored over the extended periods that would be required to witness the effect of severe drought. With the increasing interest in the influence of climate changes on the geotechnical engineering of Champlain clays, it appears important to develop methods to acquire larger numbers of displacement values over extended periods to conduct statistical studies of settlements.

Differential interferometric synthetic aperture radar (DInSAR) is a cost-effective technology that uses satellite radar images for measuring ground surface deformations and building settlements over long observation periods and large areas. This technique extracts the displacements from the phase difference of two satellite images. It was introduced in the late 1980s and early 1990s (e.g., Gabriel et al., 1989; Massonnet et al., 1993; Zebker et al., 1994). This technique is a powerful tool for monitoring the deformation patterns in earthquakes, landslides, settlements, and land subsidence (e.g., Berardino et al., 2002; Crosetto et al., 2005; Ferretti et al., 2000; Hooper et al., 2004; Mora et al., 2003; Usai, 2001, 2003; Werner et al.,

2003). Although its conventional application to image pairs can provide reliable results, errors can occur based on temporal decorrelation and atmospheric noise (Zebker et al., 1997). To mitigate these shortcomings, multi-temporal approaches (MT-InSAR; Minh et al., 2020) based on a higher number of consecutive observations have been developed to form a dense time series of archived radar images. This allows more accurate results to be obtained and longer time spans to be covered.

Small Baseline Subset (SBAS) and persistent scatterer DInSAR (PSI) are two established MT-InSAR methods. SBAS uses distributed scatterers and relies on the combination of temporally close observations (Berardino et al., 2002). PSI identifies persistent scatterers, points on the earth surface which are potentially coherent in time. The SBAS method was previously applied to the monitoring of deformation in the urban area of Montreal (Normand & Heggy, 2015). Using this technique, uplift of 1 mm/year and subsidence of 2 mm/year were correlated to hydraulic head and soil saturation changes. However, the low number of SAR images can limit the reliability of the obtained results. Although the SBAS method is comparably accurate and has better spatial coverage (Tizzani et al., 2007), implementing the PSI technique with a short temporal frequency dataset can be a more reliable option in our case study. The Sentinel-1 SAR images that were used in this study are free to access but have a lower resolution compared to the current commercial satellite products. However, owing to recent improvement in PSI technique, it is now possible to work with very large SAR databases and it can improve considerably the accuracy and reliability of the InSAR estimations.

This thesis further investigates the settlement in Champlain clays with the following objectives:

- Develop a hydro-geotechnical model based on the van der Kamp & Gale (1983) approach that can link pore pressure changes to hydro-meteorological events.

- Evaluate the van der Kamp & Gale (1983) approach for the replication of historical pore pressure time series within a shallow Champlain clay aquitard on the Sainte-Marthe study site.
- Investigate the potential of the PSI technique for the determination of deformation rates in Champlain clays using openly available Sentinel-1 radar imagery.
- Develop a simplified numerical model to simulate settlements due pore pressure changes and interactions with the atmosphere within a shallow Champlain clay aquitard and validate the numerical simulations using PSI technique. Implementation of this exercise in shallow aquitard is necessary to better reflect the conditions of Champlain clays in the Montreal region, and particularly in the Sainte-Marthe site.
- Measure and analyse long term settlements in the Montreal area using the PSI technique.

The main contributions in this dissertation can be organized into three main categories: numerical modelling of pore pressure changes, InSAR monitoring of settlements and numerical modelling of settlements. Regarding the numerical modelling of pore pressure changes, the case study for a shallow aquitard and the approach for the evaluation of missing meteorological parameters from the soil water budget using historical pore pressure time series are unique. For the numerical modelling and InSAR monitoring of settlements, to our best knowledge, this thesis presents the first attempts to apply PSI and numerical modelling to the study of settlements in Champlain clays. Application of the non-linear PSI technique to monitor soil settlement is another unique characteristic of this study, particularly in non-urban areas where it has been poorly investigated. Last, but not least, this thesis presents the first long-term monitoring of settlements in an area as large as Montreal Island using Sentinel-1 SAR images and PSI technique.

The first chapter of this thesis covers the literature on the mechanical and hydrogeological properties of Champlain clays. The unique characteristics of Champlain clays and the aspects of their mechanical behaviour associated with settlements are covered in this chapter. A detailed description of the study site is also presented.

Chapter 2 introduces the numerical model for the replication and analysis of the pore pressure data within the shallow aquitard on the Sainte-Marthe study site. The model was developed using COMSOL Multiphysics (FEM) and its MATLAB scripting interface. Based on the Biot poroelastic model, the COMSOL model simulates the pore pressure changes within the aquitard. Total stress and water table boundary conditions are applied at the top of the model. The MATLAB code can discretize the simulation and optimize the stress boundary conditions in each time step to match the pore pressure time series that are measured in the field. This Code can also apply a constrained water budget on the model based on the series of hydrological equations. The MATLAB code is presented in appendix III.

Chapter 3 describes a simplified numerical model that replicates the settlements in shallow aquitards. The numerical model is used to study the influence of clay properties, more specifically the clay stiffness, on settlements.

Chapter 4 presents the theory and methodology of InSAR monitoring. Detailed explanations of the InSAR technique that was used in this thesis for monitoring the settlements for the Sainte-Marthe study site and the Island of Montreal are presented.

Chapter 5 presents and discusses the results of this thesis. The first section compares the observed and simulated pore pressures between May 2017 and December 2019. The accuracy of the model for the water balance calculation at the Sainte-Marthe study site is also discussed in this section. The following section of this chapter presents the results of the numerical modelling of settlement at the study site between May 2017 and December 2019. The model results then will be compared with the InSAR monitored deformations that were obtained with the PSI technique. The last section of this chapters presents the major settlements that were

detected by InSAR monitoring on the Montreal Island for the period between April 2016 and February 2022.

Chapter 6 present the conclusions of this thesis for each objective. Then the current shortcomings are discussed and suggestions for further investigation are presented.

CHAPITRE 1

Hydrology and geotechnical properties of Champlain clays

Sensitive clays have a low remoulded shear strength compared to other types of clays. In Eastern Canada, large volumes of highly sensitive marine clays have been identified over vast areas that are often densely urbanized. Sensitive clays can be found in different parts of the world, especially in the northern regions that were affected by the last glaciation, such as Scandinavia and Russia. The Canadian sensitive clays, however, have characteristics that can differ significantly from other sensitive clays. These unique characteristics have led to a large number of research projects on their properties. This chapter presents a brief literature review of Champlain clays properties. First, the formation and history of Champlain clays will be discussed. Then the hydrological and geotechnical properties of Champlain clays will be presented.

1.1 Champlain clays formation

The Champlain Sea (Figure 1.1) is an inland sea that temporarily occupied the St. Lawrence and Ottawa River valleys for a period of four millennia starting around 13 000 years ago (Cronin et al., 2008). The Champlain Sea began to form when the continental glaciers began to melt and the Atlantic Ocean invaded the St. Lawrence River valley which was depressed due to the heavy load imposed by the ice sheet (Occhietti, 1989). The maximum thickness of the ice sheet in the Montreal area was about 3300 meters (Gowan et al., 2021). The Champlain Sea later shrank gradually due to the isostatic rebound and finally disappeared from the region. During the formation and regression of the Champlain Sea, thick layers of silty clays were deposited in the drainage basin of the St. Lawrence River in southern and eastern Ontario (Kenney, 1964; Quigley, 1980). These clays are often called Champlain Sea clays or Champlain clays.

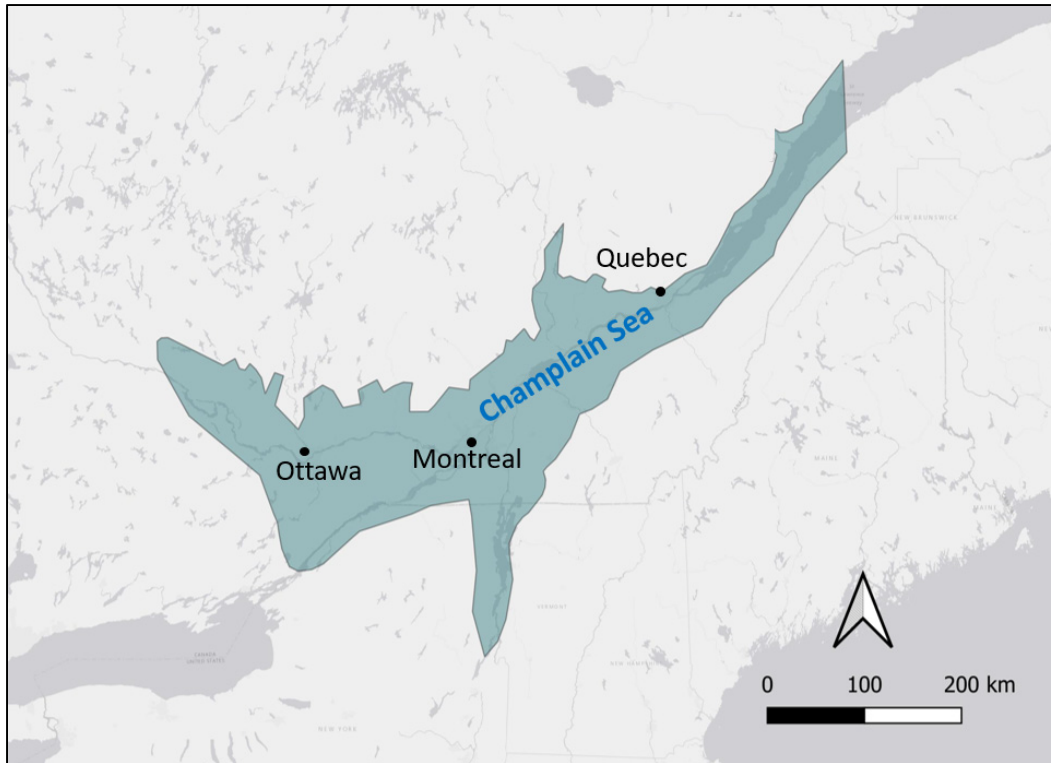


Figure 1.1 The location of the Champlain Sea redrawn from Harington (1977)

1.2 Stratigraphy of Champlain clays deposits

Defining a detailed stratigraphy that represents all Champlain clay deposits is not possible, as the sedimentation history varies between locations in the Champlain Sea basin (Richard & Occhietti, 2005). However, it is possible to define a simplified stratigraphy of the sediments left during the last glaciation and the Champlain Sea event. In surficial deposits of the Champlain Sea basin, there is often a thin layer of sand or silt close to the surface. The thickness of this layer is typically less than a few meters. The top of the clay layer is often very stiff, oxidized and fractured. The top of the intact grey clay below is generally softer with an increasing stiffness with depth. The clay properties vary with depth because of the increased loading and because of changes in the salinity of the body of water in which they were deposited. The more recent and softer deposits on top mostly have a freshwater origin, while the deeper parts of the clay layer were mainly deposited in saltwater. This is due to the gradual replacement of water from the Atlantic Ocean by fresh water in the Champlain Sea basin.

Below the clay layer, on top of the bedrock, a layer of till with a variable thickness can often be identified. The till consists of sand, silt, gravel and a little clay. Figure 1-2 illustrates two examples of stratigraphy profile around the Montreal Island.

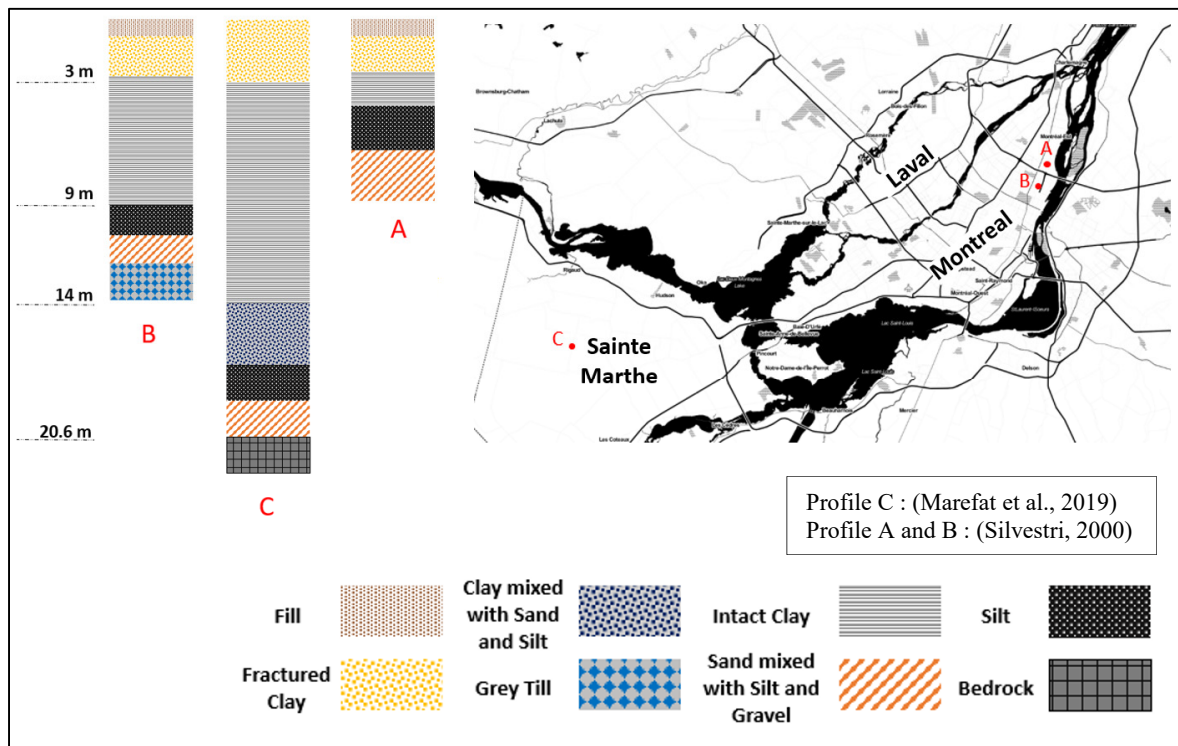


Figure 1.2 Stratigraphy of Champlain clays deposits

1.3 Particle size, mineralogy and distribution of Champlain clays

Champlain clays have a particle size distribution and mineralogy that does not perfectly match the usual definitions of “clay”. The particle size distribution of samples collected from different parts of the Champlain Sea basin shows mass percentages of particles smaller than $2 \mu\text{m}$, the most common upper size limit for clay-size particles, between 20 and 85 % (Brydon & Patry, 1961; Leroueil et al., 1983a). For instances, in some specimens analyzed by Brydon & Patry (1961) from Nicolet in Quebec and Orleans in Ontario, less than 30 % of the mass was composed of clay-sized particles. These materials can more accurately be described as clayey silt.

The main minerals in Champlain clays are not considered as clay minerals. X-ray diffraction results have shown that clay minerals represent only 9 to 34 of their mineralogy (Locat & St-Gelais, 2014). Champlain clays are mainly composed of minerals of detrital origin, including Paleozoic and Precambrian formations (Russell et al., 2011). The sediments in Champlain clays were mainly formed by the physical weathering of bedrock by glacial erosion (glacial rock-flour) (Torrance & Kirkpatrick, 2004). The non-clay minerals in Champlain clay deposits from the highest to the lowest proportions are plagioclase, K-feldspar, quartz, amphiboles, calcite and dolomite. The clay minerals of Champlain clays in order of decreasing proportion are chlorite, illite, vermiculite, and montmorillonite. Table 1-1 illustrates the detailed distribution of detrital and clay minerals in Champlain clays based on Locat & St-Gelais (2014).

Table 1.1 Mineralogy of Champlain clays based on Locat & St-Gelais (2014)

Non-Clay Minerals (Percent %)					
Plagioclase	K-feldspar	Quartz	Amphiboles	Calcite	Dolomite
19-40	6-28	3-20	6-16	1-5	0-2
Clay Minerals (Percent %)					
Chlorite	Illite	Vermiculite	Montmorillonite		
4-20	2-13	2-9	<0.1		

1.4 Hydraulic conductivity of Champlain clays

One of the distinguishing features of Champlain clays is their low hydraulic conductivity (K_h). This property makes them a good choice for the construction of landfill sites, as it limits the seepage from the clayey layers to the other layers of the soil. The thickness of Champlain clay deposits varies from a few meters to more than 100 meters in some cases. The dominant hydrologic regimes can differ based on the presence of fractures. At the top of clayey layers where fractures exist, the hydraulic conductivity is considerably higher, and fractures control the hydrologic regime. In these layers which are hydraulically more active, the general

hydraulic conductivity of the soil largely depends on the hydraulic conductivity of these fractures.

Fractured layers are affected by seasonal variations of groundwater levels. The freezing and melting of ice lenses along with groundwater level changes create these fractures in the soil. The depths of the fractured layer can vary in different areas of the St. Lawrence valley. Depths ranging between 3 and 6 m were reported for eastern Ontario (O'Shaughnessy & Garga, 1994), while other studies on the Montreal Island (Silvestri et al., 1992) and in the Lachenaie area, east of Montreal (Duhaime et al., 2017), reported depths varying between 1.8 and 2.8 m, and less than 5 m, respectively. The active layer is also called the oxidized layer because the presence of oxygen results in the oxidization of the soil. The hydraulic conductivity of the soil in the active layer was measured at 1×10^{-7} m/s (Duhaime et al., 2017) and 1.8×10^{-8} to 2×10^{-5} m/s (O'Shaughnessy & Garga, 1994).

The hydraulic conductivity is significantly lower for deeper parts of the clay deposits because of the absence of fractures. For instance, O'Shaughnessy & Garga (1994) obtained K_h values varying between 8.2×10^{-10} and 1.4×10^{-9} m/s, whereas Tavenas et al. (1983) and Duhaime et al. (2017) measured K_h respectively between 1×10^{-11} and 1×10^{-10} m/s, and 1.3×10^{-9} and 2.4×10^{-8} m/s. This hydraulically less active layer is also called the intact or unoxidized layer. The thickness of the intact layer is considered an important safety factor in the design of landfill sites. It has been measured from a few meters up to more than 100 m. It is worthy of note that hydraulic conductivity can vary in different directions of the soil. Duhaime (2012) measured a mean anisotropy ratio of 1.2 between the hydraulic conductivity of the Champlain clays of Lachenaie area in the horizontal and vertical directions.

Figure 1.3 summarizes some hydraulic conductivity results presented in the literature for intact and active clay layers of Champlain clays.

1.5.1 Undrained Shear strength

Shear strength is one of the distinctive properties of Champlain clays. It can be defined as the maximum resistance of the soil structure against a shear load before failure. Based on the drainage condition, shear strengths are categorized into undrained and drained condition that can significantly be different.

Various ranges of undrained shear strength (c_u) have been presented by different authors for Champlain clays. Based on vane shear tests conducted at different locations, Leroueil et al. (1983b) obtained c_u values ranging from 13 to 70 kPa. The lowest and highest values were respectively measured in St-Alban and Mascouche, Quebec. The range of 15-125 kPa is also reported by Leroueil et al. (1983a) for the shear strength of the Champlain clays which was obtained from pressure meter tests.

The c_u values vary significantly with depth in Champlain clays deposits. The shear strength close to the surface layer, in the oxidized layer, is considerably higher than in the intact clay layer below. However, as we go deeper in the intact clay part of the soil profile, the shear strength increases gradually. Lafleur et al. (1982), for instance, using vane the shear test, obtained the shear strength value for the Champlain clays of the Leamy Creek region in Quebec where the highest c_u , 200 kPa, was obtained at the depths of 2-3 meter and the lowest one, 50 kPa, at the depths of 7-10 meter.

The type of the implanted method can also affect the obtained c_u values. For instance, Nader (2014) examined the Champlain clay deposits of the Ottawa Valley with Cone penetration test (CPT), vane shear and laboratory method. His results showed that while the field vane shear test can give the considerably higher estimates, the CPT method results could be slightly lower than the laboratories values. He obtained respectively the ranges of 20-35, 10-55 and 50-75 kPa for the c_u from laboratory, vane shear test, and CPT.

1.5.2 Sensitivity

Sensitivity of the soil (S_t) is defined by the ratio of the shear strength in undisturbed condition to the remoulded shear strength (Equation 1.1). This factor shows how much vulnerability a soil has to lose its structural strength due to remoulding.

$$S_t = \frac{cu}{cu_r} \quad (1.1)$$

where cu_r is the remoulded undrained shear strength. Sensitivity can be determined with unconfined compression tests, field vane tests, laboratory vane tests, fall cone tests, and cone penetration test. Among these methods, the fall cone test, or Swedish cone test, is the reference method for defining the sensitivity (Garneau & Le Bihan, 1977).

Ranges of Champlain clay sensitivity have been reported by several authors. Delage (2010) obtained values ranging between 19 and 45 for Champlain clay deposits in different parts of the Quebec using the fall cone test. Very large S_t values have also been reported for Champlain clays. Torrance (1975) measured S_t values of more than 200 for the Champlain clays of the Chelsea area in the Ottawa region.

Leaching of salt from the clays is one of the main reasons for the very high sensitivity of some Champlain clay deposits (Rosenqvist, 1946; Skempton & Northey, 1952; Bjerrum, 1954; Torrance, 1975; Andersson-Sköld et al., 2005; Duhaime et al., 2013; Liu et al., 2021). The sensitivity of siltier Champlain clays is generally higher. Delage (2010) found evidences that there is a link between the higher sensitivity of silty clays and the breakage of the inter-aggregate connectors in the material. These inter-aggregate connectors strengthen the structure of the clay by establishing a link between the silt grains.

1.5.3 Preconsolidation pressure

Preconsolidation pressure σ'_p is one of the key parameters for the design of foundations and settlement calculations for regions with Champlain clays. The mechanical behaviour of Champlain clays, specifically their compressibility and shear strength, can be affected by σ'_p to a large extent.

Preconsolidation pressure is often described as the maximum overburden pressure that a soil has sustained in its geological history. This value gives us important information on the stress history of the soil. It can help us to determine the load that can be applied on a soil before irrecoverable volume change. Preconsolidation pressure is also affected by creep and aging (Bjerrum, 1967).

In eastern Canada, due to thousands of years of creep and erosion of the overburden, Champlain clays can sometimes have large values of preconsolidation pressure. Leroueil et al. (1983b) reported preconsolidation pressures ranging from 47 to 216 kPa. Duhaime et al. (2013) obtained preconsolidation values varying from 180 to 580 kPa for the Champlain clay deposit in Lachenaie. Preconsolidation value as high as 1000 kPa were reported by Demers & Leroueil (2002) for the Saint-Boniface region. The Champlain clays are in general overconsolidated. It means that the effective stress (σ') due to the overburden load is lower than σ'_p . The overconsolidation ratio (*OCR*) is a parameter that shows the degree of overconsolidation in soils. This factor is the ratio of preconsolidation pressures to the overburden effective stress:

$$OCR = \frac{\sigma'_p}{\sigma'} \quad (1.2)$$

The *OCR* of Champlain clays is normally between 1 and 4.5 (Morin et al., 1983). However, similarly to preconsolidation pressure, much higher *OCR* values have been also measured in the sensitive clay deposits of eastern Canada. For example, Demers & Leroueil (2002) obtained

an *OCR* of 28 for the clay deposit in Saint-Jean-Vianney. The *OCR* values varied from 1.1 to 28 in their study.

1.5.4 Compressibility

The compressibility of fine-grained soils originates mostly in the compressibility of their granular skeleton. The stress-strain behaviour of Champlain clays is different from other clays due to their low remoulded shear strength and high sensitivity. In general, the compression of clays is associated with a decrease of the volume of voids in the soil. This reduction of the void ratio coincides with drainage of water from the soil. Void ratio is the ratio of the volume of voids to volume of solids. The flow rate of water in fine-grained soils depends on their hydraulic conductivity and on the hydraulic gradient. Higher hydraulic gradients and K_h values result in higher flow rates and faster deformation.

To model the deformation of clayey soils, clay stiffness parameters such as compressibility (m_v) or Young's modulus (E) are needed. Stiffness parameters are typically defined in the laboratory using the stress-strain relationship obtained during the deformation of a soil specimen. Various tests can be used (e.g. oedometer or triaxial tests). The stress-strain relationship is complex and not unique for all conditions. It is affected by different parameters such as the deformation rate, stress path, disturbance level, and temperature range (Leroueil, 1996; Delage, 2010).

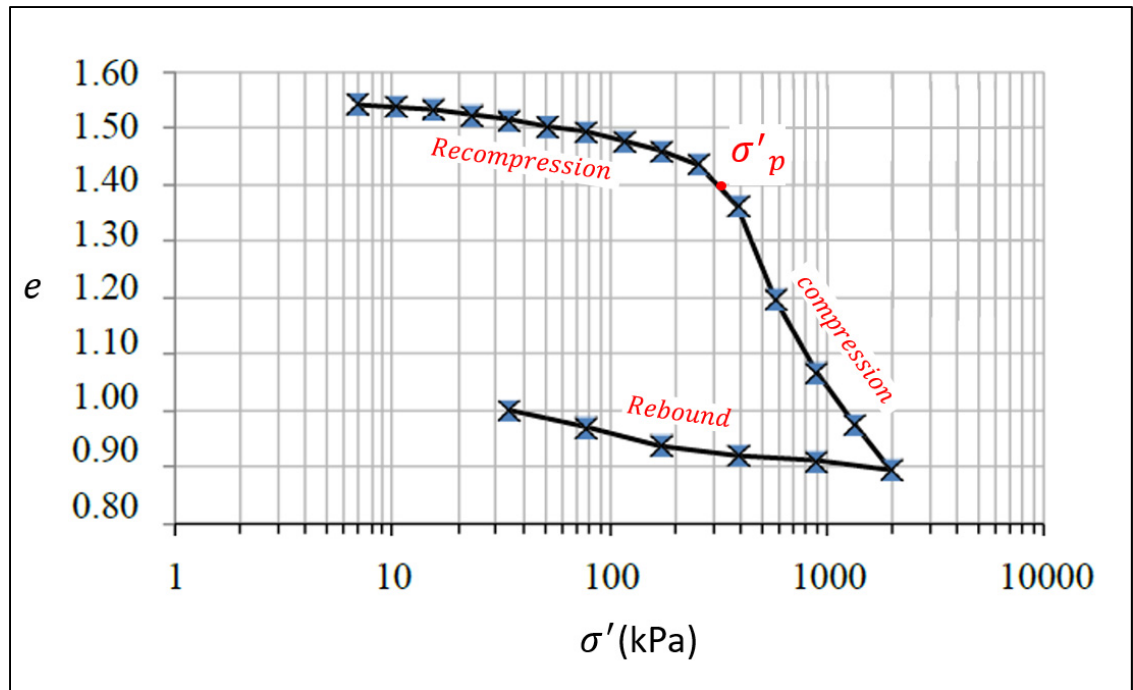


Figure 1.4 Typical stress-strain curve for a Champlain clay specimen of Lachenaie region adapted from Duhaime (2012)

Figure 1.4 shows a typical stress-strain relationship for Champlain clays. Three parts can be differentiated from this graph. The first part is the recompression state. It occurs when the applied load is lower than σ'_p . Deformations in this part of the stress-strain relationship are small. When the applied load is larger than σ'_p , strains are much larger. The final part of the curve is the rebound. It occurs during unloading.

Compressibility can be defined from the stress-strain curve using the ratio of the volumetric strain to change in effective stress for the laterally constrained deformations with the following equation (Das & Sivakugan, 2016):

$$m_v = \frac{\text{Volumetric strain}}{\text{change in effective stress}} = \frac{\Delta e}{1 + e_0 \Delta \sigma'} \quad (1.3)$$

where e_0 is the initial void ratio. The relationship between compressibility and Young's modulus is defined with the following equation:

$$m_v = \frac{(1 + \nu)(1 - \nu)}{E(1 - \nu)} \quad (1.4)$$

where ν is Poisson's ratio. The Young's modulus can be calculated from the compressibility using equation 1.4 and the Poisson's ratio.

The clay stiffness for very small strains can be calculated from the shear wave velocity (e.g., Lefebvre et al., 1994; Elbeggo et al., 2019). It is very important to note that the clay stiffness varies with the strain level. Strains can be categorized in three levels including very small, small and large strains (Figure 1.5). A higher stiffness should be considered for smaller strains for clayey materials in deformation analyses. The maximum value of the Young's modulus is referred to as E_{max} . It is applicable for very small strains. For larger strain rates, the appropriate Young's modulus can be defined from a degradation curve (Figure 1.5).

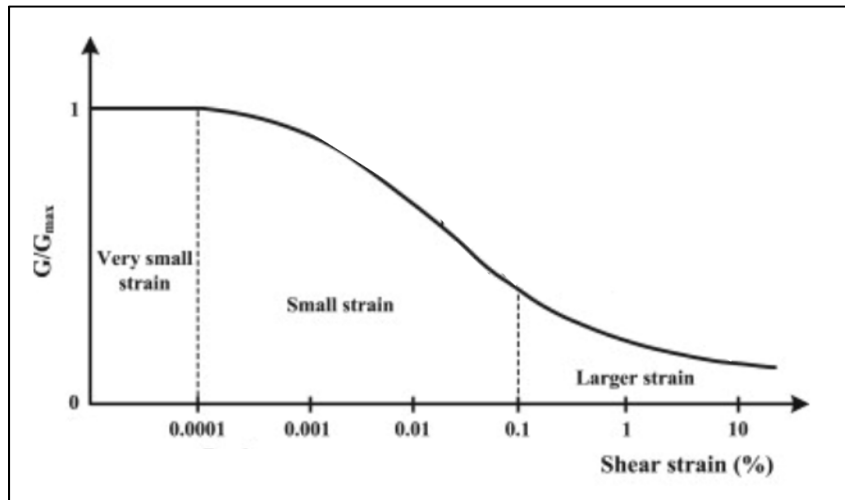


Figure 1.5 Normalised stiffness degradation curve and the three strain levels adapted from Atkinson & Salfors (1991)

Table 1.2 presents some examples of Young's modulus for Champlain clays for large, small, and very small strains. The values were reported or calculated for different locations in the

Champlain Sea basin. As it was explained earlier with Figure 1.5, smaller values of Young's modulus are obtained for larger strains. The range of modulus values spans almost three orders of magnitude.

Table 1.2 Reported or calculated Young's modulus for Champlain clays

	Reference	Location	E (MPa)
Large strains	Silvestri & Abou-Samra (2008)	Mascouche	3.00-16.00
	Silvestri & Abou-Samra (2008)	Louiseville	3.00-13.00
	Silvestri (2000)	Taillon	0.70
	Silvestri (2000)	Rameau	0.38
	Silvestri (2000)	Honoré-Beaugrand	0.74
	Silvestri (2000)	De Beurivage	0.3
	Silvestri (2000)	Souigny	0.25
	Silvestri et al. (1992)	Montreal Island	1.17
	Silvestri et al. (1992)	Montreal Island	1.75
Small strains	Silvestri & Abou-Samra (2008)	Louiseville	19.20-48.00
	Silvestri & Abou-Samra (2008)	Mascouche	25.56-46.08
	Duhaime (2012)	Lachenaie	25.60-54.40
Very small strains	Leroueil et al. (2003)	Louiseville	48.00-83.20
	Shibuya (2000)	Louiseville	96.00
	Karray & Lefebvre (2001)	Lachenaie	41.60-204.80

1.5.5 Thermal properties

In this section, the thermal conductivity and thermal expansion coefficient of Champlain clays are briefly discussed.

The thermal conductivity of Champlain clays is one of their key characteristics that have been less investigated. It might be due to limited number of applications for this property. Measurement of this property in fine-grained soils is not a difficult challenge. But determination of a value that represent a general condition is not possible as it varies for different ranges of temperature. Furthermore, as it was mentioned earlier, Champlain clays from different locations and depths have different mineral contents and particle size distributions which indeed result in different thermal conductivities. It is also worth mentioning that thermal conductivity varies depending on the temperature range (Figure 1.6).

Côté & Konrad (2007) measured the thermal conductivity of Champlain clays using laboratory experiment described by Côté & Konrad (2005) and evaluated the thermal conductivities of the solid particles using different indirect methods such as mineral content or quartz fraction. Based on this study, the solid particle thermal conductivity of a marine clay mostly varies due to the quartz content. Because quartz has a substantially higher thermal conductivity than other common minerals. The range of the evaluated solid particle thermal conductivities varied from 2.2 to 3.2 W/mK with the mean value of 2.15 W/mK for the minerals other than quartz using indirect methods. The laboratory experiments, however, measured the thermal conductivities values of the soil in the range of 0.8 to 0.97 W/mK. Earlier, Penner (1962), examined the thermal conductivity of seven Champlain clay samples in the Ottawa region. The measured thermal conductivity ranged from 0.8 to 1 W/mK, whereas the estimated solid particle thermal conductivities varied from 1.3 to 1.7 W/mK.

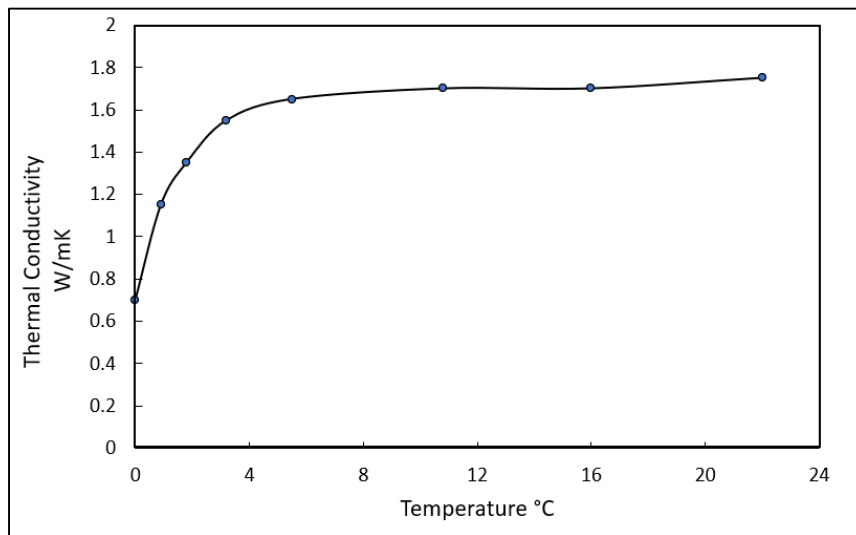


Figure 1.6 Thermal conductivity of a Champlain clay sample as a function of temperature (redrawn from Penner, 1970)

The thermal expansion coefficient (α_T) describes at which rate a material will increase in size with increasing temperatures. Thermal expansion of Champlain clay has not been studied so far. However, the thermal expansion of the minerals that constitute Champlain clays were

reported by several authors. For instance, McKinstry (1965) measured the thermal expansions of clay minerals. The measured thermal expansions ranged from 3.5×10^{-6} to $18.6 \times 10^{-6} \text{ K}^{-1}$.

Similarly to the indirect method that were mentioned earlier in this section (Côté & Konrad, 2007), we can also indirectly evaluate the thermal expansion of Champlain clays deposits for the study site that will be described in the next section. The indirect thermal expansion coefficient can be calculated using a weighted average of the thermal expansion coefficients of the clay minerals and the water content of the Sainte-Marthe Champlain clays. It was assumed that the mineral content in Sainte-Marthe is similar to the proportion reported by Locat (1995) for Saint-Zotique Champlain clays which is also in the Vaudreuil-Soulanges region. The thermal expansion of each clay mineral was set equal to the values measured in McKinstry (1965). Based on these hypothesis, the thermal expansion of the Champlain clays was evaluated as $9 \times 10^{-5} \text{ K}^{-1}$. The estimated value is close to the range of thermal expansion coefficients that were measured for Norwegian sensitive clays ($1.5 \times 10^{-5} \text{ K}^{-1}$, Li, 2018).

Frost heave deformation mainly occurs due the phase change associated with the formation of ice lenses rather than thermal expansion. This phase change coincides with water migration. The migrated water turns to ice in warmer side of the ice lens which is in thermal equilibrium condition (Konrad, 1994). In this state, the chemical potential or energy of all phases are equal in a closed system. The rate of the water migration can then be expressed by Darcy's law. Considering the conservation law, the amount of the frost heave can be calculated with the following equation:

$$h_{frost} = \frac{\rho_w}{\rho_i} SP \Delta T t_{FR} \quad (1.5)$$

where h_{frost} is the displacement associated with frost heave, ρ_i is the ice density, SP is the segregation potential, and t_{FR} is the freezing time. SP is the parameter that defines the relationship between mass flow and heat flow in freezing condition. SP can be calculated with the following equation:

$$SP = K_h \frac{u_{water} - u_{ice}}{T_{seg} - T_{frozen}} \quad (1.6)$$

where u_{water} and u_{ice} are respectively the pore water pressure at the ice lens and frozen fringe and T_{seg} and T_{frozen} are respectively freezing and segregation freezing temperatures (Figure 1.7).

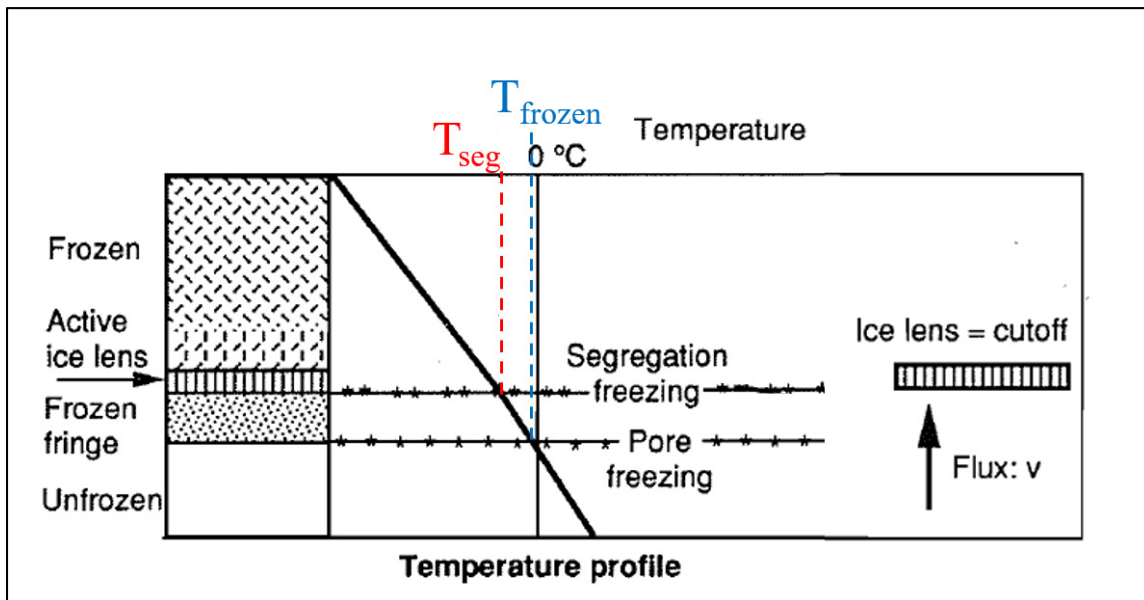


Figure 1.8 Schematic of freezing in soils adapted from Konrad (1994)

1.6 Sainte-Marthe Study site

The study site was established in 2015 for two purposes. The first objective was to evaluate the performances of fully grouted piezometers (Marefat et al., 2019). The second objective was to obtain long-term observation of pore pressure fluctuation in the Champlain Sea clay layer in Sainte-Marthe.

The location of the test sites is presented in figure 1.8. The study site is located between the Ottawa River to the North and highway 340 to the south. Highways 325 and 201, respectively, are to the East and West side of the study site.

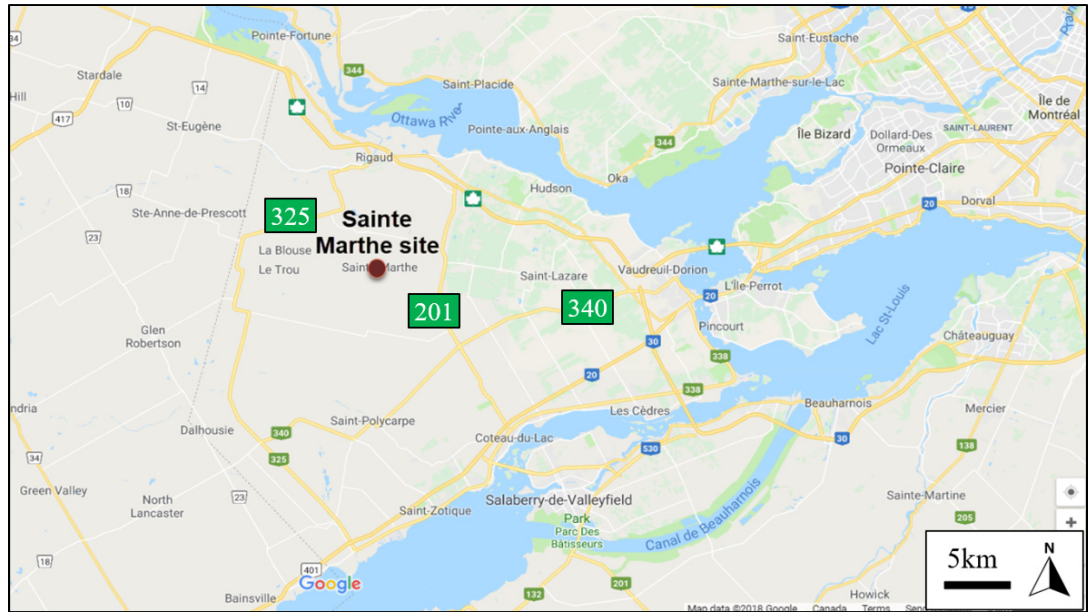


Figure 1.9 Location of the Sainte-Marthe study site

Clay is found from the surface to a depth of 16.0 m at the test site. It is fractured in the top 3.0 m and massive in the underlying 13.0 m. In the top portion of the soil profile, the clay is brownish and plastic when remoulded. The thickness of the brownish clay layer may reach up to 7.5 m. Beyond this layer, the clay is mostly gray and sensitive with sensitivity as high as 200 at a depth of around 10 m. The grey layer extends to a depth of 14.0 m. From a depth of 14.0 m, the soil becomes gradually siltier and may be mixed with sand, gravel or coarser material including erratic blocks (Marefat et al., 2019; Shafaei et al., 2018). The depth of the bedrock is 20.6 m at the study site.

Instruments at the test site monitor the pore water pressure, barometric pressure, water table depth, and temperatures at different depths of the aquitard. For this purpose, two 114 mm boreholes (F1, F2) were drilled with a wash boring method and flush-joint straight casings (Figure 1.9). The boreholes extend to a depth of 22 m into the bedrock. Borehole F2 has two standpipe piezometers with intake zones at depths of 6.1 m and 12.2 m. Borehole F1 has two Vibrating Wire Piezometer (VWP) installed at the same depths as the standpipe piezometers. The RST-VW2100-0.35 model was selected for this purpose. The VWP were installed with the fully grouted method. The VWP has a range of 0-350 kPa with an accuracy of ± 1 mm (RST

Instruments, 2019). Standpipe piezometers sealed in the bedrock were also installed in the boreholes. The standpipes are all equipped with pore pressure transducers with a full-scale range of 100 kPa. Each pore pressure transducer is equipped with a standard integral thermistor that measures the temperature inside the soil. The acronym MW and GWL in figure 1.9 stand respectively for monitoring wells and groundwater level.

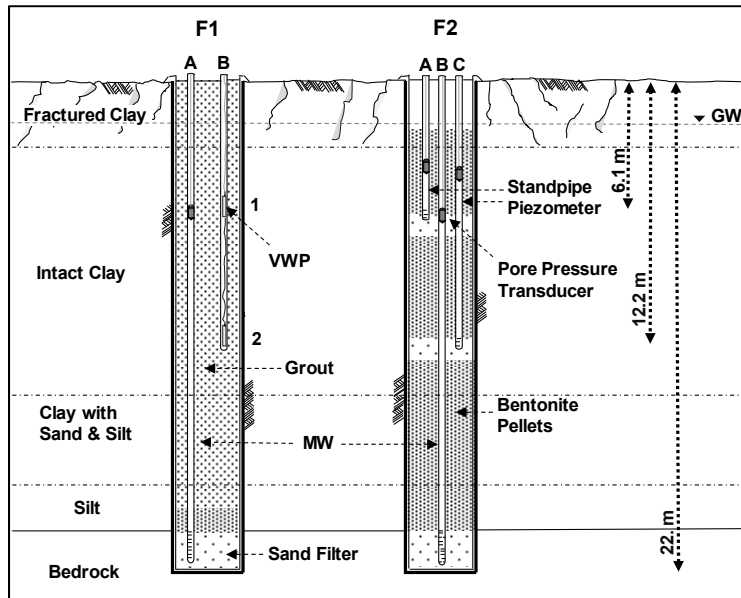


Figure 1.10 Cross-sectional profile of the study site

Geotechnical properties of the soil found at the study site are presented in figure 1.10. In this figure, M is the constrained modulus where $M=1/m_v$, W_n is the natural water content, WL is the liquid limit, and PI is the plasticity index. Undrained shear strength, liquid limit, and the sensitivity of the soil layers were obtained at the ÉTS laboratory from samples that were collected during the drilling (Marefat et al., 2019). Hydraulic conductivity was estimated with the Kozeny-Carman method (Duhaime et al., 2013). The constrained modulus was calculated from the clay Young's modulus and Poisson's ratio. The Young's modulus was estimated based on the empirical correlations for shear wave velocity presented by Elbeggo et al. (2019). This equation was derived from measurements with the Piezoelectric Ring-Actuator Technique (P-RAT) for marine clays of the Abitibi region. These clays have characteristics that are similar to those of the Champlain clay deposit in Sainte-Marthe. The Young's modulus values were

also estimated using the deformations measured by Silvestri (2000) and Silvestri et al. (1990) for several Champlain clay deposits in Montreal and the associated water table fluctuations. The Young's modulus estimated based on the field data varied between 0.3 and 1.17 MPa. These values are much lower than those that were estimated with the empirical equation presented by Elbeggo et al. (2019) (between 6 and 76 MPa). This is due to the very low strains produced by the P-RAT measurements in Elbeggo et al. (2019) ($<10^{-3}\%$) compared to the large strains in Silvestri (2000) and Silvestri et al. (1990) (1-4 %). These two ranges of Young's modulus for different strain levels are consistent with the degradation curve presented by Seed et al. (1986) for clayey soil.

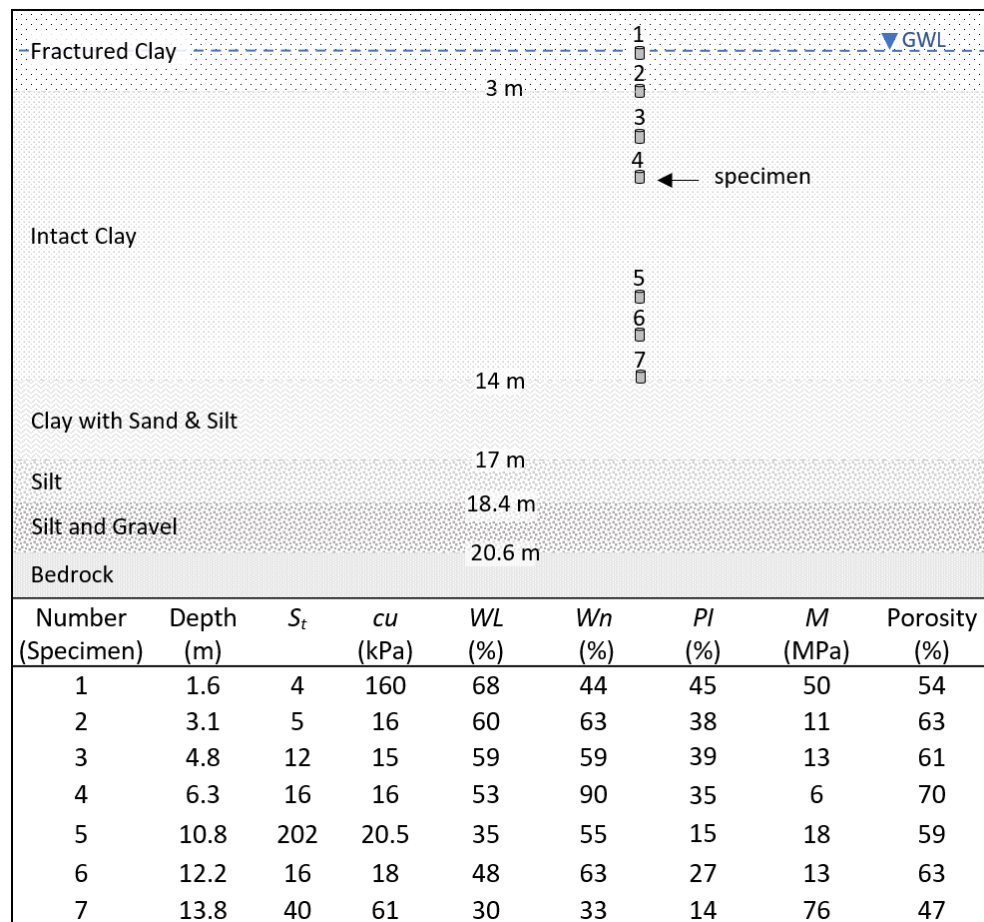


Figure 1.11 Profile and geotechnical properties of the Sainte-Marthe study site

The highest sensitivity was observed at depths of 10-11 m. Similarly to other Champlain clay deposits, the surface layer can be expected to have a much higher hydraulic conductivity than the intact clay layer. The natural water content of the soil ranged between 33 and 90 % with the highest value observed at a depth of 6.3 m. Close to the surface at the top and next to the bedrock at the bottom, the shear strength and the constrained modulus are the highest.

CHAPITRE 2

Water balance and pore pressure changes in Champlain Clays

The water content and pore pressure are key parameters to understand the mechanical behaviour of Champlain clays. The lowering of the groundwater level is one of the main causes of soil settlement. A lowering of the groundwater level leads to a decrease of the pore pressure and an increase of the effective stress. This results in a higher load on the soil skeleton and deformation. In combination with internal erosion and mineral dissolution, a lowering of the groundwater level can sometimes lead to the formation of sinkholes (Figure 2.1).

Pore pressure in soil can change due to many factors. A sudden load at the soil surface in undrained conditions can increase the pore pressure inside a fine-grained soil. Pore pressure changes can also be induced by pumping or injection of a fluid into the porous medium. Pore pressure changes can be caused by mechanical movements such as landslides or settlements, atmospheric effects like heavy precipitation or rising temperatures, and groundwater flow from other locations.

Important information can be extracted from pore pressure time series. For instance, the interaction of soil and atmosphere is reflected in the pore pressure time series. From this information, the water balance of the soil can be calculated.

In this chapter, a framework is presented to replicate the pore pressure time series within layers of intact Champlain clays and to estimate the missing components of the water budget for the study site such as runoff rate and snow storage. First, the background theory including the stress-strain relationship along with some hydrological equations will be discussed. In the following section, the methodology for estimating the water balance of the soil based on pore pressure time series will be explained. In this regard, a computer program along with a series of hydrological equations will be presented.



Figure 2.1 A giant sinkhole in Iran due to water depletion (France24, 2018)

2.1 Background Theory

In this section, the principal theories dealing with the mechanical behaviour of soil and flow in porous media will be discussed. Then, based on the requirements of this study, a simplified combination of these theories, the van der Kamp & Gale (1983) theory, will be explained. This simplified theory will be used to show the influence of overburden stress, barometric pressure, and tidal effect on the pore pressure time series measured in aquitards. Finally, the modified equations will be utilized to analyse the pore pressure time series and estimate the overburden stress and hydrologic parameters such as precipitation.

2.1.1 Stress-deformation relationship of soil

The effective stress concept was first stated by Terzaghi (1925). Based on this theory, an external load applied on a saturated porous media is borne by the porous media skeleton and the liquid phase occupying the voids. In fine-grained soils with a low permeability, an increase in the overburden load, or total stress, is first compensated by an excess pore pressure. This excess pore pressure dissipates with time, and the total stress increase is transferred gradually to the porous media skeleton. The part of the load carried by the porous media skeleton is

called the effective stress. Based on this theory, deformation and shear resistance changes are associated with changes in effective stress. Based on this principle and using several assumptions, Terzaghi (1943) also developed the theory of one-dimensional consolidation.

According to Terzaghi (1925; 1943), consolidation occurs when the water content of a saturated soil decreases because of the expulsion of water in response to the application of a static load. The external stress that is applied on the soil results in its particles moving more tightly together and in a reduction of the soil bulk volume. In saturated soils, this external load causes the expulsion of the water from the soil.

The consolidation properties of a soil can be determined using an oedometer test. The relationship between the void ratio and the logarithm (base 10) of the effective stress is described by the compression index. When the load is removed from a soil, it rebounds and regains a part of its previous volume. When reloaded, the soil will reconsolidate in accordance with a recompression curve and the recompression index (Zeitoun & Wakshal, 2013).

Terzaghi one-dimensional consolidation theory can only be applied for one-dimensional problems in homogenous porous media under constant loads. Therefore, this method is simplistic and cannot justify all the soil deformations resulting from consolidation.

Considering all these drawbacks, Biot (1941) extended the Terzaghi (1925) theory (appendix I). While the Terzaghi theory is limited to one-dimensional consolidation, the Biot theory applies to 3D deformation and water flow and can include different arbitrary loads. Biot considered most of the basic assumptions of the Terzaghi theory. The soil is isotropic, the stress-strain relationship is reversible, the relation between the stress and the strain is linear, strains are small and water is incompressible. Contrarily to Terzaghi, Biot does not assume that the soil is saturated.

Assuming the water movement in the soil obeys Darcy's law, the following differential equations can express the stress-strain relationship and estimated the 3D consolidation of the soil:

$$G\nabla^2 u_x + \frac{G}{1-2\nu} \frac{\partial \epsilon}{\partial x} - \alpha \frac{\partial u}{\partial x} = 0 \quad (2.1)$$

$$G\nabla^2 v_y + \frac{G}{1-2\nu} \frac{\partial \epsilon}{\partial y} - \alpha \frac{\partial u}{\partial y} = 0 \quad (2.2)$$

$$G\nabla^2 w_z + \frac{G}{1-2\nu} \frac{\partial \epsilon}{\partial z} - \alpha \frac{\partial u}{\partial z} = 0 \quad (2.3)$$

$$\frac{k_h}{\rho_w g} \nabla^2 u = \alpha \frac{\partial \epsilon}{\partial t} + \frac{1}{M_b} \frac{\partial u}{\partial t} \quad (2.4)$$

where G is the shear modulus, ρ_w is the density of the material, g is the gravitational acceleration, α is the Biot-Willis coefficient, ϵ is the volumetric strain, u is the pore pressure, ∇^2 is the Laplace operator ($\partial^2/\partial x^2 + \partial^2/\partial y^2 + \partial^2/\partial z^2$), u_x , v_y , w_z are the displacement components respectively in the x , y , z directions, and M_b is the Biot modulus. The coefficient $1/M_b$ is the volume of water that can be added to the soil per unit soil volume for a unit pressure increase while the soil volume is maintained constant. This parameter is better known as the constrained specific storage (S_c) (Wang, 2000).

2.1.2 Van der Kamp & Gale (1983) theory

van der Kamp & Gale (1983) developed an approach to define the fluid pressure response to stress changes based on the Biot (1941) theory. They assumed that the porous media is laterally extensive so that horizontal flow effects can be neglected. In this way, equation 2.4 can be reformulated for stress-pore pressure relation as the following equation:

$$k_h \nabla^2 u = s' \frac{\partial}{\partial t} (u - \beta \sigma_t) \quad (2.5)$$

where β is a constant ranging from 0 to 1, s' is the 3D storage coefficient, and σ_t is the octahedral normal stress, or mean principal stress.

The following equation also defines volumetric strain (volume dilatation) in response to stress and pore pressure changes in the soil.

$$\epsilon = \epsilon_{xx} + \epsilon_{yy} + \epsilon_{zz} = \frac{1}{K_b} (\sigma_t - \alpha u) \quad (2.6)$$

where ϵ_{xx} , ϵ_{yy} , ϵ_{zz} are normal strains, and K_b is the bulk modulus. K_b is the ratio between pore pressure changes within a porous media and volume changes. Using this equation, the relation of pore pressure and stresses can also be presented in terms of $\sigma_t - \epsilon$ or $u - \epsilon$. Appendix II explains how this theory was developed and presents the principal equations that were proposed by van der Kamp & Gale (1983).

2.1.3 Groundwater hydraulic equation (transient flow)

In some cases, normal stress changes are directly associated with pore pressure changes. An example is the case of laterally constrained deformations (no horizontal strain) and constant vertical stress. The following stress-strain relationship applies for these hypotheses:

$$\epsilon = \epsilon_{zz} = -\frac{1}{K_b} \left(\frac{\nu}{1-2\nu} \sigma_t + \frac{\alpha}{3} u \right) \quad (2.7)$$

The transient flow in this condition then will be defined with the following equation:

$$k_h \nabla^2 u = S_s \frac{\partial u}{\partial t} \quad (2.8)$$

Where S_s is the specific storage coefficient which for incompressible solid can be obtained by the following equation:

$$S_s = \rho g \left(\alpha + \frac{n}{K_f} \right) \quad (2.9)$$

where n is the porosity of the material, and K_f is the bulk elasticity modulus of water. K_f describes the ratio between water volume changes and pore pressure changes as a fraction of the initial volume.

2.1.3.1 Pore pressure response to loading stress

For undrained conditions with no water flow in the soil, the pore pressure response to a change in the mean principal stress can be defined with the following equation:

$$u = \beta \sigma_t \quad (2.10)$$

This equation implies that the pore pressure variation for undrained conditions can be used as a measure of changes in normal stress. Earth tides and barometric pressure changes are two examples of loads applied over an extensive area that will be discussed in the following sections.

2.1.3.2 Pore pressure changes due to atmospheric pressure variation

In a homogenous porous media where there is no lateral variation of the mechanical properties, the horizontal strains associated with barometric pressure changes are negligible. The change in vertical total stress can also be assumed equivalent to barometric pressure changes (van der Kamp & Gale, 1983). Then, the pore pressure can be related to the vertical load induced by atmospheric pressure fluctuations (σ_B).

$$u = L_e \sigma_B \quad (2.11)$$

where L_e is elastic pore pressure coefficient in constrained condition or loading efficiency. Loading efficiency is the same as β for the conditions that expresses the relation between pore pressure within a porous media and vertical surface load such as atmospheric stress or barometric stress. For incompressible solids, L_e can be obtained using the following equation:

$$L_e = \frac{1/K'}{(1/K')+(n/K_f)} \quad (2.12)$$

where K' is the confined modulus of elasticity.

2.1.3.3 Pore pressure changes due to Earth tides

Earth tides affect the top surface layer of the ground with small lateral strains. If we consider that these tidal strains are known and the vertical total stress is constant, then, for undrained condition with no flow due to stress changes, pore pressure can be relates to earth tides using the following equation:

$$u = 2GL_e\varepsilon_T \quad (2.13)$$

where ε_T is the vertical strain due to earth tide. For incompressible solids, equation 2.13 reduces to:

$$u = \frac{\rho g(1 - 2\nu)\varepsilon_T}{(1 - \nu)S_s} \quad (2.14)$$

2.1.3.4 Vertical flow due to stress changes (Earth tides & barometric loading)

The previous subsections dealt with pore pressure changes in response to barometric pressure changes and earth tides under undrained condition. It was assumed that the stress changes do

not lead to water flow. Although, the horizontal flow is negligible for areas that are laterally extensive, vertical flow cannot be ignored. Vertical flow can be due to the presence of layers with contrasting mechanical properties or boundary conditions. As we assume that the formation is laterally extensive, the vertical flow does not lead to any horizontal strain (van der Kamp & Gale, 1983).

If there is no horizontal strain and the formation is undrained, the diffusion equation is valid and applicable (Equation 2.8). It is important that other than the vertical alteration of formation properties, a variation of the water table can also induce vertical flow. In fact, the water table is a top boundary condition for pore pressure in this case.

2.1.3.5 Total pressure response to earth tides and barometric loadings and vertical flow (resulted from stress changes)

By combining equations 2.8, 2.10, 2.11, 2.13, we obtain:

$$k_h \frac{\partial^2 u}{\partial z^2} = S_s \left(\frac{\partial u}{\partial t} - L_e \frac{\partial \sigma}{\partial t} - L_e \frac{\partial \sigma_B}{\partial t} - 2GL_e \frac{\partial \varepsilon_t}{\partial t} \right) \quad (2.15)$$

In this equation, the total pressure is the sum of three changes resulting from barometric loading, Earth tides, mechanical loading and vertical flow derived from stress changes. The σ_B which is the symbol of atmospheric pressure here can also represent any uniform loads applied over an extensive area (Anochikwa, 2010).

2.2 Conceptual model

A one-dimensional conceptual model will be developed in this study. This model solves the differential equations to simulate the pore pressure changes within the aquitard in response to soil moisture changes in the top layer. The governing equation in this model was derived from equation 2.15. The barometric and tidal effects were not considered in the equation as the raw

pore pressure data were corrected to remove the barometric effect and tidal effects are considered small for shallow aquitards (see section 2.3.2):

$$\frac{\partial u}{\partial t} = \frac{k_h}{S_s} \frac{\partial^2 u}{\partial z^2} + L_e \frac{\partial \sigma}{\partial t} \quad (2.16)$$

The ratio k_h/S_s is sometimes referred to as the hydraulic diffusivity. This 1D equation shows the pore pressure changes in response to stress loading and transient flow in a saturated porous medium. In this theory, the vertical stress should apply to a laterally extensive area. Deformations due to loading and flow are then mainly vertical, and it is reasonable to neglect the horizontal flow and deformations.

In our conceptual model, it was assumed that the variation of the vertical mechanical load on the domain is only induced by moisture changes:

$$\frac{\partial \sigma(0, t)}{\partial t} = \rho_w g (P_R - ET - R) \quad (2.17)$$

where P_R is the precipitation rate, ρ_w is the density of water, ET is the evapotranspiration rate, and R is the runoff rate. The stress change is in effect due in part to a change in the soil moisture content and the associated change in the level of the water table. However, the effect of the hydrologic parameters on the total stress and water table level were kept separate in the model. The level of the water table was measured with a surficial piezometer while the total stress boundary condition was optimized based on a series of methods that will be presented in section 2.4. The governing diffusion equation for pore pressure changes induced by water table fluctuation or any other changes in hydraulic boundary condition then will be only in term of transient flow similar to the Terzaghi (1925) equation for consolidation.

$$\frac{\partial u}{\partial t} = \frac{k_h}{S_s} \frac{\partial^2 u}{\partial z^2} \quad (2.18)$$

It is worth mentioning that the lateral flow is considered negligible in the model. As a result, the 1D model is laterally constrained while the deformations and transient flow were assumed to be mainly vertical. It was also assumed that the pore pressure changes in response to loading happens uniformly in each layer.

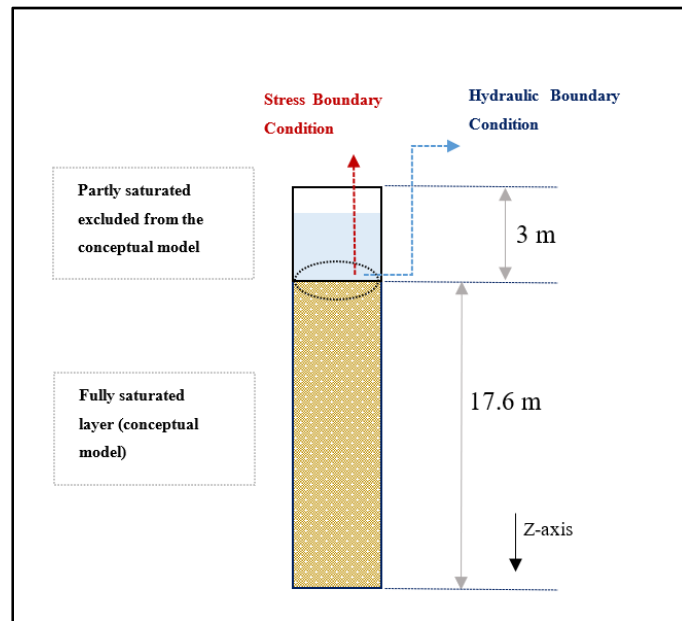


Figure 2.2 Conceptual model adapted from Anochikwa (2010)

The 1D conceptual model in this study is shown in Figure 2.2. The soil column height in the model is 17.6 m. To simplify the model, the top 3 m of oxidised crust were excluded from the domain. As a result, the conceptual model is fully saturated. Water table fluctuations and soil moisture changes (net water balance) are applied at the top of the model with boundary conditions. This simplification is mainly based on the hydraulic conductivity of the superficial layer which is several orders of magnitude higher than the bottom layer (section 1.4).

2.3 Data collection

The data that are needed for simulation of the pore pressure time series within the aquitard include meteorological data to estimate the total stress, water table data to model the transient flow in the domain, and observed pore pressure time series to calibrate the model and to estimate the missing parameters.

2.3.1 Meteorological data

The meteorological data include temperature, wind speed, relative humidity, and precipitation as rain and snow. They were obtained from an experimental station located 2.2 km away from the study site in Sainte-Marthe. The evapotranspiration was estimated using the ETO Calculator software based on the FAO Penman-Monteith method (Allen et al., 1998; Raes, 2012). The FAO Penman-Monteith method uses the following equation to estimate the evapotranspiration for a surface covered with green grass, the reference crop:

$$ET = \frac{0.408\Delta(N_{ra} - \Gamma_h) + \gamma^p \frac{900}{T_{2m} + 273} s_w (vp_s - vp_a)}{\Delta' + \gamma^p (1 + 0.34s_w)} \quad (2.19)$$

where Δ' is the slope of the vapour pressure curve, N_{ra} is the net radiation at the crop surface, Γ_h is the soil heat flux density, γ^p is the psychrometric constant, T_{2m} is the mean daily air temperature at 2 m height, s_w is the wind speed at 2 m height, vp_s is the saturation vapour pressure, and vp_a is the actual vapour pressure.

Figure 2.3 shows the ETO calculator software environment. This software needs just four parameters (air temperature, air humidity, wind speed, and sunshine hours or radiation rate) to estimate the evapotranspiration of the reference crop. The other parameters are calculated automatically by the software. In our case, only the net radiation data was obtained from the Sainte-Anne-de-Bellevue synoptic station, which is located in Saint-Lazare close to our study

site. The simulation period is 30 months from 2017/05/24 to 2019/01/24. Daily time steps were used in this simulation.

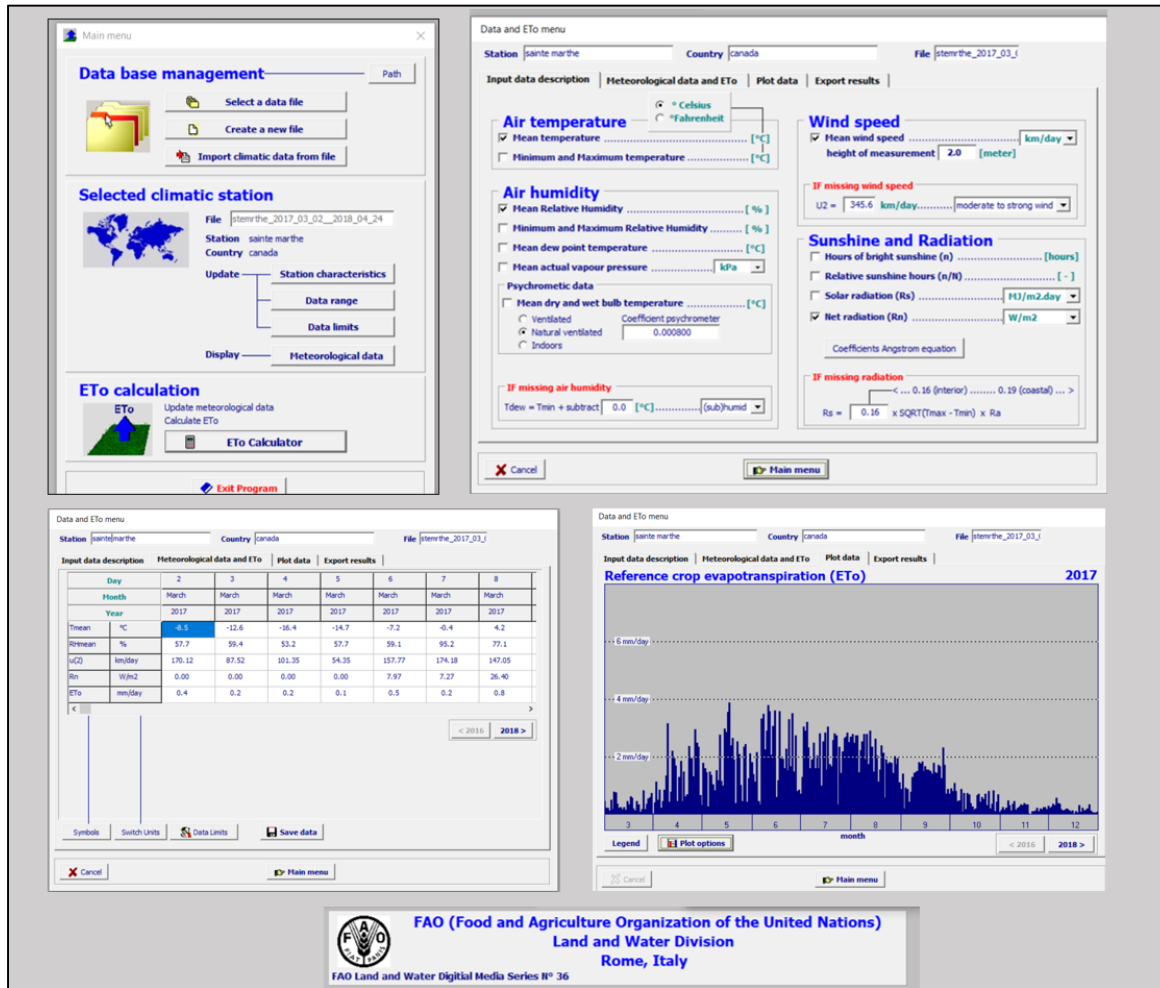


Figure 2.3 ETO calculator software

2.3.2 Pore pressure time series

The pore pressure time series were obtained from the Sainte-Marthe study site between May 2017 and January 2019 using the piezometers described in section 1.6. The raw pore pressure data was corrected for barometric effects in order to be usable for the net water balance calculation (Equation 2.17). This section present the method for pore pressure correction.

The barometric pressure effects were removed from the observed pore pressure data with the Barometric Response software from the Kansas Geological Survey (Bohling et al., 2011). The software is a standalone Windows executable program that uses an Excel workbook (Figure 2.4). This software implements the multiple regression method (MRM). In MRM, a time-lag is considered between the barometric pore pressure changes and their effects on pore pressure. This technique discretizes the barometric effects in equal time steps using a series of linear equations. The lagged values associated with barometric effects can then be detected in each time steps using the linear regression:

$$\Delta u(t) = \sum_{i=0}^j r(i) \Delta Br(t-i) \quad (2.20)$$

where $\Delta u(t)$ is the pore pressure change at time t , $\Delta Br(t-i)$ is the change in barometric pressure at time step t considering i number of lagged time steps, $r(i)$ is the regression coefficient or unit response function (BE) at lag i , and j is the maximum number of lagged time steps (Bailey, 2017; Toll & Rasmussen, 2007). The BE in each time step is estimated using linear regression between pore pressure changes and barometric pressure changes. The sum of BE values from the first time step up to the time step associated with desired time lag (j), gives the barometric response function (BRF) at that time lag:

$$BRF(n) = \sum_{i=0}^j r(i) \quad (2.21)$$

The quality of the correction in MRM can be controlled with the corresponding BRF pattern. The shape of the BRF varies if a pore pressure time series is measured in a confined aquifer, an unconfined aquifer or an aquitard. It is also sensitive to the geotechnical characteristic of the porous medium and the depth of the observation. In the present study, the range of natural pore pressure fluctuations associated with total stress changes and transient flow is similar to the range of pressure changes associated with barometric pressure, 10 m of water. As a result,

it is harder to distinguish the barometric effects from the pore pressure variations caused by other phenomenon. However, the BRF that were obtained are similar to those that were obtained in other studies that focused on pore pressure changes in aquitards (e.g., Dourado, 2018; Marefat et al., 2015).

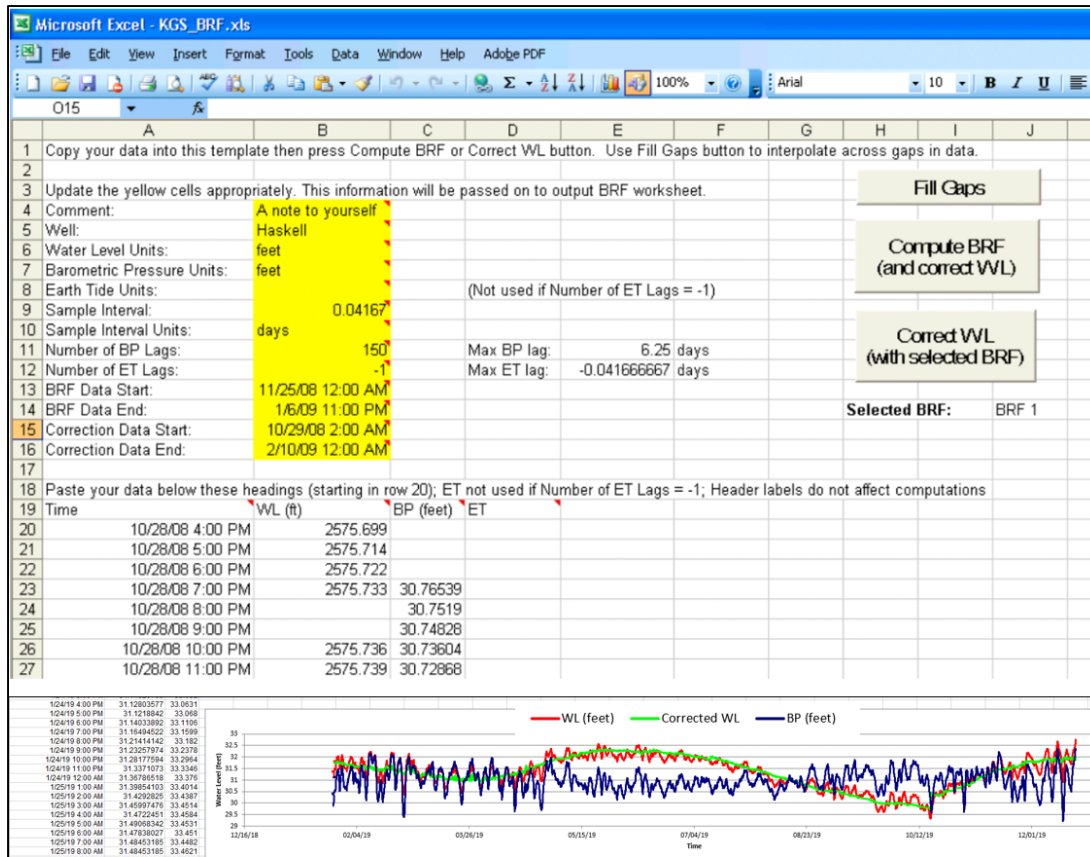


Figure 2.4 The Kansas Geological Survey Barometric Response software

Along MRM, the visual inspection method was also used to control the quality of the barometric corrections. In the visual inspection method, the barometric effects are removed with a simple linear correction:

$$U_w'(t) = (U_w(t) - Br_{avg}) - L_e (Br(t) - Br_{avg}) \tag{2.22}$$

where $U_w'(t)$ is the corrected pore pressure, $U_w(t)$ is the raw pore pressure, Br_{avg} is the mean barometric pressure, and $Br(t)$ is the barometric pressure. With this method, the pore pressure data is corrected by trial and error. Different values of the coefficient of regression (loading efficiency L_e) (Smith et al., 2013) are tested. The L_e value resulting in a smoother pore pressure time series with the minimum short term periodic fluctuations correlated with barometric effects is chosen. A comparison of results from the visual inspection method and MRM showed a good agreement. An example of raw and corrected hydraulic head time series with the BRF method is presented in figure 2.5.

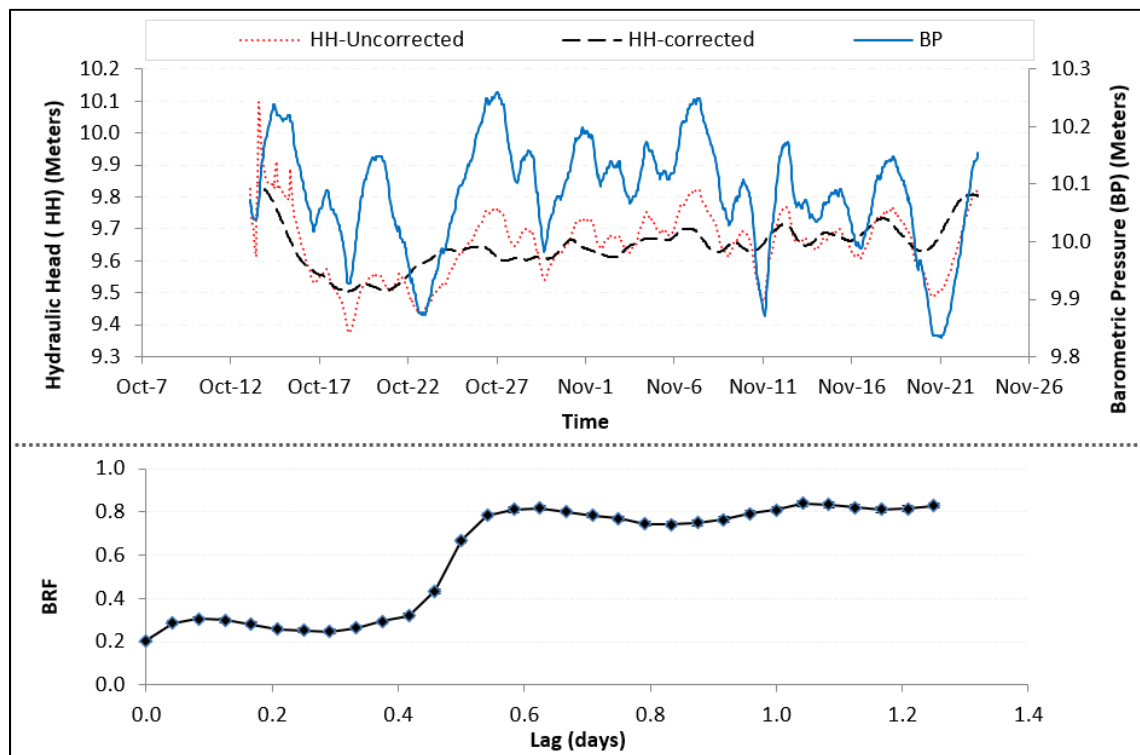


Figure 2.5 Raw and Corrected hydraulic heads for barometric effects and associated BRF time series

A Savitzky–Golay filter was applied to the corrected pore pressure for smoothing and removing the small fluctuations (Savitzky & Golay, 1964). This method is ideal for filtering the noise in time series without distortion of the general tendency. Savitzky–Golay filters smooth the time series using a polynomial fit for a desired number of neighboring points. The

number of neighboring points should be at least greater than two times the order of the polynomial. This method is similar to a weighted moving average. It replaces each value of a time series with a value derived from the adjacent values. This procedure can be formulated as a convolution where the corrected value for each point is a linear combination of adjacent data points. An example of Savitzky-Golay smoothing function for quadratic polynomial with a 5 data points filtering window is presented in equation 2.23:

$$Y_t = \frac{1}{35} (-3y_{t-2} + 12y_{t-1} + 17y_t + 12y_{t+1} - 3y_{t+2}) \quad (2.23)$$

where Y_t is the new value for the t^{th} member of the time series.

The Savitzky–Golay filter was applied on the time series with the *sgolay* function in MATLAB. In this regard, different filtering windows sizes (5-30) and polynomial orders (2-4) were examined. The best one in each case was selected based on the visual inspection. An example of a filtered hydraulic head time series with the *sgolay* function of MATLAB is presented in figure 2.6.

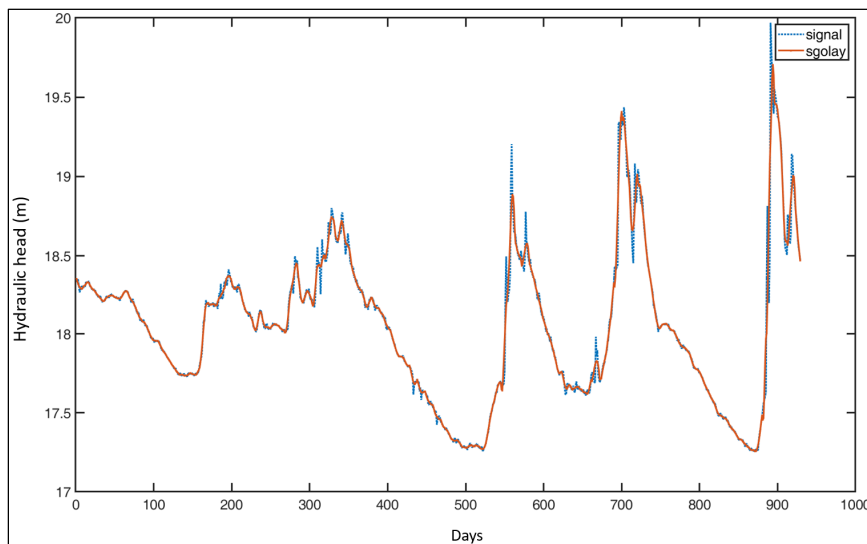


Figure 2.6 An example of the filtered and non-filtered hydraulic head time series with *sgolay* function of MATLAB for polynomial order of 3 and windows length of 11 data points

An example of the filtered and non-filtered hydraulic head time series with sgolay function of MATLAB for polynomial order of 3 and windows length of 11 data points.

Correction of Earth tidal effects was neglected as they are significantly smaller than barometric effects and a large portion is removed during the smoothing operation (Marefat, 2016).

2.4 Numerical approach

Equations 2.2 and 2.4 were solved using the finite element method (FEM). In this study, a model was developed using COMSOL Multiphysics (COMSOL, 2021). COMSOL Multiphysics is a finite element code that allows the user to solve preprogrammed or custom differential equations. In this study, the coupled Biot-Darcy feature of COMSOL was used. The model can simulate the changes in pore pressure in response to external loads. The water conservation (Equation 2.4) and static equilibrium equations (Equation 2.2) are coupled through the pore pressure and volumetric strain.

The Biot-Darcy feature in COMSOL is limited to 2D and 3D models. As a result, a 2D geometry was selected for all simulations. The boundary conditions were used to obtain results that are consistent with a 1D geometry with laterally constrained deformation and vertical groundwater flow. The 2D geometry is a rectangle with a width of 1 m and a length of 17.6 m (Figure 2.7). The model domain is divided into six layers based on the observed hydraulic and mechanical properties. The thickness of these layers from the top to the bottom are respectively 1.7, 2.8, 3.5, 3.0, 1.3, and 5.3 m (Figure 2.7).

In this numerical approach, the continuous cumulative loads will be applied. In more detail, by the occurrence of new precipitation, net water balance will increase incrementally. The volume of evapotranspiration and runoff will be subtracted from the net water balance. In the following sections, a MATLAB script and a set of developed hydrological equations will be presented. Using these equations, the missing atmospheric parameters such as runoff and snow storage can be estimated.

In this study, the incremental formulation is being used by numerical models. In fact, the changes of boundary conditions are calculated over the specified time steps. As a result, to form the stress loading, the daily net water balance will cumulatively be added to the domain (Equation 2.24).

$$\sigma(0, t_i) = \rho_w g \sum_0^i (P_R - ET - R) \quad (2.24)$$

where i is the counter for daily times steps.

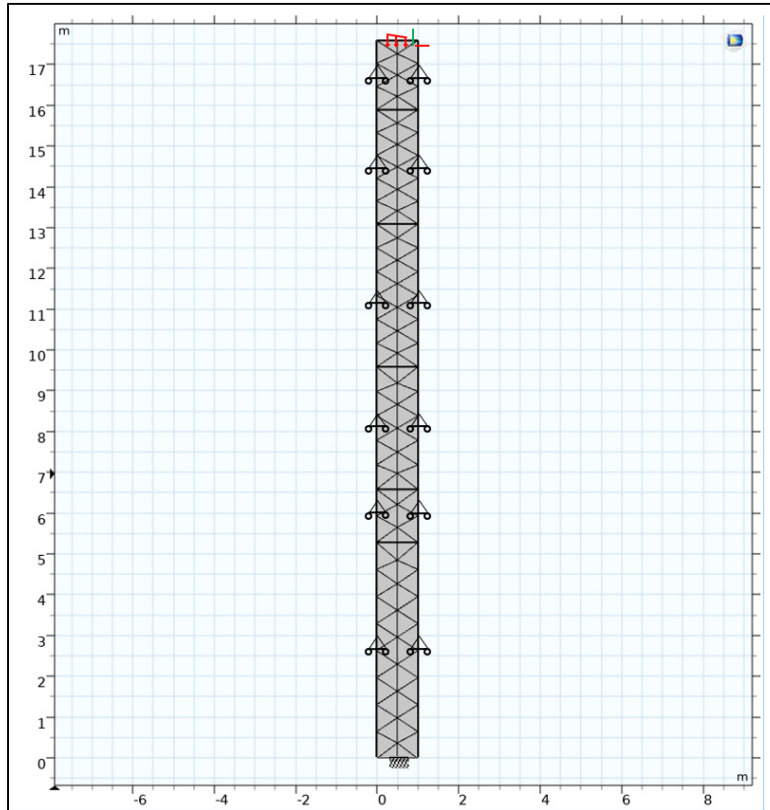


Figure 2.7 Mesh and geometry in COMSOL

2.4.1 Boundary and initial conditions:

Boundary conditions are necessary to solve the water conservation and static equilibrium equations. The domain is laterally constrained to replicate 1D flows and deformations. The lateral boundary conditions are therefore assumed to be zero flux and roller. Based on the conceptual model, soil moisture loading and the transient flows induced by the water table movements should be applied on the top boundary. The moisture loading estimated using equation 2.24 is imposed on the domain as a stress boundary condition (Figure 2.8). The transient flow effects can be imposed on the domain by defining the hydraulic head condition (Equation 2.19). The hydraulic head at the top boundary is then estimated from the groundwater level time series measured in the field for the simulation period. The bottom boundary is fixed in all directions and the hydraulic head is set equal to the hydraulic head measured in the bedrock well.

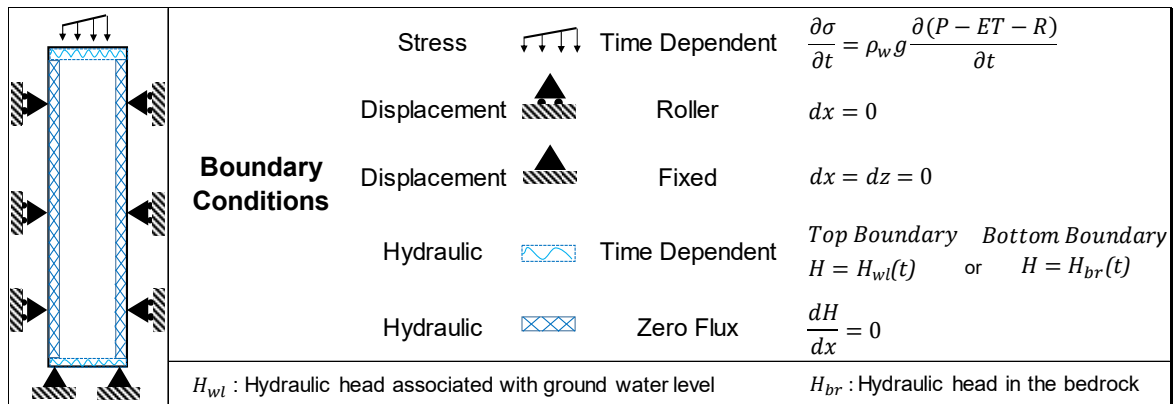


Figure 2.8 Hydraulic and mechanical boundary conditions in the model

The initial values of hydraulic head and displacements were calculated with a steady-state simulation. In this simulation, the hydraulic head boundary conditions were obtained from the initial values of the water table and bedrock hydraulic head. A free displacement (zero total stress) condition was applied at the top of the model. The displacement boundary conditions for the sides and base of the domain were the same as for the transient simulation. A zero flux condition was applied on the sides of the domain.

2.4.2 Material properties

The material properties in Biot's poroelasticity model include poroelastic and hydraulic properties. These properties consist of Young's modulus, porosity, Poisson's ratio, saturated density, Biot-Willis coefficient, and intrinsic permeability. These properties were measured or estimated for the different layers of the porous medium. Distinct property values were assigned for each layer.

Table 2.1 Poisson's ratios in sensitive clays

*	Material and condition	Poisson's ratio	*	Material and condition	Poisson's ratio
1	Saturated Clays (Undrained)	0.50	10	Saturated Clays (Undrained)	0.40-0.50
2	Champlain Clays (Test fills-Undrained)	0.49	11	Soft Clays (Bucket foundations-Drained)	0.30
3	Champlain Clays (Test fills-Undrained)	0.30	12	Champlain Clays (Drained)	0.20
4	Sensitive Clays (Drained-Undrained)	0.30-0.50	13	Sensitive Clays (Saint-Jean-Vianney Clays-Drained)	0.33
5	Champlain Clays (Undrained)	0.50	14	Champlain Clays (Drained)	0.30
6	Soft Clays (Drained)	0.30	15	Clay Till (Drained)	0.33
7	Natural Clays Undrained Loading	0.50	16	Silty Clays (Undrained)	0.46
	Fully drained	0.30	17	Champlain Clays (Undrained)	0.50
8	Champlain Clays (Drained)	0.35	18	Sainte-Monique Sensitive Clays (Drained)	0.25
9	Saturated Clays (Undrained)	0.50	19	Champlain Clays (Drained-Undrained)	0.30-0.50

* : 1-Skempton & Bjerrum (1957) 2-Rochelle et al. (1974) 3-Tavenas et al. (1974) 4-Tavenas et al. (1975) 5-Leroueil et al. (1978) 6-Banerjee & Stipho (1978) 7-Tavenas et al. (1979) 8-Yong & Silvestri (1979) 9-Davidovici (1985) 10-Sharma et al. (1990) 11-Zdravkovic (2001) 12-Silvestri (2003) 13-Hinchberger & Qu (2009) 14-Taechakumthorn & Rowe (2012) 15-Anochikwa et al. (2012) 16-Cui et al. (2014) 17-Elbegg et al. (2013) 18-Locat et al. (2014) 19-Marefat (2016)

Choosing an appropriate value for Poisson's ratio is difficult. Table 2.1 summarizes the values that were used by different authors. Poisson's ratio varies based on the saturation and the drainage condition of the domain. In saturated clay, it can range from 0.4 in drained condition to 0.5 in undrained condition. In partially saturated clay, it can decrease to 0.3 or even lower values (Sharma et al., 1990; Tavenas et al., 1975; Tavenas et al., 1979). The clay can be considered saturated in this study for the chosen domain. The long-term response of a clay layer to total stress changes and time-dependent boundary conditions corresponds to drained

condition. Poisson’s ratio influences the stress-strain relationship and settlements. The maximum strain at the top of the domain varies from 4.4×10^{-4} with $\nu = 0.49$ to 7×10^{-3} with $\nu = 0.2$ (Table 2.2). The simulated hydraulic head time series are also affected by Poisson’s ratio.

Table 2.2 The sensitivity of the strain and displacement to Poisson’s ratio

Poisson's ratio	Maximum estimated strain at top of the domain	Maximum estimated displacement at top of the domain (mm)
0.20	7.0×10^{-3}	45.0
0.25	6.5×10^{-3}	37.5
0.30	5.8×10^{-3}	35.0
0.35	4.8×10^{-3}	29.0
0.40	3.6×10^{-3}	23.0
0.45	2.0×10^{-3}	13.5
0.47	1.3×10^{-3}	8.80
0.49	4.4×10^{-4}	3.33

Figure 2.9 illustrates the hydraulic head time series for different Poisson’s ratios. It compares the simulated and observed hydraulic head time series considering the full saturation of the domain throughout the simulation period ($0.4 < \nu < 0.5$). Based on these results, the value of 0.45 was selected for Poisson’s ratio.

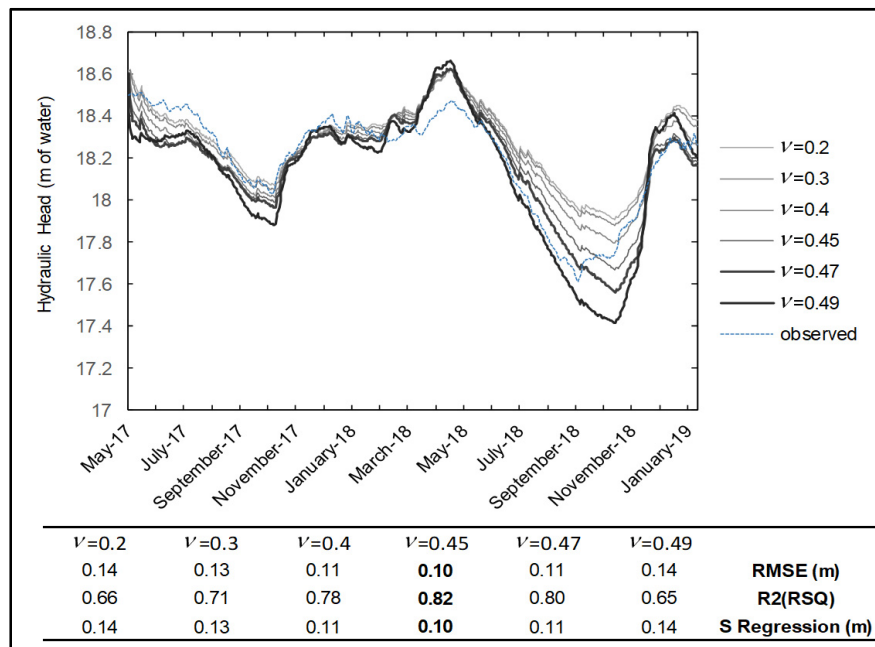


Figure 2.9 Simulated hydraulic head time series for different Poisson’s ratio

The density and porosity values were estimated from the natural water contents that were provided by Marefat et al. (2019). The values of intrinsic permeability (k_p) were estimated using the Kozeny-Carman method based on water properties at 10°C (Chapuis & Aubertin, 2003; Duhaime et al., 2013):

$$k_p = k_h \frac{\mu}{\rho_w g} = 10^A \frac{e^3 \mu}{g_{sp}^2 C_{sp}^2 (1 + e) \rho_w g} \quad (2.25)$$

where e is the void ratio, μ is the dynamic viscosity of water, g_{sp} is the specific gravity of the solid phase, C_{sp} is the specific surface, and A is a constant that depends on properties of the fluid and the tortuosity of the pore network. The optimal value of A was found to be 1.1 for Champlain clay (Duhaime et al., 2013). C_{sp} can be estimated using the following relationship:

$$C_{sp} = \frac{1000}{\frac{1.3513}{WL} - 0.0089} \quad (2.26)$$

Where WL is expressed as a percentage and C_{sp} is in m²/g. Young's modulus values were estimated using the experimental equation that was proposed by Elbeggo et al. (2019) for Abitibi Clay. Among the sensitive clays characterized by Elbeggo et al. (2019), the Abitibi clay is the one whose characteristics most resemble those of Sainte-Marthe clay. The selected equation estimates the normalized shear wave velocity of the soil (V_{s^*}) based on its overconsolidation and void ratios:

$$V_{s^*} = 1210CR^{0.2}(e)^{-0.67} \quad (2.27)$$

The shear wave velocity V_s can then be calculated using the following equation:

$$V_s = V_{s^*} \left(\frac{\sigma'_v}{\sigma_B} \right)^{0.25} \quad (2.28)$$

where σ'_v is the vertical effective stress.

The maximum shear modulus is calculated from the shear wave velocity using equation (2.29).

$$G_{max} = \rho_{tot}(V_s)^2 \quad (2.29)$$

where G_{max} is the maximum shear modulus and ρ_{tot} is the bulk density.

Finally, Young's modulus can be obtained by equation 2.30.

$$E_{max} = G_{max}(1 + 2\nu) \quad (2.30)$$

Concerning the value of Poisson's ratio (0.45), the maximum Young's modulus here is about twice the value of maximum shear modulus. It is worthy of note that the largest strain in the simulation is about 1.3×10^{-3} , which is in the large strains range ($\varepsilon > 1.3 \times 10^{-3}$). As it was mentioned in section 1.5.4, in this range, the Young's modulus of the soil is smaller than its maximum value and needs to be reevaluated with a proper degradation curve (Atkinson, 2000). For this purpose, the degradation curve proposed by Karray et al. (2016) for Ile Perrot Champlain clay was selected for the estimation of Young's modulus at large strains (Equation 2.31).

$$\frac{E}{E_{max}} = 0.2037\varepsilon^{-0.304} \quad (2.31)$$

The strain profile shows that the strains are very small for depths larger than 0.7 m. As a result, the top layer was subdivided into two sections of 0.7 and 3.8 m. The Young's modulus time series calculated with the degradation curve for each time step were then applied to the upper section (0.7 m) using a time series in COMSOL. A constant Young's modulus corresponding to the maximum value was selected for the other layers. Table 2.3 shows the average geotechnical properties for each layer.

Table 2.3 Geotechnical properties for the Sainte-Marthe study site

Depths (m)	Porosity (-)	Poisson's ratio (-)	Young's modulus (MPa)	Saturated density (kg/m ³)	Permeability (m ²)
3.0-7.5	0.60	0.45	3.10	1592	4.81×10^{-17}
7.5-11.0	0.65	0.45	7.04	1689	1.83×10^{-16}
11.0-14.0	0.60	0.45	26.88	1726	1.06×10^{-16}
14.0-15.3	0.47	0.45	46.00	1906	7.69×10^{-17}
15.3-20.6	0.40	0.45	46.00	1896	4.57×10^{-14}

2.4.3 MATLAB script

The applied stress on the soil surface is a critical variable for the analysis of pore pressure changes in the soil. For an initial estimation of pore pressure changes, the stress values can be obtained using equation 2.24 assuming the absence of runoff. This will be referred to as the baseline scenario (BS, $\rho_w g \Sigma(P-ET)$). This method was implemented before in several studies (e.g., Anochikwa et al., 2012; Barr et al., 2000). However, the assignation of a zero runoff to the model is not a realistic assumption to calculate the applied stresses in clayey soils with high runoff potential. To overcome this problem, a script was developed using the COMSOL LiveLink interface with MATLAB. This script can correct the stress values by analyzing the COMSOL model results for pore pressure. The main logic behind these corrections is to find the optimum stress time series based on a comparison of simulated and recorded pore pressures in the aquitard (Figure 2.10). Two methods were used in the MATLAB script for stress correction: the perfect stress method (PSt), and the net water balance method (NWB).

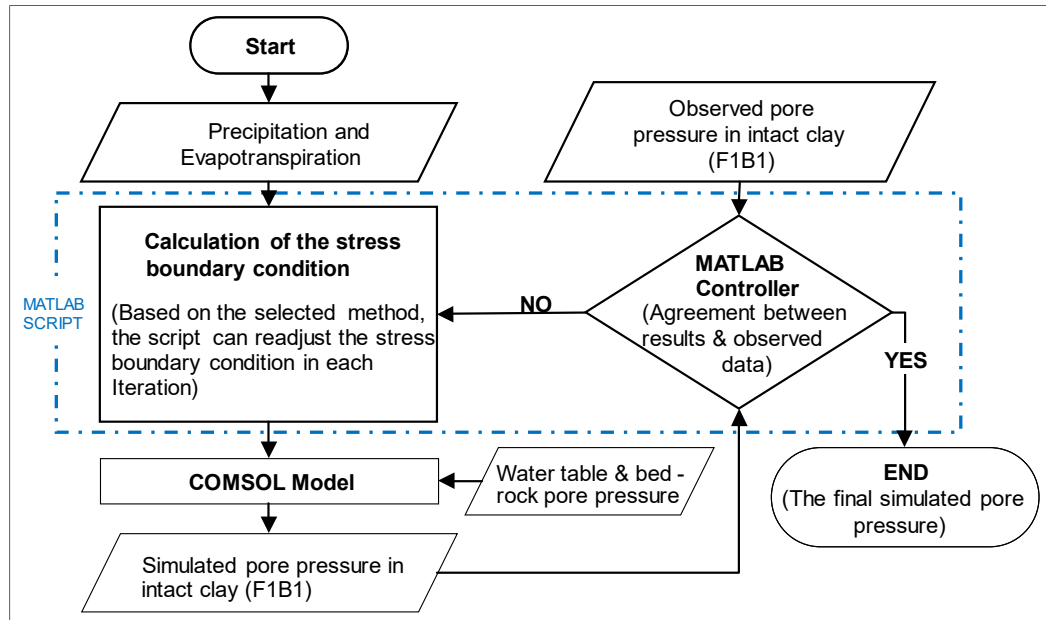


Figure 2.10 Simulation steps in pore pressure correction

2.4.3.1 Perfect Stress Method (PSt)

In the PSt method, the script corrects the total stress values with the Newton-Raphson technique. The observed pore pressure at depth of 12.2 m in each time step along with the corresponding simulated pore pressure are used for correction of the stress values:

$$\sigma_{j+1}(i) = \sigma_j(i) + (u^*(i) - u'_j(i)) \frac{(\sigma_j(i) - \sigma_{j-1}(i))}{(u'_j(i) - u'_j(i))} \quad (2.32)$$

where $\sigma_{j+1}(i)$ is the total stress on day i for iteration $j+1$ of the Newton-Raphson method. $u^*(i)$ is the measured pore pressure on day i , and $u'_j(i)$ is the FEM pore pressure on day i for iteration j of the Newton-Raphson method. The range of the total stress is not limited and it only varies based on the desired precision of the results. Since the pore pressure change is directly related to the stress change, it is always possible for the FEM pore pressure to match perfectly the field measurement. The main drawback of this method is that it does not verify if the net water balance associated with the estimated stresses is realistic.

2.4.3.2 Net Water Balance Method (NWB)

The NWB method is similar to the PS method but the stress range is limited by the soil water budget. This method puts constraints on the stress time series based on the net water balance. While the precipitation and evapotranspiration are known, runoff is the only component of water balance equation that is unknown and must be calculated by the MATLAB script.

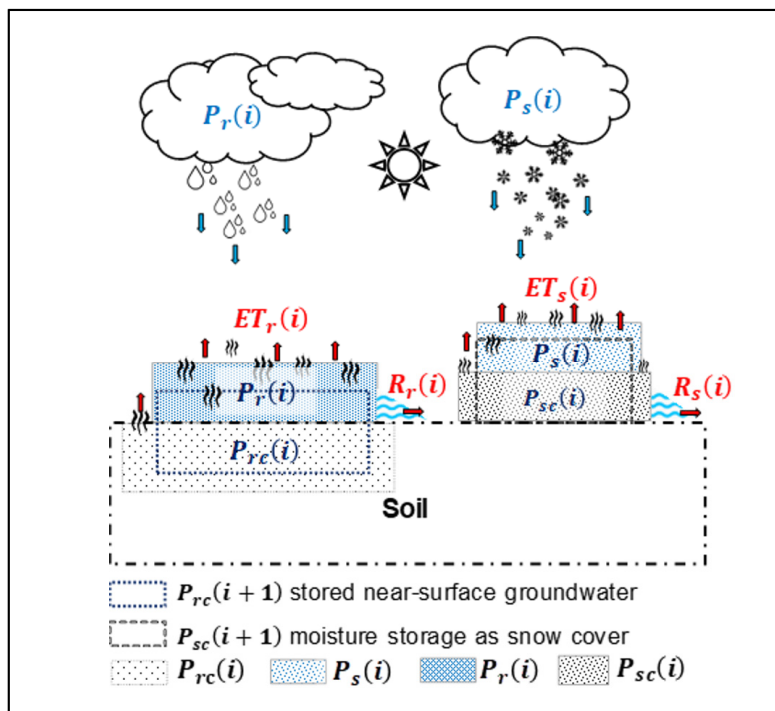


Figure 2.11 Components of the water balance equation

For accurate estimation of the water budget, the precipitations in forms of rain and snow were separated. Based on this hypothesis, the hydrological equations were developed to consider the storage of water as both snow and rain. Snow is stored as snow cover (P_{sc}) whereas rain is stored as near-surface groundwater (P_{rc}). Both components are added to the moisture storage (Figures 2.11 and 2.12). The stored water in one step can then be added to the available water budget of the following steps. This accumulated stored water is called the water available for runoff (A_{wr}). The A_{wr} on the day i is expressed as the sum of precipitation as rain (P_r) and snow

(P_s , in equivalent water height), and the snow cover accumulated from the previous time step (P_{sc} also in equivalent water height):

$$A_{wr}(i) = P_r(i) + P_s(i) + P_{sc}(i) \quad (2.33)$$

With this hypothesis, the same runoff rate (R) is applied to all components of runoff in each time step. R is a coefficient between 0 and 1 that represents the fraction of A_{wr} that leaves the system as runoff. For the rain component of runoff, the runoff for time step i is only applied to the rain:

$$R_r(i) = R(i) P_r(i) \quad (2.34)$$

where R_r is the amount of rain leaving the system as runoff. For snow, the runoff is assumed to be proportional to the sum of precipitation as snow and the snow cover:

$$R_s(i) = R(i) (P_s(i) + P_{sc}(i)) \quad (2.35)$$

where R_s is the amount of snow leaving the system as runoff. The water available for evapotranspiration (A_{wet}) is not the same as A_{wr} . Evapotranspiration is assumed to impact the water stored as snow and rain at the beginning of the time step and the precipitation net of runoff:

$$A_{wet}(i) = (P_r(i) + P_s(i) + P_{sc}(i))(1 - R(i)) + P_{rc}(i) \quad (2.36)$$

where $P_{rc}(i)$ corresponds to the amount of water stored as near-surface groundwater at the beginning of day i . The evapotranspiration of liquid water (ET_r) is proportional to the near-surface groundwater storage and rain, while the evapotranspiration of snow (ET_s) is proportional to the snow cover and precipitation as snow:

$$ET_r(i) = ET(i) \frac{P_r(i)(1 - R(i)) + P_{rc}(i)}{A_{wet}(i)} \quad (2.37)$$

$$ET_s(i) = ET(i) \frac{(P_s(i) + P_{sc}(i))(1 - R(i))}{A_{wet}(i)} \quad (2.38)$$

where $ET(i)$ is the total evapotranspiration for day i calculated as described in section 2.4.1. The new near-surface groundwater storage and snow cover at the end of day i can be calculated using a simple water budget:

$$P_{rc}(i + 1) = P_{rc}(i) + P_r(i) - ET_r(i) - R_r(i) \quad (2.39)$$

$$P_{sc}(i + 1) = P_{sc}(i) + P_s(i) - ET_s(i) - R_s(i) \quad (2.40)$$

The total stress at the beginning of each day is calculated from the weight of a water column equivalent to the groundwater storage and snow cover:

$$\sigma(i) = \rho_w g (P_{rc}(i) + P_{sc}(i)) \quad (2.41)$$

The $P_{sc}(i+1)$ value should either be zero or positive. Negative values should be replaced with zero and the water deficit should be transferred to $P_{rc}(i+1)$. These simplifications and assumptions were made for making the model as simple as possible since the aim of this study is not to develop a hydrological model.

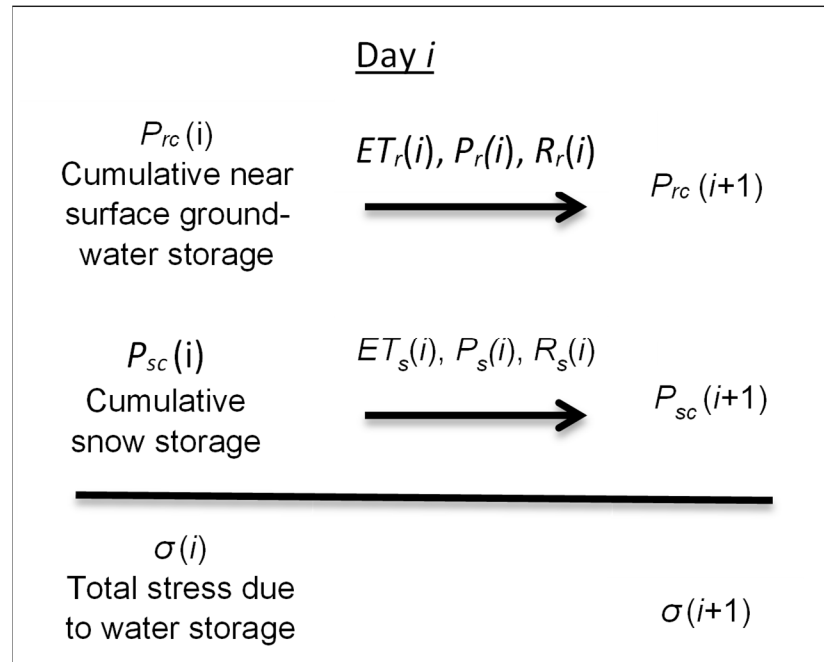


Figure 2.12 Schematic representation of the time-stepping scheme for the day i

The MATLAB script employing equations 2.33-2.41 imposes a hydrological constraint on the water budget and consequently on the $\sigma(i)$ values. The boundaries of this constraint are defined regarding the R coefficient. The R coefficient is the main parameter that changes in the NWB method and the rest of unknown parameters are defined respect to that. The upper limit of stress range occurs when there is no runoff. The lower limit is observed when the R coefficient takes its highest value. This maximum R can be specified by the user.

The $R(i)$ values were obtained using the Newton-Raphson method:

$$R_{j+1}(i) = R_j(i) + \left(u^*(i) - u'_j(i) \right) \frac{\left(R_j(i) - R_{j-1}(i) \right)}{\left(u'_j(i) - u'_{j-1}(i) \right)} \quad (2.42)$$

where indices $j-1$ and $j+1$ stand for the iteration numbers as in equation 2.32. Contrarily to the σ values with the PS method, the $R(i)$ values are bounded by 0 and 1, or some other upper value set by the user. The upper and lower $R(i)$ limits were used to estimate the slope of the

relationship between u and R for the first iteration (i.e., $R_1(i) = 0$ and $R_2(i) = 1$). It is worth mentioning that in cases where $R_{j+1}(i)$ is out of the range $(0, R_{max})$, the script replaces it with 0 or R_{max} .

CHAPITRE 3

Numerical modelling of soil deformation in Champlain Clays

The initial principles of poroelastic theory that were proposed by Biot (1941) only cover linear-elastic behaviour. Later, with the progresses that were made by several researchers (e.g., Biot, 1955, 1956, 1972, 1973; Verruijt, 1969; van der Kamp & Gale, 1983; Wang, 2000; Cheng, 2016), the poroelastic theory was generalized to account for more complex behaviour. Concepts such as viscoelasticity, micromechanics, thermoelasticity, and non-linear rheology were added to the initial theory. Linear stress-strain relations for porous media (Biot, 1941) and the van der Kamp and Gale (1983) theory were presented in section 2.2. These approaches are simplistic and cannot model more complicated deformation in porous media. For instance, the volume change associated with temperature change is an important phenomenon that was neglected in the stress-strain equations in section 2.2.

In cold regions where radical temperature changes occur periodically, thermal effects can play a key role in the behaviour of clayey soils. As a result, a more general form of linear poroelasticity including thermal effects is presented in this chapter.

This chapter first presents a brief literature review of settlements in cohesive soil. Then the constitutive equations including the thermal effect for isotropic poroelastic material will be explained. In the following section, more specific stress-strain and transient flow relationships that were derived with some simplifications for our case study will be defined. Finally, the methodology that was used for the numerical modelling of soil deformation in Champlain clays for the Saint Marthe study site will be discussed in detail.

3.1 Settlement definition

The terms settlement and subsidence are often used interchangeably in the literature to refer to a downward movement of the soil. Some authors distinguish settlement as the result of an external load and subsidence as the result of other phenomena that cause a volume change in

the soil or bedrock, such as dissolution, pore pressure changes and internal erosion (e.g., CMWgeosciences, 2017; The commercial law practice, 2021). Based on these definitions, the settlement of foundations after their construction is an example of settlement. The term settlement will be used in this study to encompass all downward movement of the soil. The term settlement is more widely used by geotechnical engineers.

Settlements due to an external load are often divided in three components: immediate, primary and secondary settlement. Immediate settlement occurs immediately after an increase in overburden pressure, before pore pressure dissipation. Immediate settlement in cohesive soils has historically been interpreted with elastic stress-strain relationships. The 1D immediate settlement under a uniformly loaded area can be estimated using the following general equation (Fang, 2013; Skempton & Bjerrum, 1957):

$$ST_i = C_s q' B_d \left(\frac{1 - \nu^2}{E} \right) \quad (3.1)$$

where ST_i is the immediate settlement, C_s is the shape and rigidity factor, q' is the uniformly distributed load, and B_d is the width of the loaded area. The consolidation settlement occurs after the immediate settlement as the pore pressure dissipates. Consolidation settlement is associated with an increase in effective stress. Secondary consolidation or creep occurs over time and is not associated with changes in effective stress.

Consolidation settlement can be expressed in terms of void ratio:

$$ST_c = \frac{\Delta e}{1 + e_0} L_0 \quad (3.2)$$

where ST_c is the total consolidation settlement (primary and secondary), Δe is the decrease in void ratio due to consolidation, e_0 is the initial void ratio, and L_0 is the initial thickness of the soil layer.

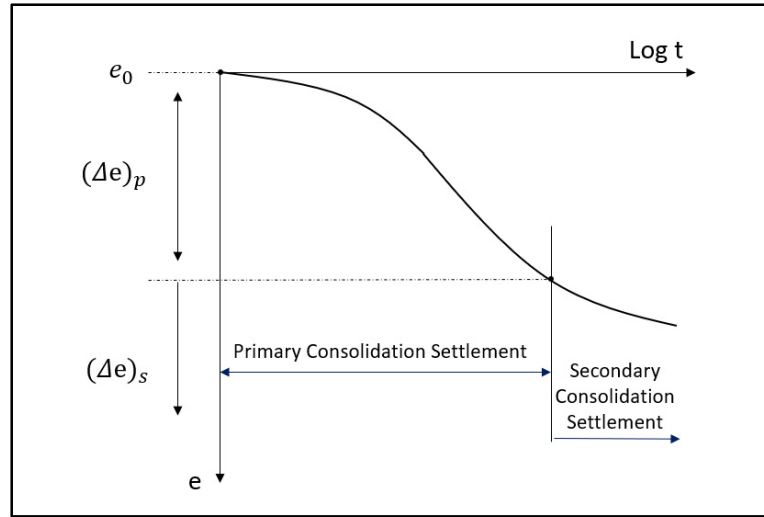


Figure 3.1 Primary and secondary consolidation settlement adapted from Mesri & Choi (1985)

Figure 3.1 illustrates the void ratio changes during the consolidation settlement of a cohesive soil. The void ratio reductions Δe_p and Δe_s are respectively associated with primary and secondary compression.

Primary and secondary consolidation can be evaluated using empirical models. For instance, a conservative empirical model of Morissette et al. (2001) can predict the long-term settlements of embankments of clays. It is worth mentioning that for overconsolidated clay, the settlement is relatively small as long as the change in vertical effective stress ($\Delta\sigma'$) does not exceed the difference between σ'_p and the in situ effective stress (σ'_{ins}). The settlements for larger effective stress increments can be considerably larger. The proposed empirical equation can estimate the settlement based on the the ratio between $\Delta\sigma'$ and $(\sigma'_p - \sigma'_{ins})$, and the OCR value.

$$\epsilon = 0.342 \log \frac{\Delta\sigma'}{(\sigma'_p - \sigma'_{ins})} + 0.214 \log OCR - 0.0904 \quad (3.3)$$

Comparisons with case studies showed that the settlements obtained with this equation have a $\pm 33\%$ margin of error. A correction factor was also presented for highly compressible clays with a high water content.

3.1.1 Soil settlement in cohesive soils

Most studies on settlements have focused on settlements associated with external loads, especially earth fills. These studies often involve large settlements and plastic deformations. D'Appolonia et al. (1971), for instance, presented an improved method to estimate the immediate settlement of the soil based on the finite difference method. This method could consider the effect of local yielding in elastic theory. Using this method, the actual settlement can be estimated based on the elastic settlement. Earth fills as was mentioned earlier is one of the external loads that causes settlement in cohesive soils. Test fills are the best-established method to examine the compaction progress in any kind of soil. Tavenas et al. (1974) and La Rochelle et al. (1974) examined the stability of the Champlain deposit of Saint-Alban when loaded with different test fills. Tavenas et al. (1974) observed that the mechanical behaviour of the soft soil is elastic until the load reaches 60 % of the failure stress. The critical height of the test fills for which non-linear stress-strain deformations were observed varied between 1.8 to 2.7 m, or approximately 50% of the failure height. It was also suggested that a Poisson's ratio of 0.3 instead of 0.5 leads to more realistic immediate settlement estimations. La Rochelle et al. (1974) observed settlements as large as 15 cm at the soil surface under the middle of their test embankment after 2 days when the height of the fill reached 3.89 m. This study showed that considering the full mobilization of the friction angle can be a logical assumption in stability analysis of similar test fills. They also showed that considering the residual undrained shear strength instead of the conservative minimum strength in stability analyses of fills can be helpful in order to avoid underestimating the safety factor.

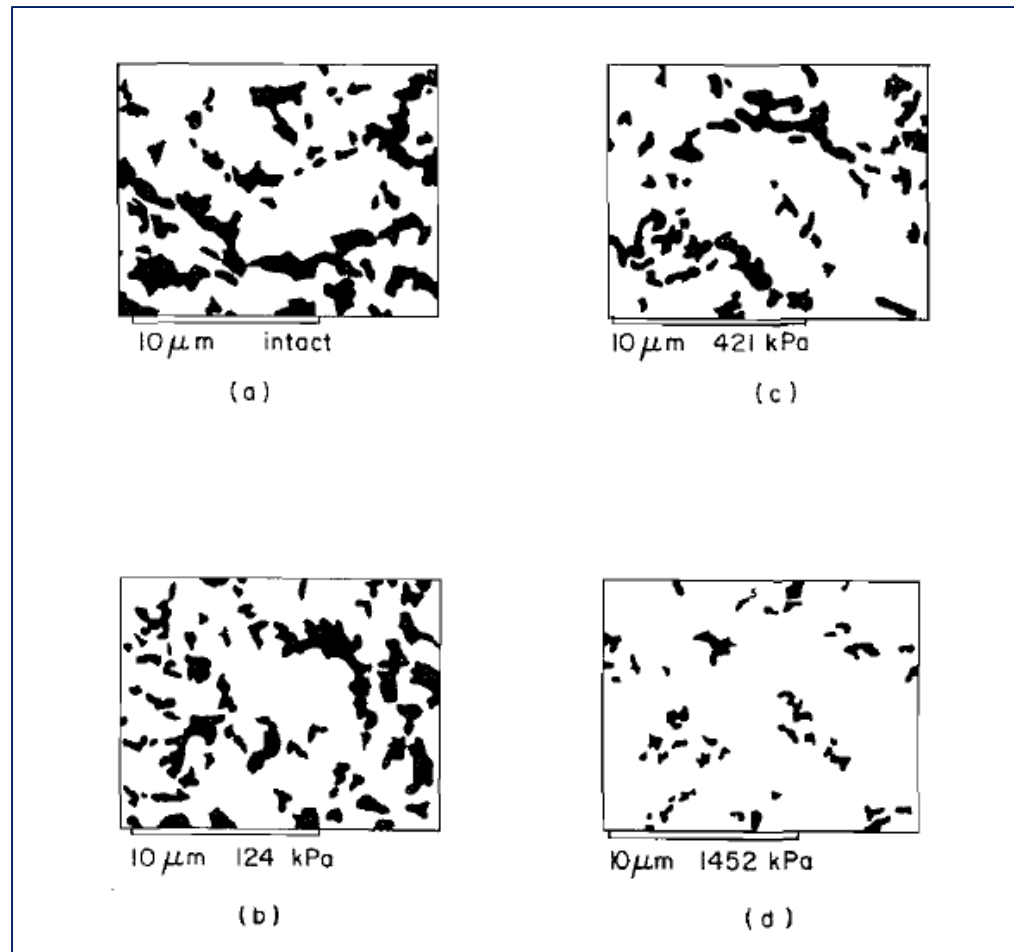


Figure 3.2 Porosity distribution of Champlain clay specimens under different stress levels adapted from Delage & Lefebvre (1984)

Many studies have focused on the development of stress strain-relationship of clay or their behaviour at the microscopic scale. Delage & Lefebvre (1984) studied the consolidation of Champlain clays at the microscopic scale. This study revealed the existence of interaggregate and aggregate links in confined soils where the aggregated structure is proved to be more resistance to remolding. It was demonstrated that in a cohesive soil, by progression of the consolidation, the size of the affected interaggregate pores declines to the end of the process. In other words, only the largest pore are affected for a given increment in consolidation. They also estimated that intra-aggregate pores represent around 70 % of the total porosity in Champlain clays of Saint-Marcel. Figure 3.2 shows how the pore average size decreases by increasing the stress level.

As mentioned in chapter 1, marine clays of formerly glaciated regions have a complex behaviour due to salt leaching. Bjerrum (1967) studied the effect of geological process including leaching, delayed consolidation and cation exchange of minerals on settlement of foundations constructed over normally consolidated Norwegian clays. He showed that leaching can heavily affects the properties of normally consolidated clays and increase their sensitivity. He also showed that secondary consolidation leads to an increase in shear strength of the soil caused by a decrease of the void ratio.

The number of studies focusing on the settlements associated with climate is limited. In this regard, it was showed that there is a strong correlation between water deficit and settlement in Champlain clays deposits. The relationship between rainfall deficit and foundation settlements was investigated by Silvestri et al. (1990). A new approach to estimate the water budget inside the soil was implemented in this study. Reported foundations problems and rainfall deficits values for the period between 1930 and 1988 were compared. It was demonstrated that there is a strong link between rainfall deficit and foundation problems. In the studied period, whenever the rainfall deficits passed a 209 mm threshold, more serious foundations problems were reported in Montreal buildings. Later, Silvestri et al. (1992) monitored the soil water content at different depths using a neutron moisture probe for a 3-year period (1987-1989). In the studied period, rainfall deficit, soil water content, and surface settlements were compared together. These observations showed that the water content of the soil changes seasonally. These seasonal variations are more significant near the surface and can reach a depth of 1.2 m in areas far from trees and 2.8 m next to trees. A differential settlement of 100 mm was observed over the same period in shallow foundations constructed in clay deposits next to deep rooted trees. Silvestri (2000) investigated the relationship between observed foundation and ground settlements, and the soil water content and pore pressure head time series for the period 1990-1993. Five study sites on Montreal Island were established. The results showed that the foundation walls and the ground next to the trees are most vulnerable to soil moisture variation. It was also found that the settlements correspond approximately to the moisture deficit divided by 3 for Champlain clay deposits of the Montreal area. For instance, a water depletion of 260 mm on the Rameau study site led to a ground settlement of 83 mm.

In this study we are trying to investigate the relationship between fluctuations of the soil moistures and soil settlement of Champlain clays using a simple numerical modelling. This has been less investigated in the former studies that some of them briefly reviewed in this section. The temperature fluctuation effects on settlement of cohesive soils have also been poorly studied. Furthermore, in the rare numbers of the studies in this context (Yu et al., 2020a; Yu et al., 2020b) often, very complicated models have been developed that their implantation by the general users is not easy. Freeze-thaw cycles and other temperature effects on soil settlement will also be included in this simplistic numerical modeling.

3.2 Linear poroelasticity

As it was mentioned earlier, poroelastic theory describes the relationship between fluid flow and deformation in a saturated porous media. Earlier in the section of 2.1, we described the principal theories dealing with the mechanical behaviour of soil and flow in porous media. We used the simplified form of this theory which was developed by van der kamp & gale (1983) to simulate the pore pressure fluctuations due to stress changes within a porous media. The focus of chapter 2 was simulation of pore pressure changes rather than estimation of the soil deformation. The temperature effects were also neglected from the numerical modeling.

The linear form of poroelasticity including the relations between strain and effective stress was presented by Wang (2000) and Neuzil (2003). In linear poroelasticity, six strain components can be defined using equations 3.4 and 3.5:

$$\varepsilon_{xx} = \frac{\partial u_x}{\partial x}, \quad \varepsilon_{yy} = \frac{\partial v_y}{\partial y}, \quad \varepsilon_{zz} = \frac{\partial w_z}{\partial z} \quad (3.4)$$

$$\varepsilon_{xy} = \frac{1}{2} \left(\frac{\partial u_x}{\partial y} + \frac{\partial v_y}{\partial x} \right), \quad \varepsilon_{xz} = \frac{1}{2} \left(\frac{\partial u_x}{\partial z} + \frac{\partial w_z}{\partial x} \right), \quad \varepsilon_{yz} = \frac{1}{2} \left(\frac{\partial v_y}{\partial z} + \frac{\partial w_z}{\partial y} \right) \quad (3.5)$$

where u_x , v_y , and w_z are displacement components in x , y , and z directions. Using equation 2.6, the volume strain can be defined from the normal stresses and pore pressure with the following equation:

$$\epsilon = \epsilon_{xx} + \epsilon_{yy} + \epsilon_{zz} = \frac{1}{K_b} \left(\frac{\sigma_{xx} + \sigma_{yy} + \sigma_{zz}}{3} - au \right) \quad (3.6)$$

Including the thermal effects, the constitutive equations of poroelasticity can define the changes in normal strains in each direction knowing the associated pore pressure, stresses, and temperature (Equations 3.7-3.9):

$$\epsilon_{xx} = \frac{1}{2G} \left(\sigma_{xx} - \frac{\nu}{(1+\nu)} \sigma_t \right) - \frac{\alpha}{3K_b} u - \alpha_T T \quad (3.7)$$

$$\epsilon_{yy} = \frac{1}{2G} \left(\sigma_{yy} - \frac{\nu}{(1+\nu)} \sigma_t \right) - \frac{\alpha}{3K_b} u - \alpha_T T \quad (3.8)$$

$$\epsilon_{zz} = \frac{1}{2G} \left(\sigma_{zz} - \frac{\nu}{(1+\nu)} \sigma_t \right) - \frac{\alpha}{3K_b} u - \alpha_T T \quad (3.9)$$

Where α_T is the thermal expansion coefficient. These equations can be reformulated for the relation between displacement, pore pressure, and temperature:

$$G \nabla^2 u_x + \frac{G}{1-2\nu} \left(\frac{\partial^2 u_x}{\partial x^2} + \frac{\partial^2 v_y}{\partial x \partial y} + \frac{\partial^2 w_z}{\partial x \partial z} \right) = \alpha \frac{\partial u}{\partial x} + G \frac{2(1+\nu)}{1-2\nu} \alpha_T \frac{\partial T}{\partial x} \quad (3.10)$$

$$G \nabla^2 v_y + \frac{G}{1-2\nu} \left(\frac{\partial^2 u_x}{\partial y \partial x} + \frac{\partial^2 v_y}{\partial y^2} + \frac{\partial^2 w_z}{\partial y \partial z} \right) = \alpha \frac{\partial u}{\partial y} + G \frac{2(1+\nu)}{1-2\nu} \alpha_T \frac{\partial T}{\partial y} \quad (3.11)$$

$$G \nabla^2 w_z + \frac{G}{1-2\nu} \left(\frac{\partial^2 u_x}{\partial z \partial x} + \frac{\partial^2 v_y}{\partial z \partial y} + \frac{\partial^2 w_z}{\partial z^2} \right) = \alpha \frac{\partial u}{\partial z} + G \frac{2(1+\nu)}{1-2\nu} \alpha_T \frac{\partial T}{\partial z} \quad (3.12)$$

Equations 3.10-3.12 represent the thermoelastic and poroelastic coupling in porous media where the linear deformations induced either by temperature or pore pressure change can be addressed.

3.2.1 One dimensional deformation in porous media induced by thermal and mechanical loads

Settlements in soft clays can occur without an increase in the overburden stress. Deformation can occur slowly due to creep, but faster deformations mostly result from rapid changes in pore pressure or temperature. Rapid changes in pore pressure can be due to changes in the local water balance, for instance increased evapotranspiration or decreased precipitation. As a result, temperature and pore pressure are two parameters that play a crucial role in the deformation of clayey soils. Deformation due to water deficits, pore pressure decrease, only occurs in form of subsidence while the deformation due to temperature change might result in upward or downward movement of the soil.

In cold regions, freezing temperatures can also cause significant heave during winter and thaw consolidation in late spring or early summer. Intact clays newly exposed to freeze-thaw cycles are especially prone to large heave and thaw settlement. Konrad et al. (1995) compared the deformation of clay newly exposed to freezing conditions and weathered crust already exposed to thousands of freeze-thaw cycles. The newly exposed clay showed mean heave and thaw settlement of 19.0 and 21.6 cm, respectively, for a permanent settlement of 2.6 cm. For the weathered crust, the mean heave and thaw settlement were both 5.7 cm, thus confirming that the heave observed in the weathered crust is reversible. Modelling of freeze-thaw phenomena is a complex approach (e.g., Dumais and Konrad 2018). In this study, frost heave was simulated with a less complicated approach assuming some simplifications. In general, more emphasis was put on the impact of pore pressure and temperature changes throughout the clay layer as the scope of this study was long-term deformation of clay profiles with a weathered crust.

It is an acceptable assumption that the deformation in a laterally extensive deposits of fine-grained soils with a gentle slope like our study site (slope less than 1%) be considered mainly vertical (van der Kamp & Gale, 1983). As a result, the linear poroelastic theory in one dimensional form was implemented for investigating the effects of pore pressure and temperature changes on the structural deformation of the sensitive clays.

Neglecting the lateral stress and strains, equation 3.11 can be reformulated into one dimensional form (Equation 3.13). The vertical strain ($-\partial v_y/\partial y$) can then be expressed by the following equation:

$$-\frac{\partial v_y}{\partial y} = \frac{-u}{M} - \frac{(1 + \nu)}{(1 - \nu)} \alpha_T T \quad (3.13)$$

where v_y is the vertical displacement or displacement in y direction, y is the elevation with respect to the bedrock. The thermal expansion (α_T) was presented earlier in section 1.5.5. The constrained modulus (M) is defined as:

$$M = \frac{2G(1 - \nu)}{(1 - 2\nu)} \quad (3.14)$$

Equation 3.13 shows that the strain, the derivative of the displacement, can be obtained from the pressure and temperature.

Assuming that the displacement is initially equal to 0 throughout the profile, equation 3.13 can be rewritten as follows:

$$-\frac{\partial v_y}{\partial y} = \frac{-(u - u_{init})}{M} - \frac{(1 + \nu)}{(1 - \nu)} \alpha_T (T - T_{init}) \quad (3.15)$$

where u_{init} and T_{init} are the depth-dependent initial conditions for pressure and temperature. This definition allows the strain and displacements to be set at 0 at the beginning of the simulation.

3.2.1.1 Frost deformations

Frost deformation can be included in equation 3.15 by introducing a $\Delta V_f(T)$ function that accounts for the volume change associated with the liquid water to ice phase change assuming a closed system without external water supply:

$$-\frac{\partial v_y}{\partial y} = \frac{-(u - u_{init})}{M} - \frac{(1 + \nu)}{(1 - \nu)} \alpha_T (T - T_{init}) + \frac{\Delta V_f(T)}{3} \quad (3.16)$$

where ΔV_f is the volume change induced by freezing per unit volume of clay. The division by 3 in equation 3.16 relates the volume change proportion to linear expansion assuming isotropic behaviour.

A schematic picture of this function is presented in figure 3.3. This function is related to the soil freezing characteristic curve (SFCC) which relates the volume of frozen water in a soil with respect to the temperature for a closed system. Based on the shape of the experimental SFCC that are presented in the literature, ΔV_f should follow a power law with progressively decreasing rates of volume change with decreasing temperature (Wang et al. 2022). In Figure 3.3, it is assumed that the freezing volume change occurs linearly between $T=0$ °C and $T=T_{frozen}$ where T_{frozen} is the temperature for which the water phase change is completed inside the soil. The full volume change is calculated based on Konrad et al. (1995) by the following equation:

$$\Delta V_{f(fully\ developed)} = 0.09n \quad (3.17)$$

Equation 3.17 assumes a full saturation and a 9 % volume increase due to the liquid water – ice phase change. As it will be shown later in the thesis, even if this approach is highly simplified, the magnitude of the heave obtained with equation 3.17 is generally comparable

with the heave and thaw settlement observed in the field for the oxidized crust of Champlain clay deposits (e.g. Konrad et al. 1995; Silvestri 2000).

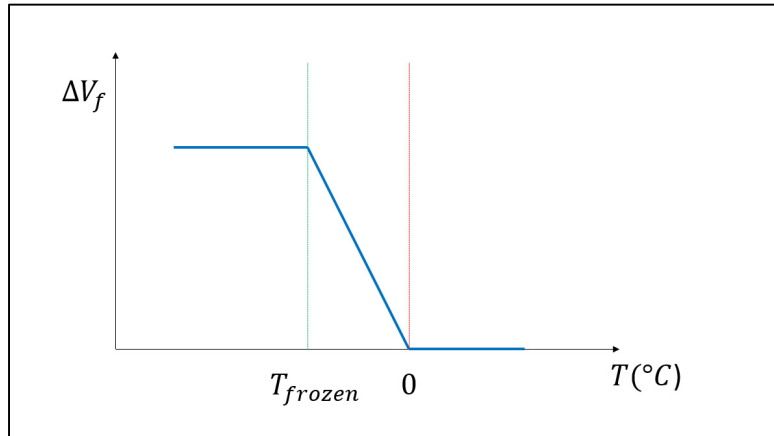


Figure 3.3 ΔV_f function

3.3 Methodology

3.3.1 Numerical modelling of deformations of Sainte-Marthe study site

As it was mentioned earlier, a laterally constrained 1D model is used in this study. The model based on the proposed approach should be able to successfully estimate the major deformation in our study site. Pore pressure changes induced by mechanical loads and temperature fluctuation are two main factors that define the deformation in the soil. However, the accurate estimate can not be easily achieved where the shallow aquitard at the top compared to the aquitard at the bottom has a different range of mechanical and hydrological properties and can behave very differently exposing to temperature changes or mechanical loads. As a result, a model is needed that can differentiate their distinctive qualities and manage uniquely each of the shallow top layer or the deeper intact layer of the soil.

3.3.1.1 Conceptual Model

The conceptual model simulates the soil vertical deformation using two domains, A and B, with different hypotheses (Figure 3.4). Domain A is associated with the oxidized layer at the top of the soil profile. Domain B models the intact clay layer below the oxidized layer to a depth of 12.2 m where the lowest fully grouted piezometer is installed. The displacements below a depth of 12.2 m were excluded from the numerical simulation based on the assumption that displacements are larger near the top of the clay profile.

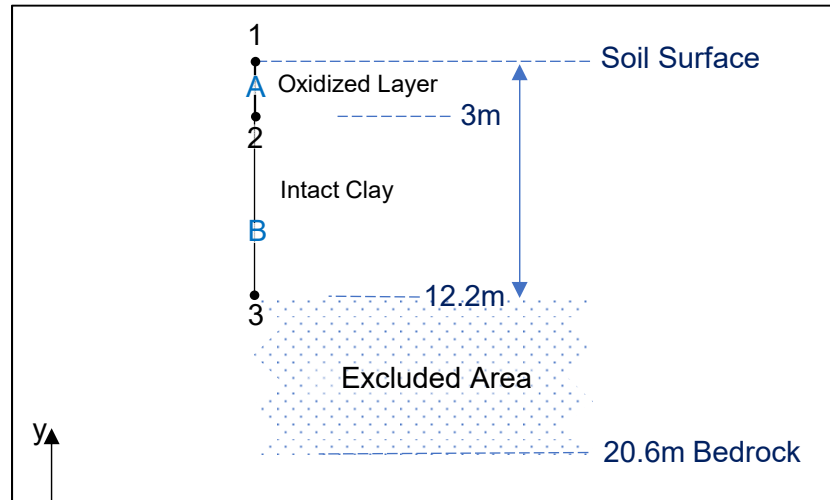


Figure 3.4 Conceptual model

A few simplifications were introduced in the model. The interaction between deformation and pore pressure and temperature changes was assumed one-sided as the influence of deformation on the two other terms were not taken into account. The porous media is assumed to be homogenous and fully saturated. The surface temperature of the soil was assumed equal to the air temperature, no convection boundary condition was considered.

3.3.1.2 Partial differential equation (PDE) in COMSOL

In chapter 2, the pore pressure changes in the shallow aquitard of the Sainte-Marthe study site were simulated using a coupled hydro-mechanical model based on the Biot-poroelasticity feature in 2D. The preprogrammed Biot-poroelasticity feature couples the solid mechanic and Darcy physics. Although the conceptual model was developed for a 1D geometry, due to limitations of the solid mechanic feature, a 2D model was implemented. Results consistent with the 1D geometry were obtained by setting the appropriate boundary conditions. The focus of the numerical model presented in chapter 2 was to identify the missing atmospheric parameters with the MATLAB interface

In this section, we develop our own COMSOL model with a combination of ready-to-use physics and custom partial differential equations (PDE) to model deformations in the clay layer. The custom PDE interface allowed to develop a proper 1D coupled thermo-hydro-mechanical model without resorting to a 2D model. The PDE interface also gives us more freedom to modify the model as the ready-to-use physics impose more restriction on the user.

Custom PDE functions are accessible in COMSOL in general, coefficient, wave, and weak forms. The coefficient form of the PDE interface was implemented in this study. In the coefficient form, a general PDE template can be modified by defining the associated coefficients. Equation 3.18 shows the PDE template for the coefficient form in COMSOL.

$$c_5 \frac{\partial^2 X_i}{\partial t^2} + c_4 \frac{\partial X_i}{\partial t} + \nabla \cdot (-c_3 \nabla X_i - c_6 X_i + c_7) + c_2 \cdot \nabla X_i + c_1 X_i = c_6 \quad (3.18)$$

where X_i is the main variable, ∇ is $\partial/\partial x$, and c_1-c_6 are the coefficients that define the PDE. In case a term in equation 3.13 is not needed, the associated coefficient is set to zero.

3.3.1.3 Domain A

The displacements in domain A with and without frost heave were simulated respectively with equations 3.15 and 3.16 using the PDE feature in COMSOL (Figure 3.5). Equations 3.15 and 3.16 need the temperature and pore water pressure values to estimate the deformation. Because of the higher hydraulic conductivity in the weathered crust, the hydraulic head was assumed constant throughout the crust at any time. The weathered crust is therefore modelled in a steady-state condition. The variation of the hydraulic head in time was obtained from the groundwater levels that were measured in the surface piezometer, $GWL(t)$. The temperature in both domains is obtained from the following heat conservation equation (COMSOL 2020a):

$$(\rho c_p)_{eff} \frac{\partial T}{\partial t} - \nabla \cdot k_{eff} \nabla T = 0 \quad (3.19)$$

where $(\rho c_p)_{eff}$ is the effective volumetric heat capacity at constant pressure, k_{eff} is the effective thermal conductivity, and t is the time variable. The term “effective” refers to mean value of the property in the soil. Heat advection is not included in equation 3.19 because of the very low seepage velocity in the clay.

Parameter ν and α_T were assigned values of 0.3 and $9 \times 10^{-5} \text{ K}^{-1}$. The Poisson’s ratio was set as 0.3 is a typical value for small deformations (Tavenas et al 1974). The rough estimation of thermal expansion was calculated by the weighted average of the thermal expansions of the clay minerals as explained earlier in detail in section 1.5.5.

3.3.1.4 Domain B

Similar to domain A, displacement and temperature in domain B were calculated using equations 3.15, 3.16 and 3.19. However, the hydraulic head and pore pressure were calculated based on Darcy’s law and a water conservation equation (Equation 3.20) considering a linear storage model (COMSOL 2020b). In the storage model, the storage coefficient (S) was

specified equal to specific weight of the water divided by constrained modulus of the soil, (γ_w/M) .

$$\nabla \cdot (K_h \nabla H) = S \frac{dh}{dt} \quad (3.20)$$

Hydraulic conductivity was set at 1×10^{-9} m/s in the lower intact clay layer based on typical values for Champlain clays (e.g. Duhaime et al. 2017). The M modulus was set to both 1.3 and 50 MPa, as in the oxidized crust. The ν and αT were assigned as 0.3 and 9×10^{-5} K⁻¹ as in the weathered crust.

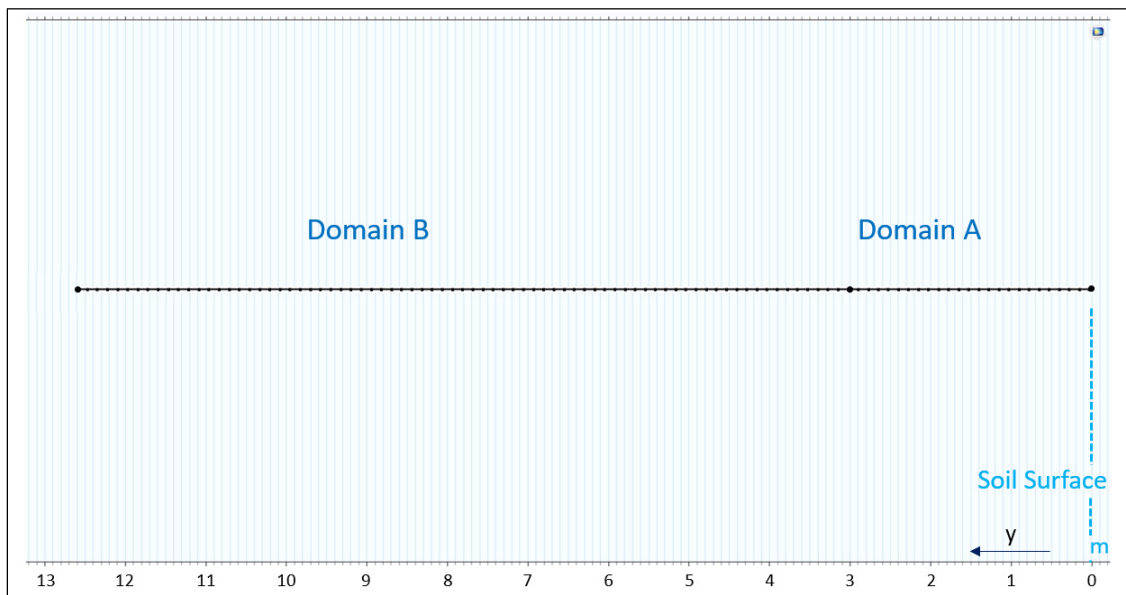


Figure 3.5 Mesh and geometry of the model in COMSOL

3.3.1.5 Boundary conditions and initial values

Table 3.1 shows the boundary conditions for domains A and B. There is no hydraulic boundary condition for domain A as pressure is assumed to be hydrostatic because of the higher hydraulic conductivity of the oxidized crust. The hydraulic time series for domain A was obtained from the top VWP. Hydraulic head at the top of domain B was set equal to hydraulic head in domain

A. Hydraulic head at the bottom of domain B was set equal to the hydraulic head time series determined from the lower VWP at a depth of 12.2 m. Displacements at the bottom of domains A and B were set equal to 0. The real displacements in domain A were calculated by summing the displacements in domain A with the displacements at the top of domain B. As mentioned earlier, the temperature at the top of domain A was set equal to the air temperature. To verify the influence of temperature on the settlements, a second scenario was tested with a constant temperature boundary equal to the mean air temperature. The temperature field in domains A and B is continuous. The temperature at the bottom of domain B was set to 7.8 °C for all simulations. This temperature reflects the approximately constant value measured by the VWP.

Table 3.1 also shows the initial conditions. In both domains, the initial values of displacement were set to 0. Initial temperatures values throughout the domain were calculated using a linear interpolation between the initial values of temperatures at the top and bottom of the domain. The initial hydraulic heads were also interpolated for domain B.

Table 3.1 Hydraulic, thermal, and displacement boundary conditions in the model

Component	Boundary	Boundary Conditions		
		Hydraulic	Displacement	Thermal
A	Top			$T(t) = T(t)_{surface/air}$
	Bottom		$u_x = 0$	
B	Top	$H(t) = GWL(t)$		
	Bottom	$H(t) = BWL(t)$	$u_x = 0$	$T(t) = T(t)_{VWP(12.6\ m)}$
Component	Initial condition			
	Hydraulic	Displacement	Thermal	
A	$H = GWL(0)$			
B	$H = H_{intp(lower\ layer)}^{*a}$	$u_x = 0$	$T = T_{intp}^{*b}$	
<p>*^a: The initial hydraulic head is calculated using linear interpolation with respect to the initial hydraulic of the top and bottom boundaries (B2, B3).</p> <p>*^b: The initial temperature head is calculated using linear interpolation with respect to the initial temperatures of the top and bottom boundaries (A1, B3).</p>				

CHAPITRE 4

InSAR monitoring of the deformation

In recent decades, the usage of remote sensing in different areas has become more common because of technological advancement. In general, remote sensing can detect the changes in quality and quantity of the physical characteristics of a studied area from a distance using sensors such as radiometric (Synthetic Aperture Radar, SAR), optical (Visible/Near InfraRed (VNIR), or pulsed laser sensors (Light Detection And Ranging, LIDAR).

With InSAR monitoring, the radiometric sensors installed in a satellite can detect the radiometric image (SAR image) of an open area on earth by sending and receiving radiometric waves. Interpretation of SAR images acquired over a period of time can give important information about the changes that happened during that period on the earth's surface. One of the valuable data that can be extracted from the SAR images is the earth's elevation data. By comparing two or more SAR images (interferometry), the ground deformation that occurred between each image can be calculated. In this study, we used the InSAR technology to monitor vertical soil deformation in the Sainte-Marthe Study site (May 2017 to December 2019) and the Montreal Island (April 2016 to Feb 2022).

In this chapter, the principles of InSAR technology and interferometry will first be explained. Then, a brief review of the usage of InSAR deformation monitoring in general and its application specifically in civil engineering will be presented. Finally, the methodology that was used in this study will be explained in detail.

4.1 InSAR Basics

SAR is a microwave system that can remotely monitor the ground surface in terms of reflected energy and distance. Microwaves can penetrate the clouds. As result, this system is functional all the time, days and nights, despite the weather condition. Interferometric SAR or InSAR by interpretation of the changes in radiation travel path knowing the

satellites position and time of the acquisitions can give the elevation data of the ground surface. Using the elevation data and a spherical model of the earth, Digital Elevation Models (DEM) of the monitored area can be produced. Comparing that with an Eternal standard DEM gives the surface deformation of the studied area. In this section, the principle of the InSAR monitoring is presented

4.1.1 Electromagnetic Radiation

In InSAR monitoring, a SAR image is made by transmitting successive pulses of radio waves to a target scene and recording their reflected echoes. Radio waves are the form of electromagnetic radiation with the longest wavelengths (Figure 4.1).

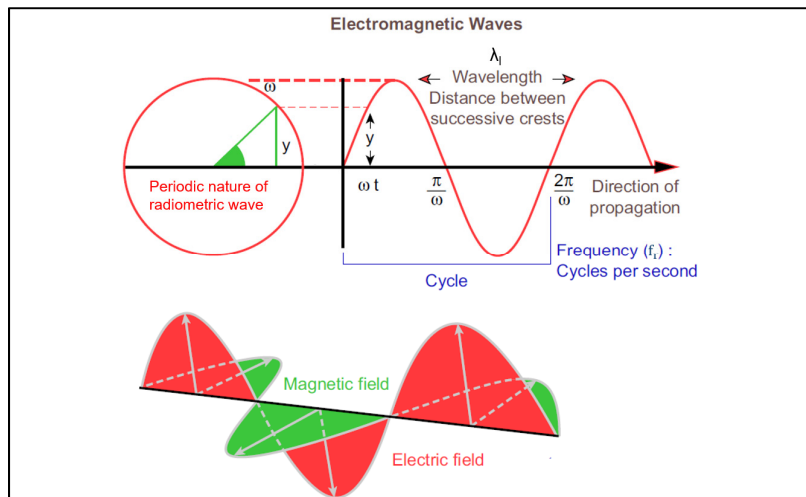


Figure 4.1 Electromagnetic wave adapted from Emery & Camps (2017)

Electromagnetic radiation is a form of energy that propagates in all directions with the properties of a wave (Emery & Camps, 2017). Frequency (f_r) and wavelength (λ_l) are two main characteristics of a wave, where f_r is the number of wave cycles that pass a fixed point in a given amount of time, and λ_l is the distance between identical points on the wave (e.g., successive crests). Figure 4.1 represents a radiometric wave and its main characteristics (f_r

and λ) along with its electric and magnetic fields. Electric and magnetic fields are perpendicular with respect to each other.

It is worth mentioning that the satellite sensor in optical imaging works in the visible, near-infrared and short wave infrared portions of the electromagnetic spectrum (range of frequencies of electromagnetic radiation). However, in SAR imaging, longer wavelengths of the centimetre or meter scale are used by the sensor. This makes it possible for radiometric waves to penetrate and see through the clouds. Radiometric wavelengths are categorized in different bands (C, X, L, P, S, K, Ku, and Ka in figure 4.2). The C, L and X bands are the most common SAR radiometric bands. The higher wavelengths signals can penetrate deeper into the target area surface. For instance, L and C band signals can penetrate to the deeper parts of the vegetation while the X band only gets reflected at the top of the canopy.

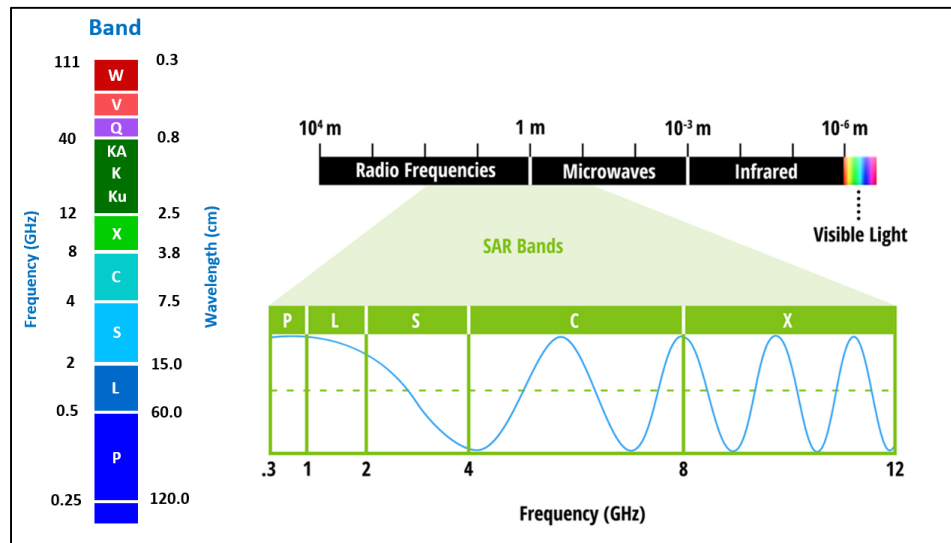


Figure 4.2 Electromagnetic spectrum adapted from Flores-Anderson et al. (2017) and Ouchi (2013)

In remote sensing, a radiometric wave reflected from a target point, or a substance has a unique spectral signature that can be used to identify the material. The spectral signature is a specific pattern obtained by plotting the reflectance variation with respect to the

wavelength of an irradiated wave. The existence of this signature is due to the physical and chemical nature of each material, which makes them emit photons of specific wavelengths when interacting with a received radiometric wave. It means that for a desired wavelength, percentage of the reflectance for each material is unique.

A radiometric wave might have low energy and long wavelength or high energy and short wavelengths. Each wavelength and energy level has its own application in remote sensing. Radiance and coherency are two important concepts in radiometric waves.

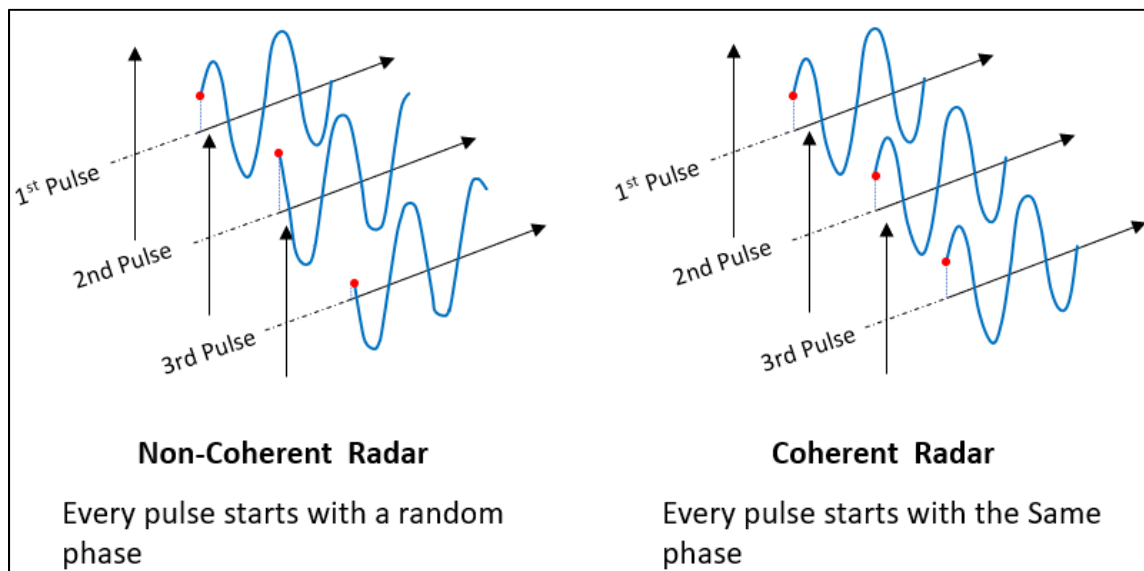


Figure 4.3 Coherent and non-coherent radar processing

Radiance is the emitted or reflected radiant flux per unit solid angle from a given surface per unit projected area. Radiance is very similar to the brightness concept. Coherency in radiometric waves means the ability of compounding two or more radiometric waves with different phases. In incoherent radiometric waves, their amplitudes are irregular or randomly related, and they cannot be compounded together (Figure 4.3). In SAR Interferometry, we use coherent radiometric waves in order to be able to differentiate and interpret the received irradiated waves from a surface.

4.1.2 Synthetic Aperture Radar (SAR)

SAR is a coherent imaging radar system. With coherent radiometry, information on the phase of the received radiometric wave is recorded with its amplitude for later processing (Hanssen, 2001). In this method, the phase of the signal should remain stable at least between its transmission and reception time. The existence of coherency makes it possible to combine successive signals transmitted and received in different locations of satellite and have a significantly finer resolution of the monitored area, about three orders of magnitude. The term synthetic aperture refers to synthetic replication of a long antenna function by a combination of the echo pulses transmitted and received from a short antenna that is constantly moving in the azimuth direction (Figure 4.4).

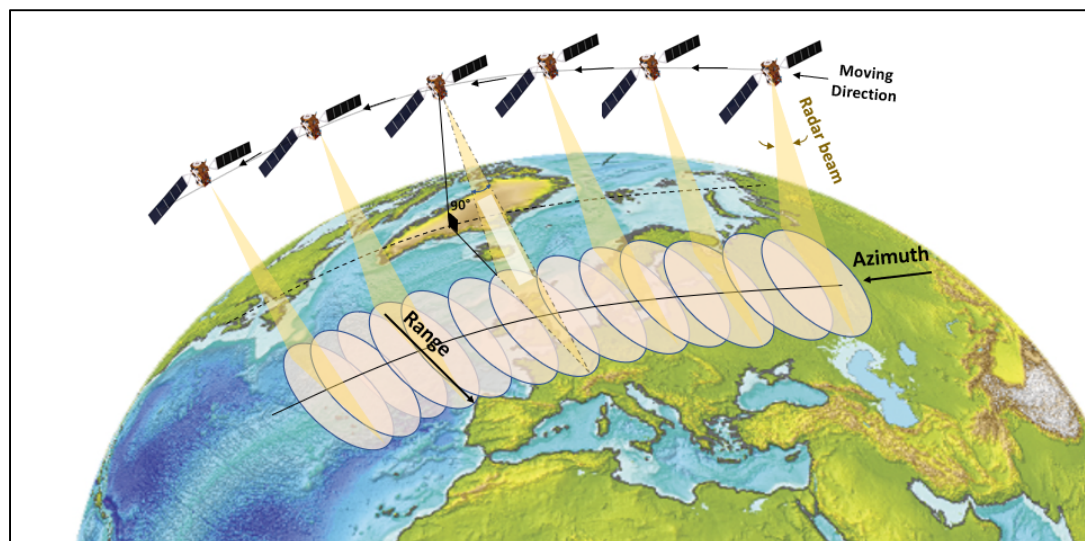


Figure 4.4 Synthetic Aperture Radar, the antenna motion along the azimuthal direction to simulate the effect of a long antenna

By this method, an image with dramatically finer resolution similar to using a very large antenna can be obtained. This occurs as the spatial resolution of the SAR image is directly related to the ratio of the wavelength to the length of the antenna (Equation 4.2). For a particular wavelength, increasing the size of the antenna, real or synthetic, results in a higher resolution.

In the SAR imaging system, resolution in range and azimuth direction are different. In range direction, the resolution is directly related to the duration of emitted pulses. For a given propagation speed, shorter pulses result in better resolution (Figure 4.5).

$$\rho_r = V_p \frac{\tau_p}{2} \quad (4.1)$$

where ρ_r is the resolution of the SAR image in range direction, V_p is the wave propagation speed in a vacuum environment and τ_p is the pulse duration.

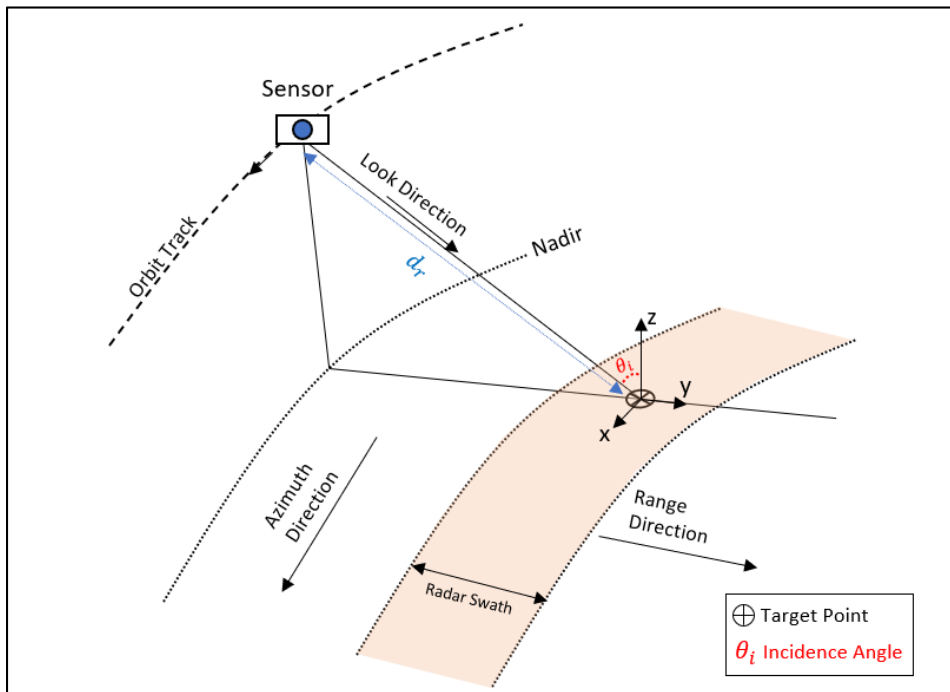


Figure 4.5 Acquisition geometry of synthetic aperture radar

To avoid a high level of noise, the high energy should be transmitted in a short time. However, this is not practical as in reality transmitter cannot effectively produce high-energy short pulses. Instead, the transmitter uses the compression technique, and they transmit longer pulses that are modulated. These modulated pulses are being processed later. In this way, a large pulse can be compressed in a shorter duration of $1/B_s$ (Alonso, 2014).

$$\rho_r = V_p \frac{1}{2B_s} \quad (4.2)$$

where B_s is the bandwidth of the retransmitted pulse.

In the azimuth direction, the resolution of the SAR image is defined with the following formula.

$$\rho'_r = d_r \frac{\lambda_l l}{2L_A} \quad (4.3)$$

where d_r is the distance between the target point and the sensor in the range direction, l is the length of antenna, and L_A is the length of the synthetic aperture in the azimuth direction. It is worth mentioning that this parameter is equal to the length of the real antenna for real aperture radar.

Spatial resolution of SAR images should not be confused with the pixel size of SAR images. The spatial resolution of the radar sensor is the size of the smallest object that can be measured by the sensor while pixel size is just the dimensions of the pixel in a processed SAR image. SAR image pixels are projected in azimuth and ground range directions. If a SAR image is in full resolution, each pixel represents an area on the ground (resolution cell) with a size equal to the spatial resolution.

To be more accurate, the spatial resolution of the radar sensor is defined by the minimum possible separation between the measurements or identified individual scatterers after removing the speckles. Speckles are granular interferences of reflected waves that occur due to insufficient spatial resolution (Figure 4.6). Speckles are not noise and they are just unwanted modifications of a signal due to interference. They can degrade the quality of radar and can be removed with various filtering algorithms. This is possible as speckles in contrast to noise are not random and they follow a pattern and can be reproduced with identical acquisition condition.

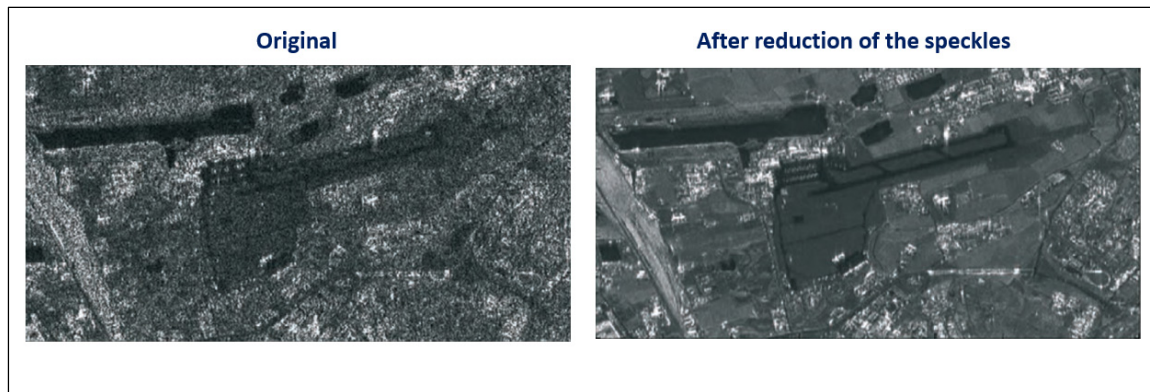


Figure 4.6 A SAR image of an airport with clearly speckle effects adapted from Ferretti et al. (2007)

4.1.3 Sentinel-1

In this study, open access Sentinel-1 satellites SAR images were utilized. In this section, the Sentinel-1 mission, and its product features will be explained.

Sentinel-1 satellites were launched in 2014 as a part of the European Union's Copernicus programme. Sentinel-1 is the constellation of twin polar-orbiting satellites, Sentinel-1 A and Sentinel-1 B (Figure 4.7). Sentinel-1 products have numerous applications such as ice extent monitoring, ship tracking, forest management, ground motion detection, marine oil spill detection and monitoring, climate change monitoring, and even humanitarian missions.



Figure 4.7 Sentinel-1 A satellite before launch taken from European Space Agency (2014)

The C-SAR instrument was developed by EADS Astrium GMBH of Germany. This instrument carries C-band sensors. The central frequency of the Sentinel-1 satellites is 5.405 GHz. Active phased antennas with right-looking angles were installed in both Sentinel-1 satellites. The Sentinel-1 satellites can store data up to 1410 GB and the transmission speed of data is 520 Mbit/s (European Space Agency, 2021).

C-band sensor is a perfect choice for ocean and ice monitoring, ship navigation tracking, and monitoring of land areas with moderate or lower vegetation cover (Flores-Anderson et al., 2017). The best possible spatial resolution in sentinel-1 products is $5 \text{ m} \times 5 \text{ m}$.

The sentinel-1 satellites revisit time is 2 weeks. However, with the two constellations of satellites, a 6-day repeat cycle of data can be obtained. Sentinel-1 satellites can cover the whole world by the collection of short-time visits (Figure 4.8).

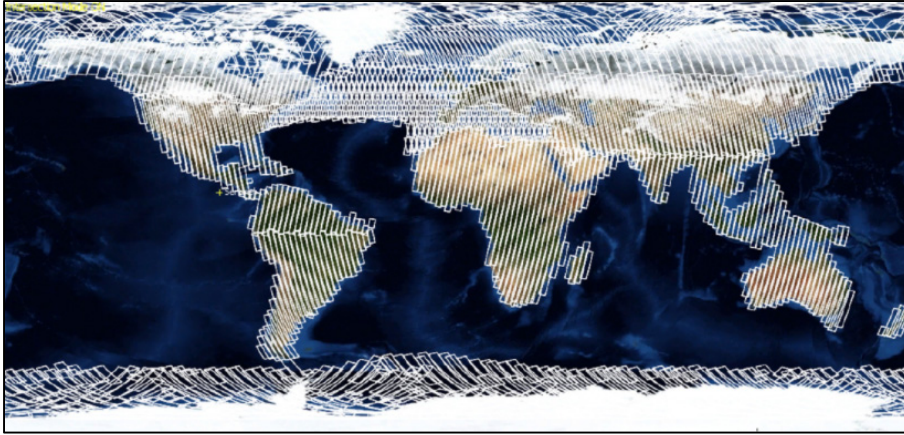


Figure 4.8 Sentinel-1 satellites coverage taken from European Space Agency (2014)

The sentinel-1 sensors provide polarized signals. In polarized signals, the electric field only oscillates in one direction. Dual-polarization is available with the C-SAR instrument of Sentinel-1 where the transmitted and received signal can be both vertical or horizontal (VV-VH) or the combination of them (HV-VH). In this study, the VV polarization was used as it most appropriate polarization for ground elevation monitoring purposes.

Sentinel-1 has four acquisition modes; strip map (SM), interferometric wide swath (IW), extra-wide swath (EW), and wave (WV). SM mode has an 80 km swath width. In this mode, the sensor provides one image for each polarization mode in six adjacent swaths. Six predefined elevation beams (S1-S6), each with four different incidence angles were set for this operation mode. This mode is used for little islands and special cases (European Space Agency, 2021). All polarizations are provided in this mode (Figure 4.9).

EW mode is a good option for the ocean and ice monitoring, specifically in arctic areas. The total swath size is 400 km. It has five sub-swaths and the provided resolution is $20 \text{ m} \times 40 \text{ m}$. In addition to mechanical steering in range detection, the beam in this mode is electronically steered both backward and forward in the azimuth direction using the TOPSAR technique. The TOPSAR technique enhances the quality of the image and

improves the interferometric capability by better alignment of the retrieved images. All polarizations are available in this mode.

WV mode is an acquisition mode designed for the detection of the global ocean waves and their directions and heights. The spatial resolution of this mode is $5 \text{ m} \times 5 \text{ m}$. The sensor operates by moving diagonally on several vignettes in 100 km intervals. The ground coverage of each vignette is $20 \text{ km} \times 20 \text{ km}$. The HH and VV polarizations are available in this mode.

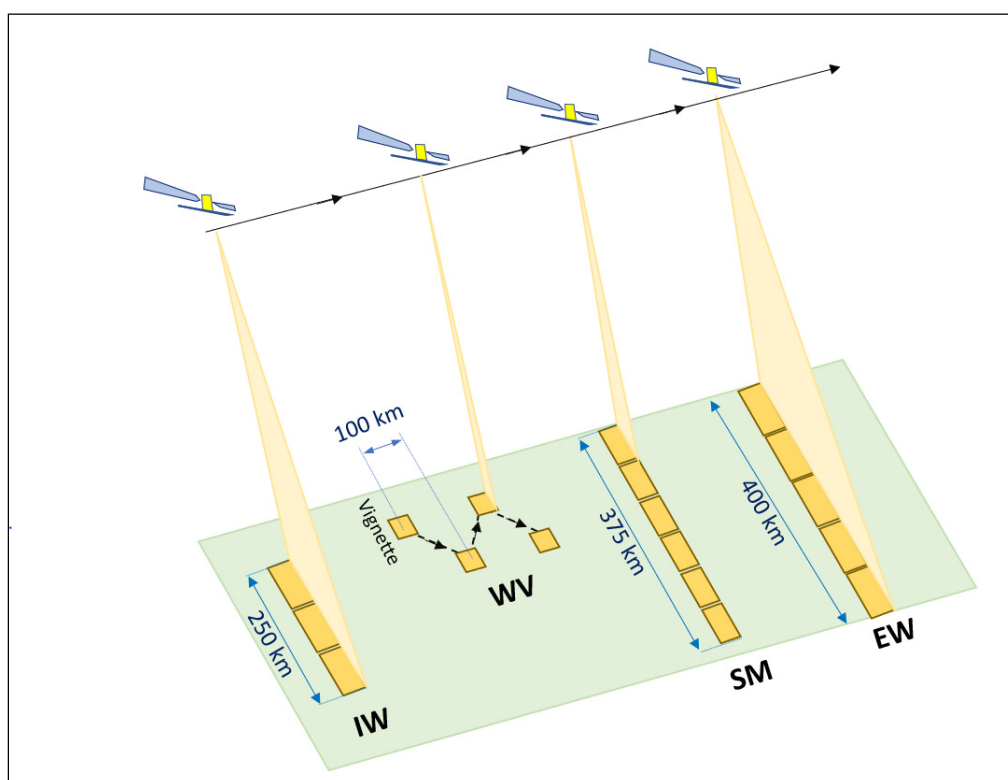


Figure 4.9 Sentinel-1 acquisition modes

IW mode has a large swath of 250 km and a spatial resolution of $5 \text{ m} \times 20 \text{ m}$. Each product has three sub-swaths. This mode is suggested for interferometric purposes where the function of the sensor provides more overlap in the azimuth direction (Hanssen, 2001). Similar to EW, in this mode also TOPSAR technique is utilized to improve the quality of

the SAR images. This mode in VV polarization is selected for this study, as it is a reliable mode with good coverage for interferometric processes.

Three levels of data are available for Sentinel-1 SAR products: level 0, level 1, and level 2. Level 0 is associated with raw unprocessed data. Level 1 is the most widely used product for most purposes. Level 2 products are geophysical data designed specifically for the study of the oceans. it contains products for wind speed, waves and ocean height. These products are all geolocated data derived from the level-1 SM and WV mode products.

The level-1 data has two types: single look complex (SLC) and ground range detected (GRD). GRD products are Focused SAR images that are geolocated to the ground range using the available Earth ellipsoid model at the time of the acquisition. These products are also processed by the Multilook technique. The Multilook technique reduces the noise level in SAR images by averaging the adjacent pixels. GRD products are available in three levels of resolution: low, medium, and full. GRD products only have amplitude information and cannot be used for SAR interferometry. They are used mainly for sea ice monitoring, oil spill detection, oceans wind and waves monitoring, and land use detection.

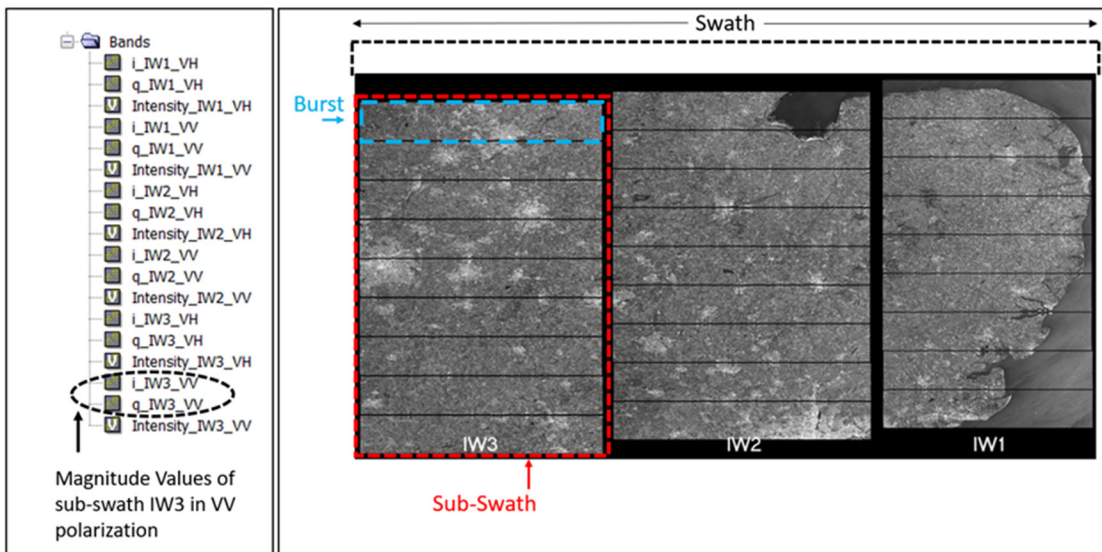


Figure 4.10 A Sentinel-1 SLC product in IW mode

SLC products are the most common form of SAR images for interferometry as they contain both amplitude and phase information. Amplitude and phase information are recorded for each pixel using a complex magnitude value respectively as i (e.g., i_{IW3_VV}) and q (e.g., q_{IW3_VV} , figure 4.10). SLC products in IW mode have three sub-swaths. Each sub-swath image includes several bursts where each one is a unique SAR image. In SAR interferometry, each burst is first processed separately. Based on the size of the study area and necessities of the project, the bursts can then be combined and analyzed together. There are overlaps between bursts and sub-swaths in order to avoid missing any ground coverage. In this study, we used the SLC products for our study area.

4.2 InSAR in geotechnical engineering

InSAR technology has been implemented widely in different areas of engineering. Ease of use, the possibility of going back in time using historical data, the existence of freely accessible data and software, fast processing time, and the possibility of undertaking studies over very large areas are among the reasons for the increasing popularity of this technology. InSAR is increasingly used alongside or even preferred in some cases to laboratory and in situ measurements with conventional methods. Some successful applications of this technology in geotechnical engineering are briefly presented in this section.

InSAR monitoring have been widely used in geotechnique for landslide monitoring (e.g., François, 2007; Novellino et al., 2021; Riedel & Walther, 2008; Savvaidis, 2003; Tofani et al., 2013). This technology can be combined with GPS observation (e.g., Riedel & Walther, 2008) or in situ monitoring (Tofani et al., 2013) to study geometry and kinematics of landslides. This combination other than improving the accuracy in terms of landslides patters, can also helps the researchers to investigates landslides in considerably larger areas. For instance, Tofani et al. (2013) showed how InSAR monitoring can improve defining of the boundaries or the state of activity in the Santo Stefano d'Aveto landslide. In this case, the measured landslide velocities in the line of sight in one location were -22 mm/year and

-20 mm/year respectively for inclinometer and InSAR monitoring while in another location both methods obtained -13 mm/year velocities.

InSAR monitoring have also been used in geotechnical studies of earthquakes and volcanic activities (e.g., ElGh arbawi & Tamura, 2015; Hu et al., 2012; Intrieri et al., 2013). InSAR monitoring has been used for 3D monitoring of the coseismic displacement (Hu et al., 2012) or long-term analysis of the displacement in the affected area and identification of the landslides related to volcanic activity (Intrieri et al., 2013). It has been proved that InSAR monitoring is an effective method for detection of the displacement patterns induced by earthquake or volcanic activities. For instance, comparing the displacement map obtained by InSAR closely fitted the observed fault that triggered the 2010 earthquake in New Zealand (Hu et al., 2012). InSAR monitoring can be used as a landslide early warning system by monitoring and identification of movement patterns in areas with a high risk of landslides (Intrieri et al., 2013).

InSAR can be used to calibrate or verify the results of the FEM models that dealt with displacement simulation (e.g., Feorronato et al., 2013; François, 2007, Raspini et al., 2014, Peduto et al. 2017). For instance, Feorronato et al. (2013) used InSAR measurement to calibrate a FEM model that was designed for simulation of the ground displacements induced by gas storage activity. Calibration of the model was achieved by trying the range of values for the soil compressibility and finding the optimum values in loading and unloading cases. François (2007) is one of the earliest attempts that compared the FEM simulation with InSAR monitoring. In this study, a FEM model was developed to simulate the ground displacements in an area as large as 64,000 km² affected by the Triesenberg landslides. The results from this model were then compared with the displacement times series obtained earlier by InSAR monitoring (Colesanti & Wasowski, 2004). The results showed a good agreement between displacement patterns that were obtained from FEM simulation and InSAR monitoring. Raspini et al. (2014) used InSAR monitoring for verifying the result of the FEM model that was implemented for the simulation of the soil settlement in area with water scarcity. The model used Mohr-Coulomb elastic model for the

2D simulation of the consolidation. The model based on the observed pore pressure records simulates the ground deformation. In this study, the InSAR monitoring was first assessed with available leveling measurement in four benchmarks. InSAR Monitored settlements in four benchmarks were -2.8, -4.2, -3.2, and -4.1 cm/year while obtained in situ measurement with leveling were respectively -3.2, -4.6, -3.8, and -4.2 cm/year. Obtained results from the FEM model later were validated with InSAR. The range of the deformations in FEM simulations were 10.4 to 27.4 cm while the monitored deformations with InSAR were 9.8 to 26.2 cm. Peduto et al. (2017) is another successful application of inSAR monitoring for validation of the FEM model results. In this study, InSAR was used for monitoring the settlement in railway tracks. Using the observed deformations with InSAR and FEM modelling, a predictive model of settlement was presented. The model can predict the secondary settlement in railway tracks constructed on soft clay soils. Comparison of the results from this predictive model with the observed deformation showed the reliability of the model in the prediction of the settlement. Using this method, a low-cost monitoring system was presented for maintenance of the rail tracks in areas prone to large secondary settlements.

There are also other examples of using InSAR for monitoring the settlement in building (e.g., Millio et al., 2018; Ritter & Frauenfelder, 2021), bridge (e.g., D'Amico et al., 2020), and tunnels (e.g., Reinders et al., 2021). In Millio et al. (2018), the high-resolution SAR images in X-band were implemented in this study. In this study, the InSAR measurements first was evaluated with precise levelling measurement on the ground. 2.5 mm standard deviation was observed between the InSAR and ground leveling measurements which is reasonable. The deformation results from the InSAR and greenfield method were compared together. The greenfield method is a conventional in situ method for the measurement of the building's settlement. This study demonstrated that the greenfield method overestimates the deformation. It also showed that high-Resolution InSAR can be as accurate and cost-effective method compared to traditional in situ measurements. It can also cost-effectively provide a denser deformation map for larger areas. It was also proved that InSAR can be a helpful tool for the long-term monitoring of settlement and identifying the risk associated

with that. For instance, an innovative method was presented by Reinders et al. (2021) that with use of InSAR before, during and after the tunnel construction could resolve the phase ambiguity from the short time displacement time series

It is worth mentioning that combination of the Satellite based InSAR monitoring with other techniques such as GPS system (e.g, ElGharbawi & Tamura, 2015; Osmanoglu et al., 2011; Shimoni et al., 2017), ground based InSAR (e.g., Bozzano et al., 2011; Intrieri et al., 2013), and Unmanned Aerial Vehicle (UAV) with high-resolution ortho-photography system (Cigna et al., 2017) could improved the accuracy of the measurements. Particularly, when we are dealing with nonlinearity in ground deformations, GPS system can help a lot to reduce the ambiguity of the results. For instance, the integration of InSAR and GPS technology was implemented for monitoring the deformation in the region of Kanto in Japan (ElGharbawi & Tamura, 2015). The methodology was presented that uses the observed GPS ground-level data for calibration of the InSAR results. The GPS data allows the noise and seasonal ground movements to be filtered to obtain a deformation trend resulting purely from the earthquake.

All the studies that were mentioned in this section showed the usefulness of InSAR technology in geotechnical engineering. Enhancements in InSAR processing techniques and the increasing number of satellites with high-resolution SAR sensors have even improved this technology in terms of accuracy and reliability. In this study, we also used the latest InSAR processing techniques to keep the processing errors as minimum as possible.

4.3 DInSAR

Ground deformation monitoring is one of the most common applications of InSAR. As it was mentioned earlier, InSAR or interferometric SAR measures the phase changes between at least two SAR images to produce different products such as DEM. A sub-category of InSAR that focuses on ground deformation monitoring is differential Interferometric Synthetic Aperture Radar or DInSAR. DInSAR allows the identification of millimetric

surface deformations from space. This method has experienced growing demand in the last decade. It is based on the comparison of the retrieved phases of transmitted waves to a ground target received by the satellites at two slightly different positions within the same orbit. The returned phase can be interpreted spatially as the length traveled by the wave from the satellite to the ground target and back to the satellite. This length is proportional to the absolute distance between the satellite and ground target and the topography of the target area. It can also be affected by the atmospheric propagation delay and other noises.

The interferometric phase ($\Delta\varphi_{int}$), also called interferogram (Hanssen, 2001), of two SAR images captured from two satellite positions, M (master or reference) and S (secondary), for a target pixel moving with the ground displacement from point P1 to point P2 is estimated with the following equation:

$$\Delta\varphi_{int} = \varphi_S - \varphi_M - \frac{SP_1 - MP_1}{\frac{\lambda_L}{4\pi}} + \frac{SP_2 - MP_2}{\frac{\lambda_L}{4\pi}} + \varphi_{.sct-S} - \varphi_{.sct-M} = \varphi_{.TP} + \varphi_{.DP} + \varphi_{.sct-S} - \varphi_{.sct-M} \quad (4.4)$$

where φ_S and φ_M are the measured phases for the target pixel from the satellite positions of S and M, SP_1 , MP_1 , SP_2 , MP_2 are the distances between the satellite and the target pixel, $\varphi_{.TP}$ is the topographic phase (phase variations caused by altitude changes within the scene), $\varphi_{.DP}$ is the displacement phase in line of sight (LOS) shown as d_{los} in figure 4.11, $\varphi_{.sct-S}$ and $\varphi_{.sct-M}$ are the shifted phases associated with the scattered waves of the target pixel in satellite positions M and S (Crosetto et al., 2016).

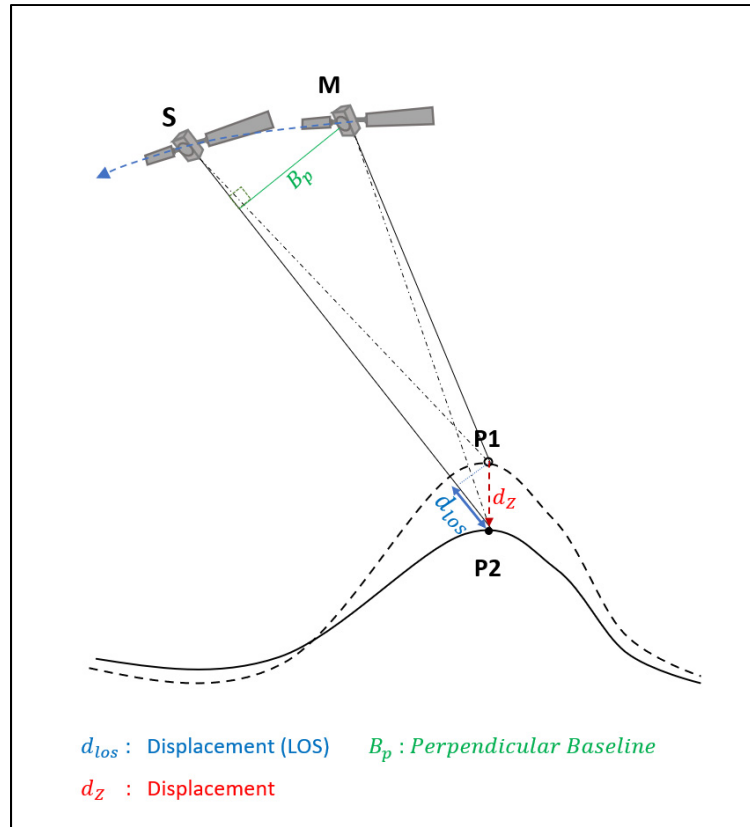


Figure 4.11 Scheme of deformation monitoring using DInSAR

The displacement phase can be obtained by cancelling all the other phase shifts and removing the topographic phase ($\varphi_{.TP}$) using an accurate digital elevation model (DEM). In practice, however, certain errors might remain due to inaccuracies of the external DEM (residual topographic error: $\varphi_{.re(tp)}$, Walter & Busch, 2012), changes of pressure, temperature or humidity between the two takes that impacts the radiation travel paths (the atmospheric delay error: $\varphi_{.re(atm)}$, Devaraj & Yarrakula, 2020), inaccuracies of the orbital data that result in miscalculation of the satellite positions (residual orbital error: $\varphi_{.re(orb)}$, Fattahi & Amelung, 2014) and residual noises ($\varphi_{.re(noise)}$). A brief description of the potential errors in a DInSAR observation is presented in equation 4.5.

$$\varphi_{int} - \varphi_{.TP} = \varphi_{.DP} + \varphi_{.re(tp)} + \varphi_{.re(atm)} + \varphi_{.re(orb)} + \varphi_{.re(noise)} + 2 \cdot i \cdot \pi \quad (4.5)$$

The last term is associated with the 2π cyclic (wrapped) nature of the interferometric phase where i is an integer. DInSAR aims at the estimation of all phase contributions and the removal or reduction of the atmospheric, topographic and residual errors, so that the remaining phase variations can be attributed to the displacement between two or more acquisitions along a time series of images.

4.4 PSI-DInSAR analysis

To analyze the phase differences of an area over time, and to relate them to surface displacement, DInSAR requires the selection of an overall reference image which defines the pixel spacing and orientates the analysis. All other images are then coregistered to this reference image by a bilinear resampling using BackGeocoding and Enhanced Spectral Diversity (ESD) algorithms (Yague-Martinez et al., 2017) which provide accurate alignment of scatterers between all image pairs. One interferogram is then computed for each image pair in the stack. Stack is the formation of the group of SAR images in SAR interferometry. For instance, in star graph formation, all the SAR interferograms are processed with SAR images (secondaries) respect to one image (master image).

Compared to single-pair approaches, multi-temporal approaches allow the identification of surfaces with temporally stable information. These so-called permanent scatterers (PS) may not be found in all parts of the image, for example due to loss of coherence over vegetated areas but grant the retrieval of coherent phase information over the investigated period which can accurately be related to surface displacement. This form of persistent scatterer interferometry (PSI) brings the advantage that temporal decorrelation is minimized and atmospheric impacts in single interferograms can be estimated and removed (Crosetto et al., 2016).

4.4.1 SARPROZ

In this study, the PSI method was implemented based on the SAR PROcessor by periZ (SARPROZ) software (Figure 4.12). SARPROZ is a MATLAB-based software developed by Perissin et al. (2011) for processing InSAR data. SARPROZ uses the PSI approach based on Ferretti et al. (2001), which introduced the first successful application of PSI. In this approach, the identification of permanent scatterers is based on temporal coherency defined based on phase stability. Phase stabilities are retrieved at each pixel in the image stack, based on the amplitude dispersion index P_d which is the ratio of the temporal standard deviation of the phase SD_ϕ to the average of the amplitude (m_a , Ferretti et al., 2001).

$$P_d = \frac{SD_\phi}{m_a} \quad (4.6)$$

By applying a certain threshold on this index, the PS pixels are identified. Accordingly, pixels which undergo large variations over the observed time span are not selected as PS candidates and excluded from the analysis. To maintain topological characteristics, a network is created which assigns neighbors to each PS. This step is important for the later unwrapping process which converts the cyclic phase information of the interferogram to a continuous surface (Figure 4.11).

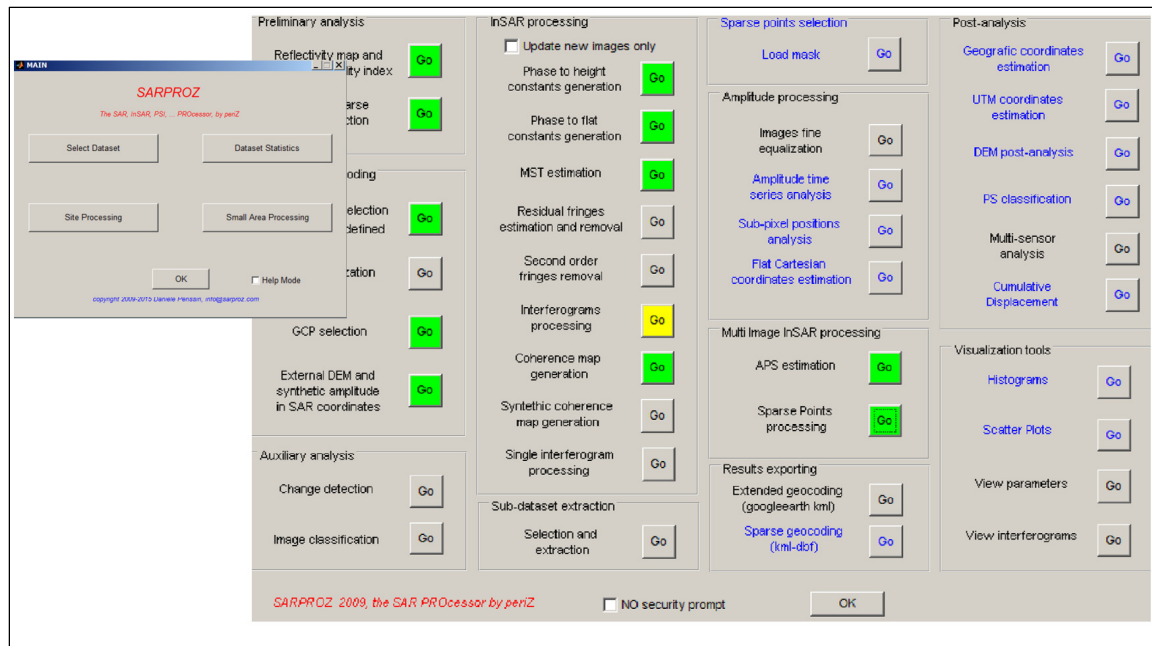


Figure 4.12 Example of SARPROZ interface

SARPROZ, similarly to Ferretti et al. (2001), uses the amplitude dispersion index for identifying the PS pixels. However, SARPROZ allows a wide variety of parameters besides temporal coherency to be utilized (e.g., spatial coherency, average amplitude, velocity, residual height). The possibility of lowering the thresholds using an iterative algorithm, and applying weights to the phase values using the Quasi-PS algorithm can loosen the restrictions of the conventional PSI method and successfully perform the PSI processing even in areas with low signal to noise ratio (SNR) and low PS density (Perissin, 2016, 2019; Perissin & Roca, 2006; Perissin & Wang, 2012). The applied weights are the spatial coherencies or amplitudes of the pixels. By applying weights, a subset of the interferograms will be selected to be involved in the estimation process of each target pixel (Perissin & Wang, 2011). Various combination of these features can be implemented based on the case necessities.

The next step after identifying the PS pixels is the selection of the reference PS pixel. The reference pixel should be temporally stable, particularly relative to deformation (Crosetto et al., 2016). The deformation analyses will then be estimated compared to the reference point.

The last step concerns the intrinsic nature of the residual errors. It applies a temporal high-pass and spatially low-pass filter on the phases, as the noises are temporally correlated while spatially uncorrelated. Subtraction of noises (residual phases, including atmospheric phase screen [APS]) via this filter brings the displacement and, consequently, velocity of each pixel.

To identify the most suitable approach to map the temporal behaviour of Champlain clays, two different approaches were implemented including conventional linear PSI and non-linear PSI. A similar strategy was also used for InSAR deformation monitoring of the Montreal Island. Both linear and non-linear methods were examined in urban areas of Montreal with different set up of the model and the best one was selected for each case based on qualitative factors such as homogeneity of PS pixel networks, the distribution, and ranges of the obtained displacement and most importantly by comparison of the obtained PS pixel time series with reported GNSS station measurements.

4.5 InSAR monitoring the deformation in the Sainte-Marthe area

In this section, the methodology for monitoring the deformations time series in Sainte-Marthe area are presented. The focus of this assessment was to analyze the soil deformation in the Sainte-Marthe study site in order to compare it with the simulated deformations obtained by FEM numerical modelling.

4.5.1 InSAR Data (SAR Images, Saint Marthe area)

66 single-look complex (SLC) SAR images acquired by Sentinel-1 A satellite between March 2017 and December 2019 in interferometric wide (IW) acquisition mode and ascending (ASC) flight direction were used for the DInSAR process (Figure 4.13). The SAR images were acquired from the orbital track 135 (sub-swath IW=1), which fully covers the study area. The SAR data monitored the same period as the meteorological and geotechnical data. VV polarization mode was selected in all analyses.

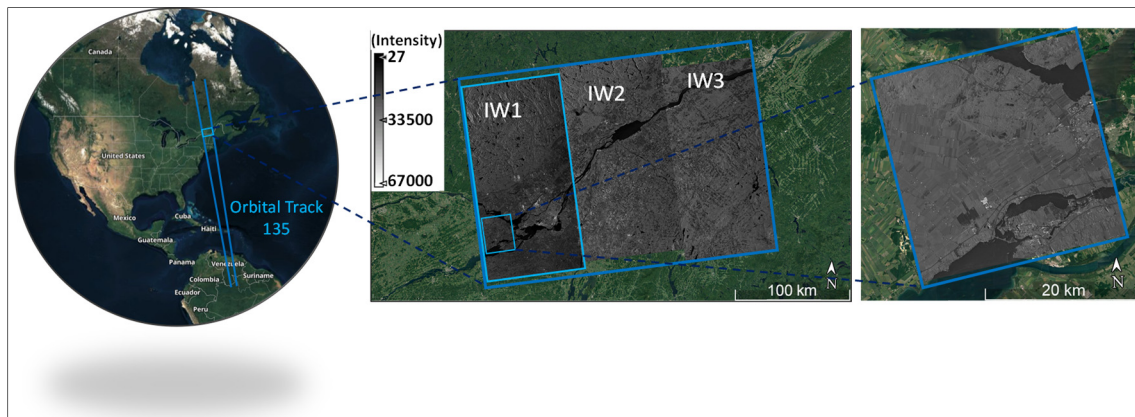


Figure 4.13 Dataset and area of interest

4.5.2 PSI-DInSAR-Pre-processing

Pre-processing of SAR images is a critical part of the PSI method. The choice of the stack formation and the selection of PS pixels can affect the quality of the APS or final estimation of deformation parameters.

4.5.2.1 Preparing the stack of interferograms

In the Sainte-Marthe case, one stack was formed with all 66 SAR images. Acquisition dates of the selected master SAR images are presented in table 4.1. The schematic graph showing the perpendicular baselines (Figure 4.9) of the dataset used in SARPROZ analysis is shown in figure 4.14. A perpendicular baseline affects the coherency of the interferometry.

Table 4.1 Specifications of analyzed datasets with SARPROZ (Sainte-Marthe)

Time Period	Number of SAR Images	Master SAR image (Acquisition Date)	Sensor	Pass	Orbital Track	Polorization	Mode	Product Type
SARPROZ (PSI-DInSAR)								
20170519-20191223	66	20180619	S-1A	ASC	135	vv	IW	SLC

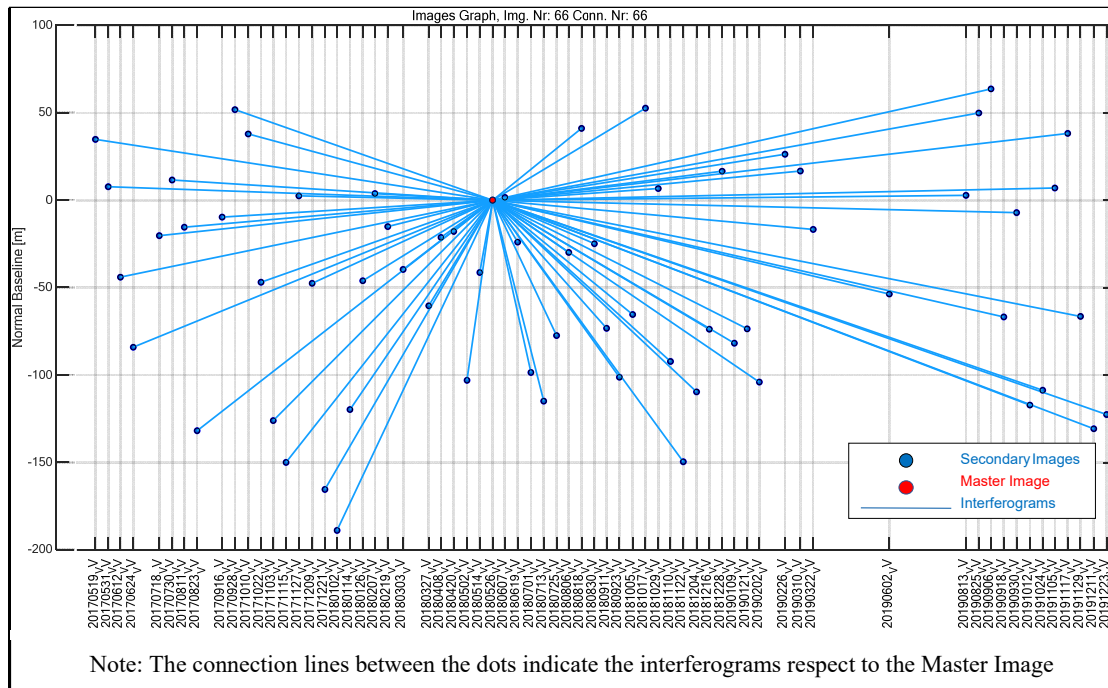


Figure 4.14 Star graph showing temporal and perpendicular baselines of the analysed dataset by SARPROZ

4.5.2.2 PSI-DInSAR-PS selection

The PS pixels were identified through an iterative approach with a preliminary selection of PS pixels and connections and further refinement by removing noisy pixels and connections. Figure 4.15 shows the final PS pixels obtained from the SARPROZ PSI analysis for the 2017/05-2019/12 period. The results obtained with the PS pixels shown on Figure 4.15 can be considered reliable due to the relatively large number of images in the stack. A large number of images implies that the scatters remain stable during a long period of time (Colesanti et al., 2003).

A Delaunay triangulation connection network between the selected PS pixels processed by SARPROZ is also illustrated in figure 4.15. This spatial graph enhances the estimations for displacements in areas with a lower density of PS pixels. A denser network of triangles in an area results in a more accurate estimation of local displacement. Applying a coherence

threshold, low coherency connections were filtered to reduce the impact of locally inaccurate information and to improve the reliability of the overall estimations. The local references were then added to the network in order to densify the spatial graph.

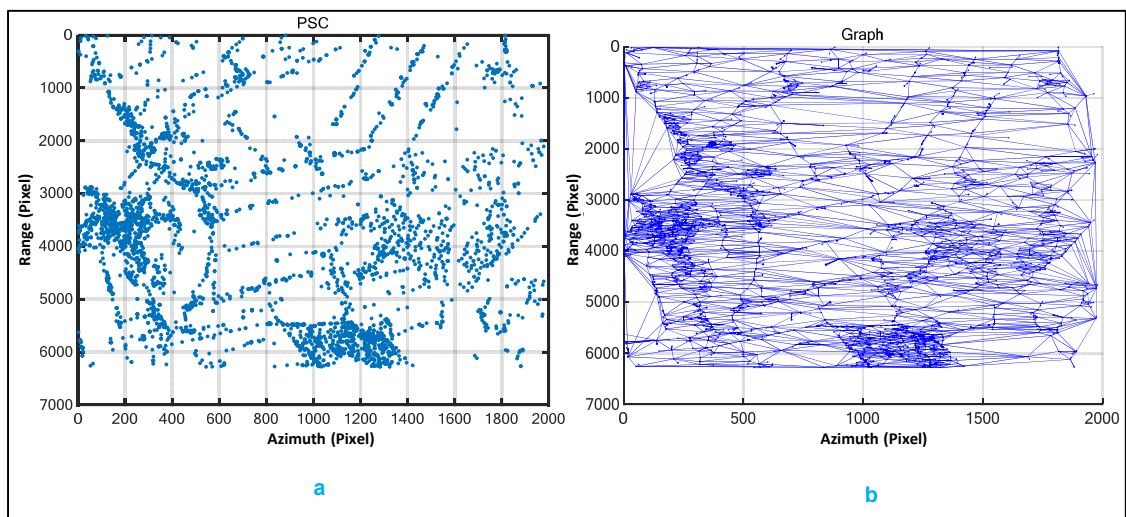


Figure 4.15 PS distributions (a) and, connection network (b) of the PS pixels in SARPROZ

4.5.3 Validation of the PS-InSAR results

For validation of the PS-InSAR estimates, deformation data from two stations in the global navigation satellite system (GNSS) were compared with the PS-InSAR results. These data were provided by real-time kinematic (RTK) networks of Canada. It is worth mentioning that the SARPROZ visualization feature automatically transforms the displacement in the line of sight to real vertical displacement (d_z) using the following equation:

$$d_z = \frac{d_{LOS}}{\cos\theta_i} \quad (4.7)$$

where θ_i is the inclination angle between the LOS and vertical direction. The GNSS stations' detailed information is presented in figure 4.16 and table 3. The linear and non-linear deformations that were obtained with PS-InSAR were compared with the deformation

recorded by the GNSS stations. The results show a good agreement, proving the reliability of the obtained PS-InSAR results for both linear and non-linear models (Figure 4.17 and Table 4.2). This agreement was achieved by comparing several PS networks and a large number of parameters sets for the linear and non-linear approaches. In general, the results obtained with the nonlinear method should be considered with caution in case of low density of time series or PS distribution. The linear approach is considered a more reliable PS-InSAR technique as it is less vulnerable to atmospheric or topographic noises. However, the linear approach cannot detect the non-linear displacements, specifically in non-urban areas where the effects of ground water level or temperature changes can be stronger. In our case, the non-linear approach achieved an acceptable agreement with the GNSS measurement.



Figure 4.16 Locations of GNSS stations and study site

Table 4.2 GNSS stations locations and validation of PS-InSAR estimations (linear)

Number	stations name	location	Latitude (± 0.0005m)	Longitude (± 0.0003m)	Altitude (± 0.0006m)	Validation		
						Linear Method		Non-Linear Method
						Velocity (mm/y)		
						GNSS	PS-InSAR	
1	SMARTNET-QCVD	Vaudreuil-Dorion	N45° 24' 51.176918"	W74° 01' 31.787385"	8.047	-3.1	-2.9	Figure 4.17
2	CANNET-VLFD	Grande-Île	N45° 17' 7.333232"	W74° 02' 9.086812"	30.652	-2.22	-2.1	

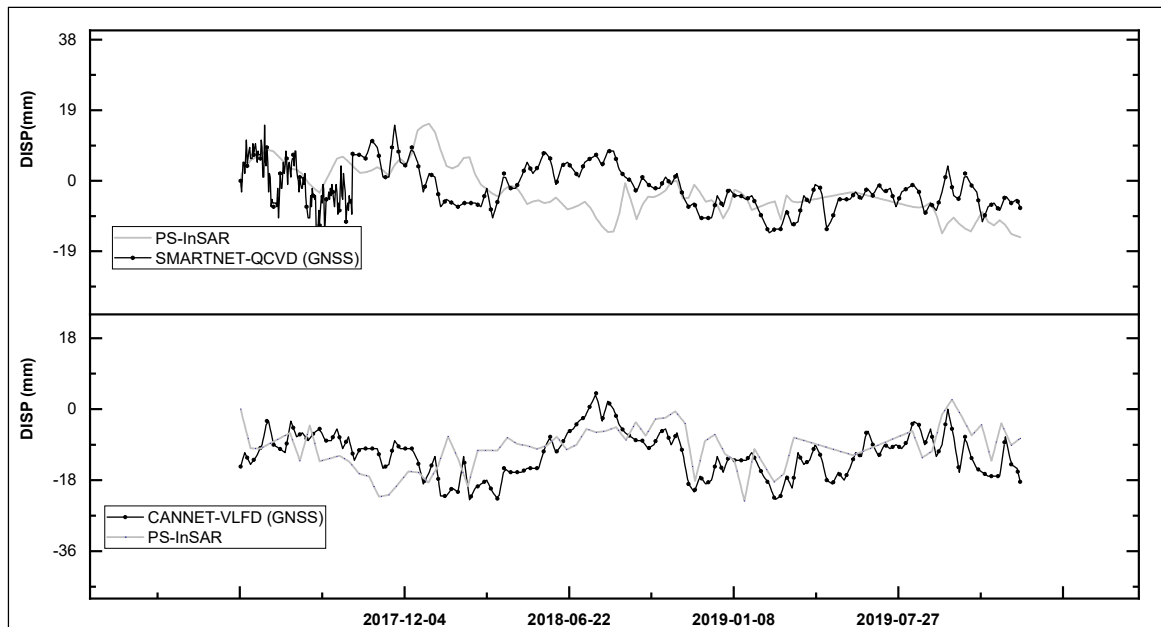


Figure 4.17 Validation of the PS-InSAR estimations (non-linear)

4.6 InSAR monitoring the deformation in the Montreal area

The same methodology as in the Sainte-Marthe case was used for the InSAR monitoring of the deformation on the Montreal Island, mainly its central area. It is worth mentioning it is not easy to carry on a one-time InSAR monitoring in the whole areas of the Montreal as it is less likely to find an overlap area between the SAR images that cover the whole target Zone and the processing will also be significantly heavier and it will be much harder for the software to converge the model. As a result, area of the Montreal were divided into smaller zones.

In the processed PS-InSAR evaluation, the existing GNSS stations in the area were used for calibration of the model as described in section 4.5.3 for the Sainte-Marthe case. The PS InSAR model was modified to include more PS pixels in three target areas chosen with geotechnical engineers from Ville de Montréal based on where they expected larger deformations. Because of the large extent of the study area, the model had to be downscaled in some areas with regards to the number of PS-points. This downscaling improves the

efficiency of the model and make the process less computationally heavy. The InSAR model was forced to prevent downscaling in the target areas. This resulted in denser PS networks for the target areas.

4.6.1 InSAR data (SAR images, Montreal area)

For the InSAR deformation processing of the Montreal area, the existing data package of Sainte-Marthe was expanded by 70 more SAR images to cover the period of the April 2016 and February 2022. The target areas of the InSAR monitoring were also shifted to the Montreal Island. The whole Montreal Island was covered in three parts. In each part, an area of the Montreal Island was processed. Figure 4.18 shows one of these three parts that covers the central part of Montreal.

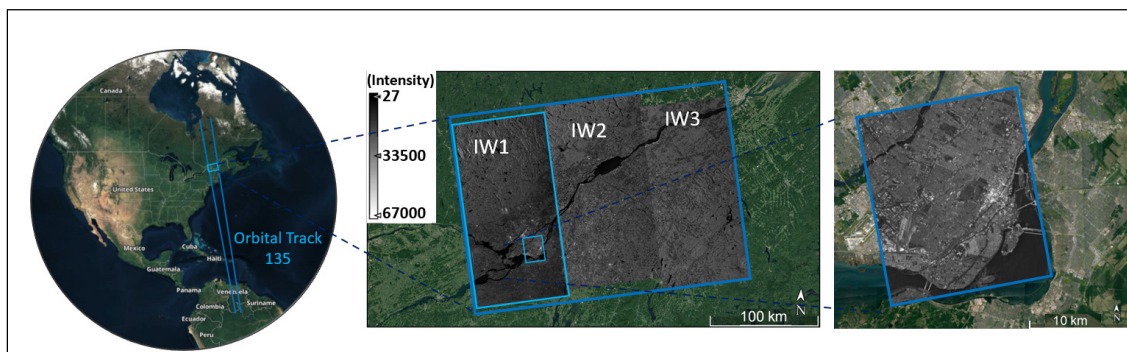


Figure 4.18 Dataset and area of the interest for Montreal Island in central zone

4.6.2 PSI-DInSAR-Pre-Processing

Another stack of interferograms was selected for the InSAR monitoring of Montreal area. The same methodology as Sainte-Marthe was also used here.

4.6.2.1 Preparing the stack of interferograms

In Montreal area, a stack of 136 interferograms was used for the InSAR process. Acquisition dates of the selected master SAR images are presented in table 4.3. The schematic graph showing the perpendicular baselines of the dataset used in SARPROZ analysis is shown in figure 4.19.

Table 4.3 Specifications of analyzed datasets with SARPROZ for Montreal

Time Period	Number of SAR Images	Master SAR image (Acquisition Date)	Sensor	Pass	Orbital Track	Polorization	Mode	Product Type
SARPROZ (PSI-DInSAR)								
20160406-20220222	136	20180725	S-1A	ASC	135	vv	IW	SLC

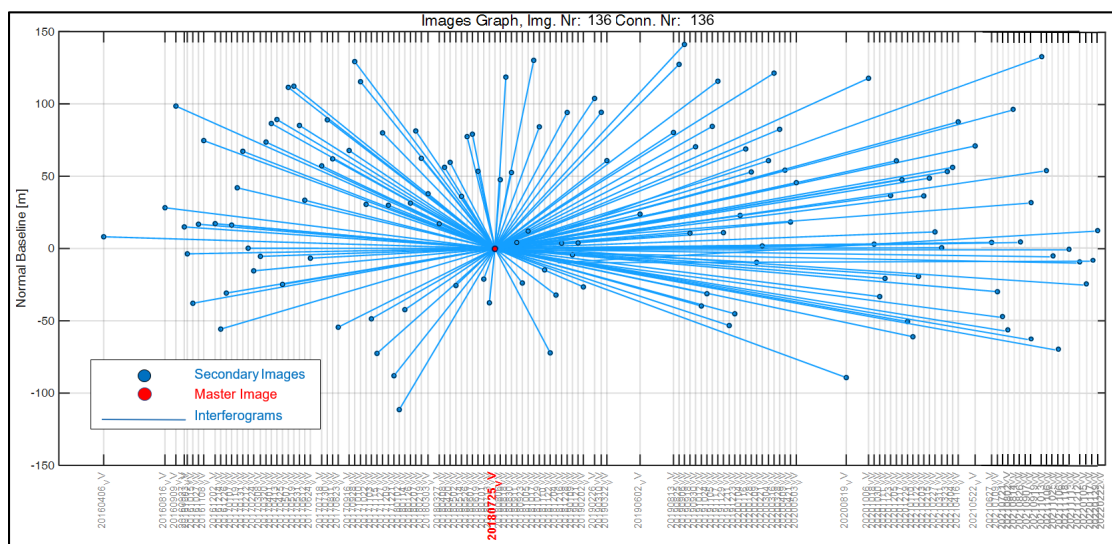


Figure 4.19 Star graph of the SAR interferograms in InSAR processing of the Montreal

4.6.2.2 PSI-DInSAR-PS selection

Figure 4.20 shows the PS distribution in the Montreal area |(central part). As expected, a denser distribution of PS pixels is obtained in urban areas of Montreal compared to Saint

Marthe area. It could be even denser in most region before applying the downscaling filter, but for efficiency purposes, it has to be downscaled to a certain level in most areas. However, there are also some areas like Mont royal in the middle of the map that due to existence of a dense vegetation cover, much lower number of PS pixel were identified.

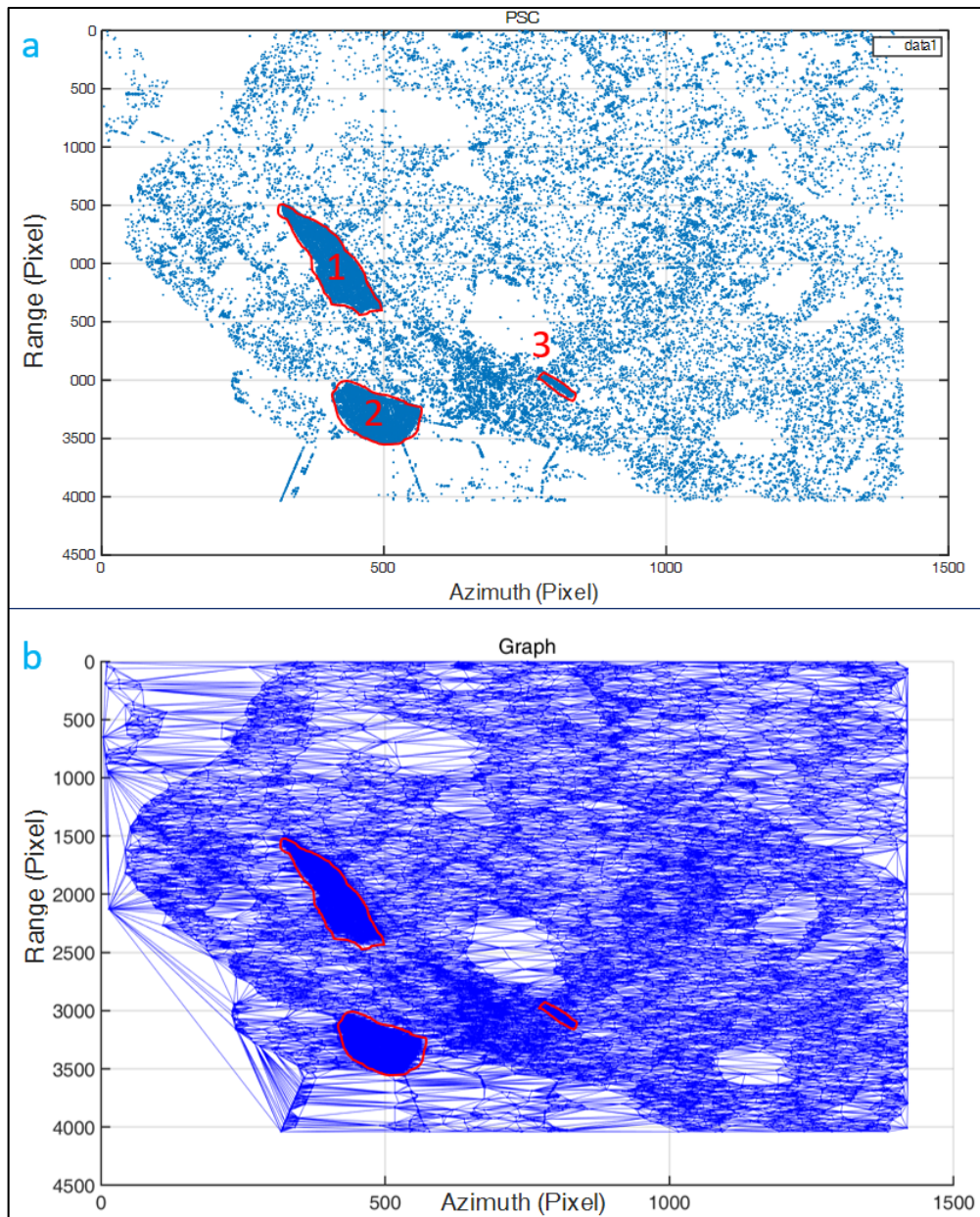


Figure 4.20 PS distributions (a) and, connection network (b) of the PS pixels in SARPROZ

As mentioned earlier, three target areas in central part of the Montreal Island were exempted from downscaling. These areas are highlighted with red lines. These three target areas are respectively the Saint-Jacques Escarpment, Parc d'entreprise pointe Sainte-Charles (PESPC), and Roy Street on Plateau Mont-Royal. The PS pixel networks in these areas are dense enough so that the individual connections cannot be distinguished in figure 4.20.

The network of the PS pixels is also presented in picture 4.18. Similarly to the Sainte-Marthe case, a Delaunay triangulation connection network was established between the PS pixels. The obtained network of PS pixels in figure 4.20 in average has more connections than the PS pixels network in figure 4.15.

The rest of the PS InSAR process in the Montreal area was the same as for the Sainte-Marthe area and was explained earlier. However, owing to stronger network of PS pixels in the Montreal area, the calibration was easier and required fewer attempts.

CHAPITRE 5

Results and discussion

This chapter presents the numerical modelling and InSAR monitoring results. The first section presents the FEM simulations described in chapter 2 for pore pressure and water balance time series for the Sainte-Marthe study site. In the second section, the numerical modelling results for the ground settlement on the Sainte-Marthe study site are presented. The third section compares the simulated and InSAR settlements for the Sainte-Marthe study site based on linear and non-linear forms of PSI. The methodology for the deformation modelling and InSAR monitoring were presented in chapters 3 and 4. The fourth section presents the InSAR monitoring results for the Montreal Island. The velocity and cumulative ground deformation time series are presented for several part of the Island.

5.1 Water balance and pore pressure simulation

This section compares and discusses the observed and simulated pore pressure time series for the F1B2 piezometer installed at a depth of 12 m, along with the observed water table and bedrock water level changes. The result for the hydraulic head time series resulting from the baseline scenario without runoff (BS), perfect stress scenario (PSt) and net water balance scenario (NWB) are also compared.

Figure 5.1 shows the changes in groundwater table elevation (GWL), bedrock water level (BWL), and intact clay hydraulic head (F1B2). The F1B2 changes can be compared with the BS scenario neglecting runoff (stress changes equal to $\rho_w g \Sigma(P-ET)$). The data span the 21 months period from 25 May 2017 through 24 January 2019. The similarity of the GWL and BWL time series is evident. The only significant difference is a sharper jump in BWL in late November 2018. The observed pore pressure changes in intact clay (OB) at a depth of 12 m has also a similar trend. However, the fluctuation amplitudes are smaller due to the dampening effects of the porous medium caused by its low permeability. The net water balance increases steadily as it does not include the runoff.

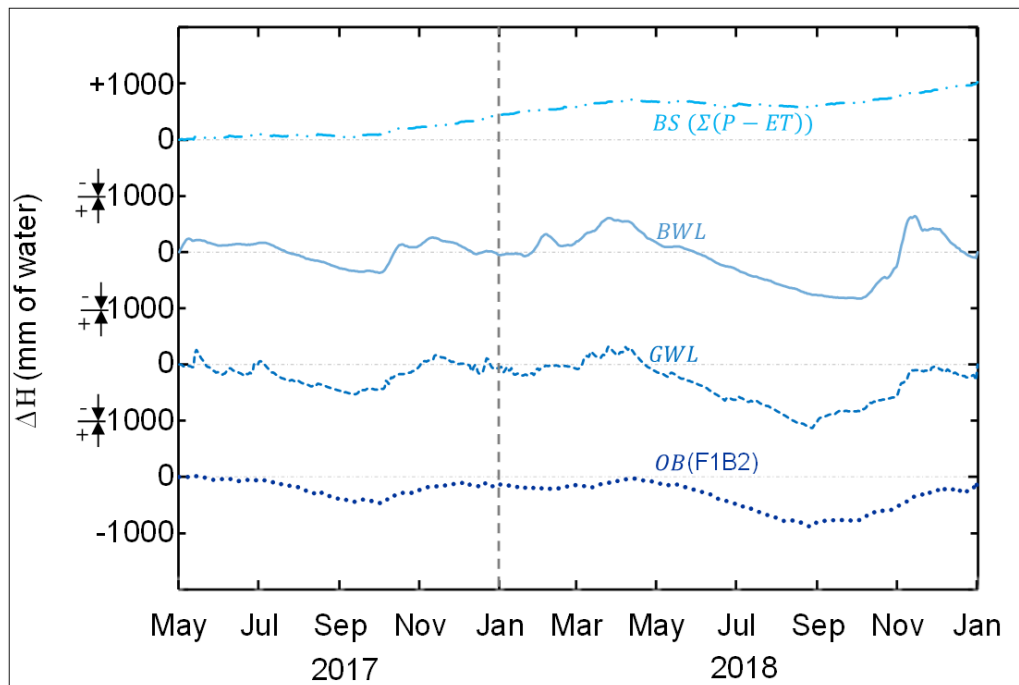


Figure 5.1 Water level changes for BS, BWL, GWL, and OB time series

The hydraulic head time series obtained with different methods of optimization are presented along with the observed values in figure 5.2. As defined by the method, there is a perfect fit between the PSt and the measured hydraulic head. The results of NWB has a generally good agreement with the experimental values, the differences are less than 100 mm of water. The effectiveness of NWB optimization is clearer when it is compared with the simulation based on the BS scenario ($\Sigma(P-ET)$).

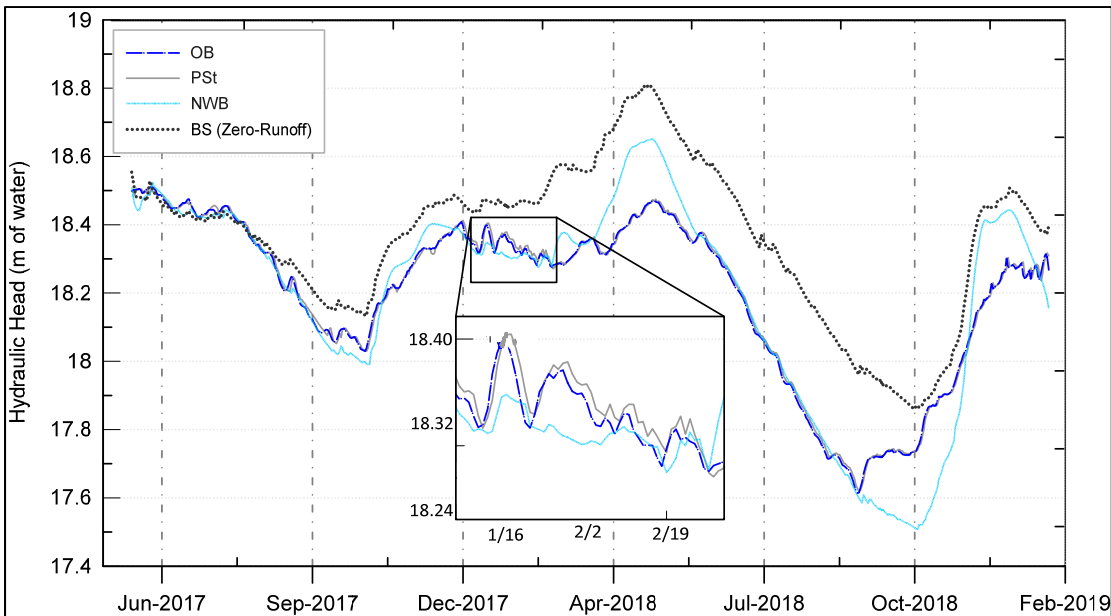


Figure 5.2 Simulated and observed hydraulic head time series for a depth of 12.2 m at F1B2

A closer look at the graph reveals the increasing difference between the experimental and NWB hydraulic head values in the second half of the simulated period starting at the beginning of 2018. Figure 5.3 gives a more detailed description of these discrepancies by presenting the meteorological parameters (P , ET , and mean temperature). It is evident that a significant difference between NWB and OB first appears during the spring freshet period of 2018 with the rising temperature.

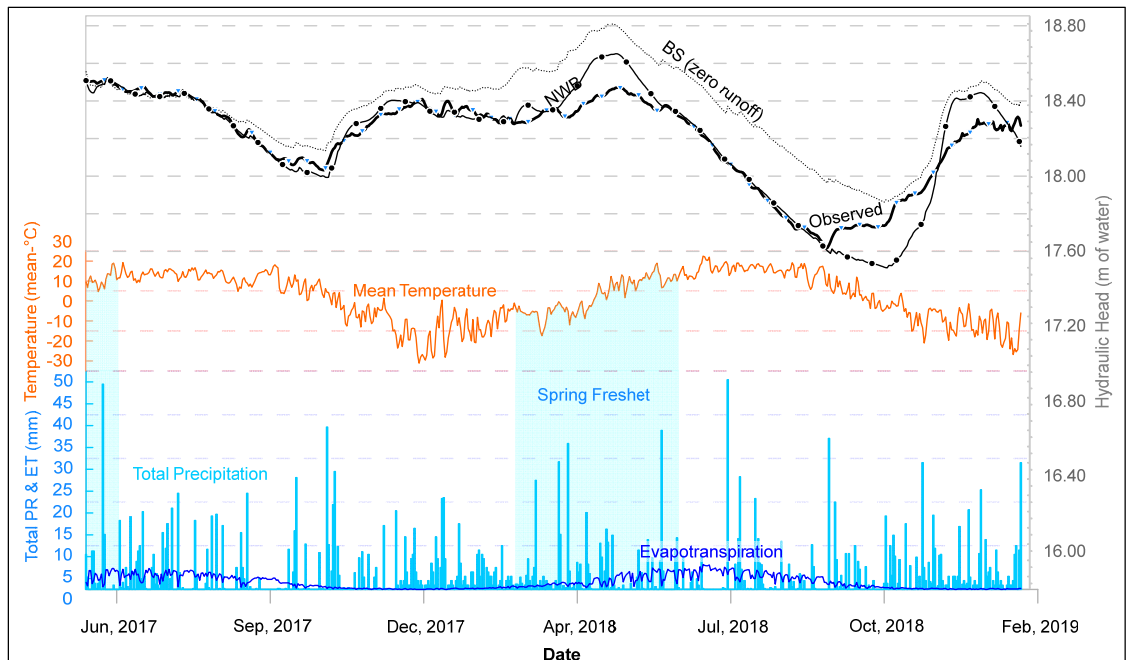


Figure 5.3 Daily precipitation, evapotranspiration, mean temperatures and simulated and observed hydraulic head in Sainte-Marthe study site

Several explanations can be given for the difference between the NWB and experimental hydraulic head values. First, it might be due to inaccuracies in meteorological data. For instance, the GMON device that measures the snow water equivalent may overestimate the snow precipitation by up to 30 % (Smith et al., 2017a). The difference might also be due to errors in the pore pressure measurements. Even with a perfect piezometer installation, measurement errors can be expected. The accuracy of the transducers measuring the water table height, the hydraulic head in the bedrock, and the pore pressure in the clay is approximately ± 30 mm (Van Essen Instruments, 2016; RST Instruments, 2019). There could also be some significant differences between the real evapotranspiration and the Penman-Monteith estimation. Evapotranspiration from tree canopies can result in soil moisture losses (Smith et al., 2017b). The boreholes of the Sainte-Marthe study site are located in the immediate neighborhood of a group of eastern pine and hackberry trees. There can be strong effects of trees root on increasing water deficiency during dry seasons (Bozozuk & Burn, 1960). The seasonal lateral movements are also considerably higher under the influence of trees due to stronger changes in soil water content (Silvestri et al.,

1992). This factor was not considered in the water budget. The spring freshet would also account for the poor optimization performance during this period. Although snow melting was considered in the water balance calculation, depending on the topography of the region, water from snowmelt can also be brought from the other territories to the catchment area of the study site in Sainte-Marthe.

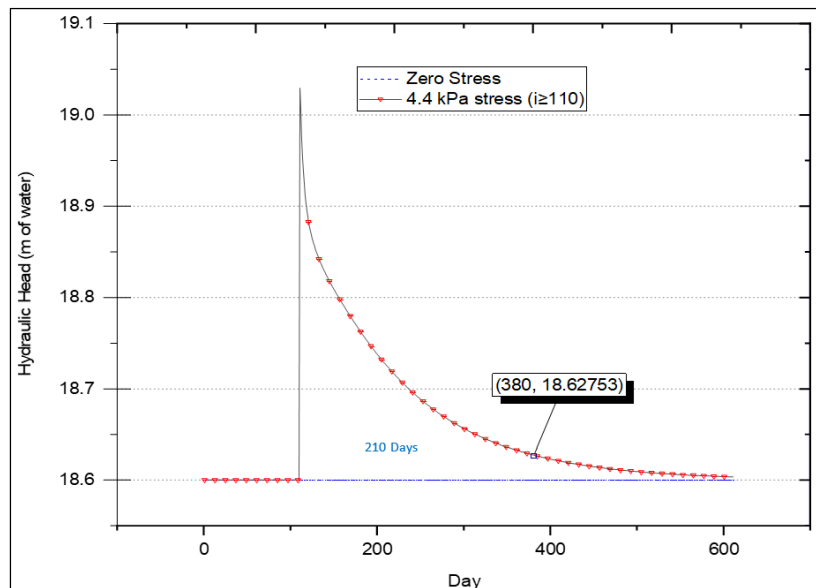


Figure 5.4 Comparison of hydraulic head values for a constant stress and after applying a 4.4 kPa stress increase on the 110th day

The cumulative nature of stress changes can be another source of error as an error in one time step will influence the following time steps. The first half of the period is also influenced by the model's initial conditions. At the beginning of the period, the piezometer record is still influenced by the transient effects of hydrological changes that occurred prior to the simulation period. The simulation's initial conditions, on the other hand, are determined based on a steady state simulation. Assuming the amplitude of the fluctuations prior to May 2017 was the same as during the simulation period, the difference between maximum or minimum and average pore pressures will be a water column of 0.45 m or 4.4 kPa. Simulation can show that the pore pressure change induced by this excess pore pressure can last about 210 days (90% of the initial increase, Figure. 5.4). This implies that

the results obtained for the first 210 days of the simulation period is still affected by prior changes in net moisture balance. In other words, arbitrary initial conditions still have an influence up to 210 days after the beginning of the simulation.

Figures 5.5 and 5.6 are focused on the runoff component. Figure 5.5 shows the change in the stress applied at the upper boundary of the numerical model, or net water balance. As can be seen, the PS method estimates more drastic changes in stress and runoff compared to the NWB method. The PS method resulted in very high runoff ratios during the summer months of 2018. It is likely due to the overestimation of the outflows (ET, R) from the water balance domain.

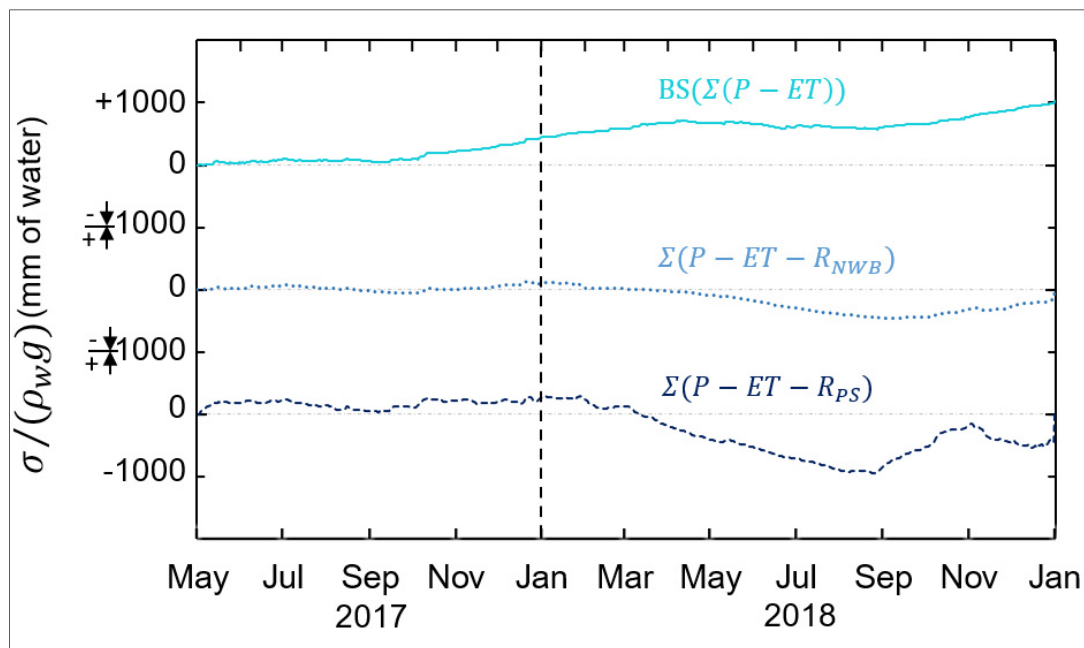


Figure 5.5 Estimated net moisture balances in BS, NWB and PS optimization scenarios

An annual water storage cycle with amplitudes of 300 and 1200 mm was estimated by the NWB and PS methods, respectively. The estimated value by the NWB method is similar to the 260 mm soil water storage change between fall and spring averages in clay deposits of Montreal (Silvestri et al., 1994). This value was calculated based on the water content

variations that were reported for the clay deposits of Maisonneuve Park in the eastern area of Montreal for the period of 5 years, 1989-1993. The change in water storage for the PS method appears large considering the total thickness of the soil profile on the Sainte-Marthe site (20.6 m).

Figure 5.6 compares the estimated and observed monthly runoff. The stress values obtained by the zero-runoff assumption and the optimization methods were also presented in figure 5.6. The PS stress time series showed sharper fluctuations than the other stress time series. It had relatively small fluctuations from May 2017 to April 2018 then a large drop from April to September 2018 followed by a sharp jump and a sudden drop respectively from September to November 2018 and November 2018 to January 2019. The NWB time series, in contrast, was almost constant with small changes before February 2018 and then gradually dropped to September 2018 and finally rose again to the end of the period. A large difference between PS and NWB time series in certain periods is related to the existence of the water storage budget in the NWB method. There are larger differences in these periods between measured and simulated hydraulic head time series that the existing water budget does not allow a perfect agreement between them. For instance, there is a significant drop in observed hydraulic head time series from April to September 2018. With the NWB method, even by allocation of the highest runoff rates, the simulated hydraulic heads are still higher than the observed ones in certain time steps. However, as there is no water budget boundary in the PS method, the model tries to compensate for it by assigning much lower stress values. It is worth mentioning that higher positive stress means more water storage while lower negative stress means more water deficiency.

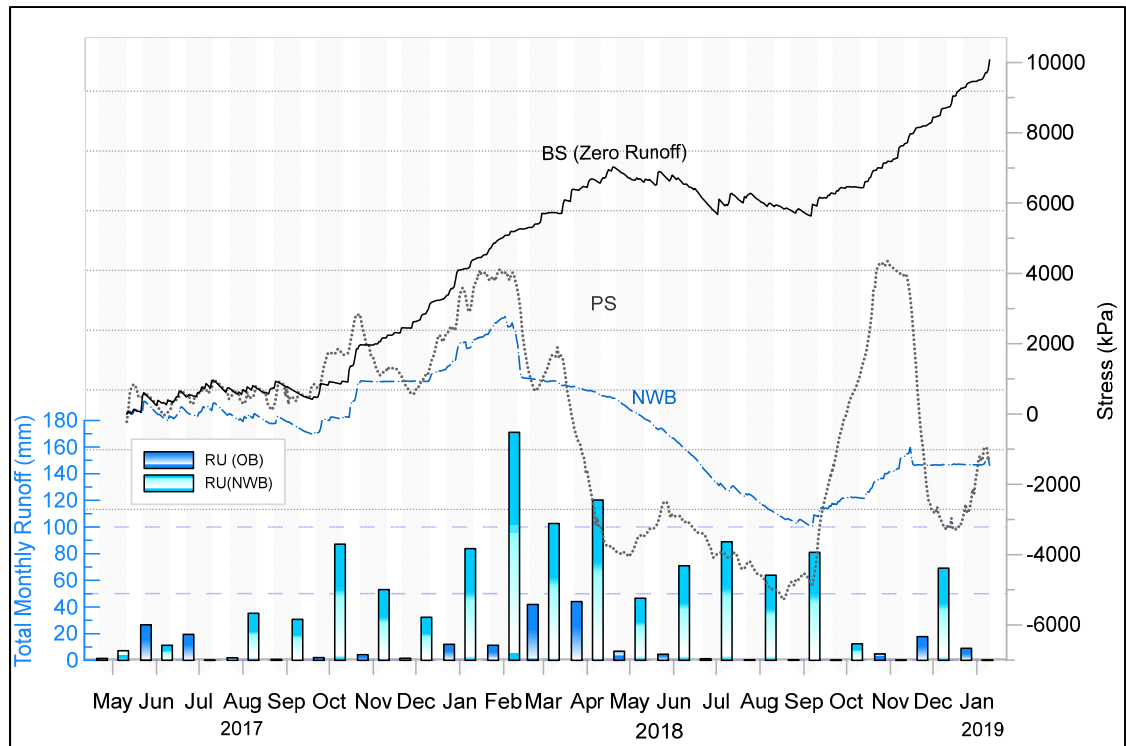


Figure 5.6 Total estimated and observed monthly runoff along with stress time series based on PS, NWB, and BS scenarios

The estimated runoff volumes were considerably higher than the observed ones, especially in summer. The runoff was calculated from the catchment hydrograph. The runoff was obtained with United States Geological Survey (USGS) PART software by removing from the hydrograph the base flow associated with ground water flow (Risser et al., 2005). It is worth mentioning that the observed runoff values are associated with the 8.8 km² Sainte-Marthe basin and the observed behaviour would be different than a catchment as small as 0.2 km². However, the trends are comparable and both the estimated and the observed values peaked in the period from January to April 2018.

5.2 Numerical modelling of settlements in Sainte-Marthe

The FEM simulation results for settlements on the Sainte-Marthe study site for the period between May 2017 to December 2019 are presented in this section. A series of scenarios

were used to verify the impact of the constrained modulus, temperature fluctuations and liquid water to ice phase change.

The pore pressure and temperature profiles define the strain in the clay and the total displacement at the ground surface (equations 3.15 and 3.16). The pore pressure and temperature profiles vary differently in time and with depth throughout a typical year. Their combined effect on the deformation is complex. The thermal expansion coefficient, the volume change function associated with the liquid water to ice phase change, and the constrained modulus control how these profiles influence the displacement. The accurate estimation of M , α_T and ΔV_f for in situ conditions is difficult to achieve. In this study, two sensitivity analyses were designed to examine independently the impact of the constrained modulus and the temperature fluctuations on settlements.

For the first sensitivity analysis, three scenarios were tested to observe the impact on the displacement time series of the M value and contrasting M values in the oxidized crust and intact clay layer. In all three scenarios, frost heave was neglected ($\Delta V_f = 0$) in order to simplify the model while the air temperature time series was applied as the upper boundary condition. Two scenarios considered constant M values of 1.3 and 50 MPa for both the crust and intact clay layer. The third scenario used a stiff crust with $M = 50$ MPa and $M = 1.3$ MPa in the intact clay layer. The third scenario with a stiffer oxidized crust is probably more realistic. Figure 5.7 shows the settlements that were obtained for the three scenarios. Both scenarios with $M = 50$ MPa in the crust resulted in a smoother curve. The modulus in the lower clay layer controls the long-term settlement whereas the crust modulus controls the short-term variation in ground surface elevation. Both scenarios with an intact clay modulus of 1.3 MPa resulted in the same settlement at the end of the simulation (29 mm). The model with the constant constrained modulus of 50 MPa resulted in around 10 mm of settlement at the end of the period.

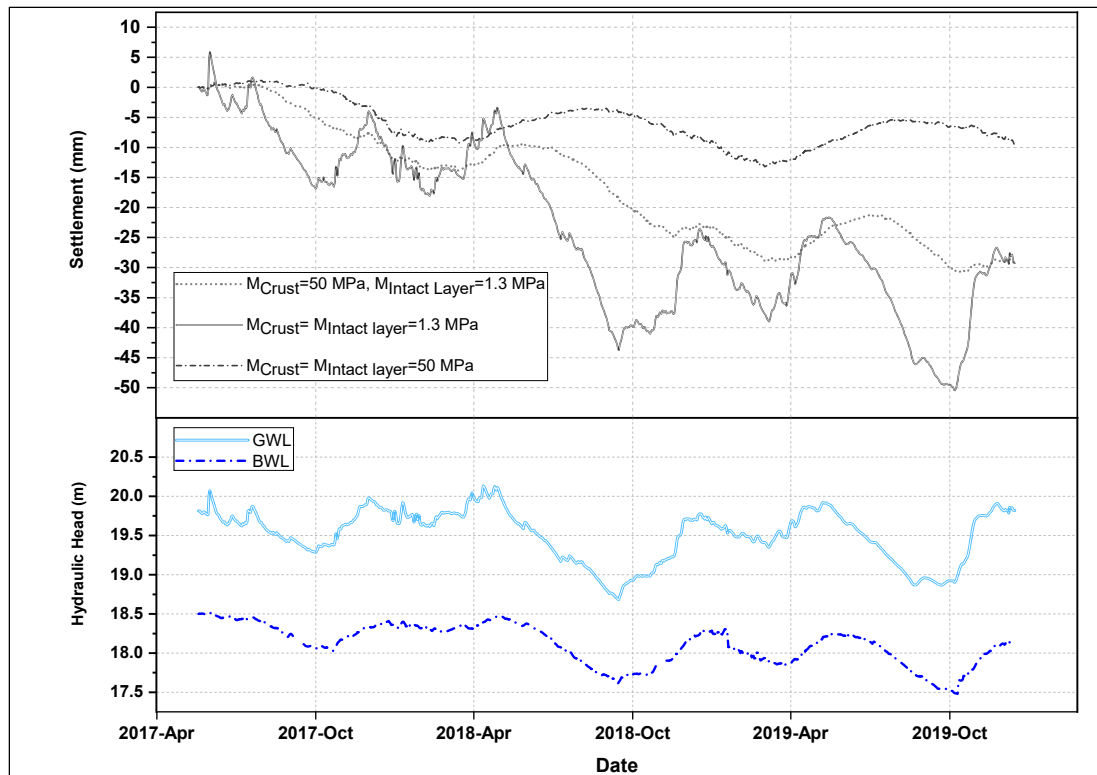


Figure 5.7 Impact of M modulus on the simulated settlement time series along with the hydraulic head time series at the surface (Ground Water Level, GWL) and the bottom of the intact layer (BWL)

The hydraulic head time series associated with the surface piezometer (GWL) and the piezometer at a depth of 12.2 m (BWL) are presented in the lower panel of figure 5.7. Comparing the hydraulic head with the settlement time series shows that their fluctuations coincide. This is more obvious for lower M values. In other words, the displacements for less rigid clay are more affected by groundwater level fluctuations, which is expected from equations 3.15 and 3.16.

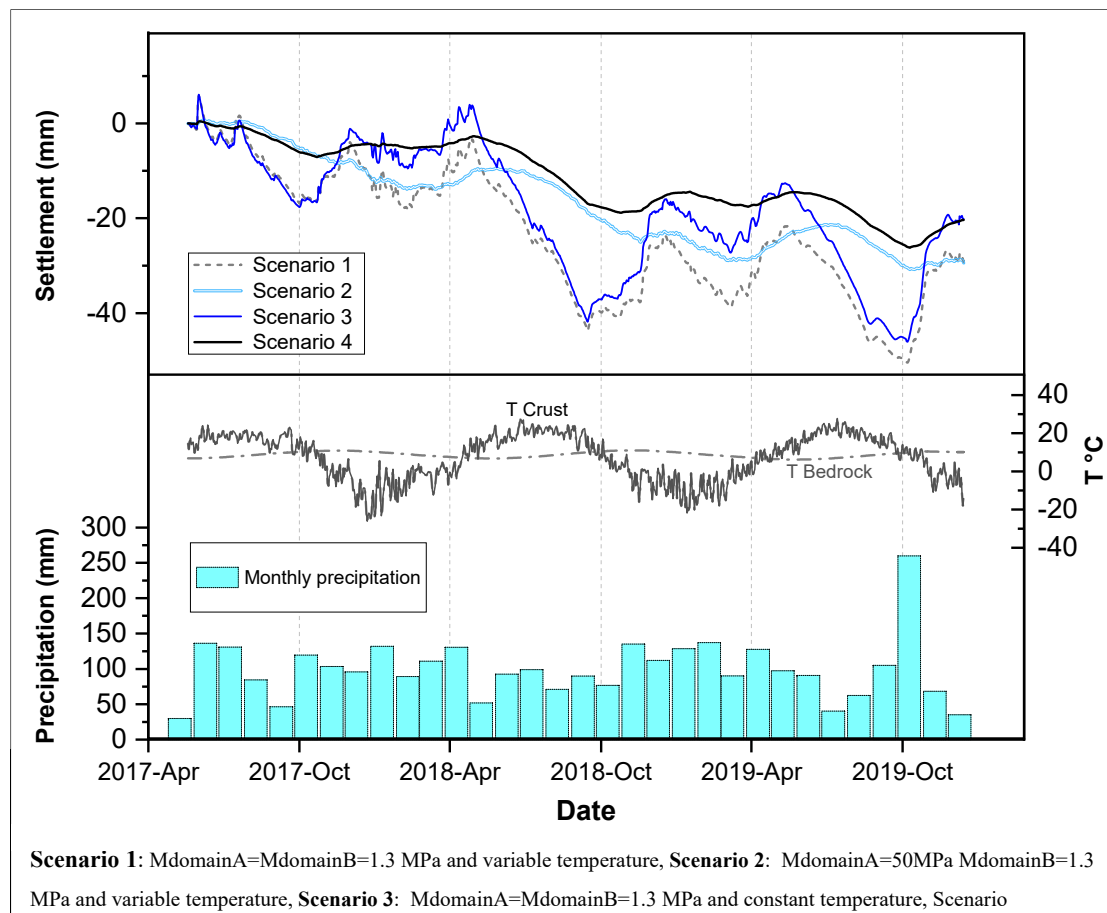


Figure 5.8 Settlement times series (FEM) for four scenarios along with the monthly precipitation and thermal boundary conditions

The impact of variable or constant temperature with varying clay stiffness was examined with four scenarios. In all four scenarios, frost heave was neglected. The air temperature time series was applied as the upper boundary condition for scenarios 1 and 2. Scenarios 3 and 4 considered a constant temperature equal to the mean annual surface temperature. Two scenarios were considered for the clay stiffness: a constant modulus $M = 1.3$ MPa in the crust and the intact clay layer (scenarios 1 and 3) and a stiffer weathered crust with $M = 50$ MPa (scenarios 2 and 4). Figure 5.8 shows the results for each scenario. The climatic variables including temperature at the surface and in the bedrock along with the monthly precipitations are presented in the lower panel. Both constant temperature scenarios led to a decrease of the winter settlement of approximately 10 mm. Scenarios 1 and 3 produced the highest settlement fluctuations, while scenarios 1 and 2 resulted in the largest settlements

at the end of the period. It is difficult to see a clear connection between the climate data and the settlement time series. Considering the temperature at the surface, no upward movements can be detected in the settlement time series in the summer periods when the temperature reaches its maximum value. The highest settlements for scenarios 1 and 3 occurred around October for each year. The largest settlement in all scenarios coincided with the highest monthly precipitation in October of 2019. However, a similar connection cannot be found in the rest of the period and higher precipitation should lead to higher pore pressures and lower settlements. As expected, the smoothest settlement time series was obtained with scenario 4 where the higher value of the constrained modulus was considered for the crust and the temperature fluctuation effect was ignored. The results for the four scenarios indicate that pore pressure has a more significant influence on settlements than temperature when heave is neglected.

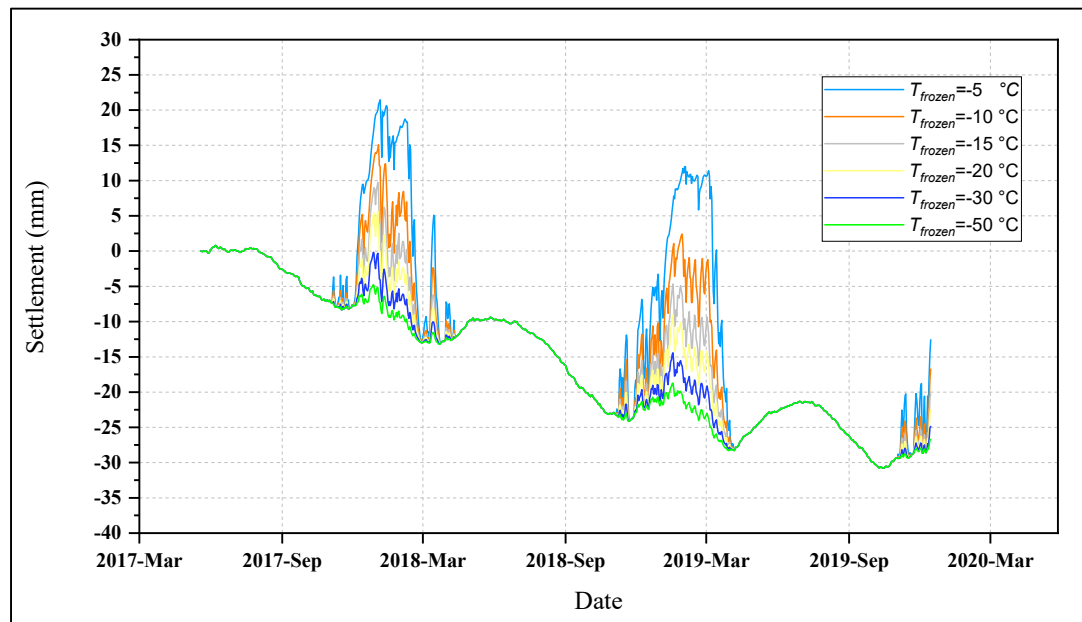


Figure 5.9 The impact of the T_{frozen} on the simulated settlement time series

The impact of T_{frozen} on the simulated settlement time series was also examined by assigning values of -5, -10, -15, -20, -30, and -50 °C to T_{frozen} in six simulations. The rest of the parameters were the same as in scenario 2 in the previous section. Figure 5.9 shows the

results of these simulations. The amplitude of the winter heave and spring freeze-thaw varies with T_{frozen} and demonstrates the effectiveness of the ΔV_f function. It can be seen that the settlement amplitude is higher for warmer T_{frozen} values. Warmer T_{frozen} values lead to an increased thickness of soil where the maximum volume change $\Delta V_{f_{max}}$ is observed.

5.3 Comparison of deformation in Sainte-Marthe based on InSAR and FEM

The results obtained with PSI for different calculation parameters were evaluated based on factors such as coherency, spatial density of PS, and their residual phase. Figure 5.10 presents the selected distribution of the PS points in the study site area colour-coded with the deformation velocity based on the linear approach for the period between May 2017 and November 2019. Negative deformation velocities imply settlements, and positive values imply heave. The estimated deformation velocity close to the study area ranges between -2 and -6 mm/year. For some PS points in other areas, settlement rate as large as -20 mm/year were monitored. The distribution of PS points was also analyzed for non-linear displacements. Among the identified PS, two points which were closer to the study site and had less signal fluctuation due to the impact of vegetation were selected to plot the time series graph (PS1 and PS2).

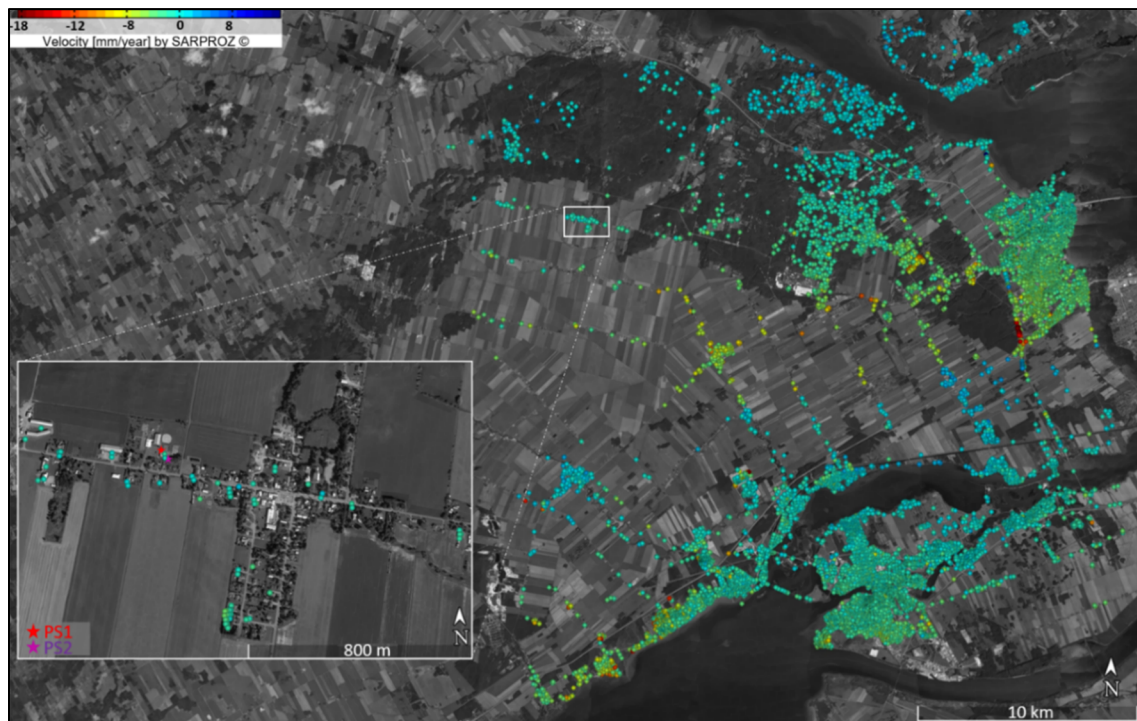


Figure 5.10 Vertical velocities of all processed PS pixels (mm/year) in time series analysis at Sainte-Marthe

Among the scenarios which were mentioned in the previous section, scenario 2 was selected for the FEM results. This scenario was considered more realistic because of the different clay stiffness for the two domains and the boundary condition with a variable temperature. Figure 5.11 compares the displacements for the FEM simulations, and PS1 and PS2 in SARPROZ with the non-linear approach. Two FEM simulations (FEM, FEM+Heave) were considered. Both simulations correspond to scenario 2 with a stiffer crust and a variable air temperature boundary. Simulation FEM+Heave also considers heave through the ΔV_f function with $T_{frozen} = -15$ °C. The results show similar trends for PSI DInSAR and the FEM simulations. All time series show a downward movement of the soil surface. The PSI time series have a higher amplitude of yearly deformation compared to the FEM time series when heave due to freezing conditions is not considered in the simulation. The lower amplitude for the numerical model could be due to the simplicity of the model and its inability in replicating all the complexity of the soil deformation. Alternatively, the higher amplitude for the PSI time series could be due to temporal noise. Comparing the results of the FEM

model (FEM, FEM+Heave) shows how the extended model, FEM+Heave, can effectively simulate the frost heave deformation in cold periods of the year. It can be seen that there are considerable differences between the graphs (FEM, FEM+Heave) during winter times. With the frost heave component, the FEM time series has better agreements with the PSI time series during cold periods. However, the amplitudes of the deformation are slightly higher in the FEM+Heave time series compared to the ones that were observed by the PSI method. It can be seen in figure 5.11 that the difference between PSI and FEM results is larger at the beginning of the period in 2017. Both PSI time series, PS1 and PS2, show strong agreement in their monitored displacements.

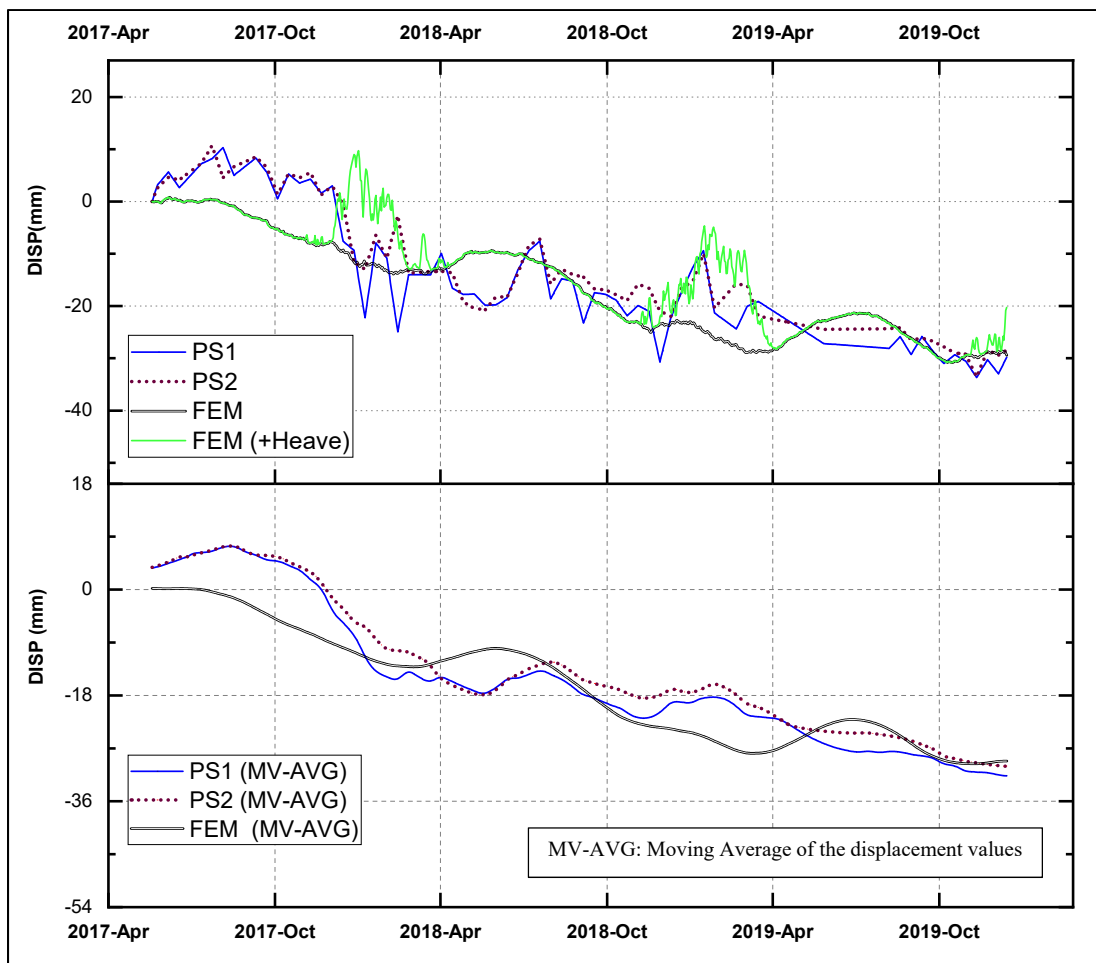


Figure 5.11 Displacement time series for FEM Scenario 2 without frost heave, FEM Scenario 2 with frost heave, and SARPROZ (PS1, PS2)

The amplitude of the yearly settlement cycles obtained with the numerical model and PSI is slightly lower than the amplitude measured in the field for sites with a weathered crust. The maximum amplitude for the numerical model was 31 mm. It was obtained by considering heave with the ΔV_f function and by using a constant M value of 1.3 MPa for the crust and intact clay layer. As a comparison, Konrad et al. (1995) obtained a maximum thaw settlement of 65 mm for their St-Alban site. Silvestri (2000) obtained a maximum amplitude for the yearly settlement cycles of 55 mm assuming maximum heave during the first settlement measurements in April. Larger settlements could be obtained with the numerical model by using a more rigorous approach for the modelling of heave with the formation of ice lenses.

Table 5.1 Statistical comparison of the FEM and PSI displacement time series

Parameter	Linear		Non-linear		FEM
	PS1	PS2	PS1	PS2	
Velocity (mm/year)	-3	-3	-10	-10	-10
Cumulative Displacement (mm)	-7	-8	-29	-28	-29

Table 5.1 compares statistically the estimated displacement time series for the PSI methods and FEM simulations. Although the non-linear approach cannot yield the deformation velocity, with simple division of total displacement by time the associated velocity was evaluated and presented here just for comparison purposes. The FEM simulations and non-linear approach yielded similar results with a velocity of -10 mm/year and total subsidence of 28 mm. The linear approach, however, resulted in a subsidence that was smaller, approximately one-third of the non-linear approach. It is worthy of note that the non-linear and linear estimations result from very different approaches. In the non-linear approach, SARPROZ uses a linear model instead of a polynomial approximation. The linear model can neglect a large portion of the total displacements which are not linear. In general, the non-linear method is more appropriate for monitoring clay deposits due to the frequently low coherency of PS points in highly vegetated areas (Perissin, 2016) and the existence of seasonal and non-linear ground movement induced by climatic variation (Rees & Thomas,

1993). The linear method would be a better choice for monitoring settlements for man-made structures in areas with a high temporal coherency of PS points.

5.4 InSAR monitoring of deformation in the Montreal area

In this section, macroscale and microscale velocity maps, and detailed deformation time series are presented for different parts of the Montreal Island. The microscale velocity maps and deformation time series were prepared for the target areas 1, 2 and 3 that were introduced in chapter 4, and other areas where considerable deformations were observed with the InSAR analysis.

Figure 5.12 shows a map of the mean vertical velocity for the Montreal Island for the period between April 2016 and February 2022. The majority of PS pixels in this figure have a low deformation rate close to zero which is defined by the green colour. The areas with the lower density of the PS pixels are generally associated with the existence of dense vegetation, a body of water, construction, or any kind of changes that result in lower temporal coherency. It is worth mentioning that often the chance for detection of large deformations in areas with a higher number of PS pixels is more. Because the model in areas with generally low coherencies might consider a large deformation as a noise.

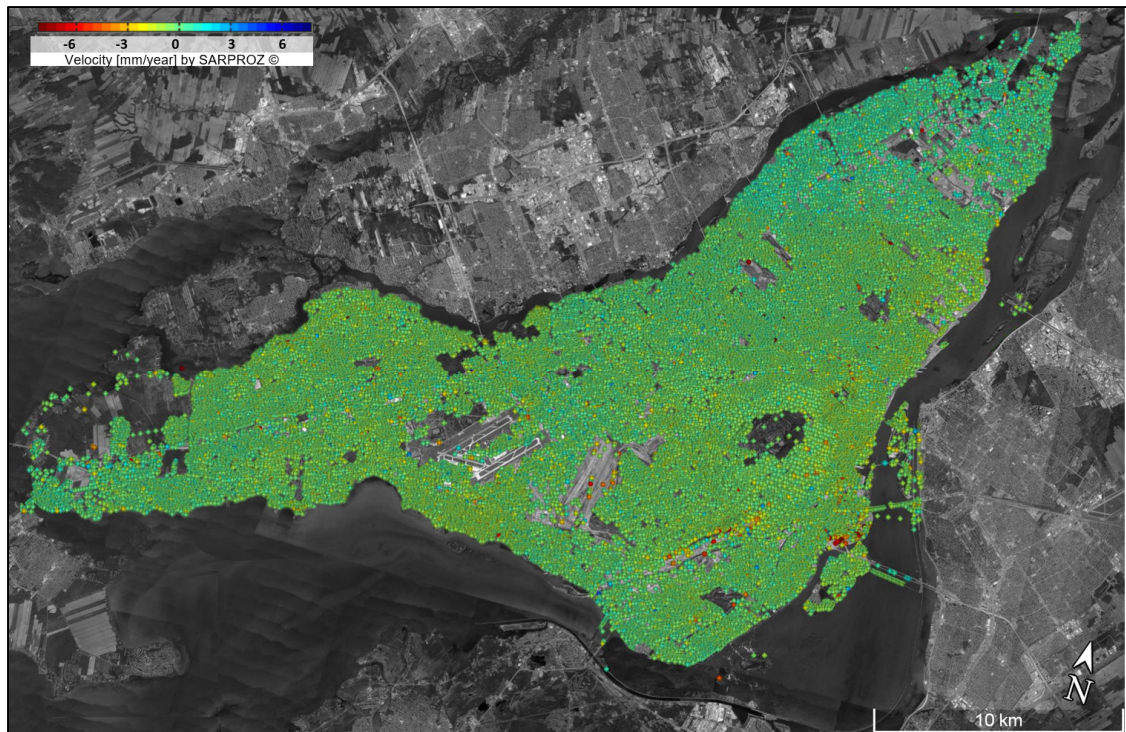


Figure 5.12 Mean velocity map for the Montreal Island

Figure 5.12 show no sign of bias. Biased velocity maps are often indicative of problems with the InSAR analysis. Bias can appear as an obvious trend in the deformation from one side of the map to the other. It can also appear as results that are considerably different in one area of the PS network, in other words as a large settlement or heave that is observed for all processed PS points of an area. The latter type of bias is often associated with an atmospheric phase that is not properly filtered and that affects the results in a specific area.

In the following sections, deformation maps of the target areas and other areas where significant settlements were obtained will be presented in more details.

5.4.1 InSAR deformation results for Saint-Jacques Escarpment (target area 1)

Figure 5.13 shows the mean velocity map for target area 1. Although the model was forced to include more PS pixels during the analysis for this area, a small number of PS pixels with reliable estimation (high coherency) were identified.



Figure 5.13 Mean velocity map for the Saint-Jacques Escarpment

The PS pixels that had a coherency lower than 65 % were filtered from our final estimation. The low coherency was due to the presence of dense trees in target area 1. The trees can block the C-band signal penetration. However, a significant number of PS pixels were obtained with proper coherency in the uphill part of the escarpment. In areas that were closer to the slope, most of the time series showed mild settlement (less than 2 mm/year). Considerable settlements were monitored for some PS pixels.

Four observed deformation velocities are highlighted on the map. The settlement velocities for PS pixels T1-1, T1-2, T1-3, and T1-4 are respectively -4.0, -2.3, -8.4, and -4.0 mm/year. The deformation time series for T1-3 is presented in figure 5.14.

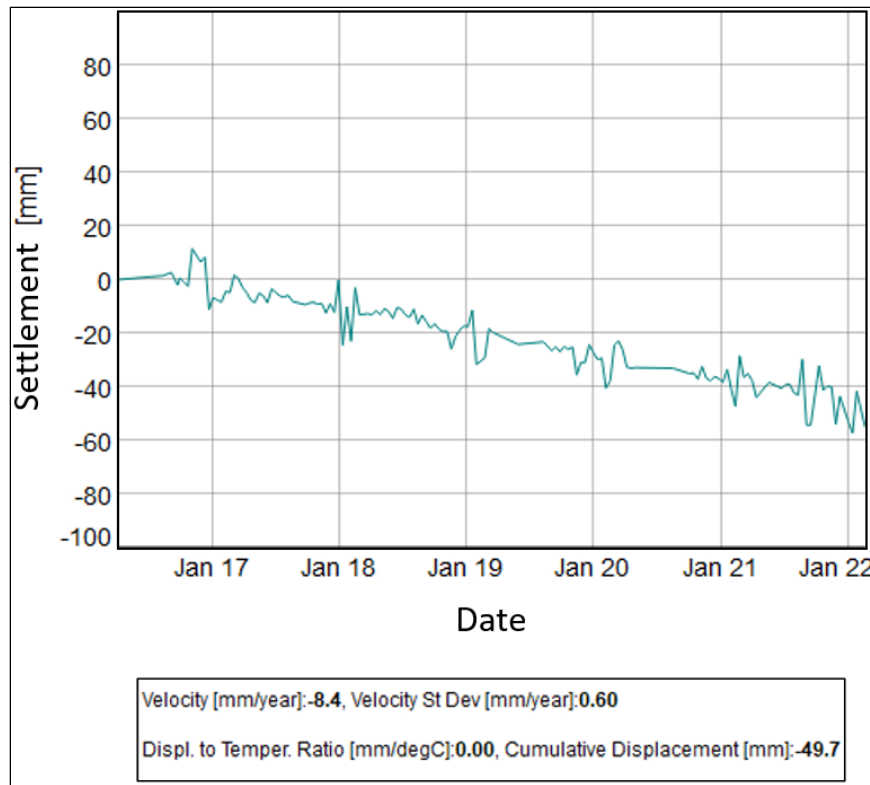


Figure 5.14 Deformation time series for PS pixel T1-3 in Saint-Jacques Escarpment

5.4.2 InSAR deformation results for Parc d'entreprise pointe Sainte-Charles (target area 2)

Figure 5.15 shows the InSAR deformation monitoring results for the PESPC area. After applying the coherency filter, most of the PS pixels were filtered from the final estimated velocities. This is most probably due to the large number of construction projects in this area. Significant settlements were observed in the southern part of the area next to the Samuel de Champlain bridge. Three PS pixels are highlighted in figure 5.16. The observed settlements for pixels T2-1, T2-2, and T2-3 are respectively -9.3, -3.6, and -8.9 mm/year. Significant settlements were monitored for the bridge entrance ramp (PS pixel T2-1) as it has been recently constructed. The time series of deformation in PS pixel T2-1 is presented in figure 5.16.

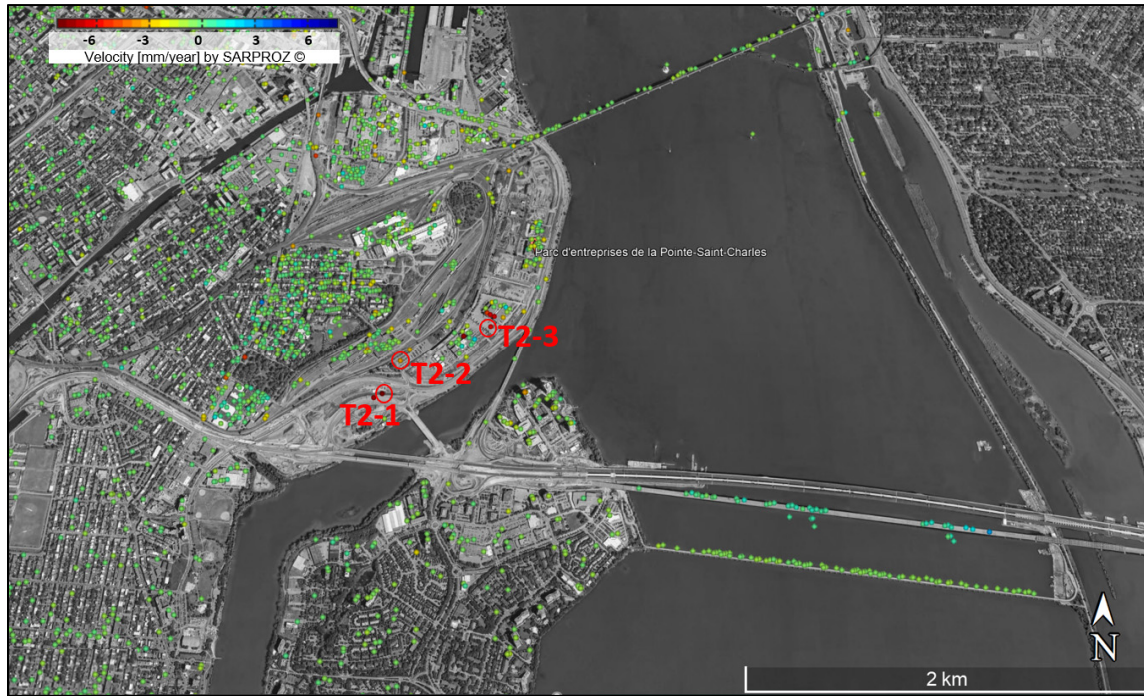


Figure 5.15 Mean velocity map of PESPC in Montreal

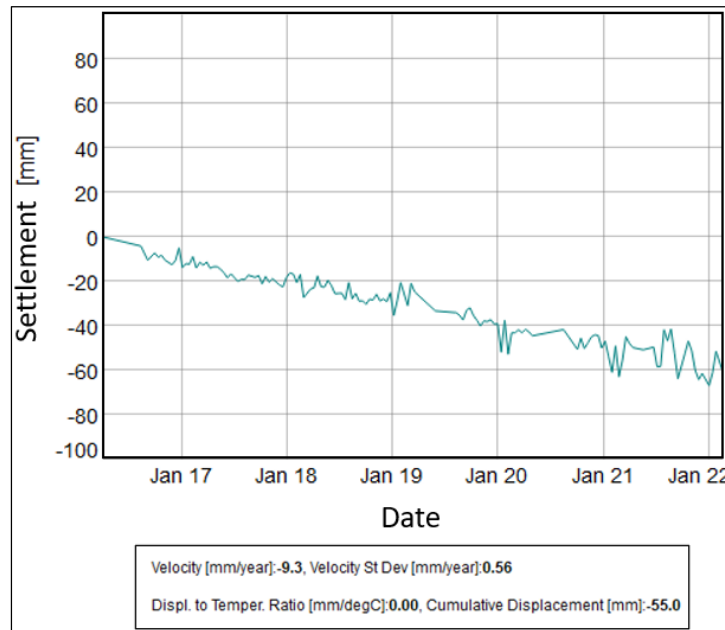


Figure 5.16 Deformation time series for PS pixel T2-1 in PESPC

There are three other PS pixels with a red colour close to pixel T2-3. This is indicative of large settlements in this parking area. High resolution Google Earth pictures from this area also show cracks on the parking pavement (Figure 5.17).

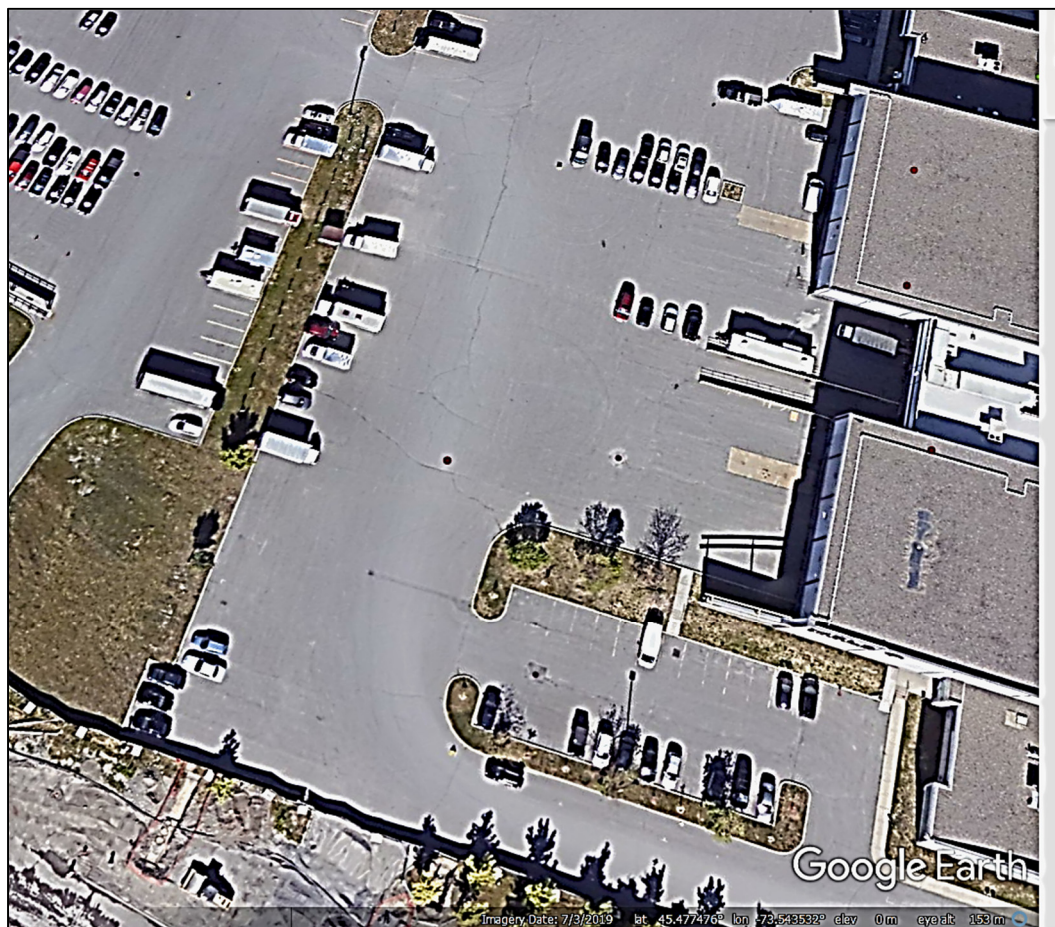


Figure 5.17 Cracks in the parking area of the PESPC

5.4.3 InSAR deformation on Roy Street (target area 3)

Figure 5.18 shows the mean velocity map for the Roy Street area on Plateau Mont-Royal. In the cross section of St Denis and Roy streets that we expected a significant settlement, only mild settlements (-2, -2.4, -2.5 mm/year) in three spots were monitored. However, at one end of the Roy Street close to the avenue du park la Fontaine between Mentana and St Andre streets, considerable settlements were spotted in three PS pixels, -4.1, -4.8, and -6.8

mm/year. An observed deformation time series in PS pixels T3-1, and T3-2 are presented in figures 5.19 and 5.20.



Figure 5.18 Mean velocity map for the Roy Street area, Montreal

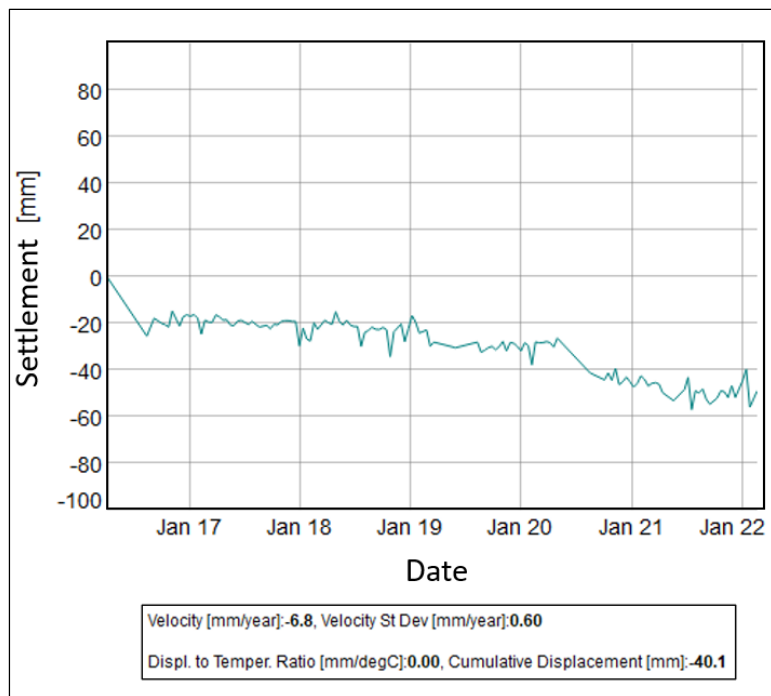


Figure 5.19 Deformation time series of PS pixel T3-1 in the Roy Street area

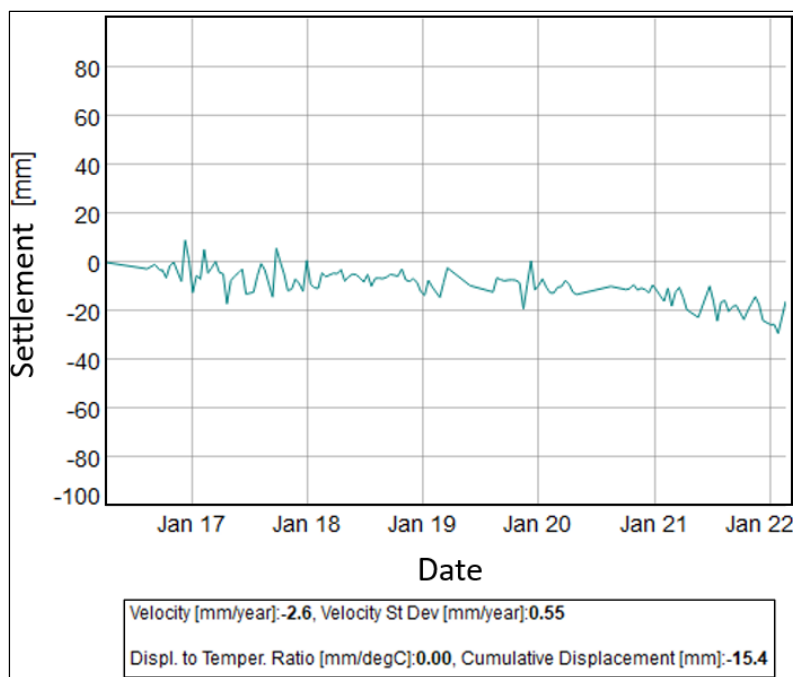


Figure 5.20 Deformation time series of PS pixel T3-2 in the Roy Street area

5.4.4 Other monitored large settlements

The large settlements that were monitored in areas outside our target areas are presented in this section. The velocity map and displacement time series of the target point are illustrated.

5.4.4.1 InSAR deformations on Boulevard de l'Île-des-Soeurs between Elgar and François Streets

Settlements as large as 28.5 mm were detected in this area (Figure 5.21). The velocity of the PS pixel was -4.8 mm/year. The associated time series is present in figure 5.22. Based on surficial geology map of Montreal this area covered mainly by a layer of till (Prest & Hode-Keyser, 1977).

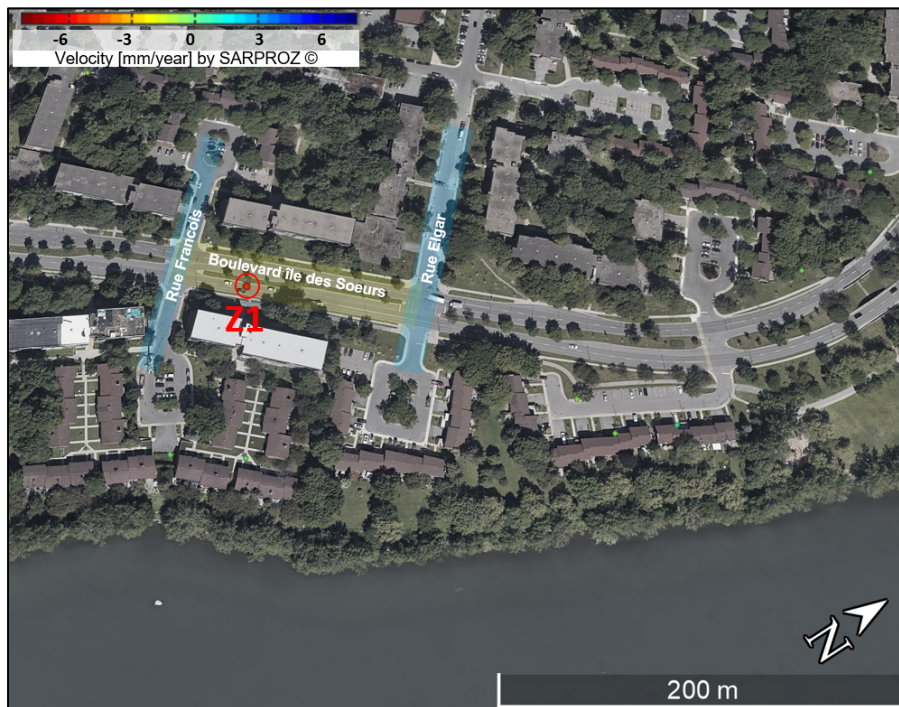


Figure 5.21 Mean velocity map for Boulevard de l'Île-des-Soeurs in Montreal

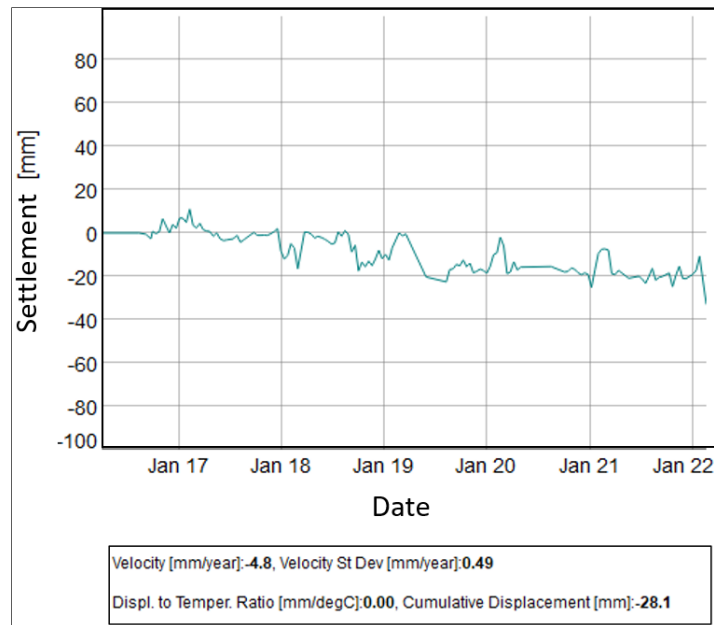


Figure 5.22 Settlement time series for PS pixel Z1, Boulevard de l'Île-des-Soeurs between Elgar and Francois Streets

5.4.4.2 InSAR deformations near the Evolo high rise building in l'Île-des-Soeurs

This Evolo building was constructed in 2017. Approximately -4mm/year of settlement was monitored since. A cumulative displacement of around -24 mm was observed for this building (Figure 5.23). The associated time series is presented in figure 5.24.



Figure 5.23 Mean velocity map of Evolo building in l'Île-des-Soeurs

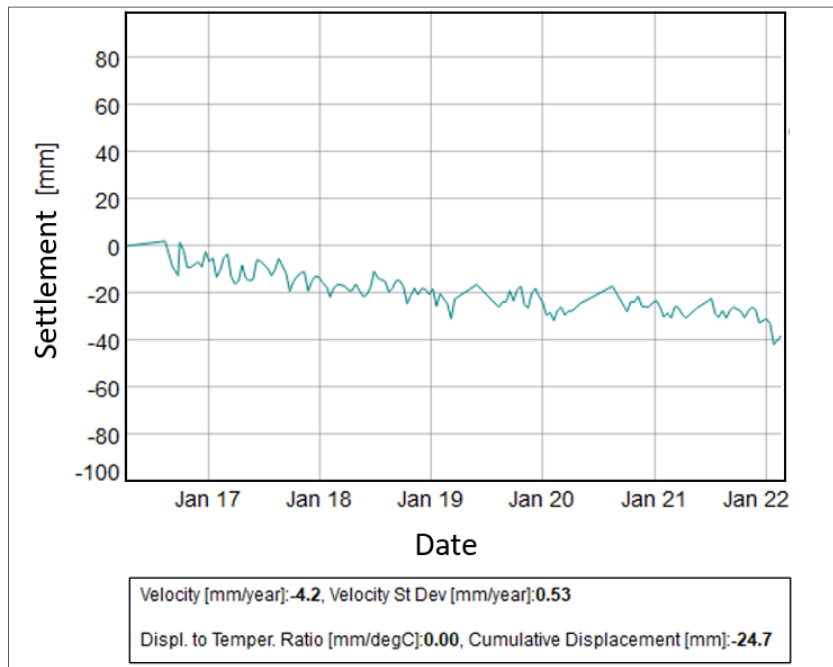


Figure 5.24 Settlement time series for PS pixel Z2, Evolo building in l'Île-des-Soeurs

5.4.4.3 InSAR deformations in Pointe-Saint-Charles

Five PS pixels with large settlements were monitored in this area (Figure 5.25). PS pixels Z3, Z5, and Z7 were identified next to a railway. The observed settlements for these PS pixels are respectively -5.4, -5.4, and -7.8 mm/year. The Z4 PS pixel monitored settlement over the train bridge next to Bassin Windmill Point. The last significant settlement in Pointe-Saint-Charles was observed in the parking area of CPE Les Casinours with the Z6 PS pixel with -6.7 mm/year. The time series associated with PS pixels Z4, Z6, and Z7 are presented in figures 5.26, 5.27, and 5.28, respectively.

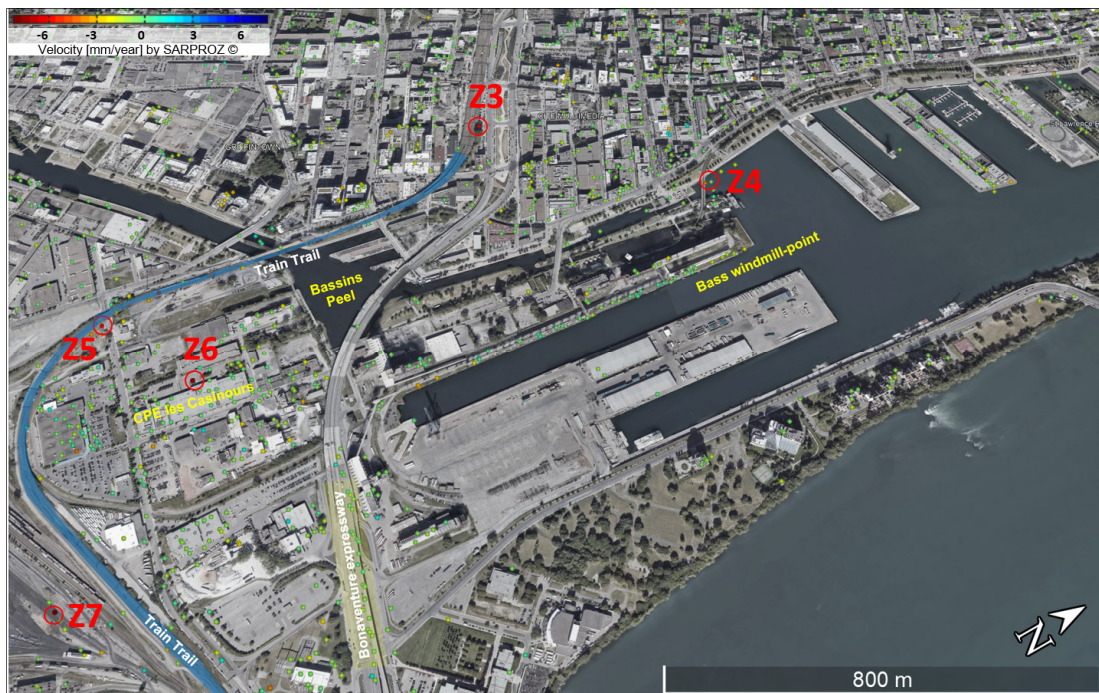


Figure 5.25 Mean velocity map for the Pointe-Saint-Charles area

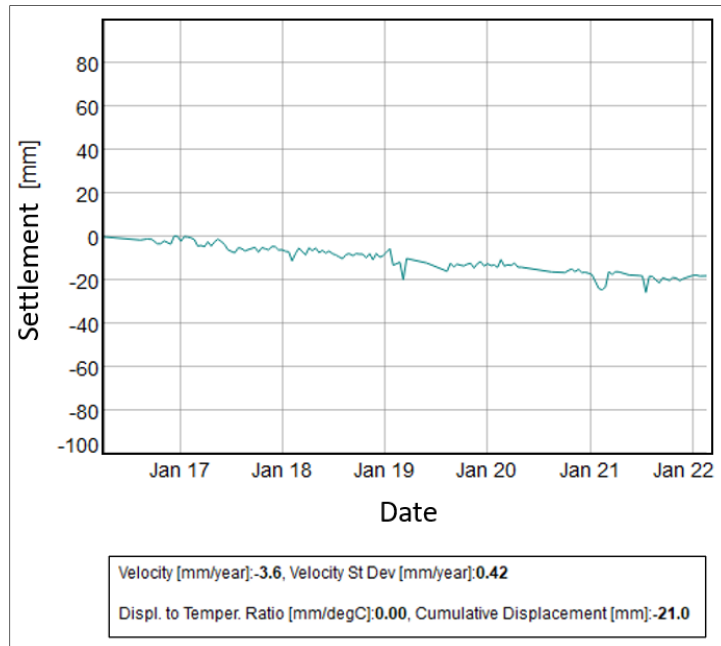


Figure 5.26 Settlement time series for PS pixel Z4 over the railway bridge next to Bass windmill-point

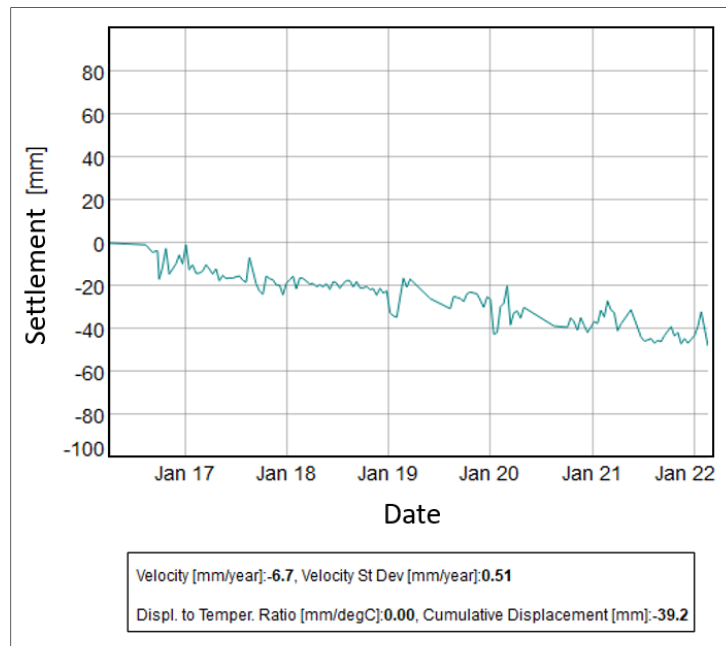


Figure 5.27 Settlement time series for PS pixel Z6 in the parking area of CPE les Casinours

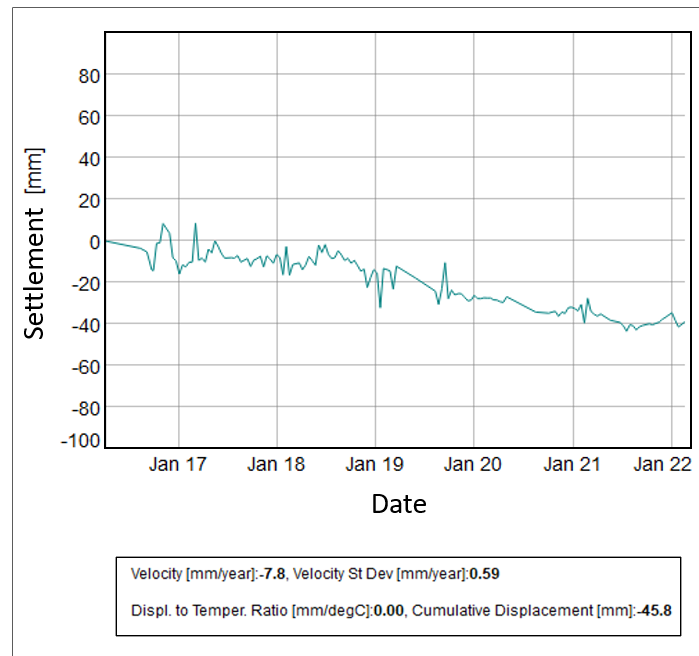


Figure 5.28 Settlement time series for PS pixel Z7 close to the railway located next to the Pointe-Saint-Charles train maintenance station

5.4.4.4 InSAR deformations in the Village-Sainte Marie-Hochelaga-De Lorimier-Plateau Mont Royal-Angus

Figure 5.29 presents the PS pixels with large settlements in the Village, Sainte-Marie, Hochelaga, De Lorimier, Angus, and Plateau Mont-Royal. In Plateau Mont-Royal, PS pixels Z10, Z11, and Z12 were detected with observed settlement velocities of -4.9, -5.5, and -5.1 mm/year, respectively. The Z11 PS pixel is located on Chapleau Street next to Baldwin Park. The associated time series is presented in figure 5.30.



Figure 5.29 Mean velocity map of Gay village, Sainte Marie, Hochelaga, De Lorimier, Le Plateau Mont Royal, and Angus areas of Montreal

Several serious foundation damage and cracks were reported in the Mercier-Hochelaga-Maisonneuve residential area in the summer of 2021 (Radio Canada, 2021). Our investigation also monitored several significant settlements in the same neighborhoods (Figure 5.29). Inside the Angus area, pixels Z13 and Z14 presented settlement velocities of -5.2, and -6 mm/year, respectively. The time series for the Z-14 pixel which is located on Joliette Street is presented in figure 5.31.

In the Village, PS pixels Z8 and Z9 presented settlements of -5.4, and -4.7 mm/year. In Hochelaga, a settlement with a velocity of -5.4 mm/year was observed on Jeanne D'Arc Avenue between Sainte-Catherine and Adam Streets (Z15 pixel). The time series for the Z15 PS pixel is presented in figure 5.32.

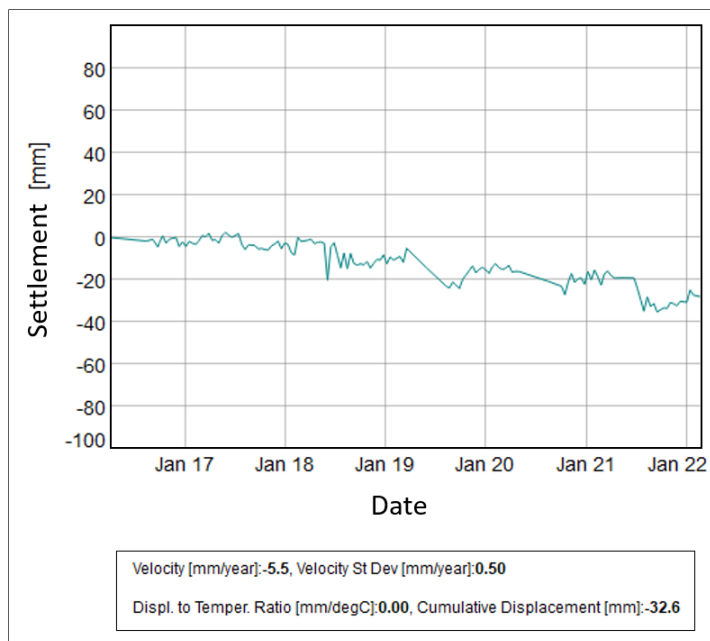


Figure 5.30 Settlement time series for PS pixel Z11 on Chapleau street next to Baldwin Park

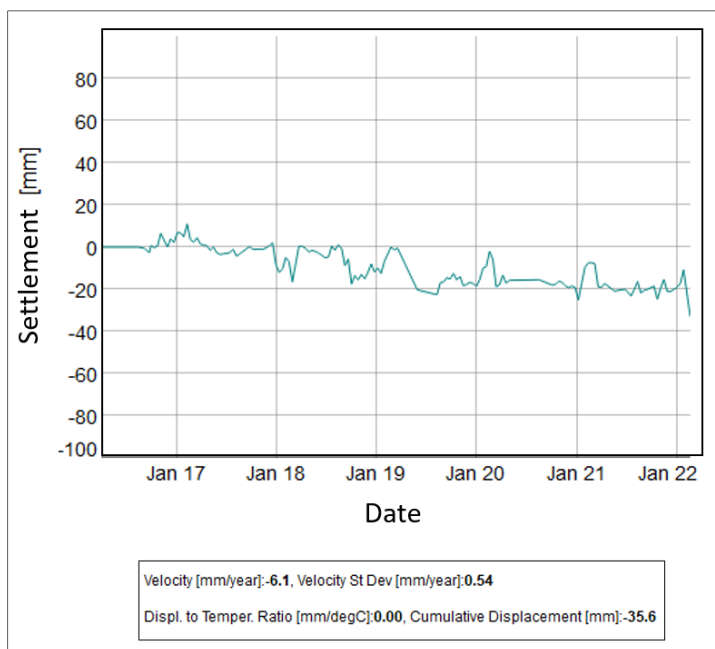


Figure 5.31 Settlement time series for PS pixel Z14 which is located on Joliette Street between Sherbrooke and Rachel Streets

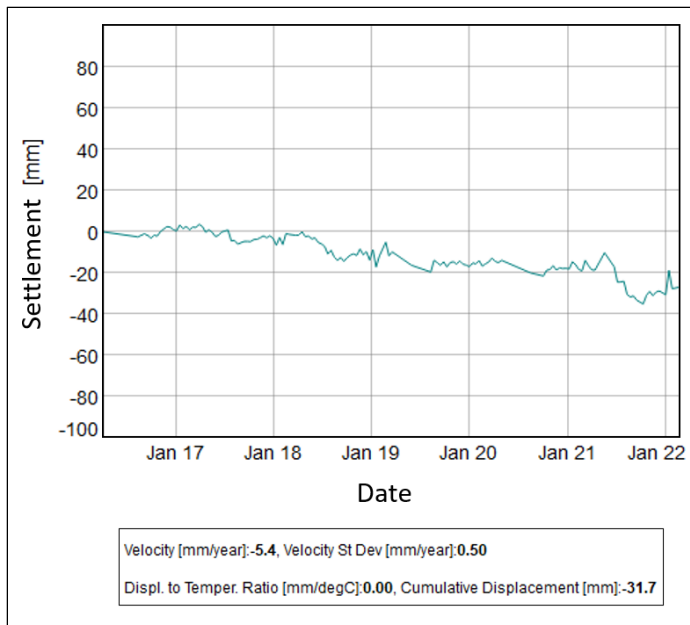


Figure 5.32 Settlement time series for PS pixel Z15 which is located on Jeanne D'Arc Avenue between Sainte-Catherine and Adam Streets

5.4.4.5 InSAR deformations in Villeray

Four PS pixels with large settlement velocities were identified in the Villeray area. Later PS pixels Z16 and Z17 were associated with settlements of -6.5 and -6.7 mm/year, respectively (Figure 5.33). These PS pixels are located in Champdoré and Villeray Parks. Pixel Z18 with a settlement of -6.9 mm/year is located on Papineau Avenue between Jean-Talon and Villeray Streets. The associated time series is presented in figure 5.34. PS pixel Z19 with a settlement velocity of -8 mm/year is located on Saint-André Street between Jean-Talon and Bélanger Streets. The associated time series is presented in figure 5.35.

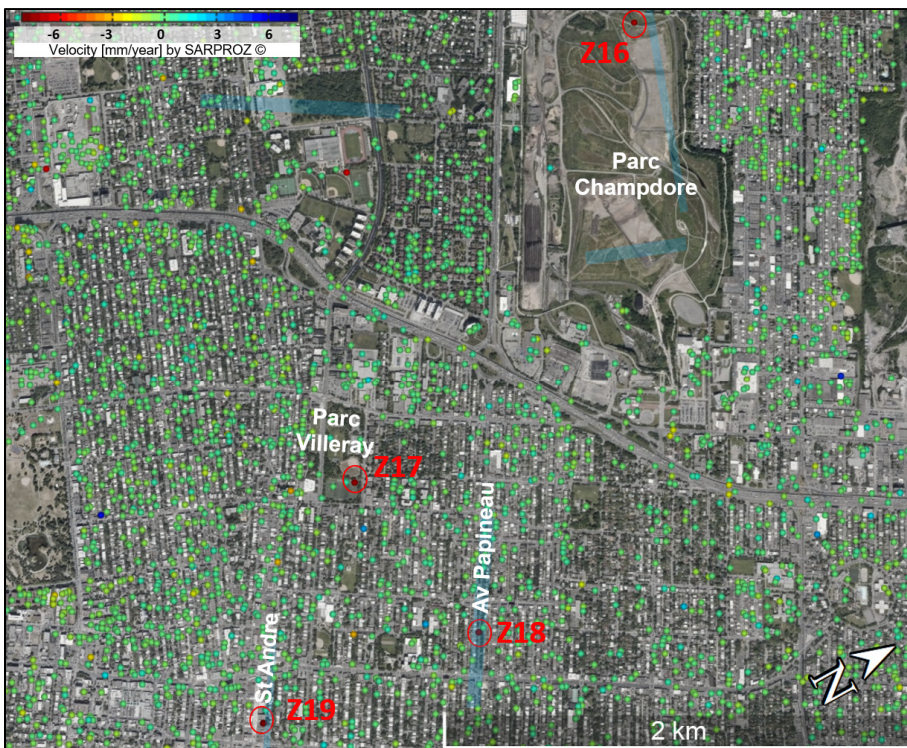


Figure 5.33 Mean velocity map for the Villeray area in Montreal

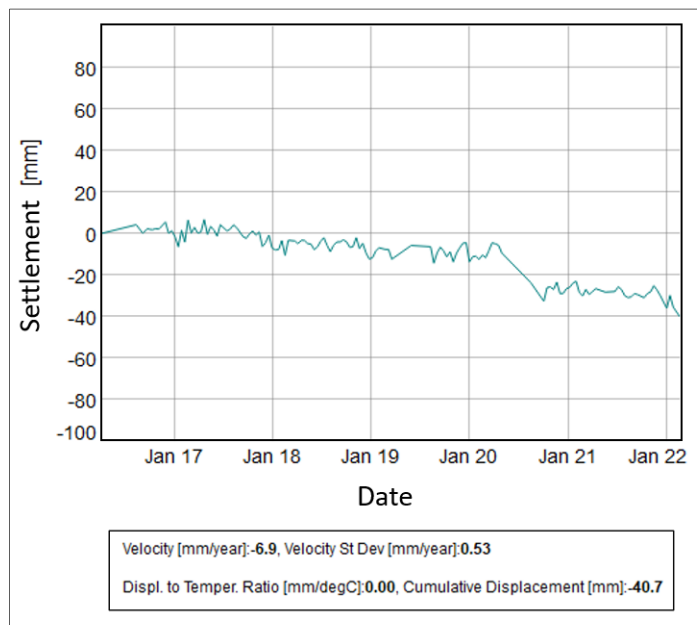


Figure 5.34 Settlement time series for PS pixel Z18 which is located on Papineau Avenue between Jean-Talon and Villeray Streets

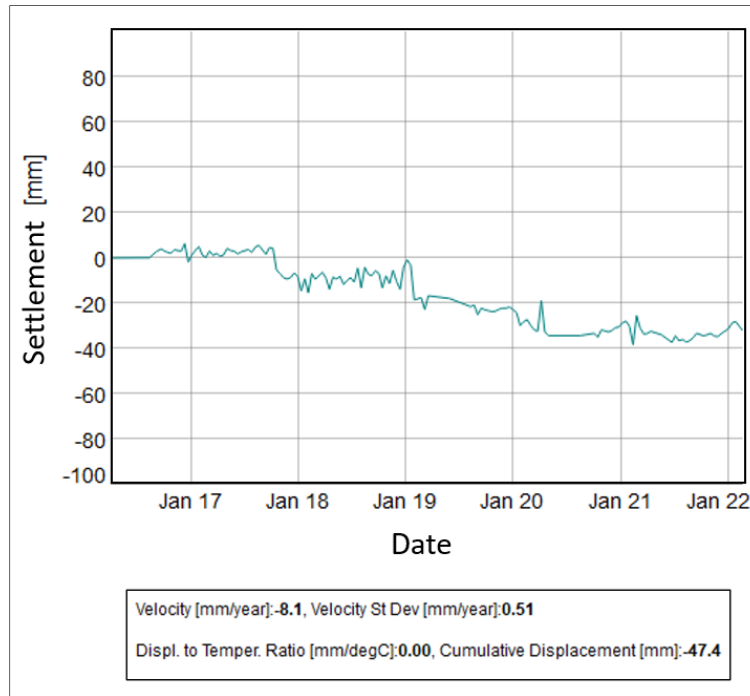


Figure 5.35 Settlement time series for PS pixel Z19 on Saint-André Street between Jean-Talon and Bélanger Streets

5.4.4.6 InSAR deformations on Boulevard de la Vérendrye near Angrignon Park

A settlement velocity of -4.4 mm/year was monitored with PS Pixel Z20 on Boulevard de la Vérendrye next to the entry of Angrignon Park (Figure 5.36). The settlement time series for PS pixel Z20 is presented in figure 5.37. A picture obtained with Google Street view also shows serious signs of cracks on this point on both sides of the boulevard (Figure 5.38).

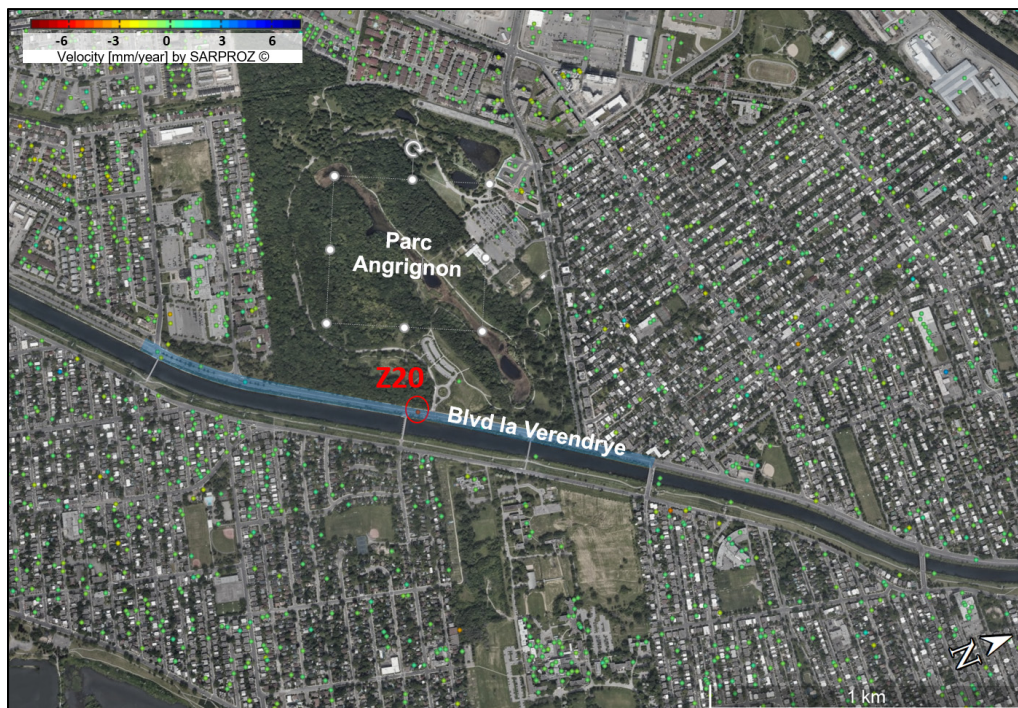


Figure 5.36 Mean velocity map of Boulevard de la Vérendrye next to the entry of the Angrignon Park

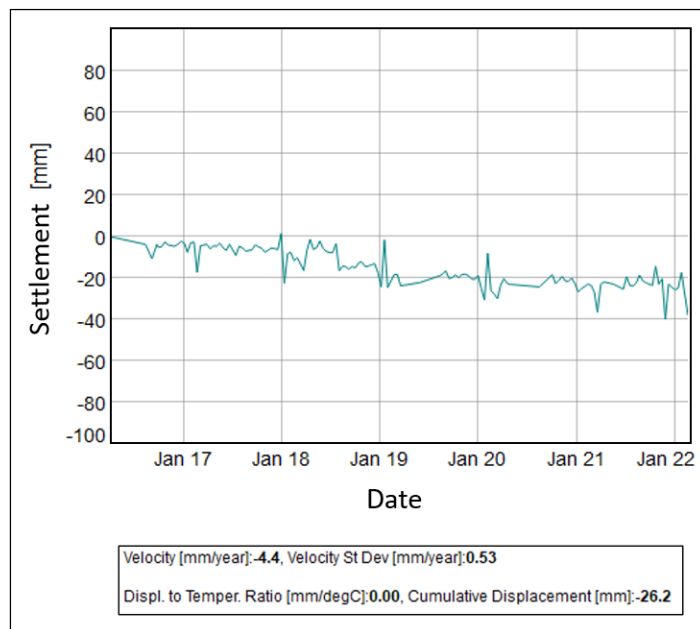


Figure 5.37 Settlement time series for PS pixel Z20 on Boulevard de la Vérendrye next to the entry of the Angrignon park



Figure 5.38 Asphalt cracks in Boulevard de la Verendrye next to the entry of the Angrignon Park

5.4.4.7 InSAR deformations in Côte Saint Luc and Lachine

Settlements with velocities of -5.5, -5.6, and -4.9 mm/year were observed for PS pixels Z21, Z22, and Z23, respectively in the Côte-Saint-Luc area (Figure 5.39). The time series associated with PS pixel Z22 is presented in figure 5.40.

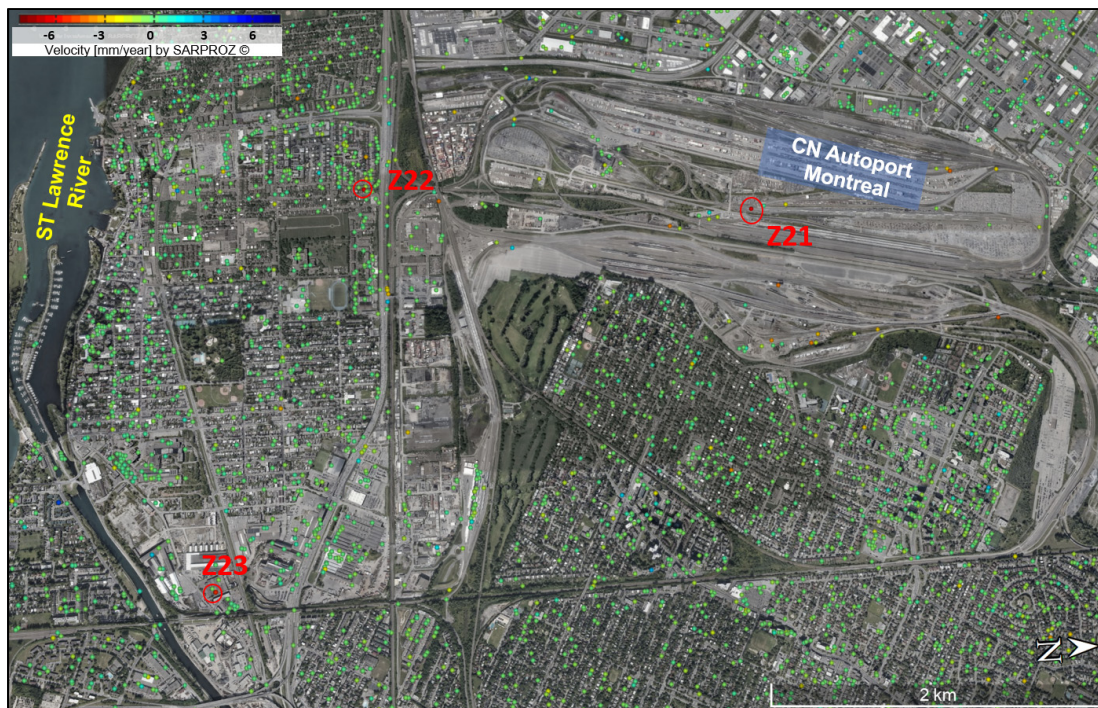


Figure 5.39 Mean velocity map for the Côte Saint-Luc and Lachine areas of Montreal

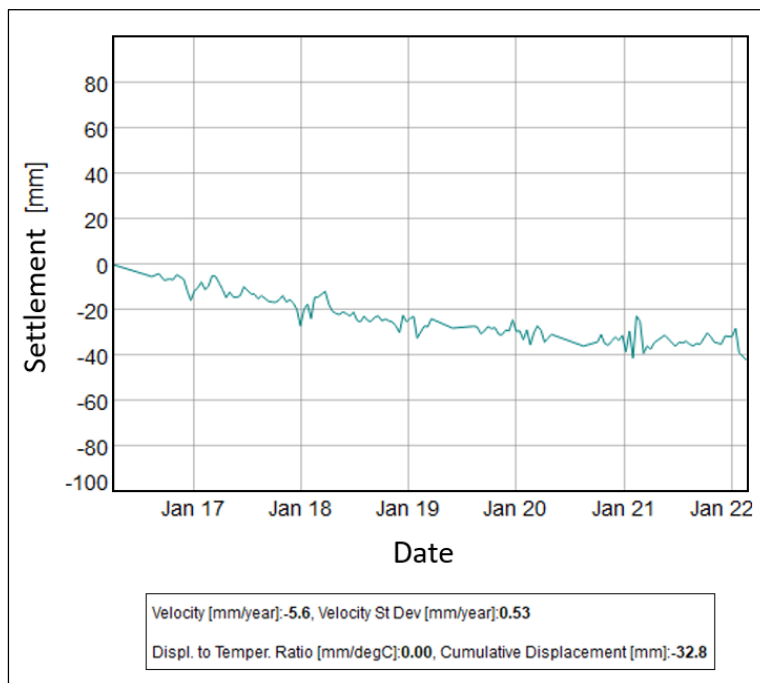


Figure 5.40 Settlement time series for PS pixel Z22 on 25^e Avenue next to Autoroute 20

5.4.4.8 InSAR deformations on Notre Dame Island

Large settlements with a velocity of -5 mm/year were monitored on Notre Dame Island, next to the entrance of the Casino de Montréal with PS pixel Z24 (Figure 5.41). The associated time series is presented in figure 5.42.



Figure 5.41 Mean velocity map for Notre Dame Island in Montreal

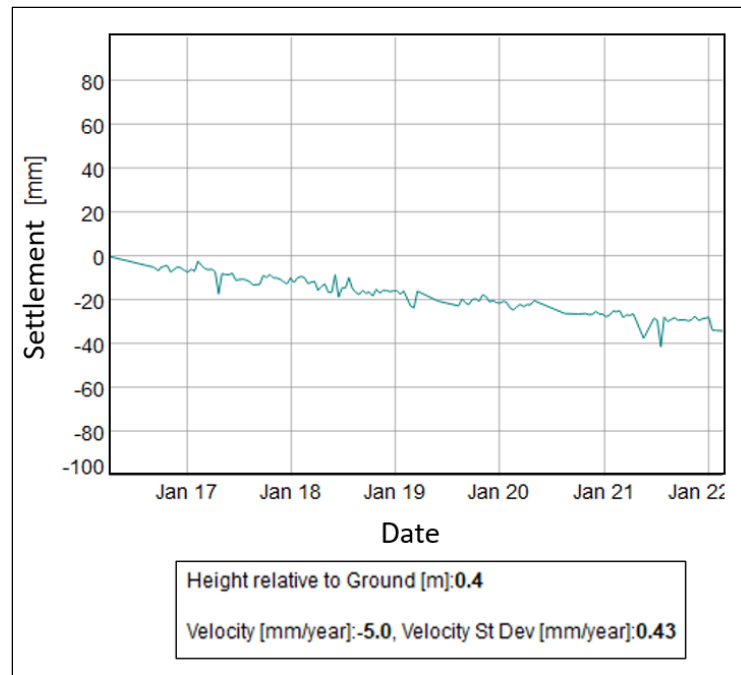


Figure 5.42 Settlement time series for PS pixel Z24 on Notre Dame Island

5.4.4.9 InSAR deformations in Westmount and Côte-des-Neiges

Four large settlements were monitored with the Z25, Z26, Z27, and Z28 PS pixels in the Westmount and Côte-des-Neiges areas next to Boulevard Décarie (Figure 5.43). The settlement velocities for these PS pixels were -5.4, -5.1, -4.8, and -7.6 mm/year, respectively. PS pixels Z25 and Z26 are in the Westmount area, while Z27 and Z28 are over the train line in the Côte-des-Neiges area. The displacement time series for PS pixels Z25 and Z28 are presented respectively in figures 5.44 and 5.45.



Figure 5.43 Mean velocity map for Westmount and Côte-des-Neiges

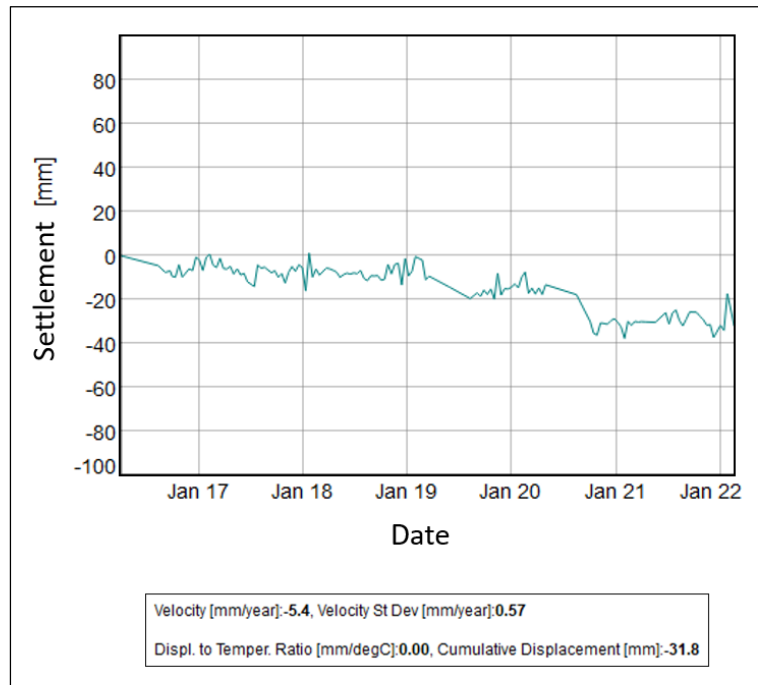


Figure 5.44 Settlement time series for PS pixel Z25 in Westmount

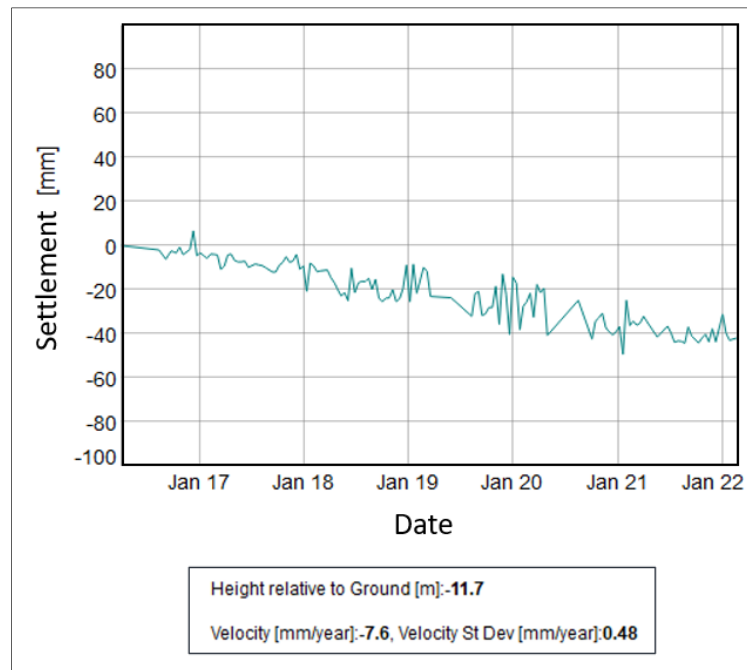


Figure 5.45 Settlement time series for PS pixel Z28 in Côte-des-Neiges

5.4.4.10 InSAR deformations in the eastern part of Montreal Island

Four PS pixels with large settlements were detected in the eastern part of Montreal Island. These four points correspond to PS pixels Z29, Z30, Z31, and Z32 (Figure 5.46). The settlement velocities for these PS pixels are respectively -6.2, -5.3, -9.9, and -5.8 mm/year. The displacement time series for PS pixels Z29 and Z31 are presented in figures 5.47 and 5.48, respectively. It is worth mentioning that earlier incidents of foundation crack were reported for four houses on Forsyth street close to Z30 PS pixel during the summers of 2000 -2012 (Métro, 2012).



Figure 5.46 Mean velocity map for the eastern part of Montreal Island

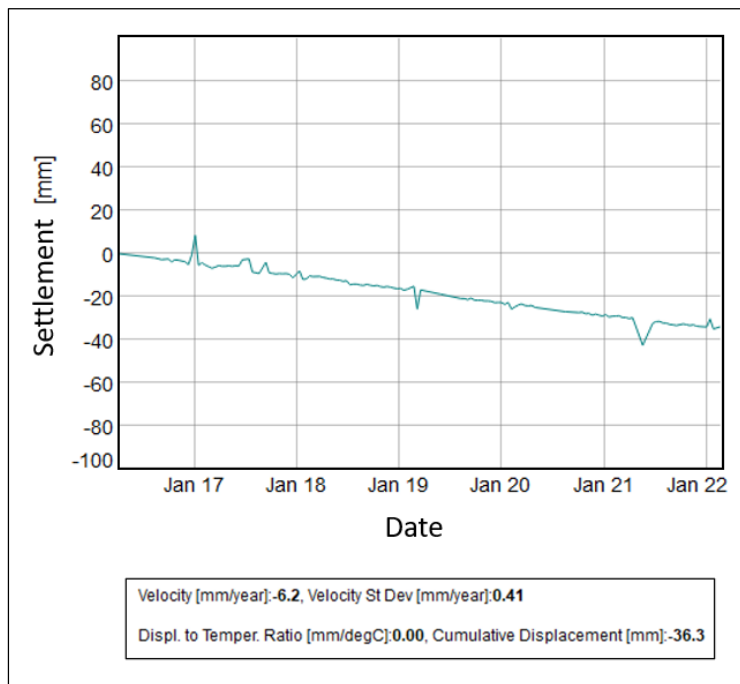


Figure 5.47 Settlement time series for PS pixel Z29 in the eastern part of Montreal Island

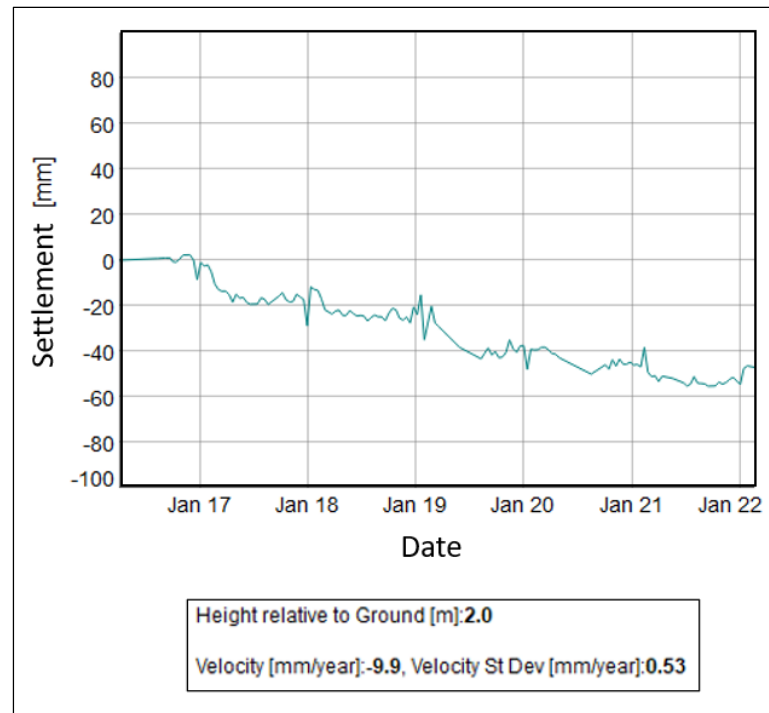


Figure 5.48 Settlement time series for PS pixel Z31 in the eastern part of Montreal Island

5.4.4.11 InSAR deformations in Lachine, Dorval and Pointe-Claire

Large settlements were detected for PS pixels Z33, Z34, and Z35 in Dorval, Pointe-Claire and Lachine (Figure 5.49). These three points correspond to settlement velocities of -6.5, -7.0, and -5.6 mm/year, respectively. The displacement time series associated with PS pixels Z33 and Z34 are presented in figures 5.50 and 5.51.

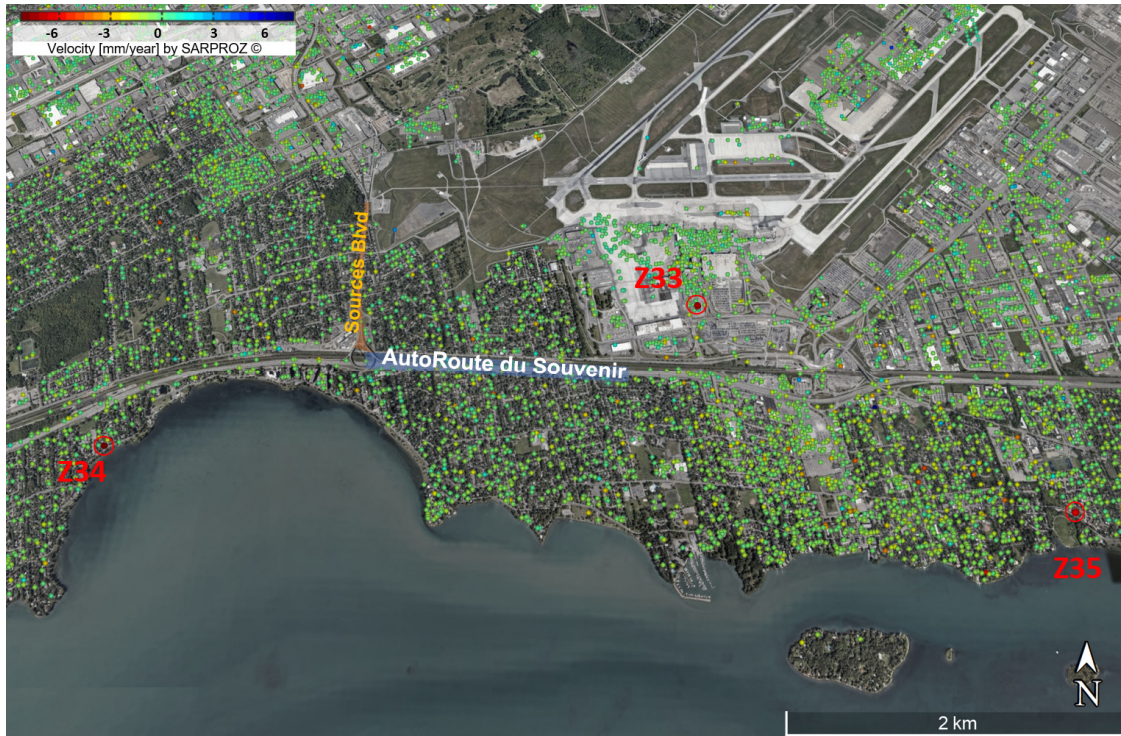


Figure 5.49 Mean velocity map for Lachine, Dorval and Pointe-Claire

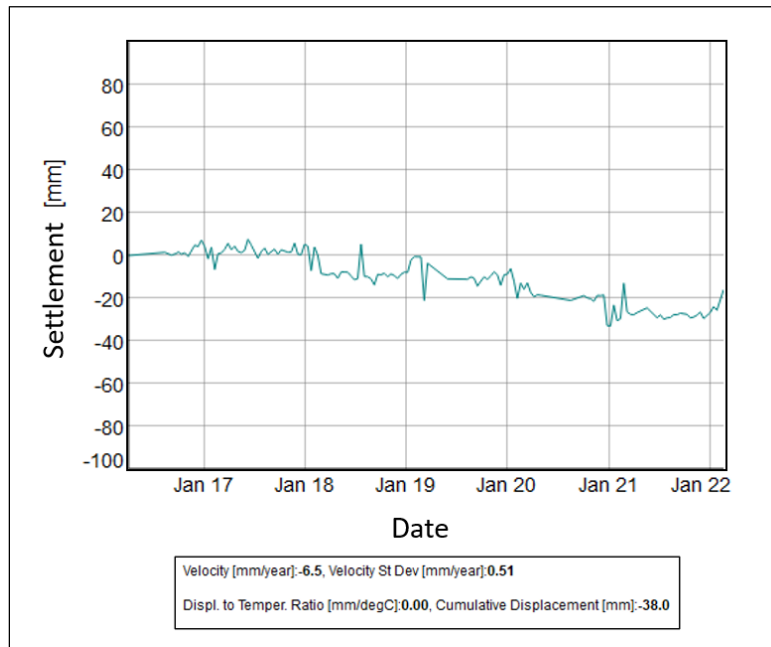


Figure 5.50 Settlement time series for PS pixel Z33 in Dorval area

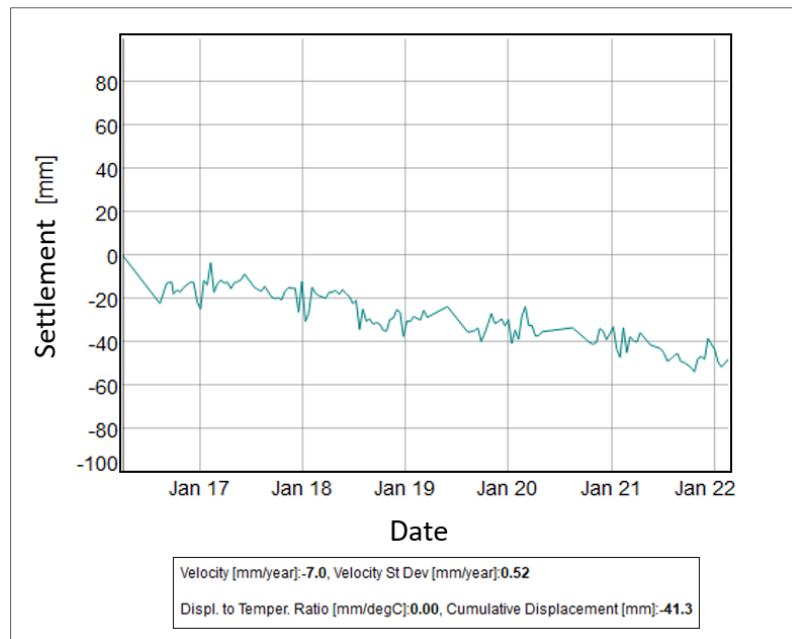


Figure 5.51 Settlement time series for PS pixel Z34 in Pointe-Claire

5.4.4.12 InSAR deformations in Dollard-des-Ormeaux and Pierrefonds-Roxboro

For Dollard-des-Ormeaux and Pierrefonds-Roxboro, settlements velocities of -6.3, -7.6, -5.5, -6.2, and -9.0 mm/year were obtained for PS pixels Z36, Z37, Z38, Z39, and Z40, respectively (Figure 5.52). The displacement time series associated with PS pixel Z38 is presented in figure 5.53. On the southern side of Dollard des Ormeaux, close to Autoroute 40, five PS pixels (Z41, Z42, Z43, Z44, and Z45) monitored settlement velocities of -6.2, -7.7, -6.4, -6.9, and -5.8 mm/year, respectively. The displacement time series associated with Z42 is presented in figure 5.54.

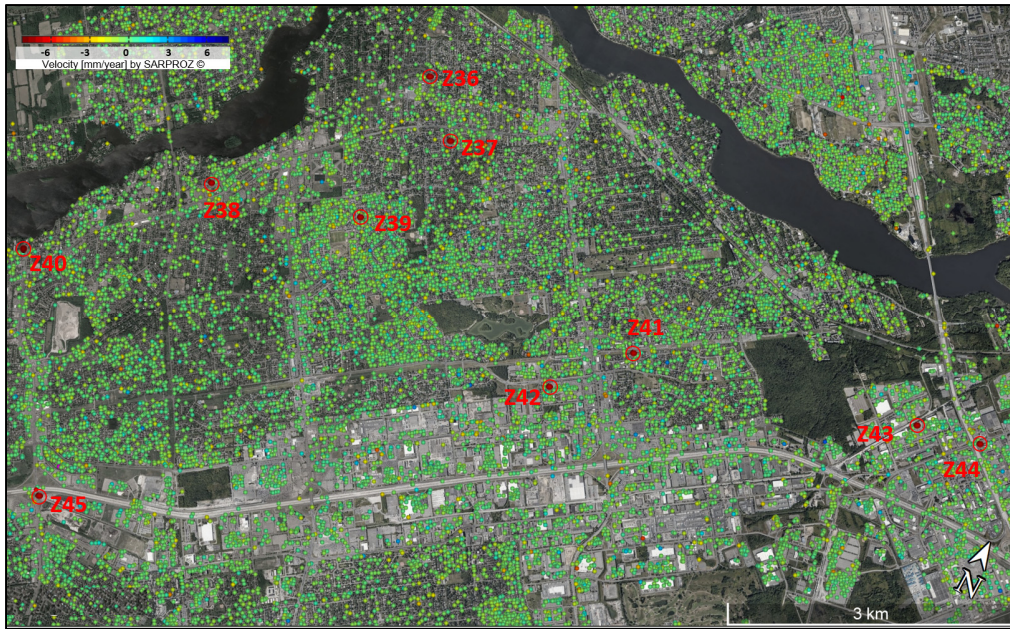


Figure 5.52 Mean velocity map of Dollard des Ormeaux

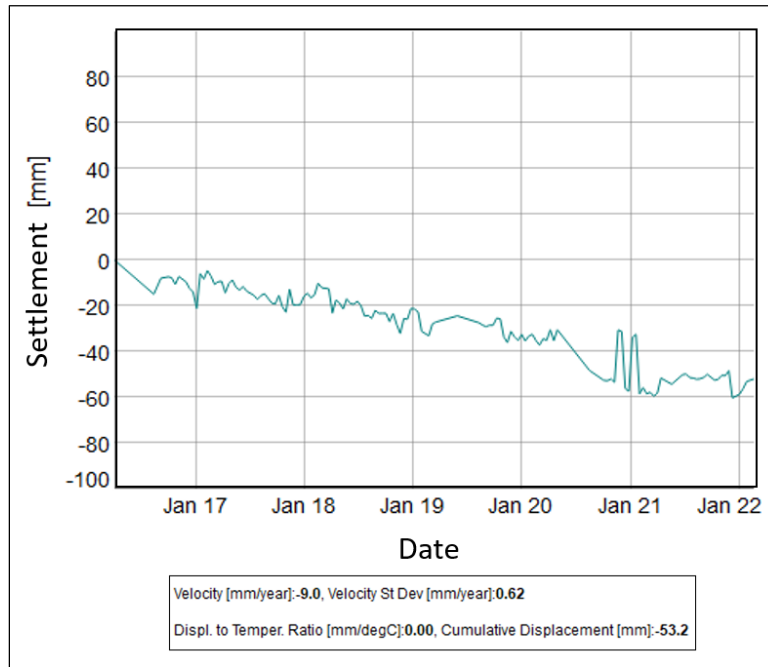


Figure 5.53 Settlement time series of PS pixel Z40 in Dollard des Ormeaux area of Montreal

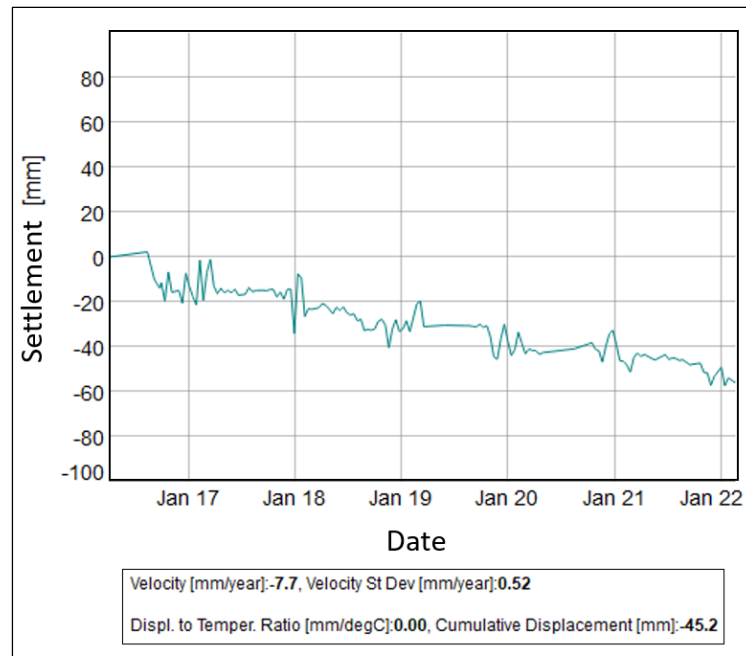


Figure 5.54 Settlement time series of PS pixel Z42 in Dollard des Ormeaux area of Montreal

5.4.4.13 InSAR deformations in Pierrefonds-Kirkland-Beaconsfield

PS pixels Z46, Z47, and Z48 could detect large settlements in the Kirkland and Beaconsfield areas in the western part of the Montreal Island (Figure 5.55). The settlement velocities for these three PS pixels were -6.9, -6.1, and -5.2 mm/year, respectively. The displacement time series associated with PS pixel Z46 is presented in figure 5.56.



Figure 5.55 Mean velocity map of Pierrefonds, Kirkland and Beaconsfield areas of Montreal

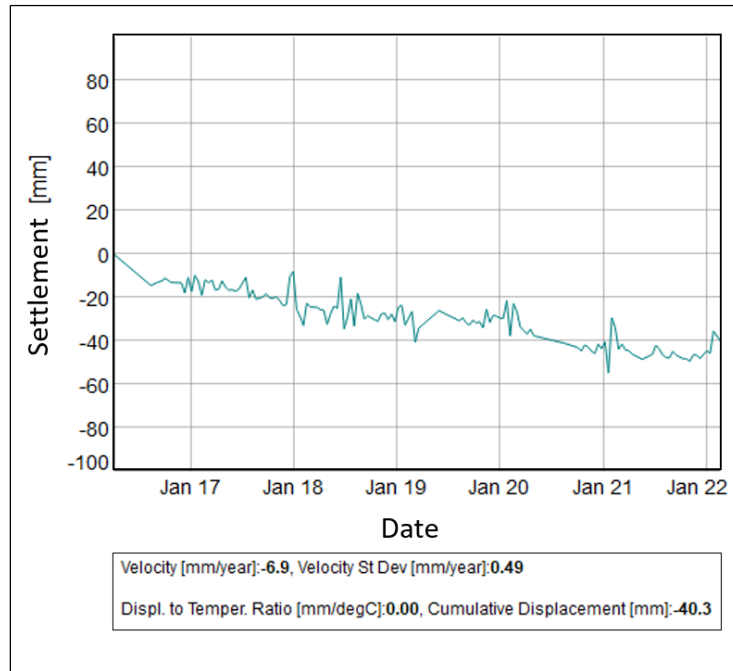


Figure 5.56 Settlement time series of PS pixel Z46 in Pierrefonds area of Montreal

5.4.5 Summary of InSAR monitoring of displacements in Montreal Island

In this section, the InSAR deformations for Montreal Island are summarized and discussed. Emphasis is put on the location of large settlements and its correlation with climate variables.

The majority of large settlements were monitored in the downtown area of Montreal. The density of PS pixels with large settlements was higher for the three target areas compared to other parts of Montreal Island. This is in part due to the downscaling that was applied in other areas and the resulting higher density of PS pixels in the target areas. The larger number of pixels with a significant settlement in the downtown area can also be explained in part by the quality of reflectors in urban areas compared to more suburban areas, for example near the western and eastern extremities of the island, where there is less vegetation.

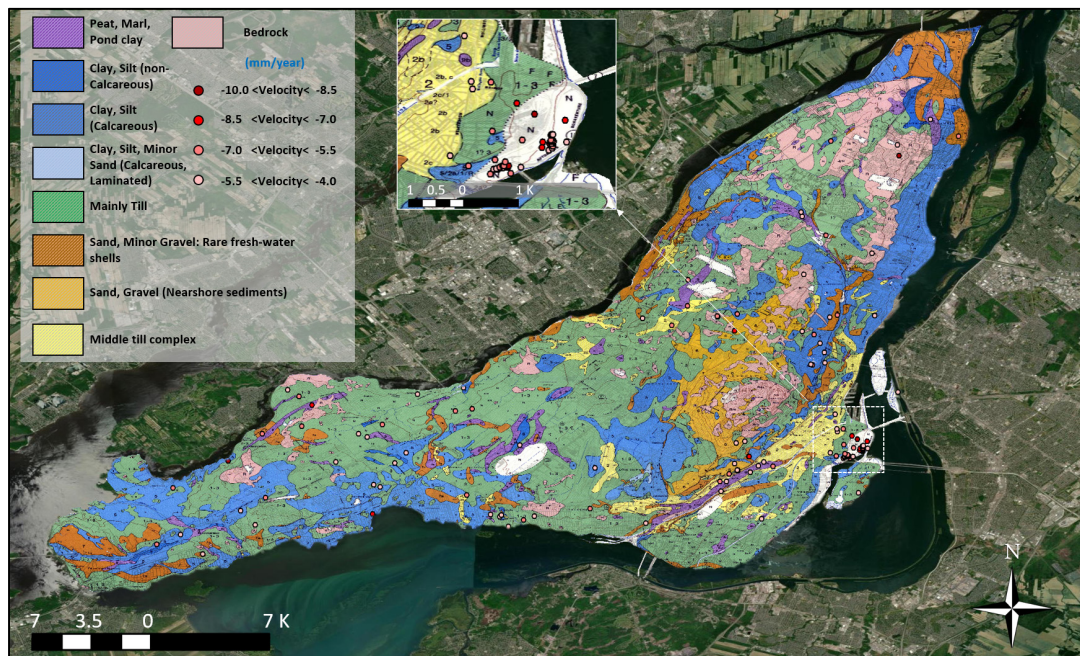


Figure 5.57 Large settlements on Montreal Island geolocated on the surficial geology map adapted from Prest & Hode-Keyser (1977)

Figure 5.57 presents the monitored large settlements on Montreal Island for the period between October 2016 and February 2022. The monitored settlements are geolocated on the surficial geology map of Montreal Island (Prest & Hode-Keyser, 1984). Among the observed settlements in known types of soils, more than 40 % of the large settlement were observed in areas with a layer of soil that contains silt, or clay (Table 5.2). 27 % of the large settlements were obtained in areas with layers of till. 22 % of the large settlements were monitored for areas covered with sand and gravel. These numbers show that the majority of settlements occurred in areas with high proportions of silt or clay. 4.9 % of the monitored large settlements were obtained over the bedrock.

It is worth mentioning that although figure 5.57 is a helpful map that can be used as a base of comparison, this map alone cannot explain entirely all the deformations that have been observed in the Montreal area. There is other information that must be taken into account in order to investigate the deformations in Montreal Island. Some of this information is briefly presented in the following paragraphs.

One of the pieces of evidence that is strongly correlated to the occurrence of large deformation is the existence of the thick layer of fill, often up to several meters, in some areas of the Montreal Island. This is not presented on the map, but it probably explains a significant number of large deformations. For instance, it could explain the settlement in the bedrock areas in Eastern Montreal. The geological studies in this area before the construction of the refinery facilities mentioned the presence of a layer of fill up to 0.9 m above the bedrock (SNC-Lavalin Group Inc, 2005).

The Pointe Saint-Charles area is particularly important with regards to fill. It is a landfill with several meters of domestic and industrial wastes. Domestic and industrial trash started to be deposited into this region between 1866 and 1966. A portion of the waterway between Pointe-Saint-Charles and Nun's Island was filled in during the 1930s and 1950s as a result of the construction of dikes and the expansion of the dump right into the river (SpacingMontreal, 2010). A landfill of up to 9 m of solid waste was also reported during

the subsurface investigation before the construction of the Samuel de Champlain Bridge (Diab et al., 2021). The presence of a thick layer of fill can clearly explain a large number of large settlements in this region.

Besides the existence of a layer of fill, there might be other reasons behind some of the large deformations that were monitored. The structure themselves can deform in some cases, irrespective of the geology like the Olympic Stadium roof's deformation which was linked with unexceptional wind speed condition (Lazzari et al., 2009). Slope stability issues can explain some vertical deformations. This could be the case for the large displacements that were monitored in Saint-Jacques Escarpment. The average slope of this area is more than 50 percent. It is also important to consider that geology is a 3D and not a 2D concept. There might be an underlying layer besides what we see on the map that be more prone to deformation. For instance, from the chronological aspect of view, units 6 and 7 (the sand layers) in the table below, were deposited after the marine clays. As a consequence, many areas with units 6 and 7 at the surface will have marine clays in their profile, below the sand layer. The map cannot show this layering. On the other hand, the numerical model that we presented earlier in this study has shown that long-term settlements can be associated with pore pressure changes in deeper, intact clay layers.

Table 5.2 Distribution of large settlements for each soil type

Soil Type	Number	Percent (%)
Unknown	32	
Mainly till	15	18.5
Sand-Gravel	6	7.4
Sand-Minor Gravel	16	19.8
Clay Silt	24	29.6
Peat, Marl, Pond clay	9	11.1
Bedrock	4	4.9
Middle till complex	7	8.6

There is a direct link between the rising temperatures which induce higher soil moisture deficit and the rate of settlement in the clayey soil (Silvestri et al., 1990; 1994). This relation was also investigated for the monitored InSAR results on Montreal Island. The average cumulative displacement of all PS pixels with a velocity larger than -7 (mm/year) was compared to the average atmospheric temperature and rain fall deficit (Figure 5.58). Rainfall deficit (RD) is the simplified form of the soil moisture deficit which is the accumulated subtractions of precipitation from evapotranspiration (Silvestri et al., 1990). It is worth mentioning that the rainfall deficit cannot be a negative value. In the fall season when precipitation exceeds the evapotranspiration, the accumulated value might become negative. The rainfall deficit, in this case, should be set as zero and the excess water is considered as runoff. It can be seen in figure 5.58 that the average of the monitored displacements shows a linear trend. This was expected as we used the linear PSI which is less sensitive to seasonal deformations. The maximum observed mean temperature has significantly risen in 2018 and remained steady after with slight variations in the following period. The rainfall deficits in 2016 and 2022 were the highest among the studied years which are associated with lower precipitation.

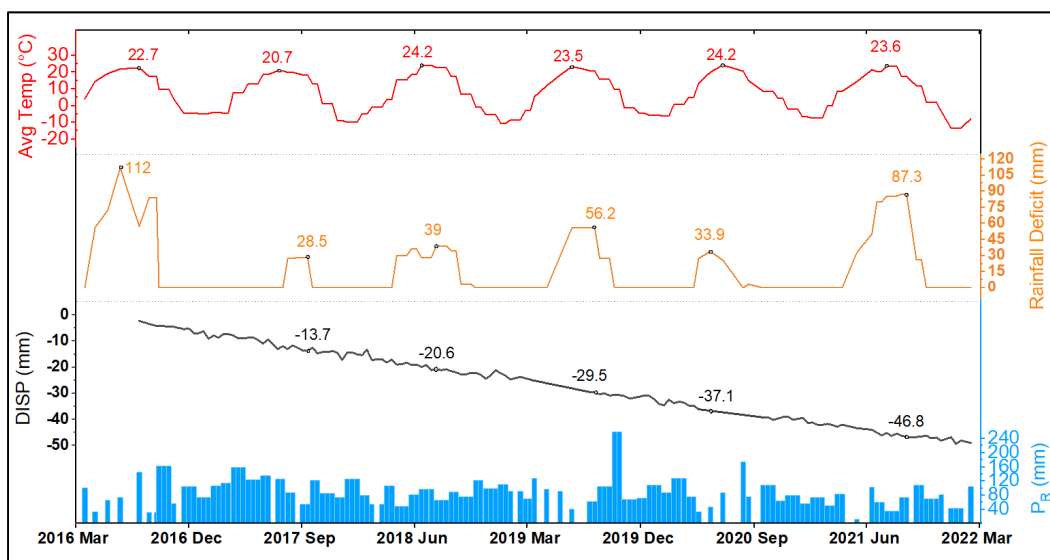


Figure 5.58 Average cumulative displacement of PS pixels with settlement velocity larger than -7 mm/year with respect to average monthly atmospheric temperature, rainfall deficit, and average monthly precipitation

Table 5.3 presents the mean yearly displacements for the PS pixels with a mean settlement velocity of more than 7 mm/year. The displacements are compared with mean temperature, total precipitation, total evapotranspiration, and mean & maximum rainfall deficits in summer from June to August. Due to the incompleteness of the settlement data, the years 2016 and 2022 were excluded from this comparison. Except for the year 2020, the settlement rate showed strong relation with the rainfall deficit rate. If we do not consider the year 2021, the integration with the r-squared value of 99 % will be obtained between the settlement rate and maximum rainfall deficit. This result is compatible with the earlier findings of Silvestri et al. (1990; 1994). It is worthy of note that all monitored PS pixels on Montreal Island were obtained with a linear approach and the non-linearity of the displacement was excluded from the analysis. The purpose of this investigation in this part of our study was not the non-linear motion of the ground and we aimed to estimate the final value of the settlement velocity in the long term over an extended area such as Montreal Island. As a result, the linear approach which is the only PSI method that provides a velocity map of the studied area was implemented.

Table 5.3 Average displacement of PS pixels with a velocity of more than -7 mm/year with respect to mean temperature, total precipitation, total evapotranspiration, mean and maximum rainfall deficits in summer from June to August

Year	Settlement avg (mm)	T avg (Jun-Aug) (°C)	Total PR (Jun-Aug) (mm)	Total ET (Jun-Aug) (mm)	RD max (mm)	RD avg (Jun-Aug) (mm)
2017	-10.8	19.8	348.0	359.2	28.5	9.2
2018	-19.4	21.9	245.8	255.0	39.0	34.6
2019	-28.3	20.9	193.6	249.8	56.2	47.3
2020	-36.2	21.6	307.4	256.5	33.9	19.9
2021	-44.4	21.9	200.1	252.4	87.3	72.0

CHAPITRE 6

CONCLUSION AND RECOMMENDATIONS

The first section of this chapter summarizes the results for each of the objectives that were mentioned in the introduction of the thesis. The second section of the chapter presents recommendations for further studies on numerical modelling and InSAR monitoring of settlements within shallow aquitards.

6.1 Conclusion

1-Evaluation of the van der Kamp & Gale (1983) approach for the replication of historical pore pressure time series within a shallow aquitard.

The first part of this study presents a detailed analysis of the pore pressure response of a shallow aquitard to seasonal changes in temperature and precipitation. Although due to the stronger presence of the transient flow in shallow aquitards accurate replication and analyzing of the pore pressure is harder to achieve, implementation of the coupled approach based on the van der Kamp & Gale (1983) theory could attend the agreeable results that closely fitted to the observed pore pressures.

2-Development of a hydrological–geotechnical model that can link the pore pressure changes to hydro-meteorological events based on the van der Kamp & Gale (1983) approach.

A new technique was proposed for calculating the total stress boundary condition at the top of a soil column to replicate the pore pressure record obtained in the field. Two methods were presented. The PS method does not consider the water balance and finds a total stress boundary condition that replicates the pore pressure record perfectly. The NWB method puts constraints on the total stress boundary condition based on a simple water balance equation. The methods were compared using data from the Sainte-Marthe study site. The

time series of observed and simulated water pressure were compared along with the seasonal and annual changes of precipitation, temperature, evapotranspiration, groundwater level and pore pressure in the bedrock. The results demonstrate the ability of the model and MATLAB interface to obtain the net water balance components. Both methods remarkably improved the accuracy of the pore pressure estimation in comparison to the BS scenario, zero runoff assumption. However, during spring freshet and other high-temperature periods, the reliability of the model decreases due to possible miscalculation of the water deficiency.

3-Development of a simplified numerical approach to replicate the settlements within shallow Champlain clay deposits.

In this research, the surface settlement of an experimental site in Sainte-Marthe was estimated using FEM simulations, monitored pore pressure changes and hydrological and meteorological parameters. The result from the FEM simulations showed a strong relationship between soil deformation, groundwater level and temperature changes. Moreover, a new simplified method for the evaluation of heave during cold weather was proposed. This simplified method can replicate the heave observed during freezing periods using a variable thermal expansion coefficient that takes into account the volume change associated with phase changes.

4-Investigation of the potential of the PSI technique for the determination of deformation rates in Champlain clays using openly available Sentinel-1 radar imagery

A PSI technique using the SARPROZ software was implemented for monitoring the displacement in the Vaudreuil-Soulanges region including the Sainte-Marthe test site. Both linear and non-linear PSI were examined in the target area. Their combined application could successfully produce velocity maps of the area along with the displacement time series of the available PS pixels within the region. However, it was harder to adjust the model and obtain highly coherent displacement time series in presence of dense vegetation.

5-Verifying the numerical simulation of settlement in Champlain clays using MT-InSAR measurement

The displacement values obtained from the FEM simulations were compared with linear and non-linear PSI measurements. A reasonable agreement was obtained using the non-linear approach for PSI. In this regard, it can be concluded that non-linear PSI could monitor the displacements more effectively by including the non-linear displacement. It should be mentioned that there are also other methods for validation of the displacement. High precision levelling and ground-based GPS techniques are the most common methods for validating displacement estimates. A GPS station close to the Sainte-Marthe experimental site and precise ground levelling was unfortunately not available. The similar downward trends of both estimates (PSI-DinSAR and FEM simulation), however, proved that both methods could be helpful tools for monitoring the soil displacement.

6-Long term measurement of settlement in Montreal area using PSI technique

The PSI technique with a linear approach was implemented for monitoring the displacement velocities all over Montreal Island with all the available Sentinel-1 SAR images before March 2022. As it was mentioned earlier, a velocity map can technically only be obtained by a linear approach. Furthermore, the linear method is considered a more reliable approach for monitoring the settlements in relatively longer periods, more than three years. The results highlighted a considerable number of spots with a significant settlement velocity on Montreal Island. In some areas, settlement velocities higher than -9 mm/year were detected by the PSI technique.

6.2 Recommendations

Recommendations are presented for the numerical modelling of pore pressure time series and settlements, and InSAR measurements.

1-Numerical modelling of the pore pressure time series within a shallow aquitard.

A comparison of the numerical modelling results with historical observations shows that the accuracy of the model decreases in certain periods. To address these errors, some inaccuracies should be improved in measurements or assessment of meteorological data and pore pressure records. For instance, a measurement of evapotranspiration would result in a more accurate water balance and improvements in the estimation of stress changes. In situ measurement of the infiltration of water can also help in the calibration of the model. Extending the observation period is another attractive idea that might provide better optimization and interpretation of pore pressure changes.

2-Numerical modelling of settlement in Champlain clays.

In FEM simulation, it is important to limit the sources of uncertainties in order to obtain more accurate estimations of displacement. In situ measurement of the mechanical properties within the Champlain clays layer is an example of method that can limit the uncertainties.

Measurement of water content at different depths of the study site can also be helpful in raising our awareness about the state of the soil regarding water depletion. It has been proved that there is a direct link among the settlement and water content changes in the clayey soils (Silvestri et al.,1990;1992).

Adding the other displacement measurement techniques always can increase our confidence about the accuracy of the numerical results. In situ measurement of the settlements at the

ground surface and deeper layers in the profile with any of the conventional methods such as GPS or extensometers will easily add another source of comparison that helps us to have a better judgment and calibrate the model.

Last, but not least, increasing the numbers of the study sites in different locations where there are Champlain clays deposits can improve the reliability of our numerical modelling.

3-InSAR monitoring of displacement.

For the future prospective, application of the latest development in DInSAR techniques or implementation of the SAR products with better resolution and shorter revisit time are suggested.

Installation of the ground reflector close to the study site by increasing the coherency can also improve the accuracy of estimations.

Application of the InSAR in combination with artificial intelligence such as machine learning, image processing or convolutional neural network can be used for spatial analysing of the relationship between the network of PS pixels displacement time series and hydrological and geotechnical parameters such as temperature, humidity, and soil moisture. These parameters can be obtained either by ground stations or remote sensing technology. For instance, SMAP satellite by NASA provides the soil moisture and freeze/thaw state of the surface soil all over the world.

Application of the InSAR in combination with satellite-based optical imagery can be also an interesting subject. There are useful information such as the classification of the target area in terms of the vegetation cover, urban structures, and water body that can be extracted from optical satellite products. Tracking changes in these areas in combination with settlement data can be helpful tool in understanding the reason behind or identifying the type of the settlement in the target area.

Governments can help the students and individual researchers who are dealing with InSAR studies by increasing the availability and affordability of highly accurate SAR images with shorter visit times such as Capella2, RADARSAT 2, SAR-Lupe, and COSMO-SkyMed. At the moment, highly accurate SAR images are either not available to the public or extremely costly.

APPENDIX I

BIOT 1940 THEORY

In this appendix, the general stress-strain equations of Biot (1940) are presented. Here, using the equilibrium condition of a stress field, Hooke's law from the theory of elasticity and considering a potential energy for the soil, we reach the following equations. These equations define the stress-strain relationship of the soil:

$$\varepsilon_x = \frac{\sigma_x}{E} - \frac{\nu}{E}(\sigma_y + \sigma_z) + \frac{u}{3B} \quad (7.1)$$

$$\varepsilon_y = \frac{\sigma_y}{E} - \frac{\nu}{E}(\sigma_x + \sigma_z) + \frac{u}{3B} \quad (7.2)$$

$$\varepsilon_z = \frac{\sigma_z}{E} - \frac{\nu}{E}(\sigma_x + \sigma_y) + \frac{u}{3B} \quad (7.3)$$

$$\gamma_x = \tau_x/G \quad (7.4)$$

$$\gamma_y = \tau_y/G \quad (7.5)$$

$$\gamma_z = \tau_z/G \quad (7.6)$$

$$\theta = \frac{1}{3H}(\sigma_x + \sigma_y + \sigma_z) + \frac{u}{R} \quad (7.7)$$

where ε and γ are the direct and shear strain components, σ and τ are the normal and shear stress components according to the x , y and z axes, and u is the water pressure increment. E , ν , and G define respectively the Young's modulus, Poisson's ratio and shear modulus. The variation in water content is represented by θ . It defines an increment of water volume per unit volume of soil. B and R are physical constants (Biot 1941). For a significant change in water

pressure, $(1/B)$ is a measure of soil compressibility while $(1/\dot{R})$ defines the change in water content.

It can be seen in the three components of the right-hand sides of equations 7.1-7.3 and 7.7 that the coefficient of the water pressure is $1/3B$. The isotropy of pore water pressure implies that water pressure cannot produce any shear stress. Thus, u is absent from equations 7.4-7.6.

Based on the Biot theory, four parameters (\dot{R} , B , E and ν) are enough to completely define the physical characteristics of an isotropic soil under equilibrium condition.

If we rewrite the equations mentioned above to show the stresses as a function of strains, we have:

$$\sigma_x = 2G \left(\epsilon_x + \frac{\nu \epsilon}{1 - 2\nu} \right) - \alpha u \quad (7.8)$$

$$\sigma_y = 2G \left(\epsilon_y + \frac{\nu \epsilon}{1 - 2\nu} \right) - \alpha u \quad (7.9)$$

$$\sigma_z = 2G \left(\epsilon_z + \frac{\nu \epsilon}{1 - 2\nu} \right) - \alpha u \quad (7.10)$$

$$\tau_x = G\gamma_x \quad (7.11)$$

$$\tau_y = G\gamma_y \quad (7.12)$$

$$\tau_z = G\gamma_z \quad (7.13)$$

where ϵ is a volumetric strain in three dimensions ($\epsilon_x + \epsilon_y + \epsilon_z$) and α is defined as:

$$\alpha = \frac{2(1 + \nu) G}{3(1 - 2\nu) B} \quad (7.14)$$

Moreover, the variation in water content is:

$$\theta = \alpha \epsilon + u/Q \quad (7.15)$$

$$\frac{1}{Q} = \frac{1}{R} - \frac{\alpha}{B} \quad (7.16)$$

where $1/Q$ defines the amount of water that can be taken by the soil under pressure for a constant soil volume.

Consider a volume of soil under a constant vertical load P_0 , with lateral confinement. If enough time is allowed for all the excess water to drain out of the soil (Biot, 1941), the axial strain in this state will be defined by the following equation:

$$e_z = \mathbf{a}u_0 \quad (7.17)$$

where coefficient \mathbf{a} is the final compressibility and is obtained with this equation:

$$\mathbf{a} = \frac{1 - 2\nu}{2G(1 - \nu)} \quad (7.18)$$

The coefficient for the state immediately after applying the load, before drainage, is defined in a different way. This coefficient is called the instantaneous compressibility (a_i). The variation in water content (θ) is zero in this state, as the excess soil water has no time to escape.

$$\mathbf{a}_i = \frac{\mathbf{a}}{1 + \alpha^2 \mathbf{a}Q} \quad (7.19)$$

APPENDIX II

VAN DER KAMP AND GALE (1983) THEORY

Based on Nur and Byedee (1971), the Biot's expression from appendix a can be written as:

$$\varepsilon_{ij} = \frac{1}{K_b} \left[\frac{(1 + \nu)}{3(1 - 2\nu)} \sigma_{ij} - \frac{\nu}{1 - 2\nu} \sigma_t \delta_{ij} - \frac{\alpha}{3} u \delta_{ij} \right] \quad (8.24)$$

where σ_t is the octahedral normal stress. It is obtained using the following equation:

$$\sigma_t = \frac{1}{3} (\sigma_{xx} + \sigma_{yy} + \sigma_{zz}) \quad (8.25)$$

$$\text{And } \alpha = 1 - \frac{K_b}{K_s} \quad (8.26)$$

where α is a parameter ranging from 0 to 1. K_b is the bulk modulus which is determined from the Young's modulus and the following equation:

$$K_b = \frac{E}{3(1 - 2\nu)} \quad (8.27)$$

In these equations, ν is Poisson's ratio, σ_{ij} is a component of stress, δ_{ij} is Kronecker delta, K_s is bulk modulus elasticity of solid, E is Young's modulus, and n is porosity. It is worthy of note that ε_{ij} , σ_{ij} , and u are just indicating the incremental variables. u is an incremental change in fluid pressure. The hydrostatic changes of pressure due to different elevation is not included in this parameter.

Based on the Biot (1941) and Nur and Bayerlee (1971) approaches, Rice and Cleary (1976) developed the following equations:

$$k_h \nabla^2 u = s' \frac{\partial}{\partial t} (u - \beta \sigma_t) \quad (8.28)$$

$$\nabla^2 \sigma_t = \lambda \nabla^2 u \quad (8.29)$$

where

$$s' = \rho g \left[\left(\frac{1}{K_b} - \frac{1}{k_s} \right) + n \left(\frac{1}{k_f} - \frac{1}{k_s} \right) \right] \quad (8.30)$$

$$\beta = \frac{1}{K_b} - \frac{1}{k_s} \left[\frac{1}{K_b} - \frac{1}{k_s} + n \left(\frac{1}{k_f} - \frac{1}{k_s} \right) \right]^{-1} \quad (8.31)$$

$$\lambda = \frac{2a(1-2\nu)}{3(1-\nu)} \quad (8.32)$$

where k_h is hydraulic conductivity, K_f is bulk modulus elasticity of water, β and λ are parameters ranging respectively from 0 to 1 and from 0 to 1.5, S' is three-dimensional storage coefficient, ρ is density of pore fluid and g is acceleration of gravity. These equations define how pore pressure reacts to stresses in a homogenous porous medium.

In the equations mentioned above, it is assumed that the single parameter of KS is enough for characterizing the deformation of the soil under different pore pressure and stresses. It is also assumed in equations 8.28, 8.29 that the shear stress does not contribute to any net dilatation. As a result, there is no term related to shear stress in these equations.

APPENDIX III

MATLAB CODE OF PORE PRESSURE TIME SERIES SIMULATION

```

%%%%%%%%%%%%%%%%%%%%%%%%%%%%%%%%%%%%%%%%%%%%%%%%%%%%%%%%%%%%%%%%%%%%%%%%%%%%%%
%
%      Runoff-Infiltration estimator script based on the hydraulic head records
%
%      By Amirhossein Shafaei and François Duhaime
%
%%%%%%%%%%%%%%%%%%%%%%%%%%%%%%%%%%%%%%%%%%%%%%%%%%%%%%%%%%%%%%%%%%%%%%%%%%%%%%

%*****
%* This program has three main parts; correction of the water table,      *%
%* correction of stress values by Perfect stress method (PS),and correction *%
%* of it by Net Water Balance (NWB) or Weighted method (WTD).           *%
%*****

%*****>>> START <<<<*****%

%%%%%%%%%%%%%%%%%%%%%%%%%%%%%%%%%%%%%%%%%%%%%%%%%%%%%%%%%%%%%%%%%%%%%%%%%%%%%%

%*****
%*   LOADING THE MODEL AND IMPORTING THE REQUIRED HYDROLOGICAL PARAMETERS   *%
%*                                                                           *%
%*****

clc
clear all

% Loading the Model and importing the initial values
model=mphload('interfaceSainte_marthe_phas2_13.mph');
ob = xlsread('p1B_observed.csv');% ob is total pressure head in depth of 12m
(sensor F1B)
st = xlsread('interfaceP_E
cumulative_STMRT_ORIGINAL_with_et_correction_interface.csv');% Setting the
initial st values
% (initial stress values) with stresses obtained by (P_ET*water density*g)
without considering any runoff
P1 = xlsread('interfacep1.csv');% total precipitation in each day
(snow+rain)
Pr = xlsread('interfacePr.csv');% total rain precipitation
Ps = xlsread('interfacePs.csv');% total snow precipitation
ET1= xlsread('interfaceET1.csv');%total evapotranspiration

```

```

% Number of the days in the simulation (should be entered by the user)
period=input('input the duration of simulation in days \n');

% Defining the stress interpolation function in COMSOL (indices start from 0
in COMSOL interpolation functions)
for i=1:period
    model.func('int1').setIndex('table', i, i-1, 0);
    model.func('int1').setIndex('table', st(i), i-1, 1);
end

% Importing and defining the water table interpolation function in COMSOL
wt = xlsread('watertable_notcrctd_interface_original.csv');
for i=1:period
    model.func('int3').setIndex('table', i, i-1, 0);
    model.func('int3').setIndex('table', wt(i), i-1, 1);
end

% Applying and saving the changes and running the simulation once
mphsave(model,'interfaceSainte_marthe_phas2_13.mph');
model.sol('sol1').runAll;

% Asking the user if he wants the script corrects the water table values and
% selecting the desired method for correction of the stress values
watertable=input(['do you want to correct the water table reference level
automatically based on' ...
    ' optimum result,\n if your answer is yes please type Y \n'], 's');
watermanual=input('do you want to correct the water table manually , if your
answer is yes please type Y \n ', 's');
perfectstress=input(['do you want to know the stress values which result in
perfect values of pore pressure in \n ' ...
    'simulation using Newton Raphson''s method , if your answer is yes
please type Y, answer no means you prefer to ' ...
    'correct the stress based on water balance method \n '], 's');
if perfectstress == 'Y' || perfectstress == 'y'
else
    %Asking the desired properties of the correction
    Weightedsteps=input(['do you want to use variable weighted steps
calibration method, if your answer is yes \n ' ...
        'please type Y,answering no means you prefer simple method of water
balance \n'], 's');
    m=input('input a desired period of correction');%m is the size of the
group,if it assigned as one it means that time

```

```

    % steps will be dealt one by one otherwise in each simulation the group
of m-timesteps will be considered for selecting the optimum stress
values(absolute sum
    %of the differences between the observed and simulated hydraulic head
for the selected time steps and m-1 time steps after)
    RA=input('what is your desired rate of change in runoff ratio between
two iterations, for example 0.1 or 0.2 \n ');
    correctionfactor=input(['do you like to use the correction factor for
expanding your available water range (P-ET-RU),\n choosing this option means
you want to ' ...
    'consider an error in your observed evapotranspiration and
precipitation, if your answer is yes please type Y \n '], 's');
    LE=input('input the remaining period in days until the changes affecting
the model, zero means the result of \n changes would affect instantly \n ');
    CFmax=1;

    %Desired ranges for expanding the water budget(minimum,maximum)
    if correctionfactor == 'Y' || correctionfactor == 'y'
        CFmax=input('input the maximum rate of correction factor, suggested
value is 1.3 ');
        CFmin=input(['input the minimum rate of correction factor, suggested
value is -0.3, be careful that although \n this factor is applied on your
precipitation but ' ...
        'the purpose of it is to consider more evapotranspiration \n ']);
    else

    %Desired maximum rate of the runoff to precipitation
    pm=input('input the maximum rate of runoff to precipitation \n ');

    end
    if Weightedsteps == 'Y' || Weightedsteps == 'y'
        jumper=0;
    else
        %If the size of group(m) is selected more than one, the jumper
method can be effective. By choosing this method, the script after correction
of m-time steps
        % jumps to m-1 time steps further, otherwise the next time step will
be corrected in next iteration
        jumper= input('do you want to use a jumper method, if your answer is
yes please type Y \n ', 's');
    end
end
end

```

```

**|*****detection or manually applying the offset in water table *****

%*****
%*          1.OPTIMUM water table offset          %*
%*          %*          %*
%*  This section using the Newton Raphson Methods finds the optimum offset %*
%*  value for the aplied water table on the model %*
%*          %*          %*
%*****

%Asking the desired level of offset for water table(manual correction)
if watermanual =='Y' || watermanual =='y'
    diffmanual=input('\n input the diver level difference for manual
correction ');
    wt=wt+diffmanual;

    %Applying a new water table interpolation function in COMSOL with the
desired offset
    for i=1:1:period
        model.func('int3').setIndex('table', i, i-1, 0);
        model.func('int3').setIndex('table', wt(i), i-1, 1);
    end

else

end
% Automatic method that
if watertable =='Y' || watertable =='y'
wtinitial=wt;

% Asking the desired accuracy of correction from the user
wtAccuracy=input('\n input the desired accuracy of correction, for example:
0.002 ');

% Runing the simulation once and extracting the results for hydraulic heads
(from the designated graph, pg5)
model.sol('sol1').runAll;
md = mphplot(model, 'pg5', 'createplot','off');
md1 = md{1}{1};
otp=md1.d;

```

```

% Applying 0.5X of initial values of water tables (The simulated hydraulic
heads regarding this water table values will then be used for the latter
graph)
for i=1:1:period
    wt1(i,:)=0.5*wt(i);
    model.func('int3').setIndex('table', i, i-1, 0);
    model.func('int3').setIndex('table', wt1(i), i-1, 1);
end

% Extracting the results for wt1=0.5wt
model.sol('sol1').runAll;
pd = mphplot(model, 'pg5', 'createplot','off');
pd1 = pd{1}{1};
otp1=pd1.d;

% Applying 3X of initial values of water tables (first guess)
for i=1:period
    wt2(i,:)=3*wt(i);
    model.func('int3').setIndex('table', i, i-1, 0);
    model.func('int3').setIndex('table', wt2(i), i-1, 1);
end

% Extracting the results for the first guess (wt2=3wt)
model.sol('sol1').runAll;
sd = mphplot(model, 'pg5', 'createplot','off');
sd1 = sd{1}{1};
otp2=sd1.d;

% Returning the water table values to its original ones
for i=1:period
    model.func('int3').setIndex('table', i, i-1, 0);
    model.func('int3').setIndex('table', wt(i), i-1, 1);
end

model.sol('sol1').runAll;

%*****
%*                                     WATER TABLE LAG_TIME GRAPH                               %*
%*                                                                              %*
%* Depending on the domain properties, it might take some time steps to see the %*
%* effectiveness of the changes in water table on hydraulic head values. the %*
%* following plot is for helping the user to detect the lag time (wtload) %*
%*****

```

```

totalwatertables(:,1)=(1:(period+1));
totalwatertables(:,2)=otp1;
totalwatertables(:,3)=otp;
totalwatertables(:,4)=otp2;

plot(totalwatertables(:,1),totalwatertables(:,2),totalwatertables(:,1),totalw
atertables(:,3),totalwatertables(:,1),totalwatertables(:,4));

    % User should based on a former graph decides about the lag times
    wtload=input('\n input the water table fluctuations loading time in days
    ');

    % This loop correct the water table values using Newton Raphson method
    for i=1:(period-wtload)

        % Displaying the number of the iteration and the differences between
        simulated and observed hydraulic heads
        disp ("i is") ;
        disp (i);
        dd(i)=(abs(otp(i+wtload)-ob(i+wtload)))/ob(i+wtload);
        disp( "diff is");
        disp (dd(i));

        % wtaccuracy is a controller for accuracy of the optimization
        while (abs(otp(i+wtload)-ob(i+wtload)))/ob(i+wtload)>wtAccuracy

            % Displaying the differences between observed and simulated hydraulic
            heads
            dd(i)=(abs(otp(i+wtload)-ob(i+wtload)))/ob(i+wtload);
            disp( "diff is");
            disp (dd(i));

            % Applying a new water table offset based on last iteration result
            mediator=wt(i);
            wt(i)=wt(i)+(((ob(i+wtload)-otp(i+wtload)))*((wt2(i)-
            wt(i))/(otp2(i+wtload)-otp(i+wtload))));
            wt2(i)=mediator;
            otp2(i+wtload)=otp(i+wtload);
            model.func('int3').setIndex('table', i, i-1, 0);
            model.func('int3').setIndex('table', wt(i), i-1, 1);

            % Running the model with new values extracting the model's outputs for
            hydraulic head
            model.sol('sol1').runAll;

```

```

md = mphplot(model, 'pg5', 'createplot','off');
md1 = md{1}{1};
otp=md1.d;

% Displaying the differences between observed and simulated hydraulic
heads
dd(i)=(abs(otp(i+wtload)-ob(i+wtload)))/ob(i+wtload);
disp( "diff is");
disp (dd(i));

end

end

%Saving the model
mphsave(model,'interfaceSainte_marthe_phas2_13.mph');

%calculating the optimum offset of water table based on Newton Raphson
optimization
leveldiff=mean(wt)-mean(wtinitial);
wt=wtinitial+leveldiff;

%Displaying the optimum offset value for water table
xdis=sprintf('water table offset (leveldiff) will be
%s',num2str(leveldiff));
display(xdis);

%Applying the offset on Model's water table values
for i=1:1:period
    model.func('int3').setIndex('table', i, i-1, 0);
    model.func('int3').setIndex('table', wt(i), i-1, 1);
end

%saving the model
mphsave(model,'interfaceSainte_marthe_phas2_13.mph');

else

```

```
end
```

```
*****|*****perfect stress method*****

%*****%
%*                2.PS Method                %*
%*                %*
%* This section using the Newton Raphson Method corrects the stress %*
%* boundary condition %*
%* %*
%*****%

% Demanding the desired accuracy of the optimization for stress values
if perfectstress == 'Y' || perfectstress == 'y'
DIFF_PSTS=input(' \n input your desired value for accuracy of calibration,
suggested number is 0.001 ');

% Applying the initial stress values as a interpolation function of COMSOL
for i=1:period
    model.func('int1').setIndex('table', i, i-1, 0);
    model.func('int1').setIndex('table', st(i), i-1, 1);
end

% Running the model
model.sol('sol1').runAll;
md = mphplot(model, 'pg5', 'createplot','off');
md1 = md{1}{1};
otp=md1.d;

% Notice: It is worthy of note that it is not possible to calculate all the
initial guesses of stress values
% at one run like water table optimization as correcting the stresses in
former timesteps affects the rates of
% changes in simulated hydraulic heads in other time steps.

% Newton Raphson's optimization loop for stress values

for i=1:period

    % Displaying the number of the iteration
    disp( "(number of iteration in perfect stress method is:");
    disp (i);

    % Applying the 4x of the stress values for initial guess of Newton
    Raphson
```

```

st2(i,:)=4*st(i);
model.func('int1').setIndex('table', i, i-1, 0);
model.func('int1').setIndex('table', st2(i), i-1, 1);

% Extraction of model's result for initial guess
model.sol('sol1').runAll;
sd = mphplot(model, 'pg5', 'createplot','off');
sd1 = sd{1}{1};
otp2(i+1)=sd1.d(i+1);
model.func('int1').setIndex('table', i, i-1, 0);
model.func('int1').setIndex('table', st(i), i-1, 1);

% limiting the iterations of correction to 25 times
for cont=1:25

% Newton Raphson loop
while (abs(otp(i+1)-ob(i))/ob(i))>DIFF_PSTS
    cont=cont+1% Counter

    % Displaying the difference between the observed and simulated
hydraulic heads
    diffst(i)=abs(otp(i+1)-ob(i))/ob(i);
    disp( "(ndiff stress is:");
    disp (diffst(i));

    % Calculation of new values based on last iteration
    mediator=st(i);
    corrector=((ob(i)-otp(i+1))*((st2(i)-st(i))/(otp2(i+1)-otp(i+1))));
    st(i)=st(i)+corrector;
    st2(i)=mediator;
    otp2(i+1)=otp(i+1);

    % Applying the new stress value and running the model
    model.func('int1').setIndex('table', i, i-1, 0);
    model.func('int1').setIndex('table', st(i), i-1, 1);
    model.sol('sol1').runAll;

    % Extracting the model's results for hydraulic head
    md = mphplot(model, 'pg5', 'createplot','off');
    md1 = md{1}{1};
    otp=md1.d;

    % Displaying the difference between the observed and simulated
hydraulic heads
    disp( "(ndiff stress is:");

```

```

        diffst(i)=abs(otp(i+1)-ob(i))/ob(i);
        disp( "(ndiff stress is:");
        disp (diffst(i));

    end
end

% saving the model
mphsave(model, 'interfaceSainte_marthe_phas2_13.mph');

else

*****Wieghted and Net Water Balance methods (WTD & NWB)*****

%*****%
%*          3. WTD and NWB methods          %*
%*                                          %*
%* This section contains the WTD and NWB methods for optimization of the %*
%* stress boundary condition                %*
%*                                          %*
%*****%

m=m-1; % To just have the period with m-time steps length

% More information about jumper method in line 80
if jumper == 'Y' || jumper == 'y'
    control=m;
else
    control=0;
end

% Asking the user if he wants to use the WTD methods
if Weightedsteps == 'Y' || Weightedsteps == 'y'

% Running the model with the initial stress values and extracting the model
results for hydraulic heads
model.sol('sol1').runAll;
md = mphplot(model, 'pg5', 'createplot','off');
md1 = md{1}{1};

```

```

otp=md1.d;

% Calculation of Alpha matrix
for i=1:period

    if i>2
        for b=1:i-1
            stt(b)=st(b);% Returning the former time step's stress value
to its' initial ones
            % and removing the applied change caused by the last
iteration
            model.func('int1').setIndex('table', b, b-1, 0);
            model.func('int1').setIndex('table', stt(b), b-1, 1);
        end
    end

    % Modified stress vector (remove 1 kPa NB: making the stress value
1kPa more negative-from the ith to the last one)
    for c=i:period
        stt(c)=st(c)-1000;
        model.func('int1').setIndex('table', c, c-1, 0);
        model.func('int1').setIndex('table', stt(c), c-1, 1);
    end

%*****
%*                               Calculation of Alpha matrix                               %*
%*                               %*                               %*
%* Alfa matrix contains a weight of each time step regarding the changes           %*
%* in stress boundary condition (more information in the paper)                     %*
%*                               %*                               %*
%*****|*****

% Running the model and extraction of the results for hydraulic head
model.sol('sol1').runAll;
md = mphplot(model, 'pg5', 'createplot','off');
md1 = md{1}{1};
otpp2=md1.d;

for j=i+1:period+1
    otpdiff=abs(otpp2-otp);
    sumalfa(i)=sum(otppdiff(i+1:period+1));%Summation of the
differences between observed and simulated hydraulic heads
    Alfa(i,j)=(otpp2(j)-otp(j))/1000;% This matrix just going to be
used for interoperation of the pore pressure (for the

```

```

        % user information-this matrix cannot be used in further
        calculation as it contains negative values)
        ZAlfa(i,j)=abs(otpp2(j)-otp(j))/1000;% This is the same as alpha
        matrix but all values are the absolute of differences as a division of 1000
        (1KP)
        ZAlfaweight(i,j)=abs(otpp2(j)-otp(j))/sumalfa(i);% In order to
        have the changes as a portion of the sum of the changes in the whole period
        and also to
        % avoid very small values
    end

end

%Removing very small and negative values from the matrix (Using this
matrix avoids further unnecessary calculation
ZAlfaweight_corrected=ZAlfaweight;
for i=1:period
    for j=1:period+1
        if ZAlfaweight_corrected(i,j)<0.001
            ZAlfaweight_corrected(i,j)=0;
        end
    end
end
end

% This matrix is going to be filled with alpha constant in next steps
alfagroup=zeros(period,period);

% parameters related to first iteration are set separately and then the
% rest of the data will be set using the following loop

%*****%
%*          CALCULATION OF THE WATER BUDGET          *%
%*                                                    *%
%* There are different parameters that should be calculated *%
%* here to define the water budget in each time step *%
%*                                                    *%
%*****%

% Defining the net water balance's parameters for the first-time step (as
we do not have any earlier step, the following parameters are always zero)
st(1)=0;

```

```

Psc(1)=0;
Prc(1)=0;
model.func('int1').setIndex('table', 1, 0, 0);
model.func('int1').setIndex('table', st(1), 0, 1);

%this matrix will be used later
j=zeros(period+1,1000);

% Defining the net water balance's parameters for the second and further
time steps
for i=2:(control+1):(period-1) % If we designates a m value more than one,
we always need a group of m data after our target time steps in order to be
able
    % to compare the model result and observed data, for the time steps
after that,after period-m-1, the biggest possible size of the group is going
to be applied.

    % Correction of m value (size of the group-this correction is essential
for successful run of model)
    if i> period-m-1
        m=m-(period-i-1);
    end

    % Displaying the main iteration
    disp('main round : _____');
    disp(i);

    % if we want to manually expand the water budget by some percent in
each iteration (CFmin,CFmax-Lines 67-71)
    if correctionfactor =='Y' || correctionfactor =='y'
        minn=CFmin;
    else
        minn=(1-pm);
    end
    max=1*CFmax;
    jj=(minn:RA:max);% This defines the range of changes in water budget
(jj is (1-Runoff) which ranges from 1-Rmax to 1)
    n=numel(jj);
    for t=1:n % Making a two dimensional matrix to have ratios in all
iteration and avoid overwriting
        j(i,t)=jj(t);
    end

    % This loop finds the optimum stress values in each time step by
applying the different runoff ratios

```

```

for k=1:n

    % N.B: To avoid non positive integer in array indices we
    calculate the first and second time steps separately. It is because we
    always have to dealt with
    % parameters that are connected to the one iteration before and
    as changing a runoff in earlier iteration affect the current stress, we have
    to work with
    % parameters in two steps before.

    if i==2
        % Defining the hydrological parameters, more information about
        % these equations in the thesis
        Awr(i-1)=Pr(i-1)+Ps(i-1)+Psc(i-1);% Available water for runoff
        if Awr(i-1)==0
            Rs(i-1)=0;% Runoff from snow
            Rr(i-1)=0;% Runoff from rain
            Awet(i-1)=0; % Available water for evapotranspiration
            ETr(i-1)=0; % Evapotranspiration from rain water
            ETs(i-1)=0; % Evapotranspiration from snow water
        else
            Rs(i-1)=(1-j(i,k))*(Ps(i-1)+Psc(i-1)) ;
            Rr(i-1)=(1-j(i,k))* Pr(i-1);
            Awet(i-1)=(j(i,k)*Awr(i-1))+Prc(i-1);
            if Awet(i-1)<0
                Awet(i-1)=0;
            end
            if Awet(i-1)==0
                ETr(i-1)=ET1(i-1);
                ETs(i-1)=0;
            else
                ETr(i-1)= ET1(i-1)*(((Pr(i-1)*j(i,k))+Prc(i-1))/Awet(i-
1));
                ETs(i-1)= ET1(i-1)*(((Ps(i-1)+Psc(i-1))*j(i,k))/Awet(i-
1));
            end
        end
        Psc(i)=Psc(i-1)+Ps(i-1)-ETs(i-1)-Rs(i-1);% Stored snow
        if Psc(i)<0 % The accumulated snow from earlier steps cannot be
a negative value
            Psc(i)=0;
        end
        Prc(i)=Prc(i-1)+Pr(i-1)-ETr(i-1)-Rr(i-1); %Stored Rain
        sts(i,k)=(Prc(i)+Psc(i))*-1.003*9.806; %defining the stress
value and applying it on the model
    end
end

```

```

model.func('int1').setIndex('table', i, i-1, 0);
model.func('int1').setIndex('table', sts(i,k), i-1, 1);

else % Defining the hydrological parameters for i=3 and more (in a
group optimization, it set only the first time step in the group, the rest
will be

% modified by the latter for loop (line 561))
Psc(i-1)=Psc(i-2)+Ps(i-2)-ETs(i-2)-Rs(i-2);
if Psc(i-1)<0
    Psc(i-1)=0;
end
Prc(i-1)=Prc(i-2)+Pr(i-2)-ETr(i-2)-Rr(i-2);
Awr(i-1)=Pr(i-1)+Ps(i-1)+Psc(i-1);
if Awr(i-1)==0
    Rs(i-1)=0;
    Rr(i-1)=0;
    Awet(i-1)=Prc(i-1);
    if Awet(i-1)<0
        Awet(i-1)=0;
    end
    if Awet(i-1)==0
        ETr(i-1)=ET1(i-1);
        ETs(i-1)=0;
    else
        ETr(i-1)= ET1(i-1)*(((Pr(i-1)*j(i,k))+Prc(i-1))/Awet(i-
1));
        ETs(i-1)= ET1(i-1)*(((Ps(i-1)+Psc(i-1))*j(i,k))/Awet(i-
1));

    end
else
    Rs(i-1)=(1-j(i,k))*(Ps(i-1)+Psc(i-1));
    Rr(i-1)=(1-j(i,k))* Pr(i-1);
    Awet(i-1)=(j(i,k)*Awr(i-1))+Prc(i-1);
    if Awet(i-1)<0
        Awet(i-1)=0;
    end
    if Awet(i-1)==0
        ETr(i-1)=ET1(i-1);
        ETs(i-1)=0;
    else
        ETr(i-1)= ET1(i-1)*(((Pr(i-1)*j(i,k))+Prc(i-1))/Awet(i-
1));
        ETs(i-1)= ET1(i-1)*(((Ps(i-1)+Psc(i-1))*j(i,k))/Awet(i-
1));

    end
end

```

```

end
Prc(i)=Prc(i-1)+Pr(i-1)-ETr(i-1)-Rr(i-1);
Psc(i)=Psc(i-1)+Ps(i-1)-ETs(i-1)-Rs(i-1);
if Psc(i)<0
    Psc(i-1)=0;
end
sts(i,k)=(Prc(i)+Psc(i))*-1.003*9.806;% calculation the stress
value and applying it on the model
model.func('int1').setIndex('table', i, i-1, 0);
model.func('int1').setIndex('table', sts(i,k), i-1, 1);

end

if m>0 % Setting the parameters for the other members of the group
,other than first one.
    % N.B: it is the worthy of note only when we want to do
the optmization for a group of m-time steps
    % the following calculation will be necessary and
effective.

    %calculation of hydrological parameters
for p=i+1:(i+m)
    Psc(p-1)=Psc(p-2)+Ps(p-2)-ETs(p-2)-Rs(p-2);
    if Psc(p-1)<0
        Psc(p-1)=0;
    end
    Prc(p-1)=Prc(p-2)+Pr(p-2)-ETr(p-2)-Rr(p-2);
    Awr(p-1)=Pr(p-1)+Ps(p-1)+Psc(p-1);
    if Awr(p-1)==0
        Rs(p-1)=0;
        Rr(p-1)=0;
        Awet(p-1)=Prc(p-1);
        if Awet(p-1)<0
            Awet(p-1)=0;
        end
        if Awet(p-1)==0
            ETr(p-1)=ET1(p-1);
            ETs(p-1)=0;
        else
            ETr(p-1)= ET1(p-1)*(((Pr(p-1)*j(i,k))+Prc(p-
1))/Awet(p-1));
            ETs(p-1)= ET1(p-1)*(((Ps(p-1)+Psc(p-
1))*j(i,k))/Awet(p-1));
        end
    else

```

```

Rs(p-1)=(1-j(i,k))*(Ps(p-1)+Psc(p-1)) ;
Rr(p-1)=(1-j(i,k))*Pr(p-1);
Awet(p-1)=(j(i,k)*Awr(p-1))+Prc(p-1);
if Awet(p-1)<0
    Awet(p-1)=0;
end
if Awet(p-1)==0
    ETr(p-1)=ET1(p-1);
    ETs(p-1)=0;
else
    ETr(p-1)= ET1(p-1)*(((Pr(p-1)*j(i,k))+Prc(p-
1))/Awet(p-1));
    ETs(p-1)= ET1(p-1)*(((Ps(p-1)+Psc(p-
1))*j(i,k))/Awet(p-1));
end
end
Prc(p)=Prc(p-1)+Pr(p-1)-ETr(p-1)-Rr(p-1);
Psc(p)=Psc(p-1)+Ps(p-1)-ETs(p-1)-Rs(p-1);
if Psc(p)<0
    Psc(p)=0;
end
% applying the new stress
sts(p,k)=(Prc(p)+Psc(p))*-1.003*9.806;
model.func('int1').setIndex('table', p, p-1, 0);
model.func('int1').setIndex('table', sts(p,k), p-1, 1);

end
end
% Running the model for applied changes and extraction of results
model.sol('sol1').runAll;
md = mphplot(model, 'pg5', 'createplot','off');
md1 = md{1}{1};
otp=md1.d;

% The optimum runoff ratios will be defined
% separately for WTD and NWB methods using the following if
% condition

% Defining the differences for WTD method
% N.B: WTD method applies the alpha-matrix on the absolute
differences of model results and observed values of hydraulic head
if Weightedsteps == 'Y' || Weightedsteps == 'y'

for II=i+1:period+1

```

```

        % defining the another matrix based on alpha matrix for
group optimization (for m=1, the ratios will be the same as the ones in the
alpha matrix)
        aa(II)=sum(ZAlfaweight_corrected(i:i+m,II))/(m+1); % N.B:
we did m=m-1 before for the correcting the length of simulation period. so,
it should be divided by m+1
        end
        for jj=1:period+1
            alfagroup(i,jj)=aa(jj);% This parameter is just defined for
checking by the user
        end
        for TT=1:period %correction of the matrix dimensions (aa matrix
has one extra column due to one day lag in COMSOL model)
            cc(TT)=aa(TT+1);
        end
        % Simple difference of simulated and observed hydraulic head
        for II=i:period
            diffot(II)=abs(otp(II+1)-ob(II));
        end

        % Applying the Alpha matrix on the differences
        diff(k)=cc*diffot';

        aa=aa*0; % To avoid mistakes regarding the values in aa(II)
matrix remained from the earlier iterations , we set all the matrix members
        % as zero after the optimization.

    else % Defining the differences for none weighted method (NWB)

        % N.B: The changing in stress in (i)th day will result in the
same day but there is always one day offset between
        % output of model resulted from the graph (as it started
fromzero in COMSOL) and the result that we are looking for.
        % Therefore, in day by day correction, the comparison should be
made for a day i+1 in outputs.

        % Simple difference of the simulated and observed hydraulic
heads
        for ff=i+LE:i+LE+m %(LE defines the lag time that can be
adjusted by the user (line 64))
            diffo(ff)=abs(otp(ff+1)-ob(ff));
        end
        diff(k)=sum(diffo);
    end
end

```

```

        end
    end

    % Finding the minimum difference for selection the optimum runoff ratio
    [M,I]=min(diff(1:n));
    Istore(i)=I;% I is the K value (loop iteration number) in the former
loop which resulted in optimum value of stress

    % Setting the optimum values of hydrological parameters by designation
the optimum runoff ratios (calculated by former for
    % loop (line474))
    % N.B: we used if condition like the former loop to avoid none positive
integers
    if i>1
        for i=i:i+control
            if i==2 % Setting the hydrological parameters for the second
time step

                Awr(i-1)=Pr(i-1)+Ps(i-1)+Psc(i-1);
                if Awr(i-1)==0
                    Rs(i-1)=0;
                    Rr(i-1)=0;
                    Awet(i-1)=0;
                    ETr(i-1)=0;
                    ETs(i-1)=0;
                else
                    Rs(i-1)=(1-j(i,I))*(Ps(i-1)+Psc(i-1)) ;
                    Rr(i-1)=(1-j(i,I))* Pr(i-1);
                    Awet(i-1)=(j(i,I)*Awr(i-1))+Prc(i-1);
                    if Awet(i-1)<0
                        Awet(i-1)=0;
                    end
                    if Awet(i-1)==0
                        ETr(i-1)=ET1(i-1);
                        ETs(i-1)=0;
                    else
                        ETr(i-1)= ET1(i-1)*(((Pr(i-1)*j(i,I))+Prc(i-
1))/Awet(i-1));
                        ETs(i-1)= ET1(i-1)*(((Ps(i-1)+Psc(i-
1))*j(i,I))/Awet(i-1));
                    end
                end
                Psc(i)=Psc(i-1)+Ps(i-1)-ETs(i-1)-Rs(i-1);
                if Psc(i)<0
                    Psc(i)=0;

```

```

end
Prc(i)=Prc(i-1)+Pr(i-1)-ETr(i-1)-Rr(i-1);
sts(i,I)=(Prc(i)+Psc(i))*-1.003*9.806;
st(i)=sts(i,I);
model.func('int1').setIndex('table', i, i-1, 0);
model.func('int1').setIndex('table', st(i), i-1, 1);

else %setting the hydrological parameters for the time steps
other than i=2
Psc(i-1)=Psc(i-2)+Ps(i-2)-ETs(i-2)-Rs(i-2);
if Psc(i-1)<0
    Psc(i-1)=0;
end
Prc(i-1)=Prc(i-2)+Pr(i-2)-ETr(i-2)-Rr(i-2);
Awr(i-1)=Pr(i-1)+Ps(i-1)+Psc(i-1);
if Awr(i-1)==0
    Rs(i-1)=0;
    Rr(i-1)=0;
    Awet(i-1)=Prc(i-1);
    if Awet(i-1)<0
        Awet(i-1)=0;
    end
    if Awet(i-1)==0
        ETr(i-1)=ET1(i-1);
        ETs(i-1)=0;
    else
        ETr(i-1)= ET1(i-1)*(((Pr(i-1)*j(i,I))+Prc(i-
1))/Awet(i-1));
        ETs(i-1)= ET1(i-1)*(((Ps(i-1)+Psc(i-
1))*j(i,I))/Awet(i-1));
    end
else
    Rs(i-1)=(1-j(i,I))*(Ps(i-1)+Psc(i-1)) ;
    Rr(i-1)=(1-j(i,I))* Pr(i-1);

    Awet(i-1)=(j(i,I)*Awr(i-1))+Prc(i-1);
    if Awet(i-1)<0
        Awet(i-1)=0;
    end
    if Awet(i-1)==0
        ETr(i-1)=ET1(i-1);
        ETs(i-1)=0;
    else
        ETr(i-1)= ET1(i-1)*(((Pr(i-1)*j(i,I))+Prc(i-
1))/Awet(i-1));

```

```

                                ETs(i-1)= ET1(i-1)*(((Ps(i-1)+Psc(i-
1))*j(i,I))/Awet(i-1));
                                end
                                end

                                Prc(i)=Prc(i-1)+Pr(i-1)-ETr(i-1)-Rr(i-1);
                                Psc(i)=Psc(i-1)+Ps(i-1)-ETs(i-1)-Rs(i-1);
                                if Psc(i)<0
                                    Psc(i)=0;
                                end
                                sts(i,I)=(Prc(i)+Psc(i))*-1.003*9.806;% Defining the
optimimum stress value and apply it on the COMSOL model
                                st(i)=sts(i,I);
                                model.func('int1').setIndex('table', i, i-1, 0);
                                model.func('int1').setIndex('table', st(i), i-1, 1);

                                end

                                % Calculation of runoff and infiltration
                                Ru(i-1,:)=(1-j(i,I))*(Pr(i-1)+Psc(i-1)+Ps(i-1));
                                infil(i-1,:)=(Pr(i-1)+Psc(i-1)+Ps(i-1))-ET1(i-1)-Ru(i-1);
                                if infil(i-1)<0
                                    infil(i-1)=0;
                                end

                                end

                                end

                                end

                                % Setting the value of last iteration
                                % N.B: Consider there is no further steps values for comparison which is
necessary in some calculations of the optimization.
                                % In this step, just the same amount of runoff ratio as former step will be
%used (last j(I)). The applied loop is not necessary. It is just to improve
%code readability and to facilitate eventual improvement to the code.
                                for i=period

                                    Awr(i-1)=Pr(i-1)+Ps(i-1)+Psc(i-1);
                                    if Awr(i-1)==0
                                        Rs(i-1)=0;

```

```

Rr(i-1)=0;
Awet(i-1)=Prc(i-1);
if Awet(i-1)<0
    Awet(i-1)=0;
end
if Awet(i-1)==0
    ETr(i-1)=ET1(i-1);
    ETs(i-1)=0;
else
    ETr(i-1)= ET1(i-1)*(((Pr(i-1)*j(i,I))+Prc(i-1))/Awet(i-1));
    ETs(i-1)= ET1(i-1)*(((Pr(i-1)*j(i,I))+Prc(i-1))/Awet(i-1));
end
else
    Rs(i-1)=(1-j(i,I))*(Ps(i-1)+Psc(i-1)) ;
    Rr(i-1)=(1-j(i,I))* Pr(i-1);
    Awet(i-1)=(j(i,I)*Awr(i-1))+Prc(i-1);
    if Awet(i-1)<0
        Awet(i-1)=0;
    end
    if Awet(i-1)==0
        ETr(i-1)=ET1(i-1);
        ETs(i-1)=0;
    else
        ETr(i-1)= ET1(i-1)*(((Pr(i-1)*j(i,I))+Prc(i-1))/Awet(i-1));
        ETs(i-1)= ET1(i-1)*(((Ps(i-1)+Psc(i-1))*j(i,I))/Awet(i-1));
    end
end
Prc(i)=Prc(i-1)+Pr(i-1)-ETr(i-1)-Rr(i-1);
Psc(i)=Psc(i-1)+Ps(i-1)-ETs(i-1)-Rs(i-1);
if Psc(i)<0
    Psc(i)=0;
end
sts(i,I)=(Prc(i)+Psc(i))*-1.003*9.806;
st(i)=sts(i,I);
model.func('int1').setIndex('table', i, i-1, 0);
model.func('int1').setIndex('table', st(i), i-1, 1);
Ru(i,:)=(1-j(i,I))*(Pr(i)+Psc(i)+Ps(i));
infil(i,:)=(Pr(i)+Psc(i)+Ps(i))-ET1(i)-Ru(i);
%As we have no further steps to use RS, Rr, ETr, ETs, Awet, and Awr
from
%this step, we can calculate them here.
Awr(i)=Pr(i)+Ps(i)+Psc(i);
if Awr(i)==0
    Rs(i)=0;
    Rr(i)=0;

```

```

Awet(i)=Prc(i);
if Awet(i)<0
    Awet(i)=0;
end
if Awet(i)==0
    ETr(i)=ET1(i);
    ETs(i)=0;
else
    ETr(i)= ET1(i)*(((Pr(i)*j(i,I))+Prc(i))/Awet(i));
    ETs(i)= ET1(i)*(((Ps(i)+Psc(i))*j(i,I))/Awet(i));
end
else
    Rs(i)=(1-j(i,I))*(Ps(i)+Psc(i)) ;
    Rr(i)=(1-j(i,I))* Pr(i);
    Awet(i)=(j(i,I)*Awr(i))+Prc(i);
    if Awet(i)<0
        Awet(i)=0;
    end
    if Awet(i)==0
        ETr(i)=ET1(i);
        ETs(i)=0;
    else
        ETr(i)= ET1(i)*(((Pr(i)*j(i,I))+Prc(i))/Awet(i));
        ETs(i)= ET1(i)*(((Ps(i)+Psc(i))*j(i,I))/Awet(i));
    end
end
Prc(i+1)=Prc(i)+Pr(i)-ETr(i)-Rr(i);
Psc(i+1)=Psc(i)+Ps(i)-ETs(i)-Rs(i);
if Psc(i+1)<0
    Psc(i+1)=0;
end
sts(i+1,I)=(Prc(i+1)+Psc(i+1))*-1.003*9.806;
st(i+1)=sts(i+1,I);
end

```

```

% Transposing the result's matrix (N*1----> 1*N)

```

```

Psc=Psc.';
Prc=Prc.';
ETr=ETr.';
ETs=ETs.';
Rr=Rr.';
Rs=Rs.';

```

```

% Saving the model with new changes and running it again and extracting the
results

```


BIBLIOGRAPHY

- Allen, R.G., Pereira, L.S., Raes, D. & Smith, M. (1998). FAO Irrigation and drainage paper. *Food and Agriculture Organization of the United Nations*, 56 (1), 26-40.
- Alonso González, A. (2014). *Multidimensional and temporal SAR data representation and processing based on binary partition trees*. (Doctoral thesis, The Polytechnic University of Catalonia, Barcelona, Spain).
- Andersson-Sköld, Y., Torrance, J. K., Lind, B., Oden, K., Stevens, R. L. & Rankka, K. (2005). Quick clay - A case study of chemical perspective in Southwest Sweden. *Engineering Geology*, 82(2), 107-118.
- Anochikwa, C.I. (2010). *A Coupled Stress-Flow Numerical Modelling Methodology for Identifying Pore-pressure Changes due to Total Soil Moisture Loading*. (Master's, thesis, The University of Saskatchewan, Saskatchewan)
- Anochikwa, C.I., van der Kamp, G. & Barbour, S.L. (2012). Interpreting pore-water pressure changes induced by water table fluctuations and mechanical loading due to soil moisture changes. *Canadian Geotechnical Journal*, 49 (3), 357–366. <https://doi.org/10.1139/t11-106>.
- Atkinson, J.H. (2000). Non-linear soil stiffness in routine design. *Géotechnique*, 50 (5), 487–508. <https://doi.org/10.1680/geot.2000.50.5.487>.
- Atkinson, J.H. & Sallfors, G. (1991). *Experimental determination of soil properties. Paper presented in 10th ECSMFE*, vol. 3, Florence, (pp. 915–956).
- Bailey, B.J. (2017). *Assessing the utility of barometric response functions in estimating hydrogeological parameters of the high plains aquifer*. (M.Sc. thesis, Department of Geology, University of Kansas, Lawrence, Kansas).
- Baracos A. & Bozozuk M. (1957). Seasonal movements in some Canadian clays. *Division of Building Research*, National Research Council.
- Banerjee, P.K. & Stipho, A.S. (1978). Associated and non-associated constitutive relations for undrained behaviour of isotropic soft clays. *International Journal for Numerical and Analytical Methods in Geomechanics*, 2 (1), 35–56. <https://doi.org/10.1002/nag.1610020104>.

- Barr, A.G., van der Kamp, G., Schmidt, R. & Black, T.A. (2000). Monitoring the moisture balance of a boreal aspen forest using a deep groundwater piezometer. *Agricultural and Forest Meteorology*, 102 (1), 13–24. [https://doi.org/10.1016/S0168-1923\(00\)00094-0](https://doi.org/10.1016/S0168-1923(00)00094-0).
- Berardino, P., Fornaro, G., Lanari, R., & Sansosti, E. (2002). A new algorithm for surface deformation monitoring based on small baseline differential SAR interferograms. *IEEE Transactions on Geoscience and Remote Sensing*, 40 (11), 2375-2383. DOI:10.1109/TGRS.2002.803792.
- Bjerrum, L. (1954). Geotechnical properties of Norwegian marine clays. *Géotechnique*, 4(2), 1- 69.
- Bjerrum, L. (1967). Engineering geology of Norwegian normally-consolidated marine clays as related to settlements of buildings. *Géotechnique*, 17(2), 83-118.
- Biot, M.A. (1941). General theory of three-dimensional consolidation. *Journal of Applied Physics*, 12(2), 155–164. DOI:10.1063/1.1712886.
- Biot, M.A. (1955). Theory of elasticity and consolidation for a porous anisotropic solid. *Journal of Applied Physics*, 26(2), 182–185.
- Biot, M.A. (1956). Theory of deformation of a porous viscoelastic anisotropic solid. *Journal of Applied Physics*, 27(5), 459–467.
- Biot, M.A. (1972). Theory of finite deformations of porous solids. *Indiana University Mathematics Journal*, 21(7), 597–620.
- Biot, M.A. (1973). Nonlinear and semilinear rheology of porous solids. *Journal of Geophysical Research*, 78(23), 4924–4937.
- Bohling, G. C., Jin, W. & Butler, J. J. (2011). Kansas geological survey barometric response function software user’s guide. *Kansas Geological Survey Open-File Report 2011-10*.
- Bozozuk M. & Burn K.N. (1960). Vertical ground movements near elm trees. *Géotechnique*, 10(1), 19-32. DOI:10.1680/geot.1960.10.1.19.
- Bozzano, F., Cipriani, I., Mazzanti, P. & Prestininzi, A. (2011). Displacement patterns of a landslide affected by human activities: insights from ground-based InSAR monitoring. *Natural hazards*, 59(3), 1377-1396.
- Brydon, J. E. & Patry L. M. (1961). Mineralogy of Champlain Sea sediments and a Rideau clay soil profile. *Canadian Journal of Soil Science*, 41, 169-181.

- Chapuis, R.P. & Aubertin, M. (2003). On the use of the Kozeny-Carman equation to predict the hydraulic conductivity of soils. *Canadian Geotechnical Journal*, 40 (3), 616-628. <https://doi.org/10.1139/T03-013>.
- Chen, C.H., Tang, C.C., Cheng, K.C., Wang, C.H., Wen, S., Lin, C.H., Wen, Y.Y., Meng, G., Yeh, T.K., Jan, J.C., Yen, H.Y., & Liu, J.Y. (2015). Groundwater-strain coupling before the 1999 Mw7.6 Taiwan Chi-Chi earthquake. *Journal of Hydrology*, 524 (1), 378–384. <https://doi.org/10.1016/j.jhydrol.2015.03.006>.
- Cheng, A.H.D. (2016). *Poroelasticity (Vol. 27)*. Cham, Switzerland: Springer International Publishing.
- Chang, C.M., & Yeh, H.D. (2016). Investigation of flow and solute transport at the field scale through heterogeneous deformable porous media. *Journal of Hydrology*, 540 (1), 142–147. <https://doi.org/10.1016/j.jhydrol.2016.05.060>.
- Cigna, F., Banks, V.J., Donald, A.W., Donohue, S., Graham, C., Hughes, D., McKinley, J.M. & Parker, K. (2017). Mapping ground instability in areas of geotechnical infrastructure using satellite InSAR and Small UAV surveying: A case study in Northern Ireland. *Geosciences*, 7(3), 51.
- CMWgeosciences. (2017). Ground settlement and subsidence. Retrieved from <https://www.cmwgeosciences.com/geotechnical-services/ground-settlement#:~:text=In%20geotechnical%20engineering%20%2C%20settlement%20is,within%20changes%20in%20soil%20stresses>.
- Colesanti, C. & Wasowski, J. (2004). *Satellite SAR interferometry for wide-area slope hazard detection and site-specific monitoring of slow landslides*. Paper presented at Ninth International conference on Symposium on Landslides, (pp. 795-802).
- Colesanti, C., Ferretti, A., Novali, F., Prati, C. & Rocca, F. (2003). SAR monitoring of progressive and seasonal ground deformation using the permanent scatterers technique. *IEEE Transactions on Geoscience and Remote Sensing*, 41 (7), 1685-1701.
- COMSOL AB. (2020a). Heat Transfer Module User's Guide. *COMSOL Multiphysics® v. 5.5*, COMSOL AB, Stockholm, Sweden.
- COMSOL AB. (2020b). Subsurface Flow Module User's Guide. *COMSOL Multiphysics® v. 5.5*, COMSOL AB, Stockholm, Sweden.

- COMSOL AB. (2021). COMSOL Multiphysics 6 Reference Manual. Available from https://doc.comsol.com/6.0/doc/com.comsol.help.comsol/COMSOL_ReferenceManual.pdf
- Cronin, T.M., Manley, P.L., Brachfeld, S., Manley, T.O., Willard, D.A., Guilbault, J.P., Rayburn, J.A., Thunell, R. & Berke, M. (2008). Impacts of post-glacial lake drainage events and revised chronology of the Champlain Sea episode 13–9 ka. *Palaeogeography, Palaeoclimatology, Palaeoecology*, 262(1-2), 46-60.
- Crosetto, M., Crippa, B. & Biescas, E. (2005). Early detection and in-depth analysis of deformation phenomena by radar interferometry. *Engineering Geology*, 79 (1-2): 81-91. DOI:10.1016/j.enggeo.2004.10.016.
- Crosetto, M., Monserrat, O., Cuevas-González, M., Devanthéry, N. & Crippa, B. (2016). Persistent scatterer interferometry: A review. *ISPRS Journal of Photogrammetry and Remote Sensing*, 115: 78-89. doi:10.1016/j.isprsjprs.2015.10.011
- Côté, J. & Konrad, J.M. (2005). Thermal conductivity of base-course materials. *Canadian Geotechnical Journal*, 42(1), 61-78.
- Cote, J. & Konrad, J.M. (2007). Indirect methods to assess the solid particle thermal conductivity of Quebec marine clays. *Canadian Geotechnical Journal*, 44(9), 1117-1127.
- Cui, Z.D., He, P.P. & Yang, W.H. (2014). Mechanical properties of a silty clay subjected to freezing-thawing. *Cold Regions Science and Technology*. 98 (1), 26–34. <https://doi.org/10.1016/j.coldregions.2013.10.009>.
- D'Appolonia, D.J., Poulos, H.G. & Ladd, C.C. (1971). Initial settlement of structures on clay. *Journal of the Soil Mechanics and Foundations Division*, 97(10), 1359-1377.
- D'Amico, F., Gagliardi, V., Ciampoli, L.B. & Tosti, F. (2020). Integration of InSAR and GPR techniques for monitoring transition areas in railway bridges. *NDT & E International*, 115, 102291.
- Das, B.M. & Sivakugan, N. (2016). *Fundamentals of geotechnical engineering*. Cengage Learning.
- Davidovici, V. (1985). *Génie parasismique (1st ed)*. Presses de l'École nationale des ponts et chaussées, Paris.

- Delage, P. (2010). A microstructure approach to the sensitivity and compressibility of some Eastern Canada sensitive clays. *Géotechnique*, 60(5), 353-368.
- Delage, P. & Lefebvre, G. (1984). Study of the structure of a sensitive Champlain clay and of its evolution during consolidation. *Canadian Geotechnical Journal*, 21(1), 21-35.
- Demers, D. and Leroueil, S. (2002). Evaluation of preconsolidation pressure and the overconsolidation ratio from piezocone tests of clay deposits in Quebec. *Canadian Geotechnical Journal*, 39(1), 174-192.
- Demers, D., Robitaille, D., Potvin, J., Bilodeau, C. & Dupuis, C. (2008). *The management of landslide risks in clay soils in Quebec*. Paper presented at 4th Canadian Conference on Geohazards: From Causes to Management. Quebec, Canada.
- Devaraj, S. & Yarrakula, K. (2020). Assessment of topographical and atmospheric errors in Sentinel 1 derived DInSAR. *Geocarto International*, 1-17. DOI:10.1080/10106049.2020.1822926.
- Diab, R., Engineer, P.G., CIE, C.K., LaRoche, M., Director, G.D. & Beaulieu, J.F. (2021). *Geotechnical Design and Construction Challenges of Samuel de Champlain Bridge in Montreal*. Paper presented at Transportation Association of Canada (TAC) 2021, Edmonton, Canada.
- Duhaime, F. (2012). *Mesure de la conductivité hydraulique du dépôt d'argile Champlain de Lachenaie, Québec: théorie et applications* (Doctoral thesis, École Polytechnique de Montréal, Montreal, Québec).
- Duhaime, F., Benabdallah, E.M. & Chapuis, R.P. (2013). The Lachenaie clay deposit: some geochemical and geotechnical properties in relation to the salt-leaching process. *Canadian Geotechnical Journal*, 50(3), 311-325.
- Duhaime, F., Chapuis, R.P., Marefat, V. & Benabdallah, E.M. (2017). Influence of seasonal hydraulic head changes on slug tests conducted in shallow low-permeability soils. *Engineering Geology*, 228, 385-394.
- Dumais, S. & Konrad, J. M. (2018). One-dimensional large-strain thaw consolidation using nonlinear effective stress–void ratio–hydraulic conductivity relationships. *Canadian Geotechnical Journal*, 55(3): 414–426. <https://doi.org/10.1139/cgj-2017-0221>
- Eden, W.J. 1977. Evidence of creep in steep natural slopes of Champlain Sea clay. *Canadian Geotechnical Journal*, 14(4): 620-627.

- Dourado, C.N. (2018). *Characterizing aquitard properties from the response of grouted vibrating wire piezometers to surface loading*. (M.Sc. thesis, Department of Civil and Geological Engineering, University of Saskatchewan, Saskatoon, Saskatchewan).
- Eden, W.J. (1977). Evidence of creep in steep natural slopes of Champlain Sea clay. *Canadian Geotechnical Journal*, 14(4), 620-627.
- Elbeggo, D., Ethier, Y., Karray, M. & Dubé, J.S. (2013). *Shear wave velocity values in Canadian Champlain Sea clays as predicted by empirical correlations*, paper presented in 66th Canadian Geotechnical Conference, GeoMontreal 2013. Montreal, QC.
- Elbeggo, D., Hussien, M.N., Ethier, Y. & Karray, M. (2019). Robustness of the P-RAT in the shear-wave velocity measurement of soft clays. *Journal of Geotechnical and Geoenvironmental Engineering*, 145(5). doi:10.1061/(asce)gt.1943-5606.0002017.
- ElGharbawi, T. & Tamura, M. (2015). Coseismic and postseismic deformation estimation of the 2011 Tohoku earthquake in Kanto Region, Japan, using InSAR time series analysis and GPS. *Remote Sensing of Environment*, 168, 374-387.
- Emery, B. & Camps, A. (2017). *Introduction to satellite remote sensing: atmosphere, ocean, land and cryosphere applications*. Elsevier.
- European Space Agency (2014). Sentinel-1 fuelled and ready. Retrieved from <https://phys.org/news/2014-03-Sentinel-fuelled-ready.html>
- European Space Agency (2021). Sentinel-1 SAR Technical Guide. Retrieved from <https://Sentinels.copernicus.eu/web/Sentinel/technical-guides/Sentinel-1-sar>
- Evans, S.G. (1997). Fatal landslides and landslide risk in Canada 1. In D. Cruden & R. Fell (Eds) *Landslide risk assessment* (pp. 185-196). Routledge.
- Fang, H.Y. (2013). *Foundation engineering handbook*. Springer Science & Business Media.
- Fattahi H. & Amelung F. (2014). InSAR uncertainty due to orbital errors. *Geophysical Journal International*, 199(1): 549-560. doi:10.1093/gji/ggu276.
- Ferretti, A., Prati, C. & Rocca, F. (2001). Permanent scatterers in SAR interferometry. *IEEE Transactions on Geoscience and Remote Sensing*, 39(1): 8-20. DOI: 10.1109/36.898661.

- Ferretti, A., Prati, C., & Rocca, F. (2000). Nonlinear subsidence rate estimation using permanent scatterers in differential SAR interferometry. *IEEE Transactions on Geoscience and Remote Sensing*, 38 (5), 2202-2212. DOI:10.1109/36.868878.
- Ferretti, A. Monti-Guarnieri, A.V., Prati, C.M., Rocca, F. & Massonnet, D. (2007). *INSAR Principles*. ESA publications.
- Ferronato, M., Castelletto, N., Gambolati, G., Janna, C. & Teatini, P. (2013). II cycle compressibility from satellite measurements. *Géotechnique*, 63(6), 479-486.
- Fiaschi, S. & Wdowinski, S. (2020). Local land subsidence in Miami Beach (FL) and Norfolk (VA) and its contribution to flooding hazard in coastal communities along the US Atlantic coast. *Ocean & Coastal Management*, 187.
- Flores-Anderson, A.I., Herndon, K.E., Thapa, R.B. & Cherrington, E. (2019). *The SAR handbook: Comprehensive methodologies for forest monitoring and biomass estimation*(1st ed). National Space Science and Technology Center. DOI: 10.25966/nr2c-s697.
- France24. (2018). A giant sinkhole opens up in drought-hit Iran. Retrieved from <https://observers.france24.com/en/20180827-giant-sinkhole-drought-iran-Hamadan>.
- François, B., Tacher, L., Bonnard, C., Laloui, L. & Triguero, V. (2007). Numerical modelling of the hydrogeological and geomechanical behaviour of a large slope movement: the Triesenberg landslide (Liechtenstein). *Canadian Geotechnical Journal*, 44(7), 840-857.
- Gabriel, A.K., Goldstein, R.M., & Zebker, H.A. (1989). Mapping small elevation changes over large areas: differential radar interferometry. *Journal of Geophysical Research, Solid Earth*, 94 (B7), 9183-9191. DOI:10.1029/JB094iB07p09183.
- Gambolati, G., Teatini, P., Baú, D., & Ferronato, M. (2000). Importance of poroelastic coupling in dynamically active aquifers of the Po river basin, Italy. *Water Resources Research*, 36 (9), 2443–2459. <https://doi.org/10.1029/2000WR900127>.
- Garneau, R., & LeBihan, J.P. (1977). Estimation of some properties of Champlain clays with the Swedish fall cone. *Canadian Geotechnical Journal*, 14(4), 571-581.
- Gowan, E.J., Zhang, X., Khosravi, S., Rovere, A., Stocchi, P., Hughes, A.L., Gyllencreutz, R., Mangerud, J., Svendsen, J.I. & Lohmann, G. (2021). A new global ice sheet reconstruction for the past 80 000 years. *Nature communications*, 12(1), 1-9.

- Hanssen, R.F. (2001). *Radar interferometry: data interpretation and error analysis* (2nd ed). Springer Science & Business Media.
- Hammer M.J. & Thompson O.B. (1966). Foundation clay shrinkage caused by large trees. *Journal of the Soil Mechanics and Foundations Division*, 92(6), 1-17. DOI:10.1061/jsfeaq.0000914.
- Harrington, C.R. (1977). Marine mammals in the Champlain Sea and the Great Lakes. *Annals of the New York Academy of Sciences*, 288(1), 508-537.
- Harp, E.L., Wells, W.G., & Sarmiento, J.G. (1990). Pore pressure response during failure in soils. *Geological Society of America Bulletin*, 102 (4), 428-438. [https://doi.org/10.1130/00167606\(1990\)102%3C0428:PPRDFI%3E2.3.CO;2](https://doi.org/10.1130/00167606(1990)102%3C0428:PPRDFI%3E2.3.CO;2).
- Hendry, M.T., Smith, L.A., & Hendry, M.J. (2017). Analysis of measured pore pressure response to atmospheric pressure changes to evaluate small-strain moduli: methodology and case studies. *Canadian Geotechnical Journal*, 55 (9), 1248–1256. <https://doi.org/10.1139/cgj-2016-0584>.
- Hinchberger, S.D. & Qu, G. (2009). Viscoplastic constitutive approach for ratesensitive structured clays. *Canadian Geotechnical Journal*. 46 (6), 609–626. <https://doi.org/10.1139/T08-133>.
- Hooper, A., Zebker, H., Segall, P. & Kampes, B. (2004). A new method for measuring deformation on volcanoes and other natural terrains using InSAR persistent scatterers. *Geophysical Research Letters*, 31 (23). DOI: 10.1029/2004GL021737
- Hu, J., Li, Z.W., Ding, X.L., Zhu, J.J., Zhang, L. & Sun, Q. (2012). 3D coseismic displacement of 2010 Darfield, New Zealand earthquake estimated from multi-aperture InSAR and D-InSAR measurements. *Journal of Geodesy*, 86(11), 1029-1041.
- Hugenholtz, C. & Lacelle, D. (2004). Geomorphic controls on landslide activity in Champlain Sea clays along Green's Creek, eastern Ontario, Canada. *Géographie physique et Quaternaire*, 58(1), 9-23.
- Intrieri, E., Di Traglia, F., Del Ventisette, C., Gigli, G., Mugnai, F., Luzi, G. & Casagli, N. 2013. Flank instability of Stromboli volcano (Aeolian Islands, Southern Italy): integration of GB-InSAR and geomorphological observations. *Geomorphology*, 201, 60-69.

- Ishihara, K., Shimizu, K., & Yamada, Y. (1981). Pore water pressures measured in sand deposits during an earthquake. *Soils and Foundations*, 21 (4), 85–100. https://doi.org/10.3208/sandf1972.21.4_85.
- Karray, M. & Lefebvre, G. (2001). *Étude parasismique pour l'agrandissement du secteur nord-BFI usine de triage Lachenaie LTEE*. Report GEO-01-07, Varennes, Québec.
- Karray, M., Hussien, M.N., Chekired, M. & Ethier, Y. (2016). *Small strain stiffness and stiffness degradation curve of sensitive Champlain clay*, paper presented at 69th Canadian Geotechnical Conference, GeoVancouver 2016. Vancouver, BC, (P. 498–509).
- Kenney, T.C. (1964). Sea-level movements and the geologic histories of the post-glacial marine soils at Boston, Nicolet, Ottawa and Oslo. *Geotechnique*, 14(3), 203-230.
- Konrad, J.M. (1994). Sixteenth Canadian Geotechnical Colloquium: Frost heave in soils: concepts and engineering. *Canadian Geotechnical Journal*, 31(2), 223-245.
- Konrad, J.M., Roy, M., Rochelle, P.L., Leroueil, S., & Bergeron, G. (1995). Field observations of frost action in intact and weathered Champlain Sea clay. *Canadian Geotechnical Journal*, 32(4), 689-700. <https://doi:10.1139/t95-068>.
- Lafleur, J., Lefebvre, G., Marcotte, M. & Silvestri, V. (1982). Shear strength of the weathered Champlain clay measured in a large diameter triaxial test. *Canadian Geotechnical Journal*, 19(4), 413-420.
- Lazzari, M., Majowiecki, M., Vitaliani, R.V. & Sietta, A.V. (2009). Nonlinear FE analysis of Montreal Olympic Stadium roof under natural loading conditions. *Engineering Structures*, 31(1), 16-31.
- Leroueil, S. (1996). Compressibility of clays: fundamental and practical aspects. *Journal of Geotechnical Engineering*, 122(7), 534-543.
- Leroueil, S., Hamouche, K., Ravenasi, F., Boudali, M., Locat, J., Virely, D., Tan, T., Phoon, K., Hight, D., & Leroueil, S. (2003). Geotechnical characterization and properties of a sensitive clay from Quebec. *Characterization and engineering properties of natural soils*, 363-394.
- Leroueil, S., Tavenas, F., & Le Bihan, J.P. (1983). Characteristic Properties of Eastern Canadian Clays. *Canadian Geotechnical Journal*, 20(4), 681-705. <https://doi.org/10.1139/t94-028>.

- Leroueil, S., Tavenas, F., Samson, L. & Morin, P. (1983). Preconsolidation pressure of Champlain clays. Part II. Laboratory determination. *Canadian Geotechnical Journal*, 20(4), 803-816.
- Leroueil, S., Tavenas, F., Trak, B., La Rochelle, P. & Roy, M. (1978). Construction pore pressures in clay foundations under embankments. Part I: the Saint-Alban test fills. *Canadian Geotechnical Journal*. 15 (1), 54–65. <https://doi.org/10.1139/t78-005>.
- Li, Y., Dijkstra, J. & Karstunen, M. (2018). Thermomechanical creep in sensitive clays. *Journal of Geotechnical and Geoenvironmental Engineering*, 144(11), 04018085.
- Liu, J., Afroz, M. & Ahmad, A. (2021). Experimental investigation of the impact of salinity on Champlain Sea clay. *Marine Georesources & Geotechnology*, 39(4), 494-504.
- Locat, J. (1995). On the development of microstructure in collapsible soils. *Genesis and properties of collapsible soils*, 93-128. Springer, Dordrecht.
- Locat J. & St-Gelais D. (2014) Nature of Sensitive Clays from Québec. In L'Heureux JS., Locat A., Leroueil S., Demers D., Locat J. (Eds), *Landslides in Sensitive Clays. Advances in Natural and Technological Hazards Research*, Vol. 36, pp. 25-37. Dordrech: Springer. https://doi.org/10.1007/978-94-007-7079-9_3.
- Locat A., Leroueil S. & Jostad H.P. (2014). Failure Mechanism of spreads in sensitive clays, in: L'Heureux, J. S., Locat, A., Leroueil, S., Demers, D., Locat, J. (Eds), *Landslides in Sensitive Clays, Advances in Natural and Technological Hazards Research 36*.
- Marefat, V. (2016). *Natural pore pressure fluctuations in a Champlain clay deposit*. (Doctoral thesis, Département des Génies Civil, École Polytechnique de Montréal, Montréal, Québec).
- Marefat, V., Duhaime, F. & Chapuis, R.P. (2015). Pore pressure response to barometric pressure change in Champlain clay: prediction of the clay elastic properties. *Engineering Geology*. 198 (1), 16–29. <https://doi.org/10.1016/j.enggeo.2015.09.005>.
- Marefat, V., Duhaime, F., Chapuis, R.P. & Le Borgne, V. (2019). Performance of fully grouted piezometers under transient flow conditions: field study and numerical results. *Geotechnical Testing Journal*. 42 (2), 433-456. <https://doi.org/10.1520/GTJ20170290>.
- Marin, S., van der Kamp, G., Pietroniro, A., Davison, B., & Toth, B. (2010). Use of geological weighing lysimeters to calibrate a distributed hydrological model for the simulation of land-atmosphere moisture exchange. *Journal of Hydrology*, 383 (3-4), 179–185. <https://doi.org/10.1016/j.jhydrol.2009.12.034>.

- Massonnet, D., Rossi, M., Carmona, C., Adragna, F., Peltzer, G., Feigl, K., & Rabaute, T. (1993). The displacement field of the Landers earthquake mapped by radar interferometry. *Nature*, *364*(6433). DOI:10.1038/364138a0.
- Mavko, G.M., & Harp, E.D. (1984). Analysis of wave-induced pore pressure changes recorded during the 1980 Mammoth Lakes, California, earthquake sequence. *Bulletin of the Seismological Society of America*, *74* (4), 1395-1407.
- McKinstry, H.A. (1965). Thermal expansion of clay minerals. *American Mineralogist: Journal of Earth and Planetary Materials*, *50*(1-2): 212-222.
- Mesri, G., & Choi, Y.K. (1985). Settlement analysis of embankments on soft clays. *Journal of Geotechnical Engineering*, *111*(4), 441-464.
- Méto. (2012). Quel lézard, ma maison se lézarde. Retrieved from <https://journalmetro.com/local/pointe-aux-trembles-montreal-est/623627/quel-lezard-ma-maison-se-lezarde/>.
- Milillo, P., Giardina, G., DeJong, M.J., Perissin, D. & Milillo, G. (2018). Multi-temporal InSAR structural damage assessment: The London crossrail case study. *Remote Sensing*, *10*(2), 287.
- Minh, D.H.T., Hanssen, R., & Rocca, F. (2020). Radar Interferometry: 20 Years of Development in Time Series Techniques and Future Perspectives. *Remote Sensing*, *12*(9), 1364. DOI:10.3390/RS12091364.
- Mora, O., Mallorqui, J.J., & Broquetas, A. (2003). Linear and nonlinear terrain deformation maps from a reduced set of interferometric SAR images. *IEEE Transactions on Geoscience and Remote Sensing*, *41* (10), 2243-2253. DOI:10.1109/TGRS.2003.814657.
- Morin, J.P., & Gervais, R. (1987). Settlement record of tower silos built on Champlain clays. *Canadian Geotechnical Journal*, *24*(4), 490-498.
- Morin, P., Leroueil, S. & Samson, L. (1983). Preconsolidation pressure of Champlain clays. Part I. In-situ determination. *Canadian Geotechnical Journal*, *20*(4), 782-802.
- Morissette, L., St-Louis, M.W. & McRostie, G.C. (2001). Empirical settlement predictions in overconsolidated Champlain Sea clays. *Canadian geotechnical journal*, *38*(4), 720-731.

- Murdoch, L.C., Freeman, C.E., Germanovich, L.N., Thrash, C., & DeWolf, S. (2015). Using in situ vertical displacements to characterize changes in moisture load. *Water Resources Research*, 51 (8), 5998-6016. <https://doi.org/10.1002/2015WR017335>.
- Nader, A. (2014). *Engineering Characteristics of Sensitive Marine Clays-Examples of Clays in Eastern Canada*. (Doctoral dissertation, Université d'Ottawa/University of Ottawa, Ottawa, Ontario).
- Neuzil, C.E. (2003). Hydromechanical coupling in geologic processes. *Hydrogeology Journal*, 11 (1), 41-83. DOI:10.1007/s10040-002-0230-8.
- Normand J.C. & Heggy E. (2015). InSAR assessment of surface deformations in urban coastal terrains associated with groundwater dynamics. *IEEE Transactions on Geoscience and Remote Sensing*, 53(12), 6356-6371. DOI:10.1109/TGRS.2015.2437368.
- Novellino, A., Cesarano, M., Cappelletti, P., Di Martire, D., Di Napoli, M., Ramondini, M., Sowter, A. & Calcaterra, D. (2021). Slow-moving landslide risk assessment combining Machine Learning and InSAR techniques. *Catena*, 203, 105317.
- Nur, A., & Byedee, J.D. (1971). An exact effective stress law for elastic deformation of rock with fluid. *Geophysics*, 76, 6414–6419.
- Occhietti, S. (1989). Quaternary geology of St. Lawrence Valley and adjacent Appalachian subregion. J. Fulton (ed.), *The Quaternary of Canada and Greenland*. Ottawa, Canada: Geological Survey of Canada.
- Osmanoğlu, B., Dixon, T.H., Wdowinski, S., Cabral-Cano, E. & Jiang, Y. (2011). Mexico City subsidence observed with persistent scatterer InSAR. *International Journal of Applied Earth Observation and Geoinformation*, 13(1), 1-12.
- O'Shaughnessy, V. & Garga, V.K. (1994). The hydrogeological and contaminant-transport properties of fractured Champlain Sea clay in Eastern Ontario. Part 1. *Hydrogeological properties*. *Canadian geotechnical journal*, 31(6), 885-901.
- Ouchi, K. (2013). Recent trend and advance of synthetic aperture radar with selected topics. *Remote Sensing*, 5(2), 716-807.
- Pacheco, F.A.L., & Fallico, C. (2015). Hydraulic head response of a confined aquifer influenced by river stage fluctuations and mechanical loading. *Journal of Hydrology*, 531 (3), 716–727. <https://doi.org/10.1016/j.jhydrol.2015.10.055>.

- Parent, M. & Occhietti, S. (1988). Late Wisconsinan deglaciation and Champlain sea invasion in the St. Lawrence valley, Québec. *Géographie physique et Quaternaire*, 42(3), 215-246.
- Peduto, D., Huber, M., Speranza, G., van Ruijven, J. & Cascini, L. (2017). DInSAR data assimilation for settlement prediction: case study of a railway embankment in the Netherlands. *Canadian Geotechnical Journal*, 54(4), 502-517.
- Penner, E. (1962). Thermal conductivity of saturated Leda clay. *Géotechnique*, 12(2), 168-175.
- Penner, E. (1970). Thermal conductivity of frozen soils. *Canadian Journal of Earth Sciences*, 7(3), 982-987.
- Perissin D. (2016) Interferometric SAR Multitemporal Processing: Techniques and Applications. In: Ban Y. (eds), *Multitemporal Remote Sensing: methods and applications*, vol 20. Springer, Cham. https://doi.org/10.1007/978-3-319-47037-5_8
- Perissin, D. (2019). SARPROZ software manual, <https://www.sarproz.com/software-manual/>
- Perissin, D., Wang, Z. & Wang, T. (2011). *The SARPROZ InSAR tool for urban subsidence/manmade structure stability monitoring in China*. Paper presented at International Symposium on Remote Sensing of Environment, Sidney, Australia, 1015.
- Prest, V. K., & Hode-Keyser, J. (1977). Geology and engineering characteristics of surficial deposits, Montreal Island and vicinity. *Geological Survey of Canada*, 75-27.
- Quigley, R.M. (1980). Geology, mineralogy, and geochemistry of Canadian soft soils: a geotechnical perspective. *Canadian Geotechnical Journal*. 17 (2), 261–285. <https://doi.org/10.1139/t80-026>.
- Raes, D. (2012). The ETo calculator reference manual version 3.2. Food and agriculture organization of the United Nations, Land and Water Division, Rome.
- Radio Canada. (2021). Des maisons endommagées à Montréal. Retrived from <https://ici.radio-canada.ca/tele/le-telejournal-18h/site/segments/reportage/371185/fissure-maison-effondrement-secheresse-propiretaire>.
- Raspini, F., Loupasakis, C., Rozos, D., Adam, N. & Moretti, S. (2014). Ground subsidence phenomena in the Delta municipality region (Northern Greece): Geotechnical modelling and validation with Persistent Scatterer Interferometry. *International Journal of Applied Earth Observation and Geoinformation*, 28, 78-89.

- Rayburn, J.A., Thunell, R. & Berke, M. (2008). Impacts of post-glacial lake drainage events and revised chronology of the Champlain Sea episode 13–9 ka. *Palaeogeography, Palaeoclimatology, Palaeoecology*, 262(1-2), 46-60.
- Reinders, K.J., Hanssen, R.F., van Leijen, F.J. & Korff, M. (2021). Augmented satellite InSAR for assessing short-term and long-term surface deformation due to shield tunnelling. *Tunnelling and Underground Space Technology*, 110, 103745.
- Rice, J.R. & Cleary, M.P. (1976). Some basic stress diffusion solutions for fluid-saturated elastic porous media with compressible constituents. *Reviews of Geophysics*, 14(2), 227–241.
- Richard, P.J. & Occhietti, S. (2005). 14C chronology for ice retreat and inception of Champlain Sea in the St. Lawrence Lowlands, Canada. *Quaternary Research*, 63(3), 353-358.
- Riedel, B. & Walther, A. (2008). InSAR processing for the recognition of landslides. *Advances in Geosciences*, 14, 189-194.
- Risser, D.W., Gburek, W.J. & Folmar, G.J. (2005). *Comparison of methods for estimating ground-water recharge and base flow at a small watershed underlain by fractured bedrock in the eastern United States* (Vol. 5038). US Department of the Interior, US Geological Survey.
- Ritter, S. & Frauenfelder, R. (2021). InSAR monitoring data to assess building response to deep excavations. In IOP Conference Series: *Earth and Environmental Science*, 18th Nordic Geotechnical Meeting (pp. 012036). IOP Publishing.
- Quigley, R.M. (1980). Geology, mineralogy, and geochemistry of Canadian soft soils: a geotechnical perspective1. *Canadian Geotechnical Journal*, 17, 261–285. Available from <http://www.nrcresearchpress.com/doi/pdf/10.1139/t80-026>.
- Robertson, P. (2007). Seismic design for Liquefaction. Available from http://www.cpt-robertson.com/pdfs/seisdesign_liq07.pdf.
- La Rochelle, P., Trak, B., Tavenas, F. & Roy, M. (1974). Failure of a test embankment on a sensitive Champlain clay deposit. *Canadian Geotechnical Journal*. 11 (1), 142–164. <https://doi.org/10.1139/t74-009>.
- Rosenqvist, I.T. (1946). Om leires kvikkaghtighet. *Statens Vegvesen Veglaboratoriet Meddelen*. 4, 5-12.

- RST Instruments, (2019). VW2100 vibrating wire piezometer instruction manual. RST Instruments LTD, Maple Ridge.
- Russell, H.A.J., Brooks, G.R. & Cummings, D.I. (2011). *Deglacial history of the Champlain Sea basin and implications for urbanization*. Paper presented at the Joint annual meeting GAC-MAC-SEG-SGA, Ottawa, Ontario (p. 96).
- Savvaïdis, P.D. (2003). Existing landslide monitoring systems and techniques. *From stars to earth and culture*, 242-258.
- Savitzky, A. & Golay, M.J.E. (1964). Smoothing and differentiation of data by simplified least squares procedures. *Analytical Chemistry*. 36 (8), 1627–1639. <https://doi.org/10.1021/ac60214a047>.
- Seed, H.B., Wong, R.T., Idriss, I.M. & Tokimatsu, K. (1986). Moduli and damping factors for dynamic analyses of cohesionless soils. *Journal of geotechnical engineering*, 112(11), 1016-1032. [https://doi.org/10.1061/\(ASCE\)0733-9410\(1986\)112:11\(1016\)](https://doi.org/10.1061/(ASCE)0733-9410(1986)112:11(1016)).
- Shafaei, A., Duhaime, F. & Marefat, V. (2018). *Numerical simulation of pore pressure changes in Champlain clays - Sainte-Marthe study case*. Paper presented at the 71th Annual Canadian Geotechnical Conference, GeoEdmonton 2018, GeoEdmonton, AB.
- Shafaei, A., Duhaime, F., Baraër, M., & Marefat, V. (2019). *Runoff and infiltration estimates based on pore pressure changes in shallow aquitards*. Paper presented at the 72st Canadian Geotechnical Conference, GeoSt.Johns 2019, St. John's, NL.
- Sharma, H.D., Dukes, M.T. & Olsen, D.M. (1990). Field measurements of dynamic moduli and Poisson's ratios of refuse and underlying soils at a landfill site, In: Landva, A. (Eds), *Geotechnics of Waste Fills—Theory and Practice*. ASTM International., West Conshohocken, (pp. 57–70). <https://doi.org/10.1520/stp25299s>.
- Shibuya, S. (2000). Assessing Structure of Aged Natural Sedimentary Clays. *Soils and Foundations*, 40(3), 1-16.
- Shimoni, M., Lopez, J., Walstra, J., Declercq, P.Y., Bejarano-Urrego, L., Verstrynge, E., Derauw, D., Hayen, R. & Van Balen, K. (2017). *GEPATAR: a geotechnical based PS-InSAR toolbox for architectural conservation in Belgium*. Paper presented in In 2017 IEEE International Geoscience and Remote Sensing Symposium (IGARSS) (pp. 5555-5558). IEEE.
- Silvestri, V. (2000). Performance of shallow foundations on clay deposits in Montréal Island. *Canadian Geotechnical Journal*, 37(1), 218-237.

- Silvestri, V. (2003). Assessment of self-boring pressuremeter tests in sensitive clay. *Canadian Geotechnical Journal*, 40 (2), 362–387. <https://doi.org/10.1139/t02-121>.
- Silvestri, V., Tabib, C., & Behidj, F. (1994). Observations and modelling of soil water content changes around trees. *Canadian Journal of Civil Engineering*, 21(6), 980–989. DOI:10.1139/194-103.
- Silvestri, V., & Abou-Samra, G. (2008). Analysis of instrumented sharp cone and pressuremeter tests in stiff sensitive clay. *Canadian Geotechnical Journal*, 45(7), 957-972.
- Silvestri, V., Soulie, M., Lafleur, J., Sarkis, G. & Bekkouche, N. (1990). Foundation problems in Champlain clays during droughts. I: rainfall deficits in Montréal (1930–1988). *Canadian Geotechnical Journal*, 27(3), 285-293.
- Silvestri, V., Soulié, M., Lafleur, J., Sarkis, G. & Bekkouche, N. (1992). Foundation problems in Champlain clays during droughts. II. Case histories. *Canadian Geotechnical Journal*, 29(2), 169-187.
- Skempton, A.W., & Bjerrum, L. (1957). A contribution to the settlement analysis of foundations on clay. *Géotechnique*, 7 (4), 168–178. <https://doi.org/10.1680/geot.1957.7.4.168>
- Skempton, A. W., & Northey, R. D. (1952). Sensitivity of clays. *Géotechnique*, 3(1), 30-53.
- Schmertmann, J.H. (1978). Guidelines for cone penetration test: performance and design (No. FHWA-TS-78-209). United States. Federal Highway Administration.
- Smith, L.A., van der Kamp, G. & Jim Hendry, M. (2013). A new technique for obtaining high-resolution pore pressure records in thick claystone aquitards and its use to determine in situ compressibility. *Water Resources Research*, 49 (2), 732–743. <https://doi.org/10.1002/wrcr.20084>.
- Smith, C.D., Kontu, A., Laffin, R. & Pomeroy, J.W. (2017a). An assessment of two automated snow water equivalent instruments during the WMO Solid Precipitation Intercomparison Experiment. *The Cryosphere*, 11 (1), 101–116. <https://doi.org/10.5194/tc-11-101-2017>.
- Smith, C.D., van der Kamp, G., Arnold, L. & Schmidt, R. (2017b). Measuring precipitation with a geolysimeter. *Hydrology and Earth System Sciences*, 21 (10), 5263–5272. <https://doi.org/10.5194/hess-21-5263-2017>.

- SNC-Lavalin Group Inc. (2005). *Étude d'impact sur l'environnement-Addition de réservoirs de produits pétroliers à la raffinerie de Petro-Canada à Montréal* (Rapport principal: Petro-Canada no 603809). Montreal: SNC-Lavalin Environnement Inc.
- Sophocleous, M., Bardsley, E., & Healey, J. (2006). A rainfall loading response recorded at 300 meters depth: Implications for geological weighing lysimeters. *Journal of Hydrology*, 319 (1-4), 237–244. <https://doi.org/10.1016/j.jhydrol.2005.06.031>.
- SpacingMontreal. (2010). Down in the Dumps of Pointe-Saint-Charles history. Retrieved from <http://spacing.ca/montreal/2010/12/27/down-in-the-dumps-of-pointe-saint-charles-history>.
- Taechakumthorn, C. & Rowe, R.K. (2012). Performance of a reinforced embankment on a sensitive Champlain clay deposit. *Canadian Geotechnical Journal*. 49 (8), 917–927. <https://doi.org/10.1139/T2012-053>.
- Tavenas, F., Chagnon, J.Y. & Rochelle, P.L. (1971). The Saint-Jean-Vianney landslide: observations and eyewitnesses accounts. *Canadian Geotechnical Journal*, 8(3), 463-478.
- Tavenas, F., Chapeau, C., La Rochelle, P. & Roy, M. (1974). Immediate settlements of three test embankments on Champlain clay. *Canadian Geotechnical Journal*. 11 (1), 109–141. <https://doi.org/10.1139/t74-008>.
- Tavenas, F., Jean, P., Leblond, P. & Leroueil, S. (1983). The permeability of natural soft clays. Part II: Permeability characteristics. *Canadian Geotechnical Journal*, 20(4), 645-660.
- Tavenas, F., Mieussens, C. & Bourges, F. (1979). Lateral displacements in clay foundations under embankments. *Canadian Geotechnical Journal*. 16 (3), 532–550. <https://doi.org/10.1139/t79-059>.
- Tavenas, F.A., Blanchette, G., Leroueil, S., Roy, M. & Rochelle, P. L. (1975). Difficulties in the in situ determination of K_0 in soft sensitive clays. In N.C Raleigh (Eds), *In Situ Measurement of Soil Properties.*, (pp. 450).
- Terzaghi, K. (1925). The Terzaghi Theory of Effective Stress. In V.I. Osipov (Ed.), *Physicochemical Theory of Effective Stress in Soils*. (pp. 1–55). Springer Briefs in Earth Sciences.
- Terzaghi, K. (1943). Theory of consolidation. *Theoretical Soil Mechanics* (pp.265-296). Chapman and Hall. doi:10.1680/geot.1964.14.1.1.

- The commercial law practice. (2021). Subsidence or settlement . Retrieved from <https://thecommerciallawpractice.com/subsidence-or-settlement>.
- Theis, C. V. (1935). The relation between the lowering of the piezometric surface and the rate and duration of discharge of a well using ground-water storage. *Eos, Transactions American Geophysical Union*, 16 (2), 519–524. <https://doi.org/10.1029/TR016i002p00519>.
- Tizzani, P., Berardino, P., Casu, F., Euillades, P., Manzo, M., Ricciardi, G.P., Zeni, G., & Lanari, R. (2007). Surface deformation of long valley caldera and mono basin, California, investigated with the SBAS-InSAR approach. *Remote Sensing of Environment*, 108(3), 277-289. DOI:10.1016/j.rse.2006.11.015.
- Tofani, V., Raspini, F., Catani, F. & Casagli, N. (2013). Persistent Scatterer Interferometry (PSI) technique for landslide characterization and monitoring. *Remote Sensing*, 5(3), 1045-1065.
- Toll, N.J. & Rasmussen, T.C. (2007). Removal of barometric pressure effects and earth tides from observed water levels. *Ground Water*. 45 (1), 101–105. <https://doi.org/10.1111/j.1745-6584.2006.00254.x>.
- Torrance, J.K. (1975). On the role of chemistry in the development and behavior of the sensitive marine clays of Canada and Scandinavia. *Canadian Geotechnical Journal*, 12(3), 326-335.
- Torrance, J.K. (1983). Towards a general model of quick clay development. *Sedimentology*, 30(4), 547-555.
- Torrance, J.K. & Kirkpatrick, R. (2004). Detrital ooids of Holocene age in glaciomarine Champlain Sea sediments, Gatineau, Quebec, Canada. *Canadian Journal of Earth Sciences*, 41(6), 765-773.
- Usai, S. (2001). A new approach for longterm monitoring of deformations by differential SAR interferometry. Ph.D. thesis, *Department of Applied Sciences, Delft University of Technology*, Delft, Netherlands.
- van der Kamp, G. (2001). Methods for determining the in situ hydraulic conductivity of shallow aquitards - an overview. *Hydrogeology Journal*, 9 (1), 5–16. <https://doi.org/10.1007/s100400000118>.

- van der Kamp, G. & Gale, J.E. (1983). Theory of earth tide and barometric effects in porous formations with compressible grains. *Water Resources Research*, 19(2): 538–544. DOI:10.1029/WR019i002p00538.
- van der Kamp, G., & Maathuis, H. (1991). Annual fluctuations of groundwater levels as a result of loading by surface moisture. *Journal of Hydrology*, 127 (1-4), 137–152. [https://doi.org/10.1016/0022-1694\(91\)90112-U](https://doi.org/10.1016/0022-1694(91)90112-U).
- van der Kamp, G., & Schmidt, R. (1997). Monitoring of total soil moisture on a scale of hectares using groundwater piezometers. *Geophysical Research Letters*, 24 (6), 719–722. <https://doi.org/10.1029/97GL00521>.
- van der Kamp, G., & Schmidt, R. (2017). Review: Moisture loading-the hidden information in groundwater observation well records. *Hydrogeology Journal*, 25 (8), 2225–2233. <https://doi.org/10.1007/s10040-017-1631-z>.
- Verruijt, A. (1969). Elastic storage of aquifers. In: R. J. M. De Wiest (ed), *Flow through porous media* (pp 331–336).
- Walter, D. & Busch, W. (2012). Influences of DEM quality parameters on the topographic phase correction in DInSAR. *2012 IEEE International Geoscience and Remote Sensing Symposium*, July (pp. 3927-3930). IEEE.
- Wang, H. F. (2000). *Theory of linear poroelasticity with applications to geomechanics and hydrogeology*. Princeton University Press, Princeton, New Jersey.
- Wang, S., Yang, Z.J. & Yang, P. (2017). Structural change and volumetric shrinkage of clay due to freeze-thaw by 3D X-ray computed tomography. *Cold Regions Science and Technology*, 138, 108-116. <https://doi.org/10.1016/j.coldregions.2017.03.007>.
- Wang, C., Li, S., Lai, Y., Chen, Q., He, X., Zhang, H., & Liu, X. (2022). Predicting the Soil Freezing Characteristic From the Particle Size Distribution Based on Micro-Pore Space Geometry. *Water Resource Research*, 58(1), 1–15. <https://doi.org/10.1029/2021WR030782>.
- Werner, C., Wegmuller, U., Strozzi, T., & Wiesmann, A. (2003). *Interferometric point target analysis for deformation mapping*. Paper presented at International Geoscience and Remote Sensing Symposium. 10.1109/IGARSS.2003.1295516.
- Yague-Martinez, N., De Zan, F. & Prats-Iraola, P. (2017). Coregistration of interferometric stacks of Sentinel-1 TOPS data. *IEEE Geoscience and Remote Sensing Letters*, 14(7): 1002-1006. doi:10.1016/0016-7061(72)90014-6.

- Yong, R.N. & Silvestri, V. (1979). Anisotropic behaviour of a sensitive clay. *Canadian Geotechnical Journal*, 16 (2), 335-350. <https://doi.org/10.1139/t79-033>.
- Yu, F., Guo, P., Lai, Y., & Stolle, D. (2020). Frost heave and thaw consolidation modelling. Part 1: A water flux function for frost heaving. *Canadian Geotechnical Journal*, 57(10), 1581–1594. <https://doi.org/10.1139/cgj-2019-0218>.
- Yu, F., Guo, P., Lai, Y., & Stolle, D. (2020). Frost heave and thaw consolidation modelling. Part 2: One-dimensional thermohydromechanical (THM) framework. *Canadian Geotechnical Journal*, 57(10), 1595–1610. <https://doi.org/10.1139/cgj-2019-0218>.
- Zdravkovic, L., Potts, D. M. & Jardine, R. J. (2001). A parametric study of the pull-out capacity of bucket foundations in soft clay. *Géotechnique*, 51 (1), 55-67.
- Zeitoun, D.G. & Wakshal, E. (2013). *Land subsidence analysis in urban areas : the Bangkok metropolitan area case study*. Springer Science & Business Media. Available from <https://link.springer.com/book/10.1007%2F978-94-007-5506-2>.
- Zebker, H.A., Rosen, P.A., Goldstein, R.M., Gabriel, A., & Werner, C.L. (1994). On the derivation of coseismic displacement fields using differential radar interferometry: The Landers earthquake. *Journal of Geophysical Research: Solid Earth*, 99 (B10), 19617-19634. doi:10.1029/94jb01179.
- Zebker, H.A., Rosen, P.A., & Hensley, S. (1997). Atmospheric effects in interferometric synthetic aperture radar surface deformation and topographic maps. *Journal of geophysical research: solid earth*, 102(B4),7547-7563. DOI:10.1029/96jb03804.

